# Bistatic Processing - Analysis and Verification

Koba Natroshvili

*A dissertation submitted to the*
University of Siegen
*in partial fulfillment of the requirements for the degree of*
Doktor-Ingenieur (Dr.-Ing.) in Electrical Engineering

Supervisors:

1. Prof. Dr.-Ing. habil. O. Loffeld

2. Prof. Dr.-Ing. J. Ender

IPP Multi Sensorics, Center for Sensor Systems (ZESS)
Department of Electrical Engineering
University of Siegen

Date of Oral Examination: 21 Dec 2007

# Acknowledgments

This doctoral work is the result of my work on the Bistatic Synthetic Aperture Radar focusing problem at the Zentrum für Sensorsysteme (ZESS).

My special thanks are addressed to Prof. Otmar Loffeld for offering me the PhD position within the International Postgraduate Programme "Multi Sensorics" and for motivating and supporting me during all these years. Despite of his busy schedule he was always ready to discuss my ideas and to give his critical comments on the results of different implementations.

I want to express my gratitude to my second supervisor, Prof. Joachim Ender from Forschungsgesellschaft für angewandte Naturwissenschaften e.v. (FGAN) for encouraging my experimental and theoretical studies.

All the presented results would not have been possible without the great help of the ZESS staff who always assisted me and gave me help, if necessary. I am especially thankful to Dr. Stefan Knedlik and Silvia Niet-Wunram for the help in all paper work during my stay at ZESS.

I cannot list here all the names, but I would still like to mention a few colleagues from SAR group: Dr. Holger Nies, Dr. Robert Wang, Amaya Medrano-Ortiz, Ulrich Gebhardt, Valery Peters. Thank you for all the information you provided me and for your great friendship.

I am grateful to Prof. Fabio Rocca from Milan Polytechnic University; Prof. Frank H. Wong, Prof. I. Cumming and Dr. Yew Lam Neo from University of British Columbia; Prof. Bernhard Bundschue from Technical Highschool of Meserburg; Prof. Mihai Datcu, Prof. Richard Bamler and Prof. Alberto Moreira from DLR (Germany Aerospace Center) for diverse discussions and useful ideas that inspired my doctoral work.

The greatest motivation for my PhD studies I received from my wife Shorena and my daughter Elene.

Thank you again for your support, understanding and great patience!

# Abstract

Interest in Bistatic and Multistatic SAR (Synthetic Aperture Radar) systems has grown in the last decade. They bring additional benefits to conventional monostatic SAR systems, such as flexibility, cost reduction, reduced vulnerability, etc. At the same time, processing complexity for bistatic configurations is much higher than for conventional monostatic processors. Until now only some numerical and intuitive solutions were given in this respect. No analytical solution is available.

In this work we will focus on bistatic SAR processing problems. The algorithms we will develop are based on a point target reference spectrum derived at our research institute. In the beginning we will derive the bistatic formula itself, which contains quite lengthy and complex mathematical expressions. In the derivation, some approximations are used. We will therefore consider the constraints of validity. Later, we will demonstrate the performance of the bistatic formula with simulation by focusing the single and group of point targets.

In the very general arbitrary configuration, the processing is range and azimuth time dependent. We will focus on increased complexity configurations. In this respect, we will first consider the Tandem case and the translationally invariant case. Later, we will extend the focusing task to the general case, which is the most challenging bistatic configuration. This will be accomplished by compensating the scaling in both range and azimuth directions. Here, transmitter and receiver are moving on non-parallel trajectories with non-equal velocities. We will see that azimuth time variance causes additional scaling of Doppler frequency. As the first approximation, the focusing of the general bistatic SAR will be solved by separating the scaling in range and azimuth frequency directions.

Some modules of our current bistatic algorithm will be substituted later by a truly 2D scaling approach. We will derive the 2D Inverse Scaling approach and show some focusing results obtained from simulated raw data.

# Kurzfassung

Das Interesse an bi- und multistatischen SAR (Synthetic Aperture Radar) Systemen ist im letztem Jahrzehnt stark angewachsen. Diese neuartigen SAR-Systeme, bei denen sich Sender und Empfänger an unterschiedlichen Positionen befinden, weisen bezüglich konventioneller monostatischer Systeme zusätzliche Vorteile auf, wie beispielsweise höhere Flexibilität, Kostenreduktion, höhere Ausfallsicherheit, etc.

Gleichzeitig ist die Komplexität der SAR-Prozessierung für bistatische Anordnungen weit aus größer als es für die gängigen monostatischen Prozessoren der Fall ist. Bisher sind in diesem Zusammenhang nur einige numerische und intuitive Lösung bekannt. Es steht keine analytische Lösung zur Verfügung.

Der Schwerpunkt dieser Arbeit liegt auf den Problemen der bistatischen SAR-Verarbeitung. Die entwickelten Algorithmen basieren auf dem bistatischen Punktziel-Referenzspektrum, welches im Zentrum für Sensorsysteme (ZESS) hergeleitet wurde. Zuerst wird die bistatische Formel hergeleitet, welche einige längliche und mathematisch komplexe Ausdrücke aufweist. Diese Herleitung enthält einige Näherungen, so dass auch Gültigkeitskriterien für allgemeine bistatische Anordnungen berücksichtigt und erfüllt werden müssen. Später wird die Leistungsfähigkeit der bistatischen Formel durch die Fokussierung einzelner und gruppierten Punktzielen simulativ überprüft.

Im allgemeinen Fall (ungleicher Geschwindigkeitsvektoren für Sender und Empfänger) ist die bistatische Prozessierung Entfernungs- und Azimutzeitabhängig. Die Prozessierung solcher höher komplexen Anordnungen ist ebenfalls Teil dieser Arbeit. Beginnend mit Anordnungen mit konstantem Differenzvektor zwischen Sender und Empfänger wird der Fokussierungsalgorithmus auf den allgemeinen Fall erweitert. Es zeigt sich, dass die Azimutzeitvarianz eine zusätzliche Dopplerfrequenzskalierung hervorruft, so dass bei dem allgemeinen bistatischen Fall eine Reskalierung in Richtung beider Frequenzachsen erfolgen muss.

Als ein erster Ansatz zur Fokussierung von bistatischen SAR-Daten wird eine getrennte Skalierung in Entfernung- und Azimutfrequenzrichtung durchgeführt. Einige Module des bistatischen Algorithmus werden später durch einen 2D-Skalierungsansatz ersetzt. Dabei wird der 2D-Inverse-Scaling-Ansatz hergeleitet und einige Fokussierungsergebnisse, welche durch simulierte Rohdaten gewonnen wurden, gezeigt.

# Abbreviations

| | |
|---|---|
| ASI | Agenzia Spaziale Italiana (Italian Space Agency) |
| BPTRS | Bistatic Point Target Reference Spectrum |
| CS | Chirp Scaling |
| CNES | Centers National d'Etudes Spatiales (French Space Agency) |
| DEM | Digital Elevation Model |
| dB | Decibel |
| DLR | Deutsches Zentrum für Luft- und Raumfahrt (Germany Aerospace Center) |
| EADS | European Aeronautic Defense and Space Company |
| ERS | European Remote Sensing Satellite |
| FGAN | Forschungsgesellschaft für Angewandte Naturwissenschaften (Research Establishment for Applied Natural Sciences) |
| FHR | Forschungsinstitut für Hochfrequenzphysik und Radartechnik (Research Institute for High Frequency Physics and Radar Techniques) |
| FFT | Fast Fourier Transformation |
| GPS | Global Positioning and Navigation System |
| GC | General Case |
| IDL | Interactive Data Language |
| InSAR | Interferometric Synthetic Aperture Radar |
| IS | Inverse Scaling |
| IFFT | Inverse Fast Fourier Transformation |
| INS | Inertial Navigation System |
| ISLR | Integrated Side Lob Ratio |
| J-ERS | Japanese Remote Sensing Satellite |
| MPTRS | Monostatic Point Target Reference Spectrum |
| MSP | Method of the Stationary Phase |
| PT | Point Target |
| PCA | Point of Closest Approach |
| PSP | Point of Stationary Phase |
| PTR | Point Target Response |
| PSLR | Peak Side Lobe Ratio |
| PRF | Pulse Repetition Frequency |
| SRTM | Shuttle Radar Topography Mission |
| SAR | Synthetic Aperture Radar |
| TI | Translationally Invariant |
| ZESS | Zentrum für Sensorsysteme (Center for Sensorsystems) |

# Notations

| | |
|---|---|
| $\tau$ | Azimuth (slow) time |
| $t$ | Range (fast) time |
| $f$ | Range frequency |
| $f_\tau$ | Azimuth frequency |
| $c$ | Speed of light in vacuum |
| $P(R_{0R}, \tau_{0R})$ | Point target location (given in the receiver's coordinates) |
| $R_{0R}$ | Slant range at the receiver's point of closest approach |
| $\tau_{0R}$ | Azimuth time as the point of closest approach is reached |
| $R_0$ | Slant range of closest approach (monostatic case) |
| $R_0(\min)$ | Minimum slant range of the complete footprint (monostatic case) |
| $\tau_0$ | Azimuth time at the point of closest approach (monostatic case) |
| $\vec{v}_R$, $\vec{v}_T$ | Receiver's and transmitter's velocity vectors |
| $v_R$, $v_T$ | Receiver's and transmitter's velocities (magnitudes) |
| $\vec{R}_R(\tau, R_{0R}, \tau_{0R})$ | Receiver's slant range vector |
| $\vec{R}_T(\tau, R_{0R}, \tau_{0R})$ | Transmitter's slant range vector (given in the receiver's coordinates) |
| $\sigma(R_{0R}, \tau_{0R})$ | Backscattering coefficient (given in the receiver's coordinates) |
| $G_l$ | Point target reference spectrum |
| $f_0$ | Range carrier frequency |
| $S_l(f)$ | Spectrum of the transmitted chirp signal |
| $\tilde{\tau}_R$, $\tilde{\tau}_T$ | Receiver's and transmitter's points of stationary phase |
| $\tilde{\tau}$ | Common bistatic point of stationary phase |
| $\tau_{cb}$ | Center of the common bistatic azimuth window |
| $k_r$ | Chirp sweep rate |
| $\phi_R$, $\phi_T$ | Receiver's and transmitter's half phase terms |
| $\mathbb{F}$ | Forward Fourier transformation; |
| $\mathbb{F}^{-1}$ | Inverse Fourier transformation; |
| $a_0$, $a_2$ | Parameters necessary for our bistatic processing approach; |
| $\vec{d}(t)$ | Vectorial baseline from the transmitter to the receiver; |
| $B_{az}$, $B_r$ | Azimuth and range bandwidths |
| $f_{\tau dc}$ | Azimuth Doppler centroid |
| $t_e$ | Time sampling variable |
| $f_e$ | Frequency sampling variable |

# 1 Introduction, Overview and Structure of the Document

Bistatic SAR systems, as opposed to monostatic SAR constellations, offer considerable degrees of freedom in choosing transmitter (illuminator) and receiver (passive) motion trajectories. The increased flexibility of the design of bistatic SAR missions, however, pays a price with an increased complexity of the processing.

In chapter 2 we will describe the concept of Synthetic Aperture Radar (SAR). We will make a short excursion in the history of SAR and discuss the benefits and possibilities of conventional SAR systems. We will then explain the concept of bistatic SAR and its corresponding benefits. Some airborne bistatic experiments were already successfully accomplished; we will discuss them and consider the future spaceborne bistatic missions like TanDEM-X, Interferometric Cartwheel, Interferometric Pendulum and hybrid bistatic experiments.

A big part of our work is based on the bistatic point target reference spectrum (BPTRS), derived at ZESS by Prof. Loffeld and our SAR team [1]. We will make a detailed derivation of the bistatic formula in chapter 3.

In chapter 4 we will interpret the BPTRS. We will explain in detail terms of BPTRS, such as bistatic phase term, quasi-monostatic phase term, amplitude term, etc. Monostatic case can be considered as the particular bistatic case when the transmitter and the receiver are located on the same platform. We will prove that, for monostatic case, the bistatic point target reference spectrum converges to the monostatic point target reference spectrum. In the same chapter we will interpret the different terms of bistatic point target reference spectrum for different bistatic configurations like general bistatic case, translationally invariant configuration and constant offset configuration. We will prove that, for constant offset configuration, our bistatic point target reference spectrum converges to the so called ‘Rocca’s Smile’.

In deriving BPTRS, some approximations were used. Therefore, the detection of the borders of the validity for bistatic point target reference spectrum is an important issue. In chapter 5 we will derive the constraints of validity. We will derive four constraints: two for the transmitter side and two for the receiver side. We will demonstrate the constraints, considering the particular bistatic configurations, and bring some simulation results.

In chapter 6 we will demonstrate the performance of BPTRS by focusing single and groups of point targets. We do this initially for a single point target. For this reason, we have created the bistatic simulator. Assuming straight line trajectories, we can generate arbitrary bistatic configuration. Using a bistatic simulator, we will simulate different bistatic configurations and generate the raw data for scenes with single point and groups of point targets. Later, we will focus them by the BPTRS.

Bistatic focusing for groups of point targets will be extended analytically for the complete scene. In our bistatic processing we will use some modules of monostatic SAR process developed at ZESS[1]. The monostatic processing itself is based on the Inverse Scaling algorithm. We will explain the monostatic Inverse Scaling algorithm in chapter 7.

In chapter 8 we will develop the focusing algorithms for different bistatic configurations. We will start with the simplest cases of azimuth time invariant configurations. Here the processing is considerably simplified in comparison with the general case, where the transmitter and the receiver move at different velocities in different directions. The first configuration of this class is Tandem configuration. We will solve Tandem spaceborne configuration analytically and solve Tandem airborne configuration by dividing the complete scene in range blocks. The next configuration we will consider is translationally invariant

[1] *Zentrum für Sensorsysteme* (Center for Sensorsystems)

configuration. We will develop the algorithm for the translationally invariant case and bring the focusing results for the simulated and the real bistatic raw data. In the general case, the processing does not only depend on range, but also on azimuth time. This problem will be addressed using a 2D Inverse Scaling approach. The processing results will be demonstrated using simulated raw data.

The first results of measuring the bistatic processed image quality will be given in chapter 9. At first we will determine the directions of range and azimuth lines. The angles will be determined with the Radon transform. Then we will estimate the bistatic image quality by calculating range and azimuth resolutions, peak maximums and integrated and side lob ratios.

Our bistatic processing algorithm will be implemented in frequency domain. We will observe that in the general bistatic case the processing additionally azimuth time variant, causing the azimuth frequency scaling. In this respect, the 2D Inverse Scaling approach could be very successful. In chapter 10 we will explain the bases of 2D Inverse Scaling algorithm presented by Prof. Loffeld in [16].

The results and summary of the work considered in the scope of this PhD research will be analyzed in chapter 11.

# 2 Conventional Monostatic SAR and Bistatic SAR, Experiments and Upcoming Missions

In this chapter we introduce Synthetic Aperture Radar Systems. First, we will explain the principle and the benefits of conventional monostatic SAR. Then we will describe the bistatic SAR configuration. Such a configuration brings more benefits in comparison with monostatic SAR systems. We will discuss different advantages and disadvantages. Later, we will consider possible bistatic spaceborne configurations like Interferometric Cartwheel and Interferometric Pendulum.

One of the future bistatic missions will be a hybrid bistatic experiment using a satellite as the transmitter and an airplane for the receiver. TerraSAR, launched by DLR on 15 June 2007, will be used as the transmitter, and FGAN's airplane PAMIR will operate as the receiver.

In our bistatic processing approach, the different kinds of bistatic constellations are sorted in three subgroups: Tandem case, translationally invariant case and general case. We will explain all these bistatic constellations.

## 2.1 Conventional Monostatic SAR

Radar has been employed for electronic observance since World War II, and since that time, it has experienced recognizable technological boosts. Conventional radar systems were used to detect the distance and velocity of the moving object. Different processing approaches improved the possibilities of radar systems. One of the applications of radar systems is Synthetic Aperture Radar (SAR). In 1953, Carl A. Wiley was the first to publish the basic SAR principles in his work titled 'Pulsed Doppler Radar and Means'. SAR is an image processing method based on signal processing, in which the satellite or airplanes are used to carry transmitting and receiving antennas. It generates photographic images (similar to maps) of the different scenes of the Earth and, by comparing the images to those from conventional radar systems, increases the geometrical resolution dramatically. Reflective features of the individual objects are rendered with grey tones or with colors.

In optical imaging, the sun is used as the radiation source. In SAR systems, the transmitting system, located on a moving satellite or an airplane, is used as the radiation source. Received signals are not ready images, only data. By means of appropriate processing, the raw data can be transformed to a SAR image. A benefit of the SAR system is that it can give unrestricted service irrespective of solar radiation and time of day. Furthermore, the wavelengths of microwave transmitted signals are selected in a way such that attenuation of waves in the atmosphere is minimized. The resonance frequencies of molecules in the atmosphere are not in the bandwidth of the transmitted signal. This means that SAR can be used in any weather condition, even if the transmitting system is flying in deep clouds.

The SAR images are used for different types of scientific applications like geology and archaeology, for forestry classification and inventory of cultivation areas and for determination of soil humidity. Interferometric SAR gives the possibility of generating 3D images. Normally, a SAR image is two-dimensional, but since SAR data is complex, it contains phase information in addition to magnitude. By combining two or more coherent images of the same scene, taken from different positions, it is possible to acquire height information by triangulation, which can be used for 3D mapping.

We have an example of a SAR image in Figure 2.1. It is a fully polarimetric E-SAR image of Oberpfaffenhofen, including the DLR facilities in the image center. The image is obtained from two dual-polarized SAR systems working in C-band.

Figure 2.1. Fully polarimetric E-SAR image of Oberpfaffenhofen (Courtesy of DLR - German Aerospace Center).
Different polarizations are colored as HH-green, HV-red, VV-blue.

## 2.2 Benefits of Bistatic and Multistatic SAR in Comparison with Monostatic SAR

In conventional monostatic missions, the transmitter and receiver are located on the same carrier. In the last decade, bistatic and multistatic SAR systems became very attractive. They give additional benefits, such as flexibility, reduced vulnerability in military applications, cost reduction, increased resolution by combining the images taken from different sensors, etc. All these benefits come at the expense of increased complexity.

Bistatic radar is not a new concept, and its fundamental principles were demonstrated many years ago [64], even before development of operational monostatic radar. However, the interest in bistatic radar has dropped since the invention and demonstration of the monostatic radar after 1930. Most of the users were fascinated with the radar operated from the single site. Since that time, the bistatic radar has been rediscovered several times, mainly for military applications, such as for a precise target location or receiver camouflage. Only recently have the bi- and multistatic radar systems attracted interest with regard to SAR, and a number of bistatic and multistatic systems are under development. Proposed multistatic systems can be divided into fully and semi-active configurations. Most of the thorough overview of bi- and multistatic missions is given in [44].

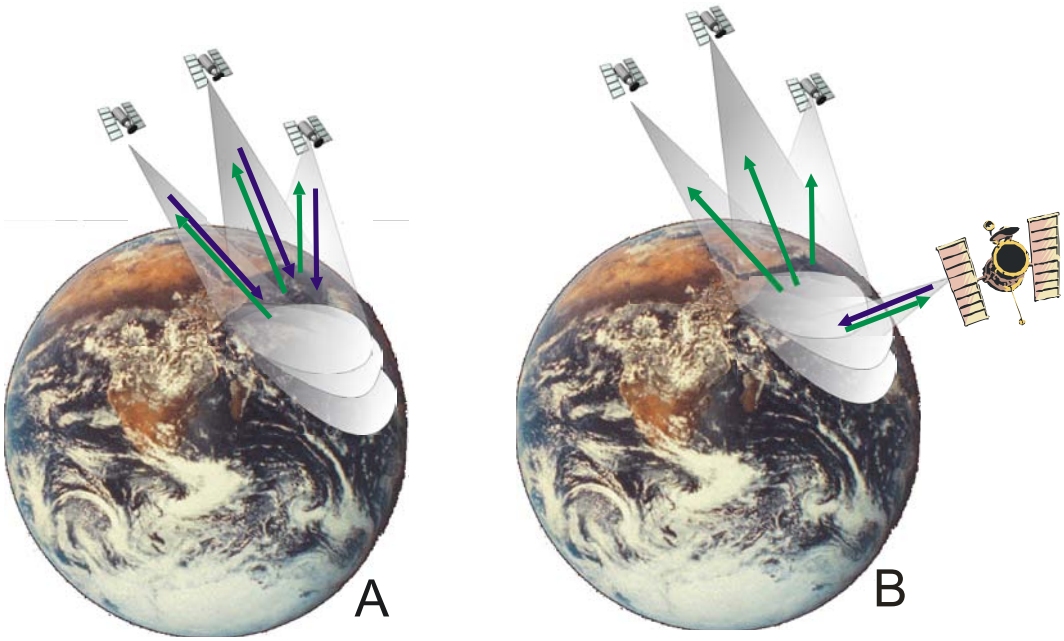


Figure 2.2. /A/ Fully active multistatic constellation; /B/ semi active multistatic system.

In a fully active configuration, each radar has both transmitter and receiver capabilities. Each individual mobile sensor is a transmitter and a receiver at the same time, enabling individual SAR recording and, additionally, taking part in bistatic SAR. Different bistatic SAR combinations are possible. Semi-active radar systems combine one active illuminator and one or more passive receivers, as shown in Figure 2.2-B. An example of such a system is the Interferometric Cartwheel proposed in [49] and the Interferometric Pendulum proposed by DLR[1].

Distributed functionality in bi- and multistatic SAR allows a natural separation of radar payloads and, therefore, will strongly support the use of small, low cost satellites in the future. For example, the deployable antennas and reduced power demands of passive receivers enable the reduction of system costs. The satellites' constellations will allow having a modular design, re-using major building blocks, and short development time, increasing flexibility and reducing costs. Bi- and multistatic configurations in highly reconfigurable and scalable satellite configurations will be used for a broad spectrum of remote sensing applications. In the following section, we will consider the potential benefits of bi- and multistatic SAR.

### 2.2.1 Frequent Monitoring of the Same Scene

Users very often need to have continual time access to up-to-date SAR data of some scene of interest. The revisit times of current spaceborne SAR sensors range from several days to several weeks. This time is not sufficient for important applications such as a traffic monitoring, risk and disaster management or security. One promising approach in this respect could be the use of multiple mini satellites in conjunction with a geostationary illuminator. This kind of system allows a systematic reduction of the revisit times, as well as an upgrade to other imaging modes like cross-track interferometry. The multiple mini receivers share one illuminator, thereby reducing the overall costs of each complete mission.

[1] *Deutsches Zentrum für Luft- und Raumfahrt* (Germany Aerospace Center)

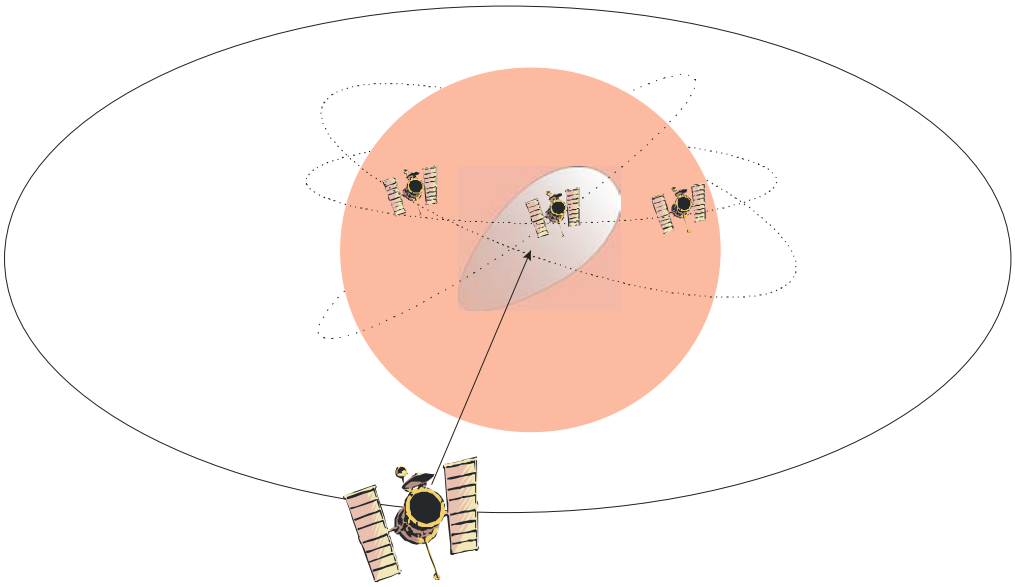

Figure 2.3. Frequent monitoring of the same scene with a geo-stationary illuminator and low Earth orbit receivers

### 2.2.2 Bistatic Observation

Bistatic SAR imaging provides additional observations for the extraction of scene and target parameters. Bistatic data may be combined with monostatic data for multi-angle observations. The segmentation and classification of radar images is expected to improve by comparing the spatial statistics of mono- and bistatic scattering coefficients. Multi-angle observations in polarimetric configuration will allow the quantitative estimation of important bio- and geophysical parameters of the Earth's surface and its vegetation cover. The increased bistatic scattering parameters of the Earth's geometry may also enhance the radiometric sensitivity of the bistatic radar. Furthermore, because of reduced retro-reflector effects for urban areas at large bistatic angles, we can improve the detection ability of low intensity scattered signals in comparison with monostatic images. Additionally, potential arises from a combined mono- and bistatic range and Doppler evaluation for target localization and velocity estimation, measurements of ocean wave spectra, analysis of bistatic scattering water surfaces, atmospheric measurements, stereogrammetic applications, etc.

### 2.2.3 Bi-, Multistatic Single Pass Interferometry

SAR interferometry is a very precise technique for extracting important bio- and geophysical parameters from information about the Earth's surface. However, because of temporal de-correlation and atmospheric distortions, conventional repeat pass interferometry is not always very efficient. Limitations caused by such problems can be avoided with a transition to bi- and multistatic systems. These systems offer a natural way to perform a single pass interferometry. Satellite formations enable a flexible imaging geometry with large baselines, thereby providing the possibility to significantly increase the interferometric performance for applications like DEM[1] generation, in comparison to a single platform system like SRTM[2]. Single pass interferometry can be implemented either in a semi-active

[1] Digital Elevation Model
[2] Shuttle Radar Topography Mission

or a fully active way. Fully active systems generally have a higher sensitivity and flexibility, have fewer tendencies to ambiguities and enable easier phase synchronization (as in a ping-pong mode with alternating transmitter or by a direct exchange of radar pulses). Furthermore, they also provide a monostatic mode as a natural fallback solution in case of problems with orbit control or instrument synchronization. On the other hand, semi-active radar constellations have a significant cost advantage and provide more interferometric baselines per monetary unit. Excellent performance may be achieved by selecting small and large baselines to resolve phase ambiguities. Additionally, multiple baseline interferometry has the potential to solve the problems that arise from volume de-correlation in vegetated areas. Another very promising opportunity is along-track interferometry, e.g. for the measurement of ice drift and ocean currents.

### 2.2.4 Large Aperture Imagery with Bi-, Multistatic Distributed Sensors

A constellation of multiple radar satellites recording the signals from a common illuminated footprint can also be regarded as a large aperture with distributed sub-aperture elements. Any linear combination of multiple receivers can be treated as an antenna array. The opportunity to form very narrow beams allows the use of a space-time variant approach to suppress range and azimuth ambiguities. This will in turn lead to a reduction of the required antenna size for each individual receiver, thereby enabling cost-effective and powerful SAR missions with broad coverage and high resolution.

Distributed aperture systems enable highly accurate velocity measurements of moving objects on the ground, and they most probably can overcome the problem of blindness against certain directions of target motion. Another opportunity they offer is performing precise target localization. A coherent combination of multiple SAR images acquired from slightly different view angles will improve the spatial resolution. Super resolution techniques may again be regarded as a formation of narrow beams, which is complementary to the ambiguity suppression mentioned above. Super resolution in range direction has the potential to overcome the bandwidth limitations for spaceborne SAR sensors available by international frequency regulations.

## 2.3 Classification of Bistatic Configurations

To rank the complexity of bistatic configurations, we divide the bistatic constellations into categories. From now on, we will use the definitions introduced in [29]. For a special case of when the transmitter and the receiver are located on the same carrier, we will have a monostatic mission. In this situation, the transmitter and the receiver move with the same velocity vectors. The monostatic configuration is shown in Figure 2.4:

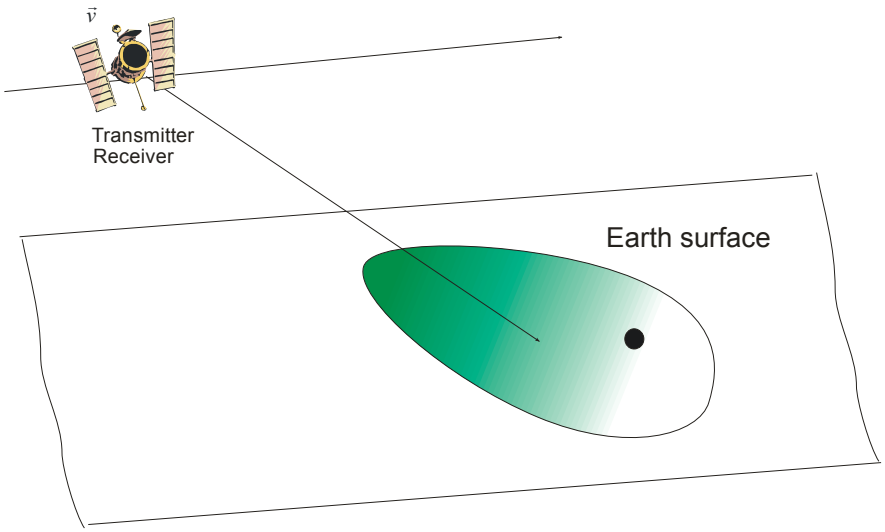


Figure 2.4. Monostatic SAR

Another type of bistatic constellation is the Tandem Case. The transmitter and the receiver move with equal velocities across the same trajectory. The offset between them is therefore kept constant during the acquisition. That is why this particular configuration is often referred as a 'stationary offset configuration' [27]. This case is shown in Figure 2.5:

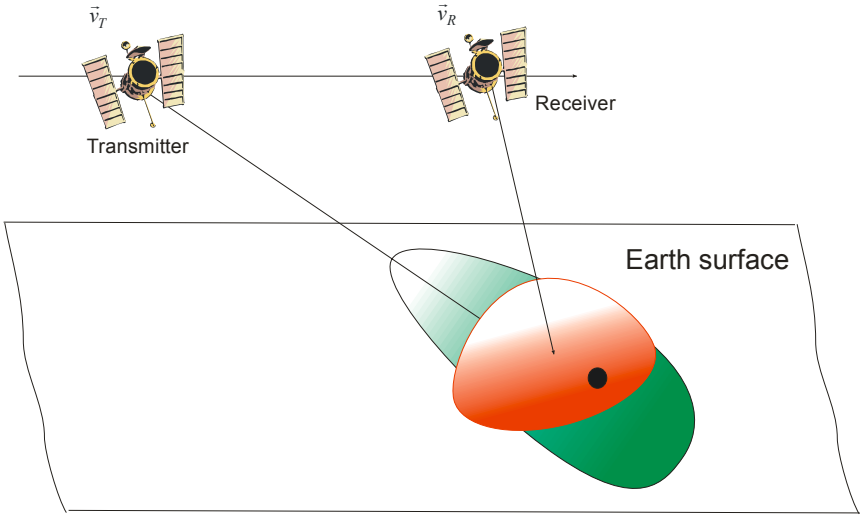


Figure 2.5. Tandem configuration

The next bistatic configuration, if we increase the complexity, is the case in which transmitter and receiver move across parallel tracks. Their velocity vectors are constant and equal; therefore, the baseline between them is constant as well. This configuration will be named 'translationally invariant configuration'. It is shown in Figure 2.6.

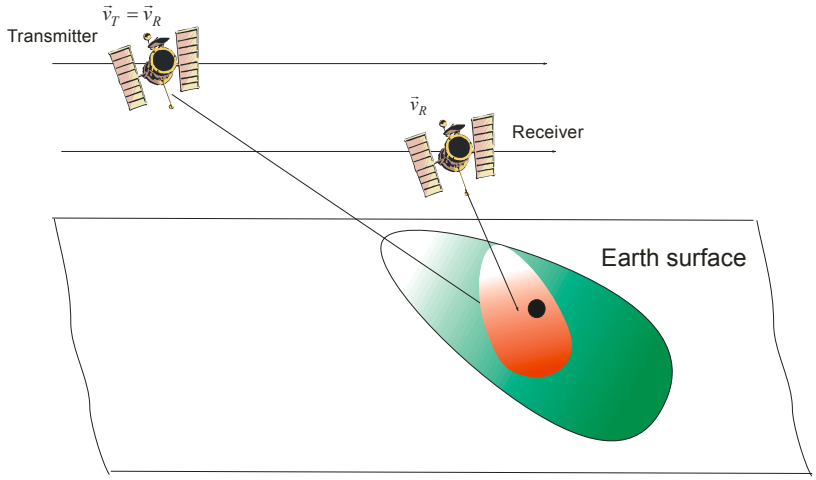


Figure 2.6. Translationally invariant configuration

The last configuration we need to describe is the general case. Here, the transmitter and the receiver move along non-parallel trajectories with non-equal velocities. During the flight we assume that the velocities of transmitter and receiver do not change and that their tracks form straight lines. This configuration is shown in Figure 2.7:

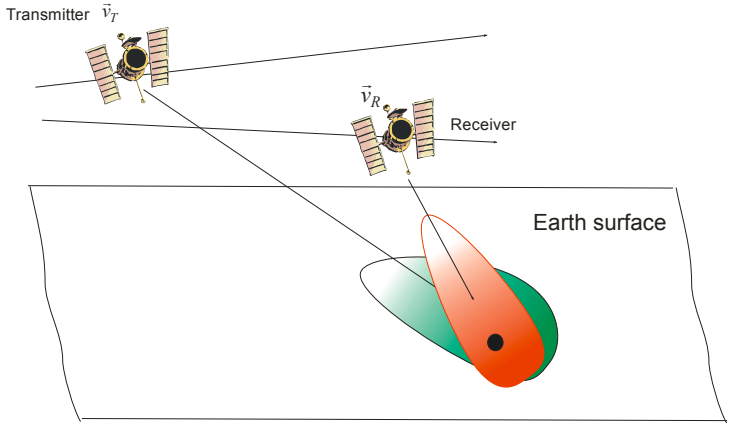


Figure 2.7. General case configuration

## 2.4 Upcoming Bistatic Constellations

D. Ausherman was first who published in [78] different ideas of bistatic focusing and later J. L. Auterman presented in first bistatic SAR images from the first airborne bistatic SAR experiment in [79].

Because of the increased interest in bistatic SAR imaginery, some airborne bistatic missions have been successfully accomplished recently. FGAN and DLR have performed airborne experiments using the translationally invariant configuration. The description of these experiments can be found in [29],[30],[31] and [68]. In the following section, we will describe some bistatic configurations which are planned to appear soon.

### 2.4.1 Hybrid Bistatic Mission

Very recently, hybrid Spaceborne-Airborne systems have attracted considerable interest [22], [23]. This is a revolutionary idea in bistatic SAR imagery. Using a transmitter located

on a satellite and a receiver located on an airplane will record the SAR raw data for further processing. This idea was first published in [77] by R. Goldstein. The principle of operation is shown schematically in Figure 2.8.

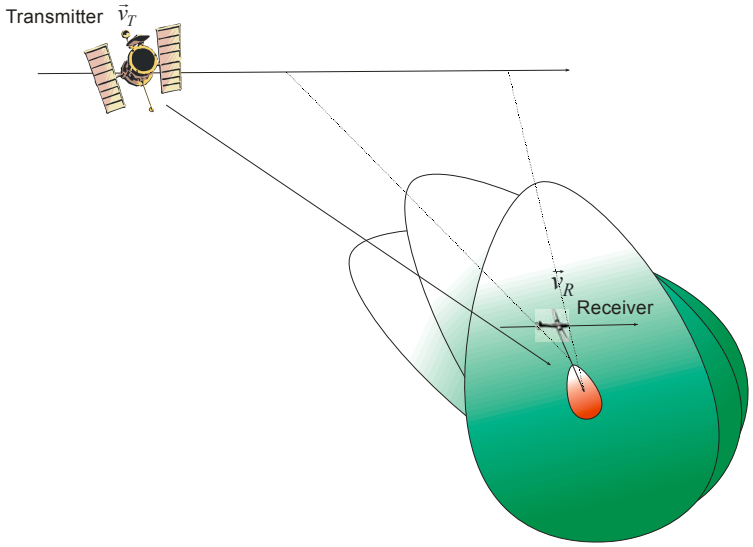


Figure 2.8. Hybrid bistatic experiment

In hybrid missions, SAR illuminator possesses an azimuth antenna footprint extension much bigger than the airplane. Therefore, it is relatively easy to arrange a common footprint. One of the realizations of this configuration will be the experiment that uses TerraSAR-X as a transmitter and FGAN's PAMIR system as a receiver. TerraSAR-X is an advanced, high resolution X-Band synthetic aperture radar system based on active phase array technology, which can operate in Spotlight, Stripmap and ScanSAR mode with full polarization capability. The TerraSAR-X instrument is operated at 9.65 GHz with selectable chirp bandwidth up to 300 MHz.

Table 2.1. Transmitter and receiver parameters of hybrid bistatic experiment

| **Parameter** | **TerraSAR** | **PAMIR** |
|---|---|---|
| Height (flat Earth assumed) | 514 km | 3000 m |
| Relative velocity | 7600 m/s | 100 m/s |
| Azimuth beam width | 0.33° | 2.9° |
| Antenna elevation angle | 2.3° | 15° |
| Maximum steering angle | ±0.75° | ±45° |
| PRF | 4KHz | 4KHz |
| Carrier frequency | 9.65GHz | 9.65GHz |
| Transmitter bandwidth | 150MHz | 150MHz |

Table 2.1 shows the parameters of the TerraSAR and the PAMIR system. Because of the huge difference between the velocities of the satellite and the airplane, normal stripmap mode is not useful in this case. The common recorded scene will be very small. By operating the transmitter in a sliding spotlight or spotlight mode and using antenna steering at the receiver side, a useful scene extension in the azimuth direction can be achieved.

We have done some simulations distributing the point targets (PT) at different locations in the scene. The individual azimuth bandwidth for each point target is around 800 Hz. For the complete azimuth bandwidth, we observed a frequency band between -2500Hz and +2500Hz. (This is due to a high azimuth time varying squint angle of the satellite during the steering.) As the PRF is around 4 KHz, we have aliasing problems in azimuth direction. A

bandwidth of 800 MHz raises hope that this mission will give us sufficient resolution in azimuth direction. In [33] the authors give an estimate for the achievable azimuth and range resolution. In the case of the TerraSAR-Pamir experiment, the range resolution is 84 cm, and the lateral resolution is 1.06 m.

### 2.4.2 TanDEM-X Mission

TanDEM-X is a mission proposal for a TerraSAR-X add-on satellite for high resolution single-pass interferometry (for more details, please see references [40],[45],[46]). This mission proposal has been selected for Phase A study within the scope of a Call for Proposals for another German Earth Observation Mission (to be launched in 2009). The mission's goal is the generation of a global Digital Elevation Model (DEM) with an accuracy corresponding to the DTED-3 specifications (12 m positing, 2 m relative height accuracy for flat terrain). This goal will be achieved by means of a second TerraSAR-X satellite (TanDEM-X) flying in a close orbit configuration with TerraSAR-X. This experiment is the first bistatic SAR spaceborne mission.

DEM generation will be performed in two different modes. The first mode uses bistatic interferometric SAR in translationally invariant configuration. The same scene will be measured simultaneously by two receivers: one operating in monostatic mode and the second one in bistatic mode. Simulations measurement avoids temporal de-correlation. Along-track baseline should be less than 2 km, and if we want to achieve high resolution DEMs, then the baseline should be less than 1 km. This mode is sketched in Figure 2.9.A.

A secondary DEM generation mode is the pursuit monostatic (Interferometric Synthetic Aperture Radar) InSAR mode (Figure 2.9.B), where two satellites are operated independently, avoiding the need of synchronization. The temporal de-correlation is still small for most of terrain types except for water and vegetation. The interferometric height sensitivity doubles with respect to bistatic operation, meaning that the baseline determination has to be more accurate.

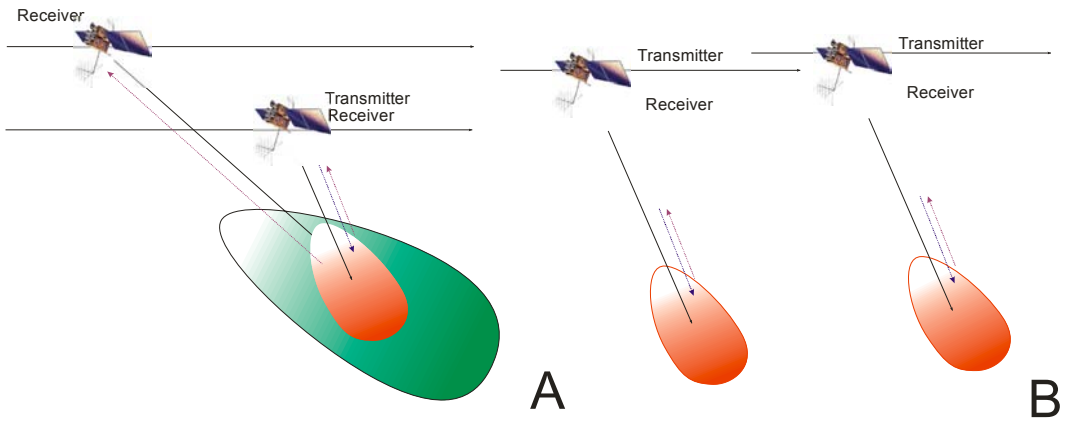


Figure 2.9. TanDEM-X operational modes: /A/ bistatic InSAR, /B/ monostatic InSAR

### 2.4.3 Interferometric Cartwheel and Pendulum

A very interesting multistatic SAR configuration was proposed in [49] by D. Massonet from CNES[1]. This concept was named as Interferometric Cartwheel. Quasi-simultaneous radar images can be produced by a low-cost system using a set of passive receivers onboard

[1] Centers National d'Etudes Spatiales (French Space Agency)

a constellation of microsatellites in a special orbital configuration. The combination of these images can improve the final resolution in range and azimuth and systematically produce across-track and along-track interferometric data.

The Interferometric Cartwheel consists of one satellite that carries the transmitter and three small satellites that rotate around the Earth, as shown in Figure 2.10.A. All satellites move around the Earth with very similar orbits. The microsatellites have the same orbit plane, the same orbit eccentricity (slightly different from the transmitter eccentricity) and the same half axes, therefore they get the same roundtrip time.

Perigee points of the microsatellites are located on the circle in the orbit plane and divide this circle in three equal angles. The times of perigee for different micro satellites are shifted in respect to each other in a way such that they are permanently in different parts of their individual orbits while rotating around Earth but are still always spatially close to each other.

The microsatellites rotate on a virtual ellipse (Figure 2.10.B), creating very stable horizontal and vertical baselines (less than 8% variation during the orbit). Relative movement of the microsatellites to each other is similar to a wheel that rotates with a constant velocity around the virtual center point. On the other hand, this center point rotates around the Earth with relatively constant velocity.

As an alternative to the Interferometric Cartwheel, DLR proposed a similar system known as Interferometric Pendulum, which has practically no orbital differences, but some operational differences with the Interferometric Cartwheel.

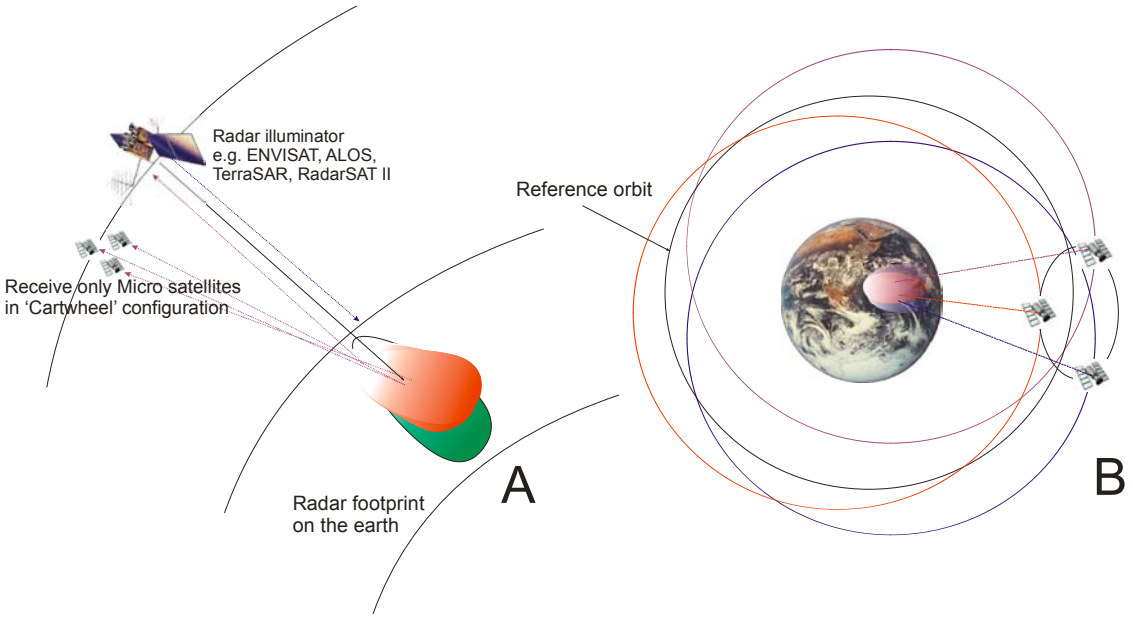


Figure 2.10. Interferometric Cartwheel

## 2.5 Bistatic Processing

In the previous section we considered bistatic and multistatic configurations and showed the benefits that they can bring in comparison to monostatic SAR. However, all these advantages come at the expense of increased processing complexity in the same comparison.

Two main families of algorithms exist for the monostatic SAR: algorithms implemented in the time domain (for example back projection algorithm), and algorithms operating in frequency domain. Time domain algorithms use interpolation; therefore, they are less computationally effective. Usually, time domain algorithms are more precise than frequency

domain algorithms; they are more flexible, and they can handle time-varying geometries. However, they have one big disadvantage: they are burdensome and slow.

The frequency domain algorithms perform the azimuth compression by using the so-called 'Stolt-interpolation' [73]. The usage of Fourier techniques makes the frequency domain algorithms efficient and easy to implement on current computer systems. The frequency domain algorithms themselves are classified in two classes. The first class consists of the so-called range-Doppler algorithms, and the second class consists of algorithms implemented in the range frequency/azimuth frequency domain. The most prominent members of the range-Doppler algorithm are the Chirp Scaling algorithm [38],[41], the Extended Chirp Scaling algorithm [39], the Non-Linear Chirp Scaling algorithm [74] and ω-k algorithms. One representative of the algorithms operating in range frequency-Doppler frequency domains is the Inverse Scaled algorithm [3],[4]. The performance of these algorithms for monostatic configuration is well known and widely discussed in scientific literature [38],[37],[3],[71].

In the bistatic case, the situation is more complex when compared to the monostatic case. In the monostatic case, the range history has a hyperbolic shape; in the bistatic case, the bistatic phase is the sum of the corresponding phase histories of the transmitter and the receiver. Therefore, the total phase history in the bistatic case no longer has the shape of a hyperbola – its shape is slightly flattened (but only in the small bistatic angle configurations), so we speak about a flat-top hyperbola. Hence, it is not possible to process the bistatic raw data with conventional monostatic processors.

The main goal of the current work is the derivation of bistatic focusing algorithms.

One of the first approaches to solve bistatic problem was given by Prof. F. Rocca and the team of the Milan Polytechnic University [27]. The bistatic acquisitions are transformed into monostatic ones by applying what is called the 'Smile' operator. The 'Smile' is equivalent to the Dip Move Out operator known in seismic literature. In a preprocessing step, first ranged compressed raw data is convolved with 'Smile'. With this operation, the bistatic problem is transformed into conventional monostatic processing. In SAR literature, the 'Smile' was first described using geometrical considerations and later transferred into microwave terms. The derivations were done for a Tandem configuration, with the transmitter and the receiver following each other with a fixed offset along a straight line. It was shown in [27] that the 'Smile' is a slowly varying short operator depending on range time, but in azimuth it is time invariant (only in the Tandem Case). Later in [28], the team tried to extend the 'Smile' concept for the general case, where the transmitter and the receiver move with different trajectories and different velocity vectors. It was shown that the 'Smile' extension for the general case is conceptually possible, but the point target reference spectrum was not given in an analytical way.

Very similar to the 'Smile' concept is the bistatic concept, derived by Prof. Loffeld and our bistatic team at ZESS[1]. It is based on the bistatic point target reference spectrum [1],[2],[9],[10],[11],[12]. The formula is valid for the general case. Analogous to the 'Smile' concept, we have the 'Bistatic deformation term'. For the general case, this term is range and azimuth time-variant. We observed that the 'Bistatic deformation term' is slowly range and azimuth time-variant, and it is a shorter operator than the 'Smile'. The detailed characteristics of the bistatic point target reference spectrum will be considered in the following chapters.

Prof. Ender and the SAR team of FGAN[2] proposed a bistatic approach based on the ω-k algorithm given in [29],[30]. The algorithm was introduced for the translationally invariant

[1] *Zentrum für Sensorsysteme* (Center for Sensorsystems)
[2] *Forschungsgesellschaft für Angewandte* Naturwissenschaften (German research establishment for applied natural sciences)

configurations. Later, FGAN performed a real bistatic SAR experiment. The data were successfully processed by FGAN [31],[32] and our SAR team at ZESS [19],[20] in parallel.

Prof. R. Bamler from DLR proposed bistatic processing using numerical transfer functions [35]. He proposed that this algorithm would solve the focusing for translationally invariant configurations. It calculates a numerical transfer function in order to correct the non-hyperbolic curvature of the bistatic phase for each range line. This operation is equivalent to the compensation using our 'Bistatic Deformation Term', or the convolution with 'Rocca's Smile' operator. It is very interesting to note that the work given in [35] showed that the assumption of the equivalent monostatic flight path in bistatic SAR is not sufficient. It is thus impossible to convert the bistatic SAR processing problem to an imagined monostatic trajectory, where monostatic trajectory is average of the transmitter and the receiver trajectories.

The SAR team of University of British Columbia from Canada, with supervision of Prof. Cumming and Prof. F. Wong, proposed a Non-Linear Chirp Scaling algorithm to solve the bistatic problem [74],[75],[76]. The approach is based on the Chirp Scaling algorithm, but uses the high order terms of Taylor series expansion. The high order terms were initially considered by introducing the 'Perturbation function' and later the 'Power series inversion'.

We would like to remark on one very important point in the derivation of the bistatic processing algorithms mentioned above. The conversion of the point target response function from azimuth time to azimuth frequency domain is normally carried out by the Method of the Stationary Phase (MSP). This method can be used if we know the exact location of the point of the stationary phase. The bistatic phase history is the sum of the transmitter and the receiver phase histories. Therefore, the calculation of the point of stationary phase for bistatic configurations is not as trivial as in monostatic case, which is the source of most problems in bistatic processing.

# 3 Point Target Reference Spectrum for Bistatic Configurations

Algorithms exist which are formulated and work in a space/time domain, a space/Doppler or in a 2D frequency domain. Our bistatic processor is implemented in the range frequency, Doppler frequency domain. To develop the processing algorithm, the spectrum of the entire SAR scene has to be derived. Since the complete scene is the integral over all individual point target reference spectra, the 2D point target spectrum must be derived first.

While in the monostatic SAR case the geometry is readily modeled and point target response functions are evaluated and carried to the frequency domain by stationary phase techniques, the situation is slightly more complex in the bistatic case. The outcoming range and phase history of any PT consists of the individual range history contributions of the transmitter and the receiver, where these contributions are variable due to the relative motion between the transmitter (illuminator) and the receiver. Furthermore, the classical monostatic correspondence between the azimuth frequency and the azimuth time, being closely related to a certain point in the orbit, is broken up, since two motion trajectories must be considered.

## 3.1 Modeling the Bistatic Geometry

In the following, we use the Born approximation, in which multiple scattering is neglected. In other words, we assume that each reflector acts independently from the others as a point scatter. In the bistatic case, the transmitter and the receiver are located on different platforms, and they move at different velocities in different directions. The geometry is shown in Figure 3.1. $\tau$ denotes the azimuth time (in SAR, it is often called *slow time*), $\tau_0$ is the azimuth time instant when the transmitter or the receiver 'sees' the point target at the closest distance (the point of closest approach, PCA). The indices 'T' and 'R' denote the transmitter and the receiver values respectively. The position $P(R_{0R}, \tau_{0R})$ of the Point target (PT) is implicitly specified by the time instant $\tau_{0R}$ when it is seen perpendicularly from the receiver track and by the corresponding slant range $R_{0R} = \left|\vec{R}_R(\tau_{0R}, R_{0R}, \tau_{0R})\right|$. Hence, $(R_{0R}, \tau_{0R})$ are the receiver's coordinates in our bistatic approach. Likewise we could also express the point target in the transmitter terms by specifying the time $\tau_{0T}$, when the point target is seen perpendicularly from the transmitter's track at the slant range $R_{0T} = \left|\vec{R}_T(\tau_{0T}, R_{0T}, \tau_{0T})\right|$. It should be noted that $(R_{0R}, \tau_{0R})$ determines the two point targets on the different sides of flying trajectory.

For simplicity we assume that the surface is flat.

The bistatic geometry for the arbitrary case is shown in Figure 3.1. For the receiver's slant range vector, the following 3D vector equation is valid at azimuth time $\tau$ :

$$\begin{aligned} &\vec{R}_R(\tau, R_{0R}, \tau_{0R}) = \vec{R}_R(\tau_{0R}, R_{0R}, \tau_{0R}) - \vec{v}_R \cdot (\tau - \tau_{0R}) \\ &\textit{where}: \\ &\vec{R}_R(\tau_{0R}, R_{0R}, \tau_{0R}) \perp \vec{v}_R \end{aligned} \tag{3.1}$$

$\vec{R}_R(\tau_{0R}, R_{0R}, \tau_{0R})$ is the slant range vector from the receiver to the PT at the point of closest approach and it is orthogonal to the receiver's velocity. For convenience, the velocities are

assumed to be constant. $\tau_{0R}$ is the azimuth time, when the PT is seen perpendicularly from the receiver's track. Likewise we have the following for the transmitter's range history:

$$\begin{aligned} &\vec{R}_T\left(\tau, R_{0T}, \tau_{0T}\right) = \vec{R}_T\left(\tau_{0T}, R_{0T}, \tau_{0T}\right) - \vec{v}_T \cdot \left(\tau - \tau_{0T}\right) \\ &where: \\ &\vec{R}_T\left(\tau_{0T}, R_{0T}, \tau_{0T}\right) \perp \vec{v}_T \end{aligned} \tag{3.2}$$

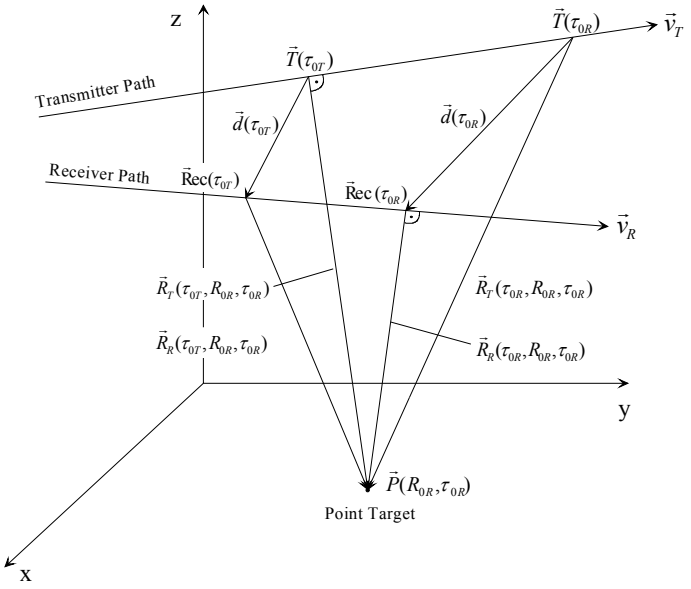


Figure 3.1. Bistatic geometry

$\vec{R}_T\left(\tau_{0T}, R_{0T}, \tau_{0T}\right)$ is the slant range vector from the transmitter to the PT at the azimuth time $\tau_{0T}$. $\tau_{0T}$ is the azimuth time, when the PT is seen perpendicularly from the receiver's track. These vectorial relations are better seen in Figure 3.2.

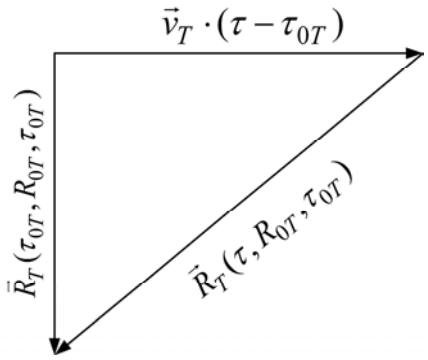


Figure 3.2. The vectorial relation in the bistatic configuration

In order to obtain the modulus of the slant ranges, we must square the vectorial expressions (3.1) and (3.2).

$$\begin{aligned}\left|\vec{R}_R\left(\tau,R_{0R},\tau_{0R}\right)\right|^2 &= \left|\vec{R}_R\left(\tau_{0R},R_{0R},\tau_{0R}\right)\right|^2 + v_R^2\cdot\left(\tau-\tau_{0R}\right)^2\\ \left|\vec{R}_T\left(\tau,R_{0T},\tau_{0T}\right)\right|^2 &= \left|\vec{R}_T\left(\tau_{0T},R_{0T},\tau_{0T}\right)\right|^2 + v_T^2\cdot\left(\tau-\tau_{0T}\right)^2\end{aligned} \tag{3.3}$$

The transmitter's motion is related to the receiver's motion by:

$$\vec{R}_T\left(\tau,R_{0R},\tau_{0R}\right) = \vec{R}_R\left(\tau_{0R},R_{0R},\tau_{0R}\right) - \vec{v}_T\cdot\left(\tau-\tau_{0R}\right) + \vec{d}\left(\tau_{0R}\right) \tag{3.4}$$

where $\vec{d}\left(\tau\right)$ is a vector from the transmitter to the receiver in Figure 3.1. In particular, $\vec{d}(\tau_{0R}) = \vec{\mathrm{Re}}c(\tau_{0R}) - \vec{T}(\tau_{0R})$ is the vectorial distance between the transmitter and the receiver at the receiver's PCA. At the azimuth time $\tau_{0R}$, when the receiver is in its point of closest approach, we have:

$$\begin{aligned}&\vec{R}_T\left(\tau_{0R},R_{0R},\tau_{0R}\right) = \vec{R}_R\left(\tau_{0R},R_{0R},\tau_{0R}\right) + \vec{d}\left(\tau_{0R}\right)\\ &\textit{and}:\\ &\left|\vec{R}_T\left(\tau_{0R},R_{0R},\tau_{0R}\right)\right|^2 = \left|\vec{R}_R\left(\tau_{0R},R_{0R},\tau_{0R}\right) + \vec{d}\left(\tau_{0R}\right)\right|^2\end{aligned} \tag{3.5}$$

Now, evaluating (3.3) at the time instant $\tau_{0R}$ and using the result of (3.5), we obtain:

$$R_{0T}^2 = \left|\vec{R}_T\left(\tau_{0T},R_{0R},\tau_{0R}\right)\right|^2 = \left|\vec{R}_R\left(\tau_{0R},R_{0R},\tau_{0R}\right) + \vec{d}\left(\tau_{0R}\right)\right|^2 - v_T^2\cdot\left(\tau_{0R}-\tau_{0T}\right)^2 \tag{3.6}$$

It should be mentioned, that $\vec{R}_T\left(\tau_{0T},R_{0R},\tau_{0R}\right)$ and $\vec{R}_T\left(\tau_{0T},R_{0T},\tau_{0T}\right)$ are used interchangeably. The reason is that $\left(R_{0R},\tau_{0R}\right)$ are coordinates, and $\vec{R}_T\left(\tau_{0T},R_{0R},\tau_{0R}\right)$ actually means that the receiver's slant range and azimuth time at the PCA are $\left(R_{0R},\tau_{0R}\right)$. The corresponding slant range and azimuth times of transmitter are $\left(R_{0T},\tau_{0T}\right)$.

Dividing (3.6) by the squared slant range at the receiver's PCA and using the relation $\vec{e}_R(\tau_{0R},R_{0R},\tau_{0R}) = \vec{R}_R(\tau_{0R},R_{0R},\tau_{0R})/R_{0R}$, the following is obtained:

$$\frac{R_{0T}^2}{R_{0R}^2} = \left|\frac{\vec{R}_T\left(\tau_{0T},R_{0R},\tau_{0R}\right)}{\vec{R}_R\left(\tau_{0R},R_{0R},\tau_{0R}\right)}\right|^2 = \left|\vec{e}_R\left(\tau_{0R},R_{0R},\tau_{0R}\right) + \frac{\vec{d}\left(\tau_{0R}\right)}{R_{0R}}\right|^2 - v_T^2\cdot\frac{\left(\tau_{0R}-\tau_{0T}\right)^2}{R_{0R}^2} = {a_2}^2 \tag{3.7}$$

which will be an important parameter in our bistatic processing approach.

### 3.1.1 Slant Range Histories

For the complete bistatic scalar range history, we then have:

$$R_g\left(\tau,R_{0R},\tau_{0R}\right) = R_R\left(\tau,R_{0R},\tau_{0R}\right) + R_T\left(\tau,R_{0R},\tau_{0R}\right) \tag{3.8}$$

indicating that the transmitter (illuminator) and the receiver contribute to the overall slant range histories individually and independently.

Table 3.1. Simulation parameters

| **Parameter** | **Symbol** | **Value** |
|---|---|---|
| Carrier Frequency | $f_0$ | 10 GHz |
| Receiver Height | $h_R$ | 1000 m |
| Transmitter Height | $h_T$ | 1035 m |
| Receiver Velocity | $v_R$ | 90 $ms^{-1}$ |
| Transmitter Velocity | $v_T$ | 80 $ms^{-1}$ |
| Slant Range Resolution | | 0.1 m |
| Azimuth Resolution (nom) | | 0.1 m |
| Azimuth Time of the Receiver's Point of Closest Approach | $\tau_{0R}$ | 1 s |
| Azimuth Center Time of the Common Window | $\tau_{cb}$ | 1 s |
| Receiver Slant Range at the Point of Closest Approach | $R_{0R}$ | 1800 m |
| Angle between the Transmitter's and the Receiver's Velocity Vector | | 1° |
| Time Difference Parameter $a_0 = \tau_{0T} - \tau_{0R}$ | $a_0$ | 14.82 s |
| Slant Range Ratio Parameter $a_2 = \frac{R_{0T}}{R_{0R}}$ | $a_2$ | 2.125 |
| Doppler Centroid | $f_{DC}$ | 808 Hz |
| Baseline Vector at the Receiver's Azimuth Point of Closest Approach | $\vec{d}(\tau_{0R})$ | $\begin{bmatrix} 2164{,}85 \\ 1248{,}88 \\ 35 \end{bmatrix}$ m |
| Bistatic Angle at the Receiver's Point of closest Approach | $\beta(\tau_{0R})$ | 25.34° |

Figure 3.3 shows the complete outcome of overall slant range histories over azimuth time for point targets at different $R_{0R}$ values. The parameters of this simulation are given in Table 3.1.

$\tau_{cb}$ is the center of the bistatic azimuth time window;

$a_0 = \tau_{0T} - \tau_{0R}$ is the azimuth time difference between transmitter and receiver times at the points of closets approach;

$a_2 = \frac{R_{0T}}{R_{0R}}$ is the ratio of the transmitter and the receiver slant ranges at the points of closes approach;

$a_0, a_2$ are two parameters that do not appear in the table accidentally. As we will see later, they are very important for our bistatic SAR focusing approach.

$\beta(\tau_{0R})$ is an angle with its vertex located on the point target and with its sides crossing the corresponding positions of the transmitter and the receiver. In this case, the angle is taken at the instant when the point target is at the receiver's point of closest approach;

The minimum slant range was subtracted in each curve for convenience. The dashed curve shows the receiver's slant range history multiplied by 2. We note that the receiver's azimuth time at point of closest approach is located at 1 second.

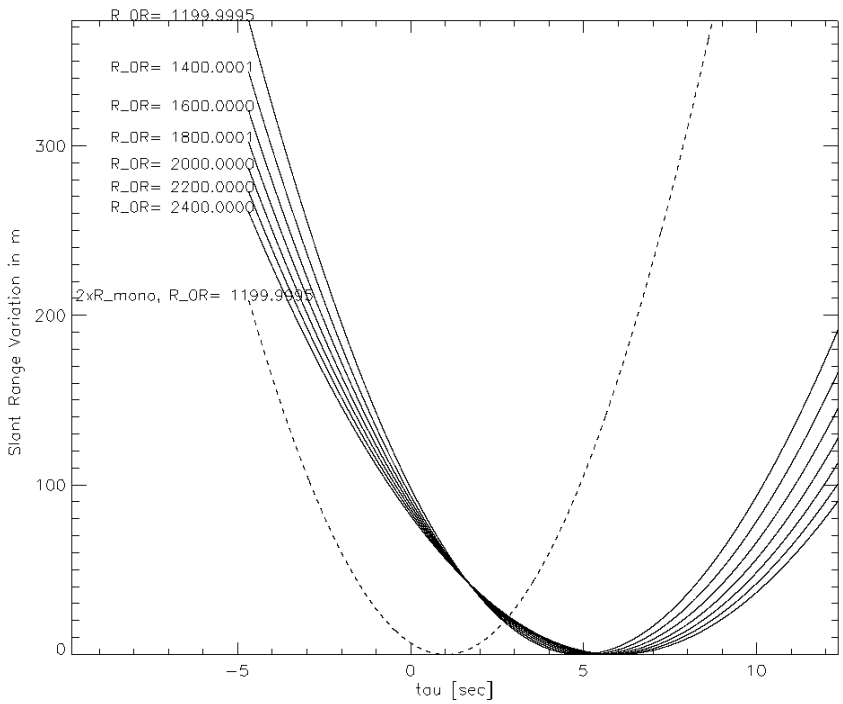


Figure 3.3. Bistatic slant range histories for different location of point targets, the dashed line shows receiver's monostatic range history

Analyzing Figure 3.3, we note that:

1. The overall slant range histories lose their hyperbolic form and look different from the receiver's slant range history. The reason for this is that the sum of two hyperbolas is no longer a hyperbola; usually the shape is flattened. That is why often it is referred to as a *flat-top hyperbola.*
2. The azimuth points, where the overall slant range is minimum, vary with $R_{0R}$. The minimum of the slant range has direct connection with the point of stationary phase. So, the stationary points vary with slant range.
3. The shape of the overall slant range history changes not only in scaling, but in quality.

A drawback of these observations is that the bistatic overall slant range history is essentially different from the monostatic slant range history; hence, bistatic SAR processing cannot be achieved by purely monostatic approaches.

## 3.2 Point Target Response

In the derivation of SAR processing approaches, the pulse shaping effect by the transmitting and receiving channels is normally neglected. Here we assume that the received signal is a shifted replica of the transmitted signal weighted with a backscattering coefficient of a point target (PT). In the bistatic case, the signal's travel time is the time from the transmitter to the scatterer plus the time from the scatterer to the receiver. This delay is calculated as:

$$t_0\left(\tau, R_{0R}, \tau_{0R}\right) = t_T\left(\tau, R_{0R}, \tau_{0R}\right) + t_R\left(\tau, R_{0R}, \tau_{0R}\right) \tag{3.9}$$

$t_T(\tau, R_{0R}, \tau_{0R})$ is the travel time of a signal from the transmitter to the point target, and it is calculated as $t_T(\tau, R_{0R}, \tau_{0R}) = \frac{R_T(\tau, R_{0R}, \tau_{0R})}{c}$, where $c$ is the speed of light in a vacuum. In the same way, $t_R(\tau, R_{0R}, \tau_{0R}) = \frac{R_R(\tau, R_{0R}, \tau_{0R})}{c}$ is the signal's travel time from the scatterer to the receiver. With these notations, we rewrite (3.9) as:

$$t_0(\tau, R_{0R}, \tau_{0R}) = \frac{R_T(\tau, R_{0R}, \tau_{0R}) + R_R(\tau, R_{0R}, \tau_{0R})}{c} \tag{3.10}$$

The received signal response is expressed as a time-delayed replica of the amplitude-weighted transmitted chirp signal. Since the received signal should be expressed in the baseband, the equivalent phase term correspondent to the delay is introduced, and the expression of the point target response is given as:

$$g_l(t, \tau, R_{0R}, \tau_{0R}) = \sigma(R_{0R}, \tau_{0R}) \cdot w(\tau - \tau_{cb}) \cdot s_l\left(t - t_0(\tau, R_{0R}, \tau_{0R})\right) \cdot e^{-j2\pi \cdot f_0 \cdot t_0(\tau, R_{0R}, \tau_{0R})} \tag{3.11}$$

$\sigma(R_{0R}, \tau_{0R})$ is a backscattering coefficient. In some references, it is referred to as the brightness of the PT. We assume that it is stationary during the acquisition. The aim of any SAR processor is to determine the backscattering coefficient for all PTs of the complete scene. $t$ is the bistatic range time. Very often the range time is referred as *fast time*. $\tau$ is the azimuth time, known as *slow time*. $w(\tau - \tau_{cb})$ is the azimuth time window. It can be expressed as a rectangular function: $w(\tau - \tau_{cb}) = rect\left(\frac{\tau - \tau_{cb}}{\tau_{lb}}\right)$. In bistatic configurations, the common footprint is the overlap of the transmitter's and the receiver's footprints. $\tau_{cb}$ is the azimuth window's center time, and $\tau_{lb}$ is the length of the common bistatic footprint. Hence, $w(\tau - \tau_{cb})$ determines the azimuth time when the PT is seen within the common bistatic footprint.

## 3.3 Point Target Spectrum

We want to implement the focusing processor in the frequency domain; we must therefore transform equation (3.11) to the Fourier domain. At first, we perform the Fourier transformation over the range time $t$. The corresponding frequency variable is $f$. After the Fourier transformation, we get:

$$G_l(f, \tau, R_{0R}, \tau_{0R}) = \sigma(R_{0R}, \tau_{0R}) \cdot w(\tau - \tau_{cb}) \cdot S_l(f) e^{-j2\pi \cdot f_0 \cdot t_0(\tau, R_{0R}, \tau_{0R})} e^{-j2\pi \cdot f \cdot t_0(\tau, R_{0R}, \tau_{0R})} \tag{3.12}$$

Reordering the terms, we get:

$$G_l(f, \tau, R_{0R}, \tau_{0R}) = \sigma(R_{0R}, \tau_{0R}) \cdot w(\tau - \tau_{cb}) \cdot S_l(f) \cdot e^{-j2\pi(f_0 + f) \cdot t_0(\tau, R_{0R}, \tau_{0R})} \tag{3.13}$$

We substitute the expression of $t_0(\tau, R_{0R}, \tau_{0R})$ from (3.10) into the equation above, and we obtain:

$$G_l(f, \tau, R_{0R}, \tau_{0R}) = \sigma(R_{0R}, \tau_{0R}) \cdot w(\tau - \tau_{cb}) \cdot S_l(f) \cdot e^{-j2\pi(f_0 + f) \cdot \frac{R_0(\tau, R_{0R}, \tau_{0R}) + R_0(\tau, R_{0R}, \tau_{0R})}{c}} \tag{3.14}$$

(3.14) expresses the point target response of the signal in the range frequency azimuth time domain. To go one step further, we need to perform the transformation from the azimuth time (slow time) to the azimuth frequency (Doppler domain). The corresponding frequency variable is $f_\tau$. We write:

$$G_l\left(f,\tau,R_{0R},\tau_{0R}\right)=\sigma\left(R_{0R},\tau_{0R}\right)\cdot S_l\left(f\right)\cdot \cdot\int_{-\infty}^{\infty} w\left(\tau-\tau_{cb}\right)\cdot e^{-j2\pi\cdot\left(f_0+f\right)\cdot\frac{R_T\left(\tau,R_{0R},\tau_{0R}\right)+R_R\left(\tau,R_{0R},\tau_{0R}\right)}{c}} e^{-j2\pi\cdot f_\tau\cdot\tau}d\tau \tag{3.15}$$

For further calculations, we do not at the moment consider the backscattering coefficient and the spectrum of the chirp signal, and we only calculate the integral:

$$I\left(f,\tau,R_{0R},\tau_{0R}\right)=\int_{-\infty}^{\infty} w\left(\tau-\tau_{cb}\right)e^{-j2\pi\left(f_0+f\right)\cdot\frac{R_T\left(\tau,R_{0R},\tau_{0R}\right)+R_R\left(\tau,R_{0R},\tau_{0R}\right)}{c}} e^{-j2\pi f_\tau\tau}d\tau \tag{3.16}$$

For the phase term inside the integral, we introduce the notation:

$$\phi_b=2\pi\left(\frac{f_0+f}{c}\cdot\left(R_T\left(\tau,R_{0R},\tau_{0R}\right)+R_R\left(\tau,R_{0R},\tau_{0R}\right)\right)+f_\tau\cdot\tau\right) \tag{3.17}$$

$\phi_b$ is a bistatic phase term, and it is the sum of the equivalent phase terms of the transmitter and the receiver:

$$\begin{aligned}\phi_T&=2\pi\left(\frac{f_0+f}{c}\cdot R_T\left(\tau,R_{0R},\tau_{0R}\right)+\frac{f_\tau\cdot\tau}{2}\right)\\ \phi_R&=2\pi\left(\frac{f_0+f}{c}\cdot R_R\left(\tau,R_{0R},\tau_{0R}\right)+\frac{f_\tau\cdot\tau}{2}\right)\end{aligned} \tag{3.18}$$

In the above we assume that transmitter and receiver have equal contributions to the overall bistatic Doppler frequency bandwidth. This assumption is true only for weak bistatic configurations. If we have big separation of transmitter and receiver, they will have strongly different Doppler frequencies and approximation of (3.18) will not be valid any more. More correct derivation based on the individual phase modulations of transmitter and receiver are made in [25], [26].

The phase term in (3.16) changes very quickly, so the phasor itself oscillates with an increasing speed. This property allows us to solve for the types of integrals in (3.16) using the Method of Stationary Phase (MSP) (appendix A). In order to apply this method, the point of stationary phase (PSP) must first be determined.

As a first step, we expand the individual phase contributions of the transmitter and the receiver around the individual points of stationary phase, $\tilde{\tau}_R$ and $\tilde{\tau}_T$, by means of a Taylor series. The expansions are stopped at the second-order term.

$$\begin{aligned}\phi_R&=\phi_R\left(\tilde{\tau}_R\right)+\dot{\phi}_R\left(\tilde{\tau}_R\right)\cdot\left(\tau-\tilde{\tau}_R\right)+\frac{1}{2}\ddot{\phi}_R\left(\tilde{\tau}_R\right)\cdot\left(\tau-\tilde{\tau}_R\right)^2+..\\ \phi_T&=\phi_T\left(\tilde{\tau}_T\right)+\dot{\phi}_T\left(\tilde{\tau}_T\right)\cdot\left(\tau-\tilde{\tau}_T\right)+\frac{1}{2}\ddot{\phi}_T\left(\tilde{\tau}_T\right)\cdot\left(\tau-\tilde{\tau}_T\right)^2+..\end{aligned} \tag{3.19}$$

The definition of the PSP means that the value of the phase terms' first derivative at this particular point is zero. Hence, we have $\frac{d\phi_R}{d\tau}_{\tau=\tilde{\tau}_R} = 0$ for the receiver and $\frac{d\phi_T}{d\tau}_{\tau=\tilde{\tau}_T} = 0$ for the transmitter. Adding both phase contributions, we get:

$$\phi_b = \phi_R(\tilde{\tau}_R) + \frac{1}{2}\ddot{\phi}_R(\tilde{\tau}_R)\cdot(\tau-\tilde{\tau}_R)^2 + \phi_T(\tilde{\tau}_T) + \frac{1}{2}\ddot{\phi}_T(\tilde{\tau}_T)\cdot(\tau-\tilde{\tau}_T)^2 .. \tag{3.20}$$

We substitute the phase term in (3.20) inside the integral in (3.16). $\phi_R(\tilde{\tau}_R)$, $\phi_T(\tilde{\tau}_T)$ are the phase values at the points of stationary phase, so they are constant. We extract the corresponding phasor out of the integral.

$$I(f, f_\tau, R_{0R}, \tau_{0R}) = e^{-j\left[\phi_R(\tilde{\tau}_R)+\phi_T(\tilde{\tau}_T)\right]}\cdot I_1(f, f_\tau, R_{0R}, \tau_{0R}) \tag{3.21}$$

The remaining integral is given by:

$$I_1(f, f_\tau, R_{0R}, \tau_{0R}) = \int_{-\infty}^{\infty} w(\tau-\tau_{cb})\cdot e^{-j\frac{1}{2}\left[\ddot{\phi}_R(\tilde{\tau}_R)\cdot(\tau-\tilde{\tau}_R)^2+\ddot{\phi}_T(\tilde{\tau}_T)\cdot(\tau-\tilde{\tau}_T)^2\right]}d\tau \tag{3.22}$$

In summary, we have a sum of two quadratic phase terms in (3.22), each one having a different maximum (or minimum) at a different position of $\tau$. Knowing that the sum of two quadratic terms is again a quadratic term with contributions up to the maximum of second-order in $\tau$. We want to express the sum of two quadratic terms as one quadratic term around one common point of stationary phase of maximum (or minimum). We therefore introduce some shorthand notations:

$$b = \ddot{\phi}_R(\tilde{\tau}_R) \text{ and } a = \ddot{\phi}_T(\tilde{\tau}_T) \tag{3.23}$$

Substituting these abbreviations, we obtain the following from (3.22):

$$\phi_s(\tau) = \ddot{\phi}_R(\tilde{\tau}_R)\cdot(\tau-\tilde{\tau}_R)^2 + \ddot{\phi}_T(\tilde{\tau}_T)\cdot(\tau-\tilde{\tau}_T)^2 = b\cdot(\tau-\tilde{\tau}_R)^2 + a\cdot(\tau-\tilde{\tau}_T)^2 \tag{3.24}$$

The expression above is a sum of two quadratic terms, and the sum remains quadratic. So, we could think about regrouping the expression above around the common bistatic PSP. However, the individual extensions are only valid for points in the vicinity of the individual PSPs. The approach of decomposing the bistatic phase history into a sum of two second-order Taylor series expansions will only be valid for azimuth times, not too far away from both individual points of the stationary phase. This requirement will impose some constraints onto the validity of the approach, which will be analyzed in a late chapter.

Now the task is to determine the common point of minimum or maximum, which will be called the common bistatic PSP. If $\tilde{\tau}$ is the common bistatic PSP, then the bistatic phase histories' first derivatives must vanish at this point, which gives us:

$$2b\cdot(\tilde{\tau}-\tilde{\tau}_R) + 2a\cdot(\tilde{\tau}-\tilde{\tau}_T) = 0 \tag{3.25}$$

Solving (3.25) for $\tilde{\tau}$, we obtain:

$$\tilde{\tau} = \frac{a\cdot\tilde{\tau}_T + b\cdot\tilde{\tau}_R}{a+b} \tag{3.26}$$

and resubstituting the abbreviations given in (3.23), we obtain for the PSP:

$$\tilde{\tau} = \frac{\ddot{\phi}_T(\tilde{\tau}_T)\cdot\tilde{\tau}_T + \ddot{\phi}_R(\tilde{\tau}_R)\cdot\tilde{\tau}_R}{\ddot{\phi}_T(\tilde{\tau}_T) + \ddot{\phi}_R(\tilde{\tau}_R)} \tag{3.27}$$

This is value of the azimuth time, where we experience a stationary phase behavior of the bistatic phase term. It can be interpreted as a weighted average, with the weighting factors being the second-order derivatives, evaluated in the corresponding points of the stationary phase. We will also need the value of the bistatic phase at the PSP, which will be used in the next chapter when we apply the MSP. We can determine this value by resubstituting (3.27) into (3.24).

$$\begin{aligned}\phi_s(\tilde{\tau}) &= a\cdot\left(\tilde{\tau}-\tilde{\tau}_T\right)^2 + b\cdot\left(\tilde{\tau}-\tilde{\tau}_R\right)^2 \\ &= a\cdot\left[\frac{a\cdot\tilde{\tau}_T + b\cdot\tilde{\tau}_R - (a+b)\cdot\tilde{\tau}_T}{a+b}\right]^2 + b\cdot\left[\frac{a\cdot\tilde{\tau}_T + b\cdot\tilde{\tau}_R - (a+b)\cdot\tilde{\tau}_R}{a+b}\right]^2 \\ &= \frac{1}{(a+b)^2}\cdot\left[b^2\cdot a\cdot\left(\tilde{\tau}_R-\tilde{\tau}_T\right)^2 + b\cdot a^2\cdot\left(\tilde{\tau}_R-\tilde{\tau}_T\right)^2\right] \\ &= \frac{b^2\cdot a + b\cdot a^2}{(a+b)^2}\cdot\left(\tilde{\tau}_R-\tilde{\tau}_T\right)^2 = \frac{a\cdot b}{a+b}\cdot\left(\tilde{\tau}_R-\tilde{\tau}_T\right)^2\end{aligned} \tag{3.28}$$

Resubstituting the values of $a$ and $b$ from (3.23), we obtain for the phase value at the PSP:

$$\phi_s(\tilde{\tau}) = \frac{\ddot{\phi}_T(\tilde{\tau}_T)\cdot\ddot{\phi}_R(\tilde{\tau}_R)}{\ddot{\phi}_T(\tilde{\tau}_T)+\ddot{\phi}_R(\tilde{\tau}_R)}\cdot\left(\tilde{\tau}_R-\tilde{\tau}_T\right)^2 \tag{3.29}$$

Now (3.29) is inserted into equation (3.20) to get the final expression of the Taylor series for the bistatic phase around the bistatic PSP:

$$\begin{aligned}\phi_s(\tau) &= \phi_s(\tilde{\tau}) + \frac{1}{2}\ddot{\phi}_s(\tilde{\tau})\cdot(\tau-\tilde{\tau})^2 \\ &= \frac{\ddot{\phi}_T(\tilde{\tau}_T)\cdot\ddot{\phi}_R(\tilde{\tau}_R)}{\ddot{\phi}_T(\tilde{\tau}_T)+\ddot{\phi}_R(\tilde{\tau}_R)}\cdot\left(\tilde{\tau}_R-\tilde{\tau}_T\right)^2 + \left[\ddot{\phi}_T(\tilde{\tau}_T)+\ddot{\phi}_R(\tilde{\tau}_R)\right]\cdot(\tau-\tilde{\tau})^2\end{aligned} \tag{3.30}$$

We proceed to solve the Fourier integral given in (3.21) by substituting the bistatic phase term given in (3.30). After reordering we get:

$$\begin{aligned}I(f,f_\tau,R_{0R},\tau_{0R}) = e^{-j\left(\phi_R(\tilde{\tau}_R)+\phi_T(\tilde{\tau}_T)\right)}\cdot e^{-j\frac{1}{2}\frac{\ddot{\phi}_T(\tilde{\tau}_T)\cdot\ddot{\phi}_R(\tilde{\tau}_R)}{\ddot{\phi}_T(\tilde{\tau}_T)+\ddot{\phi}_R(\tilde{\tau}_R)}\cdot\left(\tilde{\tau}_T-\tilde{\tau}_R\right)^2}\cdot \\ \int_{-\infty}^{\infty} w(\tau-\tau_{cb})\cdot e^{-j\frac{1}{2}\left(\ddot{\phi}_T(\tilde{\tau}_T)+\ddot{\phi}_R(\tilde{\tau}_R)\right)\cdot(\tau-\tilde{\tau})^2}\,d\tau\end{aligned} \tag{3.31}$$

Here we use the MSP, thus obtaining:

$$\begin{aligned}I(f,f_\tau,R_{0R},\tau_{0R}) = e^{-j\left(\phi_R(\tilde{\tau}_R)+\phi_T(\tilde{\tau}_T)\right)}\cdot e^{-j\frac{1}{2}\frac{\ddot{\phi}_T(\tilde{\tau}_T)\cdot\ddot{\phi}_R(\tilde{\tau}_R)}{\ddot{\phi}_T(\tilde{\tau}_T)+\ddot{\phi}_R(\tilde{\tau}_R)}\cdot\left(\tilde{\tau}_T-\tilde{\tau}_R\right)^2}\cdot \\ \cdot w(\tilde{\tau}-\tau_{cb})\cdot\frac{\sqrt{2\pi}}{\sqrt{\ddot{\phi}_T(\tilde{\tau}_T)+\ddot{\phi}_R(\tilde{\tau}_R)}}\cdot e^{-j\frac{\pi}{4}}\end{aligned} \tag{3.32}$$

The result of (3.32) is substituted in (3.15), and we obtain the searched point target reference spectrum as a final result.

$$G(f,f_\tau,R_{0R},\tau_{0R}) = \sigma(R_{0R},\tau_{0R})\cdot w(\tilde{\tau}-\tau_{cb})\cdot S_l(f)\cdot\frac{\sqrt{2\pi}}{\sqrt{\ddot{\phi}_T(\tilde{\tau}_T)+\ddot{\phi}_R(\tilde{\tau}_R)}}\cdot e^{-j\frac{\pi}{4}}\cdot e^{-j(\phi_R(\tilde{\tau}_R)+\phi_T(\tilde{\tau}_T))}\cdot e^{-j\frac{1}{2}\frac{\ddot{\phi}_T(\tilde{\tau}_T)\cdot\ddot{\phi}_R(\tilde{\tau}_R)}{\ddot{\phi}_T(\tilde{\tau}_T)+\ddot{\phi}_R(\tilde{\tau}_R)}\cdot(\tilde{\tau}_T-\tilde{\tau}_R)^2} \tag{3.33}$$

This is the *Bistatic Point Target Reference Spectrum (BPTRS)*. It will be essential for the derivation of our bistatic processing algorithms.

## 3.4 Bistatic Point Target Reference Spectrum

The Bistatic Point Target Reference Spectrum (BPTRS) given in (3.33) conceptually shows how we can combine the two monostatic phase and Doppler histories of the transmitter and the receiver to the BPTRS. We have to calculate the individual points of stationary phases, the corresponding phase arguments in those points and their second order phase derivatives.

For the receiver, the calculation is straightforward and has been documented in the open literature [24]. When considering the transmitter, we have similar expressions as for the receiver, but finally we intend to express everything in terms of the receiver's coordinates.

### 3.4.1 General Discussion

The quite general form of the bistatic point target reference spectrum, as expressed in (3.33), shows the individual contributions of the transmitter and the receiver to the bistatic representation:

- $G(f,f_\tau,R_{0R},\tau_{0R})$ is the point target reference spectrum. It depends on the range frequency $f$, the azimuth frequency $f_\tau$ and the position of the individual point target. The location of the point target (PT) in our bistatic approach is given by the receiver's coordinates $(R_{0R},\tau_{0R})$. $R_{0R}$ is the slant range when the PT is seen perpendicularly from the receiver, and $\tau_{0R}$ is the azimuth time when the receiver reaches the point of closest approach.
- $\sigma(R_{0R},\tau_{0R})$ is the backscattering coefficient expressed in the receiver's coordinates. The SAR processor must determine it for the complete scene.
- $w(\tilde{\tau}-\tau_{cb})$ is a rectangular window centered at $\tau_{cb}$.
- $\tau_{cb}$ is the azimuth time at the center of the common bistatic footprint.
- $\tilde{\tau}$ is the common bistatic point of stationary phase, given in (3.27). Since it depends on the azimuth (Doppler) frequency $f_\tau$, $w(\tilde{\tau}-\tau_{cb})$ defines the azimuth bandwidth as a rectangular window around the bistatic Doppler centroid frequency.
- $S_l(f)$ is the transmitted signal's spectrum.
- The first exponential term, $e^{-j(\phi_R(\tilde{\tau}_R)+\phi_T(\tilde{\tau}_T))}\cong e^{-j\Psi_{QM}}$, will be called a *quasi-monostatic* term.
- The second phase term, $e^{-j\frac{1}{2}\frac{\ddot{\phi}_T(\tilde{\tau}_T)\cdot\ddot{\phi}_R(\tilde{\tau}_R)}{\ddot{\phi}_T(\tilde{\tau}_T)+\ddot{\phi}_R(\tilde{\tau}_R)}\cdot(\tilde{\tau}_T-\tilde{\tau}_R)^2}\cong e^{-j\frac{1}{2}\Psi_{BI}}$, will be denoted as a *bistatic deformation* term. The nature of the quasi-monostatic and the bistatic

deformation terms, their meaning and their behavior are considered in the following chapters.

We need to further determine the components of the bistatic point target reference spectrum over range and azimuth frequency, and the coordinates of our bistatic approach $(f, f_\tau, R_{0R}, \tau_{0R})$. Similar derivations are well known for the Monostatic Point Target Reference Spectrum (MPTRS) [24]. Here we will do the derivations for the bistatic case. We start with the common bistatic point of stationary phase given in (3.27).

### 3.4.1.1 Receiver's Contributions

#### *3.4.1.1.1 Receiver's Point of Stationary Phase*

First we calculate the unknown parts related to the receiver. From (3.18) we have:

$$\phi_R(\tau) = 2\pi\left[\frac{f+f_0}{c}\cdot R_R(\tau, R_R, \tau_{0R}) + \frac{f_\tau}{2}\cdot\tau\right] \tag{3.34}$$

The first- and the second-order derivatives of the receiver's phase terms are then:

$$\dot{\phi}_R(\tau) = 2\pi\left[\frac{f+f_0}{c}\cdot \dot{R}_R(\tau, R_{0R}, \tau_{0R}) + \frac{f_\tau}{2}\right] \tag{3.35}$$

and

$$\ddot{\phi}_R(\tau) = 2\pi\left[\frac{f+f_0}{c}\cdot \ddot{R}_R(\tau, R_{0R}, \tau_{0R})\right] \tag{3.36}$$

Hence, in order to determine the phase and its derivatives, we need to obtain the corresponding receiver's slant range $R_R$ and its derivatives.

As the inner product of the vector with itself is the squared modulus of the vector. We write for the receiver's slant range vector $\vec{R}_R$.

$$R_R(\tau, R_{0R}, \tau_{0R})^2 = \vec{R}_R(\tau, R_{0R}, \tau_{0R})\cdot\vec{R}_R(\tau, R_{0R}, \tau_{0R}) \tag{3.37}$$

Differentiating the expression above, we obtain:

$$2R_R(\tau, R_{0R}, \tau_{0R})\cdot\dot{R}_R(\tau, R_{0R}, \tau_{0R}) = 2\dot{\vec{R}}_R(\tau, R_{0R}, \tau_{0R})\cdot\vec{R}_R(\tau, R_{0R}, \tau_{0R}) \tag{3.38}$$

and after the reordering, we get:

$$\dot{R}_R(\tau, R_{0R}, \tau_{0R}) = \dot{\vec{R}}_R(\tau, R_{0R}, \tau_{0R})\cdot\frac{\vec{R}_R(\tau, R_{0R}, \tau_{0R})}{R_R(\tau, R_{0R}, \tau_{0R})} \tag{3.39}$$

The derivative of the slant range vector is the negative velocity vector of the receiver.

$$\dot{\vec{R}}_R(\tau, R_{0R}, \tau_{0R}) = -\vec{v}_R \tag{3.40}$$

Now we multiply both sides of the equation given in (3.1) by $\vec{v}_R$ and obtain:

$$\vec{R}_R(\tau, R_{0R}, \tau_{0R})\cdot\vec{v}_R = \vec{v}_R\cdot\vec{R}_R(\tau_{0R}, R_{0R}, \tau_{0R}) - \vec{v}_R\cdot\vec{v}_R\cdot(\tau-\tau_{0R}) \tag{3.41}$$

At the point of closest approach, the point target is seen perpendicular to the receiver's movement. Hence the receiver's velocity vector and the slant range vector at the PCA are orthogonal, and we have $\vec{v}_R \cdot \vec{R}_R\left(\tau_{0R}, R_{0R}, \tau_{0R}\right) = 0$. Summarizing, we obtain from (3.41):

$$\vec{v}_R \cdot \vec{R}_R\left(\tau, R_{0R}, \tau_{0R}\right) = -{v_R}^2 \cdot \left(\tau - \tau_{0R}\right) \tag{3.42}$$

Inserting the result of (3.42) in (3.39), we get:

$$\dot{R}_R\left(\tau, R_{0R}, \tau_{0R}\right) = -\vec{v}_R \cdot \frac{\vec{R}_R\left(\tau, R_{0R}, \tau_{0R}\right)}{R_R\left(\tau, R_{0R}, \tau_{0R}\right)} = -\vec{v}_R \cdot \vec{e}_r\left(\tau, R_{0R}, \tau_{0R}\right) = {v_R}^2 \cdot \frac{\left(\tau - \tau_{0R}\right)}{R_R\left(\tau, R_{0R}, \tau_{0R}\right)} \tag{3.43}$$

To determine the second-order derivative, we differentiate (3.38) again and get:

$$\begin{aligned} &\dot{R}_R\left(\tau, R_{0R}, \tau_{0R}\right)^2 + R_R\left(\tau, R_{0R}, \tau_{0R}\right) \cdot \ddot{R}_R\left(\tau, R_{0R}, \tau_{0R}\right) = \\ &\dddot{R}_R\left(\tau, R_{0R}, \tau_{0R}\right) \cdot \vec{R}_R\left(\tau, R_{0R}, \tau_{0R}\right) + \ddot{\vec{R}}_R\left(\tau, R_{0R}, \tau_{0R}\right) \cdot \dot{\vec{R}}_R\left(\tau, R_{0R}, \tau_{0R}\right) \end{aligned} \tag{3.44}$$

Solving (3.44) for $\ddot{R}_R\left(\tau, R_{0R}, \tau_{0R}\right)$, and substituting (3.43), the second-order derivative of the receiver's slant range is found to be:

$$\begin{aligned} &\ddot{R}_R\left(\tau, R_{0R}, \tau_{0R}\right) = \dddot{R}_R\left(\tau, R_{0R}, \tau_{0R}\right) \cdot \frac{\vec{R}_R\left(\tau, R_{0R}, \tau_{0R}\right)}{R_R\left(\tau, R_{0R}, \tau_{0R}\right)} - \\ &\left[-\vec{v}_R \frac{\dot{\vec{R}}_R\left(\tau, R_{0R}, \tau_{0R}\right)}{R_R\left(\tau, R_{0R}, \tau_{0R}\right)}\right]^2 \cdot \frac{1}{R_R\left(\tau, R_{0R}, \tau_{0R}\right)} + \frac{\dot{\vec{R}}_R\left(\tau, R_{0R}, \tau_{0R}\right) \cdot \dot{\vec{R}}_R\left(\tau, R_{0R}, \tau_{0R}\right)}{R_R\left(\tau, R_{0R}, \tau_{0R}\right)} \end{aligned} \tag{3.45}$$

Since the velocity vector is assumed constant, its derivative is zero $\dddot{\vec{R}}_R\left(\tau, R_{0R}, \tau_{0R}\right) = -\dot{\vec{v}}_R = \vec{0}$, and using (3.42) we obtain the following simplification:

$$\ddot{R}_R\left(\tau, R_{0R}, \tau_{0R}\right) = -\frac{{v_R}^4}{R_R\left(\tau, R_{0R}, \tau_{0R}\right)^3} \cdot \left(\tau - \tau_{0R}\right)^2 + \frac{{v_R}^2}{R_R\left(\tau, R_{0R}, \tau_{0R}\right)} \tag{3.46}$$

Now returning to (3.35) and using the definition of the point of stationary phase (PSP), we have:

$$\dot{\phi}_R\left(\tilde{\tau}_R\right) = 2\pi\left[\frac{f + f_0}{c} \cdot \dot{R}_R\left(\tilde{\tau}_R, R_{0R}, \tau_{0R}\right) + \frac{f_\tau}{2}\right] = 0 \tag{3.47}$$

and:

$$\frac{f + f_0}{c} \cdot \dot{R}_R\left(\tilde{\tau}_R, R_{0R}, \tau_{0R}\right) + \frac{f_\tau}{2} = 0 \tag{3.48}$$

Now we use the slant range derivative from (3.43) and get from (3.48):

$$\frac{f + f_0}{c} \cdot \frac{{v_R}^2\left(\tilde{\tau}_R - \tau_{0R}\right)}{R_R\left(\tilde{\tau}_R\right)} + \frac{f_\tau}{2} = 0 \tag{3.49}$$

$$\text{or } \left(\tilde{\tau}_R - \tau_{0R}\right) \cdot 2{v_R}^2 = -f_\tau \cdot R_R\left(\tilde{\tau}_R\right) \cdot \frac{c}{f + f_0} \tag{3.50}$$

From the above, the azimuth time difference between the PSP and the azimuth time at the PCA is determined as:

$$\tilde{\tau}_R - \tau_{0R} = -f_\tau \cdot R_R\left(\tilde{\tau}_R\right) \cdot \frac{c}{2{v_R}^2\left(f + f_0\right)} \tag{3.51}$$

We square the expression above and get:

$$\left(\tilde{\tau}_R - \tau_{0R}\right)^2 = {f_\tau}^2 \cdot R_R\left(\tilde{\tau}_R\right)^2 \cdot \frac{c^2}{4{v_R}^4\left(f + f_0\right)^2} \tag{3.52}$$

With some rearrangements, we have:

$$\left(\tilde{\tau}_R - \tau_{0R}\right)^2 \cdot 4{v_R}^4 \cdot \left(f + f_0\right)^2 = {f_\tau}^2 \cdot R_R\left(\tilde{\tau}_R\right)^2 \cdot c^2 \tag{3.53}$$

The azimuth time difference between the receiver's PSP and the PCA determined above can be obtained in a different way. At the PCA, the velocity vector and the slant range vectors are orthogonal, so after squaring (3.1) and evaluating the expression at the receiver's PSP, we obtain:

$$R_R\left(\tilde{\tau}_R\right)^2 = {R_{0R}}^2 + {v_R}^2 \cdot \left(\tilde{\tau}_R - \tau_{0R}\right)^2 \tag{3.54}$$

That is equivalent to:

$$ {v_R}^2 \cdot \left(\tilde{\tau}_R - \tau_{0R}\right)^2 = R_R\left(\tilde{\tau}_R\right)^2 - {R_{0R}}^2 \tag{3.55}$$

The right part of this expression is substituted in (3.53), and we get:

$$4{v_R}^2 \cdot \left(R_R\left(\tilde{\tau}_R\right)^2 - {R_{0R}}^2\right) \cdot \left(f + f_0\right)^2 = {f_\tau}^2 \cdot R_R\left(\tilde{\tau}_R\right)^2 \cdot c^2 \tag{3.56}$$

We do some reordering:

$$R_R\left(\tilde{\tau}_R\right)^2 \cdot \left(4{v_R}^2 \cdot \left(f + f_0\right)^2 - {f_\tau}^2 c^2\right) = 4{v_R}^2 {R_{0R}}^2 \cdot \left(f + f_0\right)^2 \tag{3.57}$$

Thus, we have determined the receiver's slant range squared value at receiver's PCA as:

$$R_R\left(\tilde{\tau}_R\right)^2 = \frac{{R_{0R}}^2 \cdot \left(f + f_0\right)^2}{\left(f + f_0\right)^2 - \frac{{f_\tau}^2 c^2}{4{v_R}^2}} \tag{3.58}$$

Now we take the square root and obtain:

$$R_R\left(\tilde{\tau}_R\right) = R_{0R} \cdot \frac{\left|f + f_0\right|}{\sqrt{\left(f + f_0\right)^2 - \frac{{f_\tau}^2 c^2}{4{v_R}^2}}} \tag{3.59}$$

Since the square root expression is a core element of any SAR processor, and we will frequently use it in further developments, the following two new symbols are introduced:

$$\boxed{\begin{aligned} F_R\left(f,f_\tau\right) &= \left(f+f_0\right)^2 - \frac{f_\tau c^2}{4v_R{}^2} \\ F_T\left(f,f_\tau\right) &= \left(f+f_0\right)^2 - \frac{f_\tau c^2}{4v_T{}^2} \end{aligned}} \tag{3.60}$$

Substituting the symbols into (3.59), we obtain:

$$R_R\left(\tilde{\tau}_R\right) = R_{0R} \cdot \frac{\left|f+f_0\right|}{F_R\left(f,f_\tau\right)^{\frac{1}{2}}} \tag{3.61}$$

and in an analogous way:

$$R_T\left(\tilde{\tau}_T\right) = R_{0T} \cdot \frac{\left|f+f_0\right|}{F_T\left(f,f_\tau\right)^{\frac{1}{2}}} \tag{3.62}$$

Equation (3.61) is substituted in (3.51), and we express the receiver's PSP in terms of $\left(f,f_\tau,R_{0R},\tau_{0R}\right)$ variables:

$$\tilde{\tau}_R - \tau_{0R} = -f_\tau \cdot R_{0R} \cdot \frac{\left|f+f_0\right|}{\sqrt{\left(f+f_0\right)^2 - \frac{f_\tau{}^2 c^2}{4v_R{}^2}}} \cdot \frac{c}{2v_R{}^2 \cdot \left(f+f_0\right)} \tag{3.63}$$

which is equivalent to:

$$\tilde{\tau}_R = \tau_{0R} - f_\tau \cdot R_{0R} \cdot \frac{\left|f+f_0\right|}{\sqrt{\left(f+f_0\right)^2 - \frac{f_\tau{}^2 c^2}{4v_R{}^2}}} \cdot \frac{c}{2v_R{}^2 \left(f+f_0\right)} \tag{3.64}$$

The expression above could be written in an elegant way by introducing the sgn[1] function.

$$\tilde{\tau}_R = \tau_{0R} + f_\tau \cdot R_{0R} \cdot \operatorname{sgn}\left(f+f_0\right) \cdot \frac{1}{\sqrt{\left(f+f_0\right)^2 - \frac{f_\tau{}^2 c^2}{4v_R{}^2}}} \cdot \frac{c}{2v_R{}^2} \tag{3.65}$$

Hence, the final expression of the receiver's PSP is:

$$\boxed{\tilde{\tau}_R = \tau_{0R} - f_\tau \cdot R_{0R} \cdot \operatorname{sgn}\left(f+f_0\right) \cdot \frac{1}{F_R{}^{\frac{1}{2}}\left(f,f_\tau\right)} \cdot \frac{c}{2v_R{}^2}} \tag{3.66}$$

#### *3.4.1.1.2 Receiver's Phase Term at the Point of Stationary Phase*

For the next step, we need to calculate the value of the second-order derivative of the receiver's phase term at the Point of Stationary Phase (PSP). This value appears both in the

[1] signum function is defined as $\operatorname{sgn}(x) = \begin{cases} 1, & x > 0 \\ 0, & x = 0 \\ -1, & x < 0 \end{cases}$

bistatic phasor and in the amplitude factor of the bistatic point target reference spectrum. From equation (3.36) we have:

$$\ddot{\phi}_R(\tau) = 2\pi \frac{f+f_0}{c} \cdot \ddot{R}_R(\tau, R_{0R}, \tau_{0R}).$$

In (3.46), we have already determined the second-order derivative of the receiver's slant range. We substitute the expression (3.43) into (3.46) and get:

$$\ddot{R}_R(\tau, R_{0R}, \tau_{0R}) = -\frac{\dot{R}_R(\tau, R_{0R}, \tau_{0R})^2}{R_R(\tau, R_{0R}, \tau_{0R})} + \frac{{v_R}^2}{R_R(\tau, R_{0R}, \tau_{0R})} \tag{3.67}$$

We evaluate (3.67) at the PSP and obtain:

$$\ddot{R}_R(\tilde{\tau}_R) = \frac{{v_R}^2 - \dot{R}_R(\tilde{\tau}_R)^2}{R_R(\tilde{\tau}_R)} \tag{3.68}$$

In (3.69), we first determine $\dot{R}_R(\tilde{\tau}_R)$. We use (3.43), and by inserting the expression of (3.51), we get the slant range's first order derivative at the PSP as:

$$\dot{R}_R(\tilde{\tau}_R) = \frac{{v_R}^2 \cdot (\tilde{\tau}_R - \tau_{0R})}{R_R(\tilde{\tau}_R)} = -\frac{1}{R_R(\tilde{\tau}_R)} \cdot {v_R}^2 \cdot f_\tau \cdot \frac{{v_R}^2 \cdot R_R(\tilde{\tau}_R) \cdot c}{2{v_R}^2 (f+f_0)} = -\frac{f_\tau \cdot c}{2(f+f_0)} \tag{3.69}$$

Inserting the derivative above into (3.68), we get:

$$\begin{aligned} \ddot{R}_R(\tilde{\tau}_R) &= \frac{{v_R}^2 - \left[\frac{f_\tau \cdot c}{2(f+f_0)}\right]^2}{R_{0R} \cdot |f+f_0|} \cdot \sqrt{(f+f_0)^2 - \frac{f_\tau^2 c^2}{4{v_R}^2}} \\ &= \frac{4{v_R}^2 \cdot (f+f_0)^2 - f_\tau^2 c^2}{4R_{0R} \cdot |f+f_0| \cdot (f+f_0)^2} \cdot \sqrt{(f+f_0)^2 - \frac{f_\tau^2 c^2}{4{v_R}^2}} = \frac{{v_R}^2}{R_{0R}} \cdot \frac{\left[(f+f_0)^2 - \frac{f_\tau^2 c^2}{4{v_R}^2}\right]^{\frac{3}{2}}}{|f+f_0| \cdot (f+f_0)^2} \end{aligned} \tag{3.70}$$

We insert the result of (3.70) into (3.36) and get:

$$\begin{aligned} \ddot{\phi}_R(\tilde{\tau}_R) &= 2\pi \left[\frac{f+f_0}{c} \cdot \ddot{R}_R(\tau, R_{0R}, \tau_{0R})\right] = 2\pi \frac{f+f_0}{c} \cdot \frac{{v_R}^2}{R_{0R}} \cdot \frac{\left[(f+f_0)^2 - \frac{f_\tau^2 c^2}{4{v_R}^2}\right]^{\frac{3}{2}}}{|f+f_0|(f+f_0)^2} \\ &= \frac{2\pi}{c} \cdot \frac{{v_R}^2}{R_{0R}} \cdot \frac{\left[(f+f_0)^2 - \frac{f_\tau^2 c^2}{4{v_R}^2}\right]^{\frac{3}{2}} \cdot \operatorname{sgn}(f+f_0)}{(f+f_0)^2} \end{aligned} \tag{3.71}$$

Thus, the final expression for the receiver's second order phase derivative at the PSP is:

$$\boxed{\ddot{\phi}_R(\tilde{\tau}_R) = \frac{2\pi}{c} \cdot \frac{{v_R}^2}{R_{0R}} \cdot \frac{F_R^{\frac{3}{2}} \cdot \operatorname{sgn}(f+f_0)}{(f+f_0)^2}} \tag{3.72}$$

#### *3.4.1.1.3 Receiver's Phase Value at the Point of Stationary Phase*

In a similar way, we determine the receiver's phase term at the PSP. Here we insert the expression (3.66) in equation (3.34) and write:

$$\begin{aligned}\phi_R\left(\tilde{\tau}_R\right) &= 2\pi\left[\frac{f+f_0}{c}\cdot R_R\left(\tilde{\tau}_R, R_{0R}, \tau_{0R}\right)+\frac{f_\tau}{2}\cdot\tilde{\tau}_R\right] \\ &= 2\pi\left[\frac{f+f_0}{c}\cdot R_R\left(\tilde{\tau}_R, R_{0R}, \tau_{0R}\right)+\frac{f_\tau}{2}\cdot\left(\tau_{0R}-\frac{f_\tau\cdot R_R\left(\tilde{\tau}_R, R_{0R}, \tau_{0R}\right)c}{2{v_R}^2\cdot\left(f+f_0\right)}\right)\right]\end{aligned} \tag{3.73}$$

Now we substitute $R_R\left(\tilde{\tau}_R, R_{0R}, \tau_{0R}\right)$ from (3.61) and get:

$$\phi_R\left(\tilde{\tau}_R\right)=\pi f_\tau\cdot\tau_{0R}+\frac{2\pi}{c}\operatorname{sgn}\left(f+f_0\right)\cdot R_{0R}\cdot\sqrt{\left(f+f_0\right)^2-\frac{{f_\tau}^2c^2}{4{v_R}^2}} \tag{3.74}$$

In summary, we have the final expression of the *receiver's phase term at the point of stationary phase*:

$$\boxed{\phi_R\left(\tilde{\tau}_R\right)=\pi f_\tau\cdot\tau_{0R}+\frac{2\pi}{c}\operatorname{sgn}\left(f+f_0\right)\cdot R_{0R}\cdot F_R^{\frac{1}{2}}} \tag{3.75}$$

### 3.4.1.2 Transmitter's Contributions

#### *3.4.1.2.1 Transmitter's Point of Stationary Phase*

The transmitter's phase contribution is given by:

$$\phi_T\left(\tau\right)=2\pi\left[\frac{f+f_0}{c}\cdot R_T\left(\tau, R_{0R}, \tau_{0R}\right)+\frac{f_\tau}{2}\cdot\tau\right] \tag{3.76}$$

The first-order derivative of transmitter's phase term is then:

$$\dot{\phi}_T\left(\tau\right)=2\pi\left[\frac{f+f_0}{c}\cdot\dot{R}_T\left(\tau, R_{0R}, \tau_{0R}\right)+\frac{f_\tau}{2}\right] \tag{3.77}$$

The derivative of the slant range vector is the negative velocity vector of the transmitter:

$$\vec{R}_T\left(\tau, R_{0R}, \tau_{0R}\right)=-\vec{v}_T \tag{3.78}$$

In section 3.1 we derived the special dependency between the transmitter's slant range vector at any instant and the receiver's slant range vector at its Point of Closest Approach (PCA):

$$\vec{R}_T\left(\tau, R_{0R}, \tau_{0R}\right)=\vec{R}_R\left(\tau_{0R}, R_{0R}, \tau_{0R}\right)+\vec{d}\left(\tau_{0R}\right)-\vec{v}_T\cdot\left(\tau-\tau_{0R}\right) \tag{3.79}$$

In (3.38) we have the dependency between the receiver's slant range, velocity and equivalent vectorial expressions. For the transmitter, a similar expression holds:

$$R_T\left(\tau, R_{0R}, \tau_{0R}\right)\cdot\dot{R}_T\left(\tau, R_{0R}, \tau_{0R}\right)=-\vec{v}_T\cdot\vec{R}_T\left(\tau, R_{0R}, \tau_{0R}\right) \tag{3.80}$$

Using the vectorial representation in (3.79), the following expression for the transmitter's slant range is obtained:

$$\begin{aligned}\dot{R}_T\left(\tau,R_{0R},\tau_{0R}\right)&=\frac{\dot{\vec{R}}_T\left(\tau,R_{0R},\tau_{0R}\right)\cdot\vec{R}_T\left(\tau,R_{0R},\tau_{0R}\right)}{R_T\left(\tau,R_{0R},\tau_{0R}\right)}=-\vec{v}_T\cdot\frac{\vec{R}_T\left(\tau,R_{0R},\tau_{0R}\right)}{R_T\left(\tau,R_{0R},\tau_{0R}\right)}\\&=-\vec{v}_T\cdot\frac{\vec{R}_R\left(\tau_{0R},R_{0R},\tau_{0R}\right)+\vec{d}\left(\tau_{0R}\right)-\vec{v}_T\left(\tau-\tau_{0R}\right)}{R_T\left(\tau,R_{0R},\tau_{0R}\right)}\\&=\frac{{v^2}_T\cdot\left(\tau-\tau_{0R}\right)-\vec{v}_T\cdot\left(\vec{R}_R\left(\tau,R_{0R},\tau_{0R}\right)+\vec{d}\left(\tau_{0R}\right)\right)}{R_T\left(\tau,R_{0R},\tau_{0R}\right)}\end{aligned}\tag{3.81}$$

Now we differentiate (3.80) to find the second-order derivative of transmitter's slant range:

$$\dot{R}_T^2\left(\tau,R_{0R},\tau_{0R}\right)+\ddot{R}_T\left(\tau,R_{0R},\tau_{0R}\right)\cdot R_T\left(\tau,R_{0R},\tau_{0R}\right)=-\vec{v}_T\cdot\dot{\vec{R}}_T\left(\tau,R_{0R},\tau_{0R}\right)\tag{3.82}$$

The transmitter's and the receiver's velocity vectors are constant. That is why $\ddot{\vec{R}}_T$ vanishes in the expression above.

Reordering, we obtain:

$$\ddot{R}_T\left(\tau,R_{0R},\tau_{0R}\right)=\frac{-\vec{v}_T\cdot\dot{\vec{R}}_T\left(\tau,R_{0R},\tau_{0R}\right)-\dot{R}_T^2\left(\tau,R_{0R},\tau_{0R}\right)}{R_T\left(\tau,R_{0R},\tau_{0R}\right)}=\frac{{v^2}_T-\dot{R}_T^2\left(\tau,R_{0R},\tau_{0R}\right)}{R_T\left(\tau,R_{0R},\tau_{0R}\right)}\tag{3.83}$$

Using the definition of the stationary phase, the first-order derivative of the transmitter's phase must vanish in the PSP:

$$\dot{\phi}_T\left(\tilde{\tau}_T\right)=2\pi\left[\frac{f+f_0}{c}\cdot\dot{R}_T\left(\tilde{\tau}_T,R_{0R},\tau_{0R}\right)+\frac{f_\tau}{2}\right]=0\tag{3.84}$$

Hence, we have got the first-order derivative of the slant range as:

$$\dot{R}_T\left(\tilde{\tau}_T,R_{0R},\tau_{0R}\right)=-\frac{f_\tau c}{2\left(f+f_0\right)}\tag{3.85}$$

Combining (3.85) and (3.83), we get the value of second-order derivative at the transmitter's PSP:

$$\ddot{R}_T\left(\tilde{\tau}_T,R_{0R},\tau_{0R}\right)=\frac{{v_T}^2-\dot{R}_T^2\left(\tilde{\tau}_T,R_{0R},\tau_{0R}\right)}{R_T\left(\tilde{\tau}_T,R_{0R},\tau_{0R}\right)}=\frac{{v^2}_T-\dfrac{{f_\tau}^2c^2}{4\left(f+f_0\right)^2}}{R_T\left(\tau,R_{0R},\tau_{0R}\right)}\tag{3.86}$$

Next, we substitute the expression of (3.81) evaluated at $\tilde{\tau}_T$ into (3.84) and obtain the following (we use the expression given in the brackets):

$$2\frac{f+f_0}{c}\cdot\frac{{v^2}_T\left(\tilde{\tau}_T-\tau_{0R}\right)-\vec{v}_T\cdot\left(\vec{R}_R\left(\tau_{0R},R_{0R},\tau_{0R}\right)+\vec{d}\left(\tau_{0R}\right)\right)}{R_T\left(\tau,R_{0R},\tau_{0R}\right)}=-f_\tau\tag{3.87}$$

After reordering we get:

$${v^2}_T\cdot\left(\tilde{\tau}-\tau_{0R}\right)=\frac{-f_\tau c}{2\left(f+f_0\right)}\cdot R_T\left(\tilde{\tau}_T,R_{0R},\tau_{0R}\right)+\vec{v}_T\cdot\left(\vec{R}_R\left(\tau_{0R},R_R,\tau_{0R}\right)+\vec{d}\left(\tau_{0R}\right)\right)\tag{3.88}$$

Now we divide both sides of the expression above by ${v^2}_T$:

$$\tilde{\tau}_T - \tau_{0R} = \frac{-f_\tau c}{2v^2{}_T \cdot (f + f_0)} \cdot R_T(\tilde{\tau}_T, R_{0R}, \tau_{0R}) + \underbrace{\frac{\vec{v}_T}{v^2{}_T} \cdot \left(\vec{R}_R(\tau_{0R}, R_{0R}, \tau_{0R}) + \vec{d}(\tau_{0R})\right)}_{a_0} \tag{3.89}$$

In (3.89) we have introduced the new parameter $a_0$. This parameter is very important in our bistatic approach. The value and meaning of $a_0$ can be determined in the following way. First we evaluate the expression (3.79) at $\tau_{0T}$ and get:

$$\vec{R}_T(\tau_{0T}, R_{0R}, \tau_{0R}) = \vec{R}_R(\tau_{0R}, R_{0R}, \tau_{0R}) + \vec{d}(\tau_{0R}) - \vec{v}_T \cdot (\tau_{0T} - \tau_{0R}) \tag{3.90}$$

Now we multiply the expression above with $\vec{v}_T$, and as the receiver's velocity vector and slant range vectors are orthogonal at the transmitter's PCA: $\vec{v}_T \perp \vec{R}_T(\tau_{0T}, R_{0R}, \tau_{0R})$ we get:

$$0 = \vec{v}_T \cdot \left(\vec{R}_R(\tau_{0R}, R_{0R}, \tau_{0R}) + \vec{d}(\tau_{0R})\right) - v_T{}^2 \cdot (\tau_{0T} - \tau_{0R}) \tag{3.91}$$

Solving (3.91) for the time difference of the points of closest approach, we obtain:

$$\tau_{0T} - \tau_{0R} = \frac{\vec{v}_T}{v^2{}_T} \cdot \left(\vec{R}_R(\tau, R_{0R}, \tau_{0R}) + \vec{d}(\tau_{0R})\right) = a_0 \tag{3.92}$$

Which is exactly the vectorial expression for the $a_0$ introduced in (3.89), related to the bistatic geometry. Summarizing, in (3.92) and (3.7) we introduced two parameters describing the bistatic degree of a constellation, crucial for our processing approach:

$$\begin{aligned} a_0 &= \tau_{0T} - \tau_{0R} = \frac{\vec{v}_T}{v^2_T} \cdot \left(\vec{R}_R(\tau, R_{0R}, \tau_{0R}) + \vec{d}(\tau_{0R})\right) \\ a_2{}^2 &= \frac{R_{0T}^2}{R_{0R}^2} = \left|\frac{\vec{R}_T(\tau_{0T}, R_{0R}, \tau_{0R})}{\vec{R}_R(\tau_{0R}, R_{0R}, \tau_{0R})}\right|^2 = \left|\vec{e}_R(\tau_{0R}, R_{0R}, \tau_{0R}) + \frac{\vec{d}(\tau_{0R})}{R_{0R}}\right|^2 - v_T^2 \cdot \frac{(\tau_{0R} - \tau_{0T})^2}{R_{0R}^2} \end{aligned} \tag{3.93}$$

We continue with determination of the transmitter's PSP. Using the upper expression of (3.93) in (3.89), we have:

$$\tilde{\tau}_T = \tau_{0R} - \frac{f_\tau c}{2v^2{}_T \cdot (f + f_0)} \cdot \vec{R}_T(\tilde{\tau}_T, R_{0R}, \tau_{0R}) + a_0 \tag{3.94}$$

Now we multiply both sides of (3.94) with the transmitter's velocity vector $\vec{v}_T$**:**

$$(\tilde{\tau}_T - \tau_{0R}) \cdot \vec{v}_T = \vec{v}_T \cdot \left( - \frac{f_\tau c}{2v^2{}_T \cdot (f + f_0)} \cdot \vec{R}_T(\tilde{\tau}_T, R_{0R}, \tau_{0R}) + a_0 \right) \tag{3.95}$$

In the above, we need to determine $\vec{R}_T(\tilde{\tau}_T, R_{0R}, \tau_{0R})$. Evaluating (3.79) at the transmitter's PSP, we obtain:

$$\vec{R}_T(\tilde{\tau}_T, R_{0R}, \tau_{0R}) = \vec{R}_R(\tau_{0R}, R_{0R}, \tau_{0R}) + \vec{d}(\tau_{0R}) - \vec{v}_T \cdot (\tilde{\tau}_T - \tau_{0R}) \tag{3.96}$$

Now substituting (3.95) in (3.96), and after reordering, we get:

$$\vec{R}_T\left(\tilde{\tau}_T, R_{0R}, \tau_{0R}\right) = \vec{R}_R\left(\tau_{0R}, R_{0R}, \tau_{0R}\right) + \vec{d}\left(\tau_{0R}\right) + \\ + \vec{v}_T \cdot \left( \frac{f_\tau c}{2v^2{}_T \left(f + f_0\right)} \cdot \vec{R}_R\left(\tilde{\tau}_T, R_{0R}, \tau_{0R}\right) - a_0 \right) \tag{3.97}$$

We square both sides of (3.97) and get:

$$R_T{}^2\left(\tilde{\tau}_T, R_{0R}, \tau_{0R}\right) = \left(\vec{R}_R\left(\tau_{0R}, R_{0R}, \tau_{0R}\right) + \vec{d}\left(\tau_{0R}\right)\right)^2 + \\ + v^2{}_T \cdot \left( \frac{f_\tau c}{2v^2{}_T \cdot \left(f + f_0\right)} \cdot \vec{R}_R\left(\tilde{\tau}_T, R_{0R}, \tau_{0R}\right) - a_0 \right)^2 + \\ + 2\vec{v}_T \cdot \underbrace{\left(\vec{R}_R\left(\tau_{0R}, R_{0R}, \tau_{0R}\right) + \vec{d}\left(\tau_{0R}\right)\right)}_{a_0 v_T{}^2} \cdot \\ \cdot \left( \frac{f_\tau c}{2v^2{}_T \cdot \left(f + f_0\right)} \cdot \vec{R}_T\left(\tilde{\tau}_T, R_{0R}, \tau_{0R}\right) - a_0 \right) \tag{3.98}$$

In (3.98) we use the bistatic parameter $a_0$ from (3.93), and by simplifying it we obtain:

$$R_T{}^2\left(\tilde{\tau}_T, R_{0R}, \tau_{0R}\right) = \left(\vec{R}_R\left(\tilde{\tau}_{0R}, R_{0R}, \tau_{0R}\right) + \vec{d}\left(\tau_{0R}\right)\right)^2 + v^2{}_T \frac{f_\tau{}^2 \cdot c^2 \cdot R_T{}^2\left(\tilde{\tau}_T, R_{0R}, \tau_{0R}\right)}{4v_T{}^4 \cdot \left(f + f_0\right)^2} + \\ + v_T{}^2 a_0{}^2 - v^2{}_T \frac{f_\tau{}^2 \cdot c \cdot R_T\left(\tilde{\tau}_T, R_{0R}, \tau_{0R}\right)}{v_T{}^2 \cdot \left(f + f_0\right)^2} a_0 - 2v_T{}^2 a_0{}^2 + \\ + v^2{}_T \frac{f_\tau{}^2 \cdot c \cdot R_T\left(\tilde{\tau}_T, R_{0R}, \tau_{0R}\right)}{v_T{}^2 \cdot \left(f + f_0\right)^2} a_0 \\ = \left(\vec{R}_R\left(\tau_{0R}, R_{0R}, \tau_{0R}\right) + \vec{d}\left(\tau_{0R}\right)\right)^2 + \frac{f_\tau{}^2 \cdot c^2 \cdot R_T{}^2\left(\tilde{\tau}_T, R_{0R}, \tau_{0R}\right)}{4v_T{}^2 \cdot \left(f + f_0\right)^2} - v_T{}^2 \cdot a_0{}^2 \tag{3.99}$$

From the above, we determine $R^2{}_T\left(\tilde{\tau}_T, R_R, \tau_{0R}\right)$. After reordering, we get:

$$R_T{}^2\left(\tilde{\tau}_T, R_{0R}, \tau_{0R}\right) \cdot \left( 1 - \frac{f_\tau{}^2 c^2}{4v_T{}^2 \cdot \left(f + f_0\right)^2} \right) = \left(\vec{R}_R\left(\tau_{0R}, R_{0R}, \tau_{0R}\right) + \vec{d}\left(\tau_{0R}\right)\right)^2 - v_T{}^2 \cdot a_0{}^2 \tag{3.100}$$

Finally, we take the square root to obtain:

$$R_T\left(\tilde{\tau}_T, R_{0R}, \tau_{0R}\right) = \frac{\sqrt{\left[\vec{R}_R\left(\tau_{0R}, R_{0R}, \tau_{0R}\right) + \vec{d}\left(\tau_{0R}\right)\right]^2 - v_T{}^2 a_0{}^2}}{\sqrt{\left(f + f_0\right)^2 - \frac{f_\tau{}^2 c^2}{4v_T{}^2}}} \cdot \left| f + f_0 \right| \tag{3.101}$$

For convenience, we introduce the notation $\left|\vec{R}_R(\tau_{0R}, R_R, \tau_{0R})\right| = R_{0R}$, (that is, the slant range modulus at the receiver's PCA), and insert the shorthand notation into (3.101):

$$R_T\left(\tilde{\tau}_T, R_{0R}, \tau_{0R}\right) = \frac{R_{0R} \cdot \left|f + f_0\right| \cdot \sqrt{\left[\vec{e}_R\left(\tau_{0R}, R_{0R}, \tau_{0R}\right) + \frac{\vec{d}\left(\tau_{0R}\right)}{R_{0R}}\right]^2 - \frac{{a_0}^2 {v_T}^2}{{R_{0R}}^2}}}{\sqrt{\left(f + f_0\right)^2 - \frac{{f_\tau}^2 c^2}{4{v_T}^2}}} \tag{3.102}$$

Using (3.93), we obtain:

$$R_T\left(\tilde{\tau}_T, R_R, \tau_{0R}\right) = \frac{R_{0R} \cdot a_2}{F_T\left(f, f_\tau\right)^{\frac{1}{2}}} \cdot \left|f + f_0\right| \tag{3.103}$$

$\vec{e}_R\left(\tau_{0R}, R_R, \tau_{0R}\right)$ is the unit vector perpendicular to the receiver's trajectory at the PCA and is given by:

$$\vec{e}_R\left(\tau_{0R}, R_{0R}, \tau_{0R}\right) = \frac{\vec{R}_R\left(\tau_{0R}, R_{0R}, \tau_{0R}\right)}{R_{0R}} \tag{3.104}$$

Now we substitute (3.103) into (3.89) and get:

$$\begin{aligned} \tilde{\tau}_T - \tau_{0R} &= \frac{-f_\tau \cdot c}{2{v^2}_T \cdot \left(f + f\right)} \cdot \frac{R_{0R} \cdot \left|f + f_0\right| \cdot a_2}{\sqrt{\left(f + f_0\right)^2 - \frac{{f_\tau}^2 c^2}{4{v_T}^2}}} + a_0 \\ &= -\frac{f_\tau \cdot c}{2{v^2}_T} \cdot \frac{R_{0R} \cdot \operatorname{sgn}\left(f + f_0\right) \cdot a_2}{\sqrt{\left(f + f_0\right)^2 - \frac{{f_\tau}^2 c^2}{4{v_T}^2}}} + a_0 \end{aligned} \tag{3.105}$$

We are able to determine the transmitter's PSP as:

$$\begin{aligned} \tilde{\tau}_T &= \tau_{0R} - \frac{f_\tau \cdot c}{2{v^2}_T \cdot \left(f + f\right)} \frac{R_{0R} \cdot \left|f + f_0\right| \cdot a_2}{\sqrt{\left(f + f_0\right)^2 - \frac{{f_\tau}^2 c^2}{4{v_T}^2}}} + a_0 \\ &= \tau_{0R} - \frac{f_\tau c}{2{v^2}_T} \cdot \frac{R_{0R} \cdot \operatorname{sgn}\left(f + f_0\right) \cdot a_2}{\sqrt{\left(f + f_0\right)^2 - \frac{{f_\tau}^2 c^2}{4{v_T}^2}}} + a_0 \end{aligned} \tag{3.106}$$

And finally, we obtain:

$$\tilde{\tau}_T = \tau_{0R} - \frac{f_\tau \cdot c}{2{v^2}_T} \cdot \frac{R_{0R} \cdot \operatorname{sgn}\left(f + f_0\right) \cdot a_2}{F_T^{\frac{1}{2}}\left(f, f_\tau\right)} + a_0 \tag{3.107}$$

This is the transmitter's PSP expressed in the receiver's coordinates. Likewise, by resubstituting the definitions $a_0 = \tau_{0T} - \tau_{0R}$, $a_2 = \frac{R_{0T}}{R_{0R}}$ given in (3.93) in (3.107), we could get:

$$\tilde{\tau}_T = \tau_{0T} - \frac{f_\tau c}{2v^2{}_T} \cdot \frac{R_{0T} \cdot \operatorname{sgn}(f + f_0)}{F_T^{\frac{1}{2}}(f, f_\tau)} \tag{3.108}$$

which is completely symmetric to equation (3.66) and could be used as a test of reasonableness on the result of (3.107).

#### *3.4.1.2.2 Time Difference of Transmitter's and Receiver's Points of Stationary Phase*

Now we combine (3.107) with the azimuth time distance between $\tau_{0R}$ and $\tilde{\tau}_R$ given in (3.66), and we obtain the time distance between the individual points of stationary phase (PSP):

$$\begin{aligned}\tilde{\tau}_T - \tilde{\tau}_R &= -\frac{f_\tau c}{2v^2{}_T \cdot v^2{}_R} \cdot R_{0R} \cdot \operatorname{sgn}(f + f_0) \\ &= \left( v^2{}_R \cdot \sqrt{(f + f_0)^2 - \frac{f_\tau^2 c^2}{4v_R{}^2} a_2 - v^2{}_T \cdot \sqrt{(f + f_0)^2 - \frac{f_\tau^2 c^2}{4v_T{}^2}}} \right) \cdot \\ &\cdot \frac{1}{\sqrt{(f + f_0)^2 - \frac{f_\tau^2 c^2}{4v_R{}^2}} \cdot \sqrt{(f + f_0)^2 - \frac{f_\tau^2 c^2}{4v_T{}^2}}} + a_0\end{aligned} \tag{3.109}$$

Simplifying this term, we get the azimuth time difference between the transmitter's and receiver's points of stationary phase:

$$\begin{aligned}\tilde{\tau}_T - \tilde{\tau}_R &= a_0 - \\ &- \frac{f_\tau c}{2v_T{}^2 v_R{}^2} \cdot R_{0R} \cdot \left( v_R{}^2 \cdot F_R^{\frac{1}{2}}(f, f_\tau) \cdot a_2 - v_T{}^2 \cdot F_T^{\frac{1}{2}}(f, f_\tau) \right) \cdot \frac{1}{F_T^{\frac{1}{2}}(f, f_\tau) \cdot F_T^{\frac{1}{2}}(f, f_\tau)}\end{aligned} \tag{3.110}$$

This time distance is an important element of the bistatic deformation term given in (3.33).

#### *3.4.1.2.3 Transmitter's Phase Term at the Transmitter's Point of Stationary Phase*

(3.76) describes the transmitter's phase contribution at any azimuth time instant. We need to evaluate it at the Point of Stationary Phase (PSP). We start at (3.76), substitute (3.107), and further use the transmitter's slant range value at the PSP given in (3.103):

$$\begin{aligned}
\phi_T\left(\tilde{\tau}_T\right) &= 2\pi\left(\frac{f+f_0}{c}\cdot R_T\left(\tilde{\tau}_T, R_{0R}, \tau_{0R}\right)+\frac{f_\tau}{2}\cdot\tilde{\tau}_T\right)\\
&= 2\pi\left(\frac{f+f_0}{c}\cdot R_T\left(\tilde{\tau}_T, R_{0R}, \tau_{0R}\right)-\frac{f_\tau^2}{4}\cdot\frac{c}{v_T{}^2\left(f+f_0\right)}\cdot R_T\left(\tilde{\tau}_T, R_{0R}, \tau_{0R}\right)+f_\tau\frac{a_0}{2}+f_\tau\cdot\frac{\tau_{0R}}{2}\right)\\
&= 2\pi\frac{R_T\left(\tilde{\tau}_T, R_{0R}, \tau_{0R}\right)}{c\left(f+f_0\right)}\cdot\left(\left(f+f_0\right)^2-\frac{f_\tau^2c^2}{4v_T{}^2}\right)+\pi f_\tau\cdot\left(a_0+\tau_{0R}\right)\\
&= 2\pi\frac{R_{0R}\cdot\left|f+f_0\right|}{c\left(f+f_0\right)\cdot\sqrt{\left(f+f_0\right)^2-\frac{f_\tau^2c^2}{4v_T{}^2}}}\cdot\left(\left(f+f_0\right)^2-\frac{f_\tau^2c^2}{4v_T{}^2}\right)a_2+\pi f_\tau\cdot\left(a_0+\tau_{0R}\right)
\end{aligned} \tag{3.111}$$

Summarizing, we have:

$$\phi_T\left(\tilde{\tau}_T\right) = \underbrace{2\pi\frac{R_{0R}\cdot\operatorname{sgn}\left(f+f_0\right)}{c}\cdot\sqrt{\left(f+f_0\right)^2-\frac{f_\tau^2c^2}{4v_T{}^2}}}_{Monostatic\ term}a_2+\pi f_\tau\cdot\left(a_0+\tau_{0R}\right) \tag{3.112}$$

Finally, we obtain the transmitter's phase term at its PSP expressed in the local coordinates:

$$\phi_T\left(\tilde{\tau}_T\right) = \underbrace{2\pi\frac{R_{0R}\cdot\operatorname{sgn}\left(f+f_0\right)}{c}\cdot F_T\left(f,f_\tau\right)^{\frac{1}{2}}}_{Monostatic\ term}\cdot a_2+\pi f_\tau\cdot\left(a_0+\tau_{0R}\right) \tag{3.113}$$

If we pay attention to the equation above, we recognize the part of the term marked as 'Monostatic term' is similar to the monostatic phase history.

#### *3.4.1.2.4 Second Derivative of the Transmitter's Phase Term at the Point of Stationary Phase*

The second-order derivative of transmitter's phase term was given by:

$$\ddot{\phi}_T\left(\tilde{\tau}_T\right) = 2\pi\cdot\frac{f+f_0}{c}\cdot\ddot{R}_T\left(\tilde{\tau}_T, R_{0R}, \tau_{0R}\right) \tag{3.114}$$

Now we use $\ddot{R}_T\left(\tilde{\tau}_T, R_{0R}, \tau_{0R}\right)$ given in (3.86) and get:

$$\begin{aligned}
\ddot{\phi}_T\left(\tilde{\tau}_T\right) &= 2\pi\cdot\frac{f+f_0}{c}\cdot\frac{v^2{}_T-\dot{R}_T^2\left(\tilde{\tau}_T, R_{0R}, \tau_{0R}\right)}{R_T\left(\tilde{\tau}_T, R_{0R}, \tau_{0R}\right)}\\
&= 2\pi\cdot\frac{f+f_0}{c}\cdot\frac{v^2{}_T-\frac{f_\tau^2c^2}{4\left(f+f_0\right)^2}}{R_{0R}\cdot\left|f+f_0\right|}\cdot\frac{\sqrt{\left(f+f_0\right)^2-\frac{f_\tau^2c^2}{4v_T{}^2}}}{a_2}
\end{aligned} \tag{3.115}$$

Simplifying terms again, we obtain:

$$\ddot{\phi}_T\left(\tilde{\tau}_T\right) = 2\pi \frac{\operatorname{sgn}\left(f+f_0\right)}{cR_{0R}} \cdot \frac{{v_T}^2}{\left(f+f_0\right)^2} \cdot \frac{\left(\left(f+f_0\right)^2 - \frac{{f_\tau}^2 c^2}{4{v_T}^2}\right)^{\frac{3}{2}}}{a_2} \tag{3.116}$$

And finally, the second-order derivative of the transmitter's phase term at the point of stationary phase (PSP) is:

$$\ddot{\phi}_T\left(\tilde{\tau}_T\right) = 2\pi \frac{\operatorname{sgn}\left(f+f_0\right)}{cR_{0R}} \cdot \frac{{v_T}^2}{\left(f+f_0\right)^2} \cdot \frac{F_T\left(f,f_\tau\right)^{\frac{3}{2}}}{a_2} \tag{3.117}$$

Substituting $a_2 = \frac{R_{0T}}{R_{0R}}$ gives:

$$\ddot{\phi}_T\left(\tilde{\tau}_T\right) = 2\pi \frac{\operatorname{sgn}\left(f+f_0\right)}{cR_{0T}} \cdot \frac{{v_T}^2}{\left(f+f_0\right)^2} \cdot F_T\left(f,f_\tau\right)^{\frac{3}{2}} \tag{3.118}$$

## 3.5 Quasi-Monostatic Phase Term

After determining the individual phase terms and their derivatives at the transmitter's and the receiver's points of stationary phase given in (3.66), (3.72), (3.107), (3.113), (3.117), we are able to determine the quasi-monostatic term. From (3.33) we know that the quasi-monostatic term is the sum of the phase terms of the transmitter and the receiver evaluated at the points of stationary phases. Adding the expressions of (3.75) and (3.113), we obtain:

$$\begin{aligned}\phi_T\left(\tilde{\tau}_T\right) + \phi_R\left(\tilde{\tau}_R\right) &= \pi f_\tau \cdot \left(2\tau_{0R} + a_0\right) + \\ &+2\pi \frac{R_{0R}}{c} \cdot \operatorname{sgn}\left(f+f_0\right) \cdot \left(\sqrt{\left(f+f_0\right)^2 - \frac{{f_\tau}^2 c^2}{4{v_R}^2}} + \sqrt{\left(f+f_0\right)^2 - \frac{{f_\tau}^2 c^2}{4{v_T}^2}} \cdot a_2\right)\end{aligned} \tag{3.119}$$

(3.119) indicates that the quasi-monostatic term is the sum of the transmitter's and the receiver's semi monostatic phase terms.

## 3.6 Bistatic Deformation Term

In a similar way we can determine the bistatic deformation term. We need the second-order phase derivatives of the transmitter and the receiver given in (3.117) and (3.72). We then evaluate the bistatic phase term using (3.32).

We start calculating the part of the bistatic term, without the squared time interval:

$$\frac{\ddot{\phi}_T(\tilde{\tau}_T)\cdot\ddot{\phi}_R(\tilde{\tau}_R)}{\ddot{\phi}_T(\tilde{\tau}_T)+\ddot{\phi}_R(\tilde{\tau}_R)}=\frac{2\pi}{R_{0R}c}\cdot\frac{v_T{}^2\cdot v_R{}^2}{(f+f_0)^2}\cdot\operatorname{sgn}(f+f_0)\cdot$$
$$\cdot\frac{\left((f+f_0)^2-\frac{f_\tau{}^2c^2}{4v_R{}^2}\right)^{\frac{3}{2}}\cdot\left((f+f_0)^2-\frac{f_\tau{}^2c^2}{4v_T{}^2}\right)^{\frac{3}{2}}}{a_2\cdot\left(\frac{\left[(f+f_0)^2-\frac{f_\tau{}^2c^2}{4v_T{}^2}\right]^{\frac{3}{2}}\cdot v_T{}^2}{a_2}+\left[(f+f_0)^2-\frac{f_\tau{}^2c^2}{4v_R{}^2}\right]^{\frac{3}{2}}\cdot v_R{}^2\right)} \tag{3.120}$$
$$=\frac{2\pi}{R_{0R}c}v_T{}^2v_R{}^2\operatorname{sgn}(f+f_0)\cdot$$
$$\cdot\frac{\left((f+f_0)^2-\frac{f_\tau{}^2c^2}{4v_R{}^2}\right)^{\frac{3}{2}}\cdot\left((f+f_0)^2-\frac{f_\tau{}^2c^2}{4v_T{}^2}\right)^{\frac{3}{2}}}{\left((f+f_0)^2-\frac{f_\tau{}^2c^2}{4v_T{}^2}\right)^{\frac{3}{2}}\cdot v_T{}^2+a_2\cdot\left((f+f_0)^2-\frac{f_\tau{}^2c^2}{4v_R{}^2}\right)^{\frac{3}{2}}\cdot v_R{}^2}$$

The intermediate result is:

$$\frac{\ddot{\phi}_T(\tilde{\tau}_T)\cdot\ddot{\phi}_R(\tilde{\tau}_R)}{\ddot{\phi}_T(\tilde{\tau}_T)+\ddot{\phi}_R(\tilde{\tau}_R)}=\frac{2\pi}{R_{0R}c}\cdot v_T{}^2\cdot v_R{}^2\cdot\operatorname{sgn}(f+f_0)\cdot\frac{F_R^{\frac{3}{2}}(f,f_\tau)\cdot F_T^{\frac{3}{2}}(f,f_\tau)}{F_T(f,f_\tau)^{\frac{3}{2}}\cdot v_T{}^2+a_2\cdot F_R(f,f_\tau)^{\frac{3}{2}}\cdot v_R{}^2} \tag{3.121}$$

Still missing from the bistatic term is the squared azimuth time difference of the transmitter's and the receiver's points of stationary phase, calculated at (3.110). After squaring (3.110) we get:

$$(\tilde{\tau}_T-\tilde{\tau}_R)^2=\left[a_0-\frac{f_\tau c}{2v^2{}_T v^2{}_R}\cdot\frac{R_{0R}}{F_T^{\frac{1}{2}}(f,f_\tau)\cdot F_T^{\frac{1}{2}}(f,f_\tau)}\cdot\left[v^2{}_R\cdot F_R^{\frac{1}{2}}(f,f_\tau)a_2-v^2{}_T\cdot F_T^{\frac{1}{2}}(f,f_\tau)\right]\right]^2 \tag{3.122}$$

To summarize, the whole formula of the bistatic deformation phase term is the product of the expressions given in (3.121) and (3.122):

$$\Psi_{BI}(f,f_\tau)=\frac{\ddot{\phi}_T(\tilde{\tau}_T)\cdot\ddot{\phi}_R(\tilde{\tau}_R)}{\ddot{\phi}_T(\tilde{\tau}_T)+\ddot{\phi}_R(\tilde{\tau}_R)}\cdot(\tilde{\tau}_T-\tilde{\tau}_R)^2$$
$$=\frac{2\pi}{R_{0R}c}v_T{}^2\cdot v_R{}^2\cdot\operatorname{sgn}(f+f_0)\cdot\frac{F_R^{\frac{3}{2}}(f,f_\tau)\cdot F_T^{\frac{3}{2}}(f,f_\tau)}{F_T(f,f_\tau)^{\frac{3}{2}}\cdot v_T{}^2+a_2\cdot F_R(f,f_\tau)^{\frac{3}{2}}\cdot v_R{}^2}\cdot \tag{3.123}$$
$$\cdot\left[a_0-\frac{f_\tau c}{2v^2{}_T\cdot v^2{}_R}\cdot\frac{R_{0R}}{F_T^{\frac{1}{2}}(f,f_\tau)\cdot F_T^{\frac{1}{2}}(f,f_\tau)}\cdot\left[v^2{}_R\cdot F_R^{\frac{1}{2}}(f,f_\tau)\cdot a_2-v^2{}_T\cdot F_T^{\frac{1}{2}}(f,f_\tau)\right]\right]^2$$

## 3.7 Common Bistatic Point of Stationary Phase

In (3.27) we determined the azimuth time of the common bistatic point of stationary phase (PSP) as:

$$\tilde{\tau} = \frac{\ddot{\phi}_T(\tilde{\tau}_T)\cdot\tilde{\tau}_T + \ddot{\phi}_R(\tilde{\tau}_R)\cdot\tilde{\tau}_R}{\ddot{\phi}_T(\tilde{\tau}_T) + \ddot{\phi}_R(\tilde{\tau}_R)} \tag{3.124}$$

This value is important for the determination of the bistatic Doppler bandwidth and the bistatic Doppler centroid.

We start calculating the denominator. We already know the second-order phase derivatives of the transmitter and the receiver given in (3.117) and (3.72). The sum of their values yields:

$$\ddot{\phi}_T(\tilde{\tau}_T) + \ddot{\phi}_R(\tilde{\tau}_R) = 2\pi\,\mathrm{sgn}(f+f_0)\cdot\frac{c}{R_{0R}(f+f_0)^2}\cdot\left(F_R^{\frac{3}{2}}v_R^{\,2} + \frac{F_T^{\frac{3}{2}}v_T^{\,2}}{a_2}\right) \tag{3.125}$$

Or in a symmetric notation, we have:

$$\ddot{\phi}_T(\tilde{\tau}_T) + \ddot{\phi}_R(\tilde{\tau}_R) = 2\pi\,\mathrm{sgn}(f+f_0)\cdot\frac{c}{(f+f_0)^2}\cdot\left(\frac{F_R^{\frac{3}{2}}v_R^{\,2}}{R_{0R}} + \frac{F_T^{\frac{3}{2}}v_T^{\,2}}{R_{0T}}\right) \tag{3.126}$$

Now we inverse (3.125) and get for the denominator:

$$\frac{1}{\ddot{\phi}_T(\tilde{\tau}_T) + \ddot{\phi}_R(\tilde{\tau}_R)} = \frac{R_{0R}\cdot(f+f_0)^2\cdot a_2}{2\pi\cdot\mathrm{sgn}(f+f_0)\,c\cdot\left(a_2F_R^{\frac{3}{2}}v_R^{\,2} + F_T^{\frac{3}{2}}v_T^{\,2}\right)} \tag{3.127}$$

or, in symmetric notation:

$$\frac{1}{\ddot{\phi}_T(\tilde{\tau}_T) + \ddot{\phi}_R(\tilde{\tau}_R)} = \frac{(f+f_0)^2}{2\pi\cdot\mathrm{sgn}(f+f_0)\cdot c\cdot\left(\frac{F_R^{\frac{3}{2}}v_R^{\,2}}{R_{0R}} + \frac{F_T^{\frac{3}{2}}v_T^{\,2}}{R_{0T}}\right)} \tag{3.128}$$

After determining the denominator, we start calculating the first half of the numerator. It is the product of the transmitter's second-order phase derivative given in (3.117) with the PSP itself given in (3.107):

$$\begin{aligned}\ddot{\phi}_T(\tilde{\tau}_T)\cdot\tilde{\tau}_T &= \frac{2\pi}{R_{0R}c}\cdot\mathrm{sgn}(f+f_0)\cdot\frac{v_T^{\,2}}{(f+f_0)^2}\frac{F_T^{\frac{3}{2}}}{a_2}\cdot\left((\tau_{0R}+a_0) - \frac{f_\tau c}{2v_T^{\,2}}\cdot\mathrm{sgn}(f+f_0)\cdot R_{0R}\cdot\frac{a_2}{F_T^{\frac{1}{2}}}\right)\\ &= \frac{2\pi}{R_{0R}c}\cdot\mathrm{sgn}(f+f_0)\cdot\frac{v_T^{\,2}}{(f+f_0)^2}\cdot\frac{F_T^{\frac{3}{2}}}{a_2}\cdot(\tau_{0R}+a_0) - \pi f_\tau\cdot\frac{F_T}{(f+f_0)^2}\end{aligned} \tag{3.129}$$

In an analogous way we obtain the value for the receiver by using (3.72) and (3.66):

$$\ddot{\phi}_R\left(\tilde{\tau}_R\right)\cdot\tilde{\tau}_R=\frac{2\pi}{R_{0R}c}\cdot\operatorname{sgn}\left(f+f_0\right)\cdot\frac{{v_R}^2}{\left(f+f_0\right)^2}\cdot{F_R}^{\frac{3}{2}}\cdot\left(\tau_{0R}-\frac{f_\tau c}{2{v_R}^2}\cdot\operatorname{sgn}\left(f+f_0\right)\cdot R_{0R}\cdot\frac{1}{{F_R}^{\frac{1}{2}}}\right) \tag{3.130}$$
$$=\frac{2\pi}{R_{0R}c}\operatorname{sgn}\left(f+f_0\right)\cdot\frac{{v_R}^2}{\left(f+f_0\right)^2}\cdot{F_R}^{\frac{3}{2}}\cdot\tau_{0R}-\pi f_\tau\cdot\frac{F_R}{\left(f+f_0\right)^2}$$

Now we have both parts of the numerator, and hence, the sum of (3.129) and (3.130) gives:

$$\begin{aligned}\ddot{\phi}_T\left(\tilde{\tau}_T\right)\cdot\tilde{\tau}_T+\ddot{\phi}_R\left(\tilde{\tau}_R\right)\cdot\tilde{\tau}_R&=\frac{2\pi}{R_{0R}c}\operatorname{sgn}\left(f+f_0\right)\cdot\frac{1}{\left(f+f_0\right)^2}\left[\frac{{F_T}^{\frac{3}{2}}}{a_2}\cdot\left(\tau_{0R}+a_0\right)\cdot{v_T}^2+{F_R}^{\frac{3}{2}}\cdot\tau_{0R}\cdot{v_R}^2\right]-\\&\quad-\pi f_\tau\cdot\frac{F_T+F_R}{\left(f+f_0\right)^2}\\&=\frac{2\pi}{R_{0R}c}\operatorname{sgn}\left(f+f_0\right)\cdot\frac{1}{\left(f+f_0\right)^2}\cdot\frac{{F_T}^{\frac{3}{2}}\cdot\left(\tau_{0R}+a_0\right)\cdot{v_T}^2+{F_R}^{\frac{3}{2}}\cdot\tau_{0R}\cdot{v_R}^2\cdot a_2}{a_2}-\\&\quad-\pi f_\tau\cdot\frac{F_T+F_R}{\left(f+f_0\right)^2}\end{aligned} \tag{3.131}$$

Finally, we combine the numerator and the denominator and obtain:

$$\begin{aligned}\tilde{\tau}=\frac{\ddot{\phi}_T\left(\tilde{\tau}_T\right)\cdot\tilde{\tau}_T+\ddot{\phi}_R\left(\tilde{\tau}_R\right)\cdot\tilde{\tau}_R}{\ddot{\phi}_T\left(\tilde{\tau}_T\right)+\ddot{\phi}_R\left(\tilde{\tau}_R\right)}&=\frac{{v_T}^2\cdot{F_T}^{\frac{3}{2}}\cdot\left(\tau_{0R}+a_0\right)+{F_R}^{\frac{3}{2}}\cdot\tau_{0R}\cdot{v_R}^2\cdot a_2}{{F_T}^{\frac{3}{2}}\cdot{v_T}^2+{v_R}^2\cdot a_2\cdot{F_R}^{\frac{3}{2}}}-\\&\quad-\frac{\pi f_\tau\cdot c\cdot\left(F_T+F_R\right)\cdot R_{0R}\cdot a_2}{2\pi\operatorname{sgn}\left(f+f_0\right)\cdot\left({F_T}^{\frac{3}{2}}\cdot{v_T}^2+{v_R}^2\cdot a_2\cdot{F_R}^{\frac{3}{2}}\right)}\end{aligned} \tag{3.132}$$

Resubstituting $a_0=\tau_{0T}-\tau_{0R}, a_2=\dfrac{R_{0T}}{R_{0R}}$ into (3.132), we get:

$$\tilde{\tau}=\frac{\dfrac{{v_T}^2\cdot{F_T}^{\frac{3}{2}}\cdot\tau_{0T}}{R_{0T}}+\dfrac{{F_R}^{\frac{3}{2}}\cdot\tau_{0R}\cdot{v_R}^2}{R_{0R}}}{\dfrac{{F_T}^{\frac{3}{2}}\cdot{v_T}^2}{R_{0T}}+\dfrac{{v_R}^2\cdot{F_R}^{\frac{3}{2}}}{R_{0R}}}-\frac{f_\tau\cdot c\cdot\left(F_T+F_R\right)\cdot\operatorname{sgn}\left(f+f_0\right)}{2\cdot\left[\dfrac{{F_T}^{\frac{3}{2}}\cdot{v_T}^2}{R_{0T}}+\dfrac{{v_R}^2\cdot{F_R}^{\frac{3}{2}}}{R_{0R}}\right]} \tag{3.133}$$

## 3.8 Bistatic Amplitude Term

The Bistatic Point Target Reference Spectrum given in (3.33) contains amplitude term, which has the following expression:

$$Amp\left(f,f_\tau,R_{0R},\tau_{0R}\right)=\frac{\sqrt{2\pi}}{\sqrt{\ddot{\phi}_T\left(\tilde{\tau}_T\right)+\ddot{\phi}_R\left(\tilde{\tau}_R\right)}} \tag{3.134}$$

We substitute $\frac{1}{\ddot{\phi}_T\left(\tilde{\tau}_T\right)+\ddot{\phi}_R\left(\tilde{\tau}_R\right)}$ from (3.127) into (3.134) and obtain:

$$Amp\left(f,f_\tau,R_{0R},\tau_{0R}\right)=\frac{\left|f+f_0\right|}{\sqrt{c\cdot\left(\frac{F_R^{\frac{3}{2}}\cdot v_R{}^2}{R_{0R}}+\frac{F_T^{\frac{3}{2}}\cdot v_T{}^2}{R_{0T}}\right)}} \tag{3.135}$$

## 3.9 Result and Summary

(3.33) represents the Bistatic Point Target Reference Spectrum (BPTRS). In the previous chapters, we successfully expressed all the unknowns in terms of $\left(f,f_\tau,R_{0R},\tau_{0R}\right)$. The quasi-monostatic phase term is given in (3.119), and the bistatic deformation phasor is expressed in (3.123). They are substituted in (3.33), and we obtain the final expression of the BPTRS:

$$\begin{aligned}
&G\left(f,f_\tau,R_{0R},\tau_{0R}\right)=\sigma\left(R_{0R},\tau_{0R}\right)\cdot w\left(\tilde{\tau}-\tau_{cb}\right)\cdot S_l\left(f\right)\frac{\sqrt{2\pi}}{\sqrt{\ddot{\phi}_T\left(\tilde{\tau}_T\right)+\ddot{\phi}_R\left(\tilde{\tau}_R\right)}}e^{-j\frac{\pi}{4}}\cdot e^{-j\Psi_{QM}}\cdot e^{-j\frac{1}{2}\Psi_{BI}}\\
&=\sigma\left(R_{0R},\tau_{0R}\right)\cdot w\left(\tilde{\tau}-\tau_{cb}\right)\cdot S_l\left(f\right)\cdot\frac{\left|f+f_0\right|}{\sqrt{c\cdot\left(\frac{F_R^{\frac{3}{2}}v_R{}^2}{R_{0R}}+\frac{F_T^{\frac{3}{2}}v_T{}^2}{R_{0T}}\right)}}\cdot e^{-j\frac{\pi}{4}}\cdot\\
&\cdot\exp\left(-j\pi f_\tau\left(2\tau_{0R}+a_0\right)-2\pi\frac{R_{0R}}{c}\cdot\left[\sqrt{\left(f+f_0\right)^2-\frac{f_\tau{}^2c^2}{4v_R{}^2}}+\sqrt{\left(f+f_0\right)^2-\frac{f_\tau{}^2c^2}{4v_T{}^2}}a_2\right]\right)\cdot\\
&\cdot\exp\left\{-j\frac{1}{2}\frac{2\pi}{R_{0R}c}v_T{}^2v_R{}^2\cdot\frac{F_R^{\frac{3}{2}}\left(f,f_\tau\right)\cdot F_T^{\frac{3}{2}}\left(f,f_\tau\right)}{F_T\left(f,f_\tau\right)^{\frac{3}{2}}v_T{}^2+a_2F_R\left(f,f_\tau\right)^{\frac{3}{2}}v_R{}^2}\cdot\right.\\
&\left.\cdot\left[a_0-\frac{f_\tau c}{2v^2{}_Tv^2{}_R}\frac{R_{0R}}{F_T^{\frac{1}{2}}\left(f,f_\tau\right)\cdot F_R^{\frac{1}{2}}\left(f,f_\tau\right)}\cdot\left[v^2{}_RF_R^{\frac{1}{2}}\left(f,f_\tau\right)a_2-v^2{}_TF_T^{\frac{1}{2}}\left(f,f_\tau\right)\right]\right]^2\right\}
\end{aligned} \tag{3.136}$$

In a symmetric notation, substituting $a_0=\tau_{0T}-\tau_{0R}, a_2=\frac{R_{0T}}{R_{0R}}$, we would get:

$$
\begin{aligned}
G\left(f,f_\tau,R_{0R},\tau_{0R}\right) &= \sigma\left(R_{0R},\tau_{0R}\right)\cdot w\left(\tilde{\tau}-\tau_{cb}\right)\cdot S_l\left(f\right)\frac{\sqrt{2\pi}}{\sqrt{\ddot{\phi}_T\left(\tilde{\tau}_T\right)+\ddot{\phi}_R\left(\tilde{\tau}_R\right)}}\cdot e^{-j\frac{\pi}{4}}\cdot e^{-j\Psi_{QM}}\cdot e^{-j\frac{1}{2}\Psi_{BI}} \\
&= \sigma\left(R_{0R},\tau_{0R}\right)\cdot w\left(\tilde{\tau}-\tau_{cb}\right)\cdot S_l\left(f\right)\cdot\frac{\left|f+f_0\right|}{\sqrt{c\cdot\left(\frac{F_R^{\frac{3}{2}}\cdot {v_R}^2}{R_{0R}}+\frac{F_T^{\frac{3}{2}}\cdot {v_T}^2}{R_{0T}}\right)}}\cdot e^{-j\frac{\pi}{4}}\cdot \\
&\cdot\exp\left(-j\pi f_\tau\cdot\left(\tau_{0R}+\tau_{0T}\right)-j\frac{2\pi}{c}\cdot\left[R_{0R}\cdot\sqrt{\left(f+f_0\right)^2-\frac{f_\tau^2c^2}{4{v_R}^2}}+R_{0T}\cdot\sqrt{\left(f+f_0\right)^2-\frac{f_\tau^2c^2}{4{v_T}^2}}\right]\right)\cdot \\
&\cdot\exp\left\{-j\frac{\pi}{c}\cdot\frac{1}{\frac{R_{0R}}{F_R\left(f,f_\tau\right)^{\frac{3}{2}}\cdot {v_R}^2}+\frac{R_{0T}}{F_T\left(f,f_\tau\right)^{\frac{3}{2}}\cdot {v_T}^2}}\cdot\right. \\
&\left.\cdot\left[\tau_{0T}-\tau_{0R}-\frac{f_\tau c}{2}\cdot\left[\frac{R_{0T}}{{v_T}^2\cdot F_T^{\frac{1}{2}}\left(f,f_\tau\right)}-\frac{R_{0R}}{{v_R}^2\cdot F_R^{\frac{1}{2}}\left(f,f_\tau\right)}\right]\right]^2\right\}
\end{aligned}
\tag{3.137}
$$

To our knowledge, (3.136) and (3.137) were the first approach to express the point target reference spectrum for the arbitrary bistatic configurations.

The team of the Polytechnic University of Milan derived a similar formula, but for a special bistatic case in which the transmitter and the receiver follow each other on a fixed offset. The bistatic processing is done by converting the processing task to the monostatic processing, but initially convolving the raw data with the 'Smile' operator [27], [28]. This configuration is referred to as the Tandem Case in our bistatic processing; the authors from the name it 'Stationary Offset Configuration'. We found the similarity between the bistatic deformation term and the 'Smile' concept. In the following chapters, we will demonstrate the equivalence of our approach and the 'Smile' concept from Polytechnic University of Milan for the Tandem configuration.

(3.136) and (3.137) are expressed in the Fourier domain. If we do the inverse Fourier transformation, then multiplications will be transformed to convolutions. We will have a triple convolution: two terms corresponding to the semi-monostatic terms of the transmitter and the receiver, and the term corresponding to the bistatic deformation phasor. Hence, the nature of the bistatic deformation term is vital in the bistatic processing. It will be demonstrated later (and it was also observed by our colleges from the Polytechnic University of Milan [16]) that the bistatic term is a short and slowly varying operator.

### 3.9.1 Monostatic SAR as a special case of Bistatic SAR

Monostatic SAR can be understood as a special case of a bistatic configuration in which the transmitter and the receiver are located on the same carrier. Therefore, for the monostatic constellation, the bistatic formula should diverge to the monostatic formula. This is the first simple test of validity for the Bistatic Point Target Reference Spectrum (BPTRS) that we will demonstrate here.

As an example, we show the formula of the point target reference spectrum for the monostatic configuration, derived at ZESS[1]. It is described in detail in [24] and has following expression:

$$\begin{aligned} G_l^{MO}(f,f_\tau,R_0,\tau_0) &= S_l(f)\cdot\sigma(R_0,\tau_0)\cdot rect\left(\frac{f-f_c}{B_{az}}\right)\cdot\sqrt{\frac{cR_0}{2}}\cdot\frac{1}{v}\cdot \\ &\cdot\frac{f+f_0}{\left((f+f_0)^2-\frac{f_\tau^2c^2}{4v^2}\right)^{\frac{3}{4}}}\cdot e^{-j\pi/4}\cdot e^{-j2\pi f_\tau\tau_0}\cdot e^{-j\pi\frac{R_0}{c}\sqrt{(f+f_0)^2-\frac{f_\tau^2c^2}{4v^2}}} \\ &= S_l(f)\cdot\sigma(R_0,\tau_0)\cdot rect\left(\frac{f-f_c}{B_{az}}\right)\cdot\sqrt{\frac{cR_0}{2}}\frac{1}{v}\cdot \\ &\frac{f+f_0}{\left((f+f_0)^2-\frac{f_\tau^2c^2}{4v^2}\right)^{\frac{3}{4}}}\cdot e^{-j\pi/4}\cdot e^{-j2\pi f_\tau\tau_0}\cdot e^{-j\Psi_{MO}} \end{aligned} \tag{3.138}$$

- $G_l^{MO}(f,f_\tau,R_0,\tau_0)$ is the monostatic point target reference spectrum in low-pass domain.
- $\Psi_{MO}$ is a monostatic phase term $\pi\frac{R_0}{c}\cdot\sqrt{(f+f_0)^2-\frac{f_\tau^2c^2}{4v^2}}$.
- $R_0$ is the slant range at the point of closest approach (PCA).
- $\tau_0$ is the azimuth time when the PCA is achieved.
- $\sigma(R_0,\tau_0)$ is the backscattering coefficient for the point target positioned at $(R_0,\tau_0)$.
- $v$ is the sensor velocity.
- $rect\left(\frac{f-f_c}{B_{az}}\right)$ determines the azimuth frequency range, where $B_{az}$ is the azimuth bandwidth and $f_c$ is the Doppler centroid frequency.

The obvious difference with the monostatic point target reference spectrum is that the bistatic formula is longer and more complex. The quasi-monostatic term has some similarity with the monostatic phase term, but it contains the receiver's and the transmitter's phase contributions (that is why we named it as quasi-monostatic term). This phasor is crucial in the bistatic processing. Compared to the monostatic formula, the bistatic formula additionally contains the phasor with the bistatic deformations term $e^{-j\frac{1}{2}\Psi_{BI}}$. The expression of $\Psi_{BI}$ is given in (3.123).

Now we will consider the each term of (3.137) for the monostatic case. Velocities of the transmitter and the receiver are the same during the whole acquisition $v_T = v_R \cong v$. Also, because the positions of the transmitter and the receiver coincide in the monostatic case, the azimuth times and the slant ranges at the points of closest approach will be same for the transmitter and the receiver. Therefore, we have in the monostatic case $\tau_{0R} = \tau_{0T} \cong \tau_0$,

[1] *Zentrum für Sensorsysteme* (Center for Sensorsystems)

$R_{0R} = R_{0T} \cong R_0$, $a_0 = 0$, $a_2 = 1$. Hence, considering (3.60) we have: $F_R^{\frac{1}{2}}(f, f_\tau) = F_T^{\frac{1}{2}}(f, f_\tau) = F^{\frac{1}{2}}(f, f_\tau)$.

We start with bistatic deformation term. In (3.137) it has quite a lengthy expression for the general case. But, in the case of monostatic configuration, the bistatic deformation can be calculated as:

$$\Psi_{BI}(f, f_\tau) = \frac{2\pi}{c} \cdot \frac{1}{\frac{R_{0R}}{F_R(f, f_\tau)^{\frac{3}{2}} \cdot v_R{}^2} + \frac{R_{0T}}{F_T(f, f_\tau)^{\frac{3}{2}} \cdot v_T{}^2}} \cdot$$

$$\left[ \tau_{0T} - \tau_{0R} - \frac{f_\tau c}{2} \cdot \left( \frac{R_{0T}}{v^2{}_T \cdot F_T^{\frac{1}{2}}(f, f_\tau)} - \frac{R_{0R}}{v_R{}^2 \cdot F_R^{\frac{1}{2}}(f, f_\tau)} \right) \right]^2 = \tag{3.139}$$

$$= \frac{2\pi}{c} \cdot \frac{1}{\frac{R_0}{F(f, f_\tau)^{\frac{3}{2}} \cdot v^2} + \frac{R_0}{F(f, f_\tau)^{\frac{3}{2}} \cdot v^2}} \cdot \left[ \tau_0 - \tau_0 - \frac{f_\tau c}{2} \cdot \left( \frac{R_0}{v^2 \cdot F^{\frac{1}{2}}(f, f_\tau)} - \frac{R_0}{v^2 \cdot F^{\frac{1}{2}}(f, f_\tau)} \right) \right]^2 = 0$$

Hence, bistatic term phasor completely makes $e^{-j\frac{1}{2}\Psi_{BI}} = 1$.

In $w(\tilde{\tau} - \tau_{cb})$, $\tilde{\tau}$ is a common bistatic PSP given in (3.132). In the monostatic case, the transmitter's and the receiver's phase terms introduced are the same, and, therefore, they have equal points of stationary phase: $\tilde{\tau} = \tilde{\tau}_T = \tilde{\tau}_R$. $\tau_{cb}$ is the bistatic footprint center, which coincides with the monostatic footprint center. The PSP depends on azimuth frequency, and so the expression $w(\tilde{\tau} - \tau_{cb})$ determines the monostatic Doppler frequency bandwidth $rect\left( \frac{f - f_c}{B_{az}} \right)$.

Now we consider the amplitude terms. The bistatic amplitude term given in (3.137) has the expression:

$$\frac{\sqrt{2\pi}}{\sqrt{\ddot{\phi}_T(\tilde{\tau}_T) + \ddot{\phi}_R(\tilde{\tau}_R)}} \tag{3.140}$$

$\ddot{\phi}_R(\tilde{\tau}_R), \ddot{\phi}_T(\tilde{\tau}_T)$ are the expressions of the second-order derivative of the transmitter's and receiver's phase taken at their individual points of stationary phase (they are given in (3.72) and (3.117), respectively). It is obvious that for the monostatic case $\ddot{\phi}_R(\tilde{\tau}_R) = \ddot{\phi}_T(\tilde{\tau}_T)$, and they are expressed as follows:

$$\ddot{\phi}_R(\tilde{\tau}_R) = \ddot{\phi}_T(\tilde{\tau}_T) = 2\pi \frac{1}{cR_0} \cdot \frac{v^2}{(f + f_0)^2} \cdot F(f, f_\tau)^{\frac{3}{2}} \tag{3.141}$$

We substitute (3.141) into (3.140) and get:

$$\frac{\sqrt{2\pi}}{\sqrt{\ddot{\phi}_T(\tilde{\tau}_T)+\ddot{\phi}_R(\tilde{\tau}_R)}}=\sqrt{\frac{cR_0}{2}}\cdot\frac{f+f_0}{v\cdot F^{\frac{3}{4}}}=\sqrt{\frac{cR_0}{2}}\cdot\frac{1}{v}\cdot\frac{f+f_0}{\left(\left(f+f_0\right)^2-\frac{f_\tau^{\,2}c^2}{4v^2}\right)^{\frac{3}{4}}} \tag{3.142}$$

This expression is the same as the amplitude term of the monostatic point target reference spectrum given in (3.138).

A remaining term we need to consider is the quasi-monostatic term. We calculate it from (3.138):

$$\begin{aligned} e^{-j\Psi_{QM}} &= e^{-j\pi f_\tau\cdot(2\tau_{0R}+a_0)+2\pi\frac{R_{0R}}{c}\cdot\left(\sqrt{(f+f_0)^2-\frac{f_\tau^{\,2}c^2}{4v_R^{\,2}}}+\sqrt{(f+f_0)^2-\frac{f_\tau^{\,2}c^2}{4v_T^{\,2}}}a_2\right)} \\ &= e^{-j2\pi f_\tau\tau_0}\cdot e^{-4\pi\frac{R_0}{c}\cdot\sqrt{(f+f_0)^2-\frac{f_\tau^{\,2}c^2}{4v^2}}} \end{aligned} \tag{3.143}$$

We therefore see that in the monostatic case the quasi-monostatic term has exactly the same expression as a monostatic phasor $e^{-j\Psi_{QM}}=e^{-j\Psi_{MO}}$.

If we look to the result of the comparison of individual terms taken from the bistatic and the monostatic formulas, we observe that a bistatic point target reference spectrum converges to a monostatic point target reference spectrum.

# 4 Interpretation of the Bistatic Point Target Reference Spectrum for Different Configurations

The bistatic point target reference spectrum is given in (3.138). In this chapter, we consider the behavior of the bistatic point target reference spectrum for different bistatic configurations in more details. The classification of the bistatic configuration was already done in 2.3.

## 4.1 General Case

The most arbitrary configuration is the general case. The transmitter and the receiver are moving with different velocities across non-parallel trajectories. This case is azimuth time variant.

### 4.1.1 Quasi-Monostatic term

Now we will consider the parts of the bistatic point target reference spectrum (BPTRS) for different configurations in more detail. The first phasor term can be regarded as a quasi-monostatic term $e^{-j\Psi_{QM}}$, where:

$$\Psi_{QM}\left(f,f_\tau\right)=\phi_T\left(\tilde{\tau}_T,f_\tau\right)+\phi_R\left(\tilde{\tau}_R,f_\tau\right)=2\pi f_\tau\cdot\left(\frac{\tau_{0R}+\tau_{0T}}{2}\right)+$$
$$+2\pi\cdot\left[\frac{R_{0R}}{c}\cdot\sqrt{\underbrace{\left(f+f_0\right)^2-f_\tau^2\frac{c^2}{4v_R^2}}_{F_R(f,f_\tau)}}+\frac{R_{0T}}{c}\cdot\sqrt{\underbrace{\left(f+f_0\right)^2-f_\tau^2\frac{c^2}{4v_T^2}}_{F_T(f,f_\tau)}}\right] \tag{4.1}$$

Instead of the familiar single monostatic hyperbola, weighted by the doubled slant range $2\cdot R_0$ (two-way delay), we have the sum of two semi-monostatic phase histories, the first one being the one-way receiver's phase history, and the second one the one-way transmitter's phase history. Due to $R_{0R}\neq R_{0T}$, both histories differ in amplitude, and due to $v_R\neq v_T$, they also differ in shape. The linear phase term in $f_\tau$ shifts the corresponding azimuth time history to the midpoint between the individual points of closest approach. $R_{0T}$ and $\tau_{0T}$ can be determined from (3.93). Because of general vectorial dependences, $R_{0T}$, $\tau_{0T}$ and other bistatic parameters become strongly dependent on the specific bistatic configurations. For the transmitter's and the receiver's slant ranges, we have the vectorial relation given in (3.26): $\vec{R}_T\left(\tau_{0R},R_{0R},\tau_{0R}\right)=\vec{R}_R\left(\tau_{0R},R_{0R},\tau_{0R}\right)+\vec{d}\left(\tau_{0R}\right)$. Azimuth time variance means that the relation between the slant ranges is changing with azimuth time. In the case of $\dot{\vec{d}}\left(t\right)=\vec{0}$, the azimuth time variance vanishes. The relation $\dot{\vec{d}}\left(t\right)=\vec{0}$ is equivalent to $\vec{v}_T=\vec{v}_R$. For the case of equal velocity vector, both quasi-monostatic and bistatic deformation terms are range and azimuth time invariant.

Conceptually, the sum of the transformations of two semi-monostatic phase histories (giving rise to the product of the corresponding exponentials) results in the convolution in

time domain of the corresponding monostatic semi-range hyperbolas, where the convolution partners in the general case are range and azimuth time variant.

### 4.1.2 Bistatic Deformation Term

Analyzing the range histories of a bistatic sensor shown in Figure 3.3, it becomes clear that even for identical velocities the normal bistatic range history takes the form of a 'flattened' hyperbola, or a *flat-top hyperbola*. Conceptually, this flat-top hyperbola is generated by further convolving the quasi-monostatic hyperbola with the inverse Fourier transformation of the bistatic deformation phasor $e^{-j\frac{1}{2}\Psi_{BI}}$ with the following phase term:

$$\Psi_{BI}(f,f_\tau)=\frac{2\pi}{R_{0R}c}\cdot {v_T}^2\cdot {v_R}^2\cdot\frac{F_R^{\frac{3}{2}}(f,f_\tau)\cdot F_T^{\frac{3}{2}}(f,f_\tau)}{F_T(f,f_\tau)^{\frac{3}{2}}\cdot {v_T}^2+a_2\cdot F_R(f,f_\tau)^{\frac{3}{2}}\cdot {v_R}^2}\cdot$$
$$\cdot\left[a_0-\frac{f_\tau c}{2{v^2}_T\cdot {v^2}_R}\cdot\frac{R_{0R}}{F_T^{\frac{1}{2}}(f,f_\tau)\cdot F_T^{\frac{1}{2}}(f,f_\tau)}\cdot\left({v^2}_R\cdot F_R^{\frac{1}{2}}(f,f_\tau)a_2-{v^2}_T\cdot F_T^{\frac{1}{2}}(f,f_\tau)\right)\right]^2 \quad (4.2)$$

The inverse of the complex exponential contained in (4.2) turns out to be an elliptic arc in the range-azimuth time domain. Conceptually, the multiplication of the two exponentials indicates that the range history of a bistatic sensor can be expressed as a convolution of a monostatic SAR sensor's range history with a small part of an ellipse.

It is important to note that the elliptic arc has a complex value, and it shows itself a heavily varying phase; this is to be expected. The elliptic arc, as well as the quasi-monostatic hyperbola, is Dirac line consisting of non-countable infinities of 2D Dirac impulses. During the convolution, any Dirac impulse of one line (e.g. the ellipse) reproduces a shifted replica of the other; the superposition of all shifted replicas of the hyperbola must constructively interfere along the line of the flat-top hyperbola and must vanish elsewhere. This is only possible by an additional phase modulation of the elliptic arc.

Ignoring the convolution with the range chirp, we note again that in the general case a bistatic point target response can be conceptually modeled as a triple convolution: the semi-point target response of a monostatic sensor (receiver/transmitter) is first convolved with the semi-point target response of the second sensor (transmitter/receiver). The outcome is then further convolved with an elliptic arc (the bistatic deformation term). This elliptic arc, a generalized *'Smile',* might be considered as some generalization of the *'Rocca's Smile'* [27], which was derived for the constant offset case.

#### 4.1.2.1 Graphical Representation of the Bistatic Deformation Term

The result of section 4.1.2 means that for the bistatic processing we convolve the raw (range-compressed) data with the bistatic deformation term. The bistatic deformation term depends on the following variables: $(f,f_\tau,R_{0R},\tau_{0R})$. $f$ is the range frequency, $f_\tau$ is the azimuth frequency, $R_0$ is the receiver slant range at the PCA and $\tau_{0R}$ is the azimuth time at the PCA. The compensation of the bistatic deformation phasor is done in frequency domain, by multiplying the spectrum of the raw data by the complex conjugate of the bistatic deformation phasor. During this operation, the bistatic term is averaged in the range-azimuth blocks. The averaging can be possible only if, across the slant range, the bistatic phase term does not change so much that it could cause noticeable phase errors.

We can observe the behavior of the bistatic term on one particular simulation. It is the translationally invariant case with parameters given in Table 4.1:

Table 4.1. Airborne translationally invariant case

| **Parameter** | **Transmitter** | **Receiver** |
|---|---|---|
| Speed of airplanes | 110m/s | 110m/s |
| Pulse duration | 3.0μs | |
| Carrier Frequency | 10.13GHz | |
| Bandwidth | 100MHz | |
| Squint angle | 0° | 0° |
| Off nadir angle | 57° | 55° |
| Opening angle in azimuth direction | 1.8° | 1.8° |
| Opening angle in elevation | 8° | 8° |
| PRF | 1250Hz | |
| Distance between airplanes (constant) | 1000m | |

The illuminated scene consists of 10 point targets, located at the vertexes of a 2x5 matrix, where 2 is the number of range columns and 5 is the number of azimuth lines. We have generated the raw data corresponding to the scene done range compression.

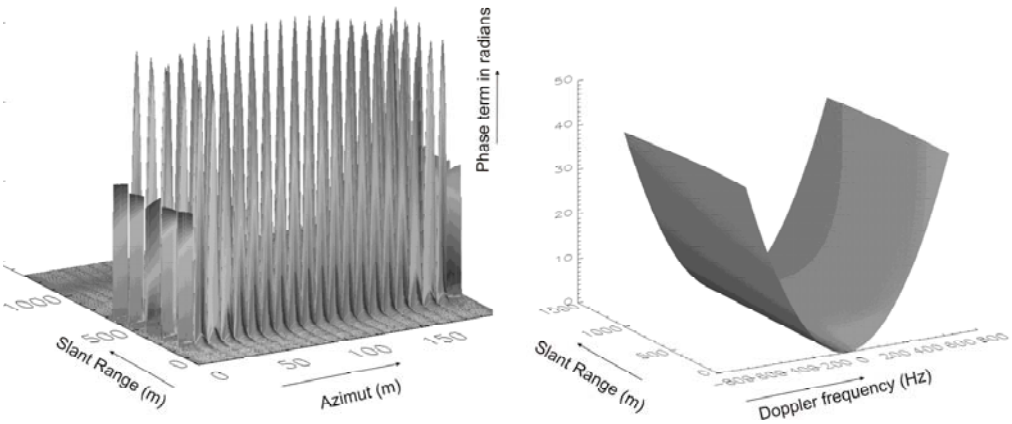


Figure 4.1. Left: magnitude of range-compressed raw data; right: bistatic phase term

We want to see how much the bistatic term changes over slant range. This case is translationally invariant; therefore, we do not have a variation over the azimuth time. On the left side of Figure 4.1, we can see the absolute value of the raw data itself. On the right side, the bistatic deformation term (phase) is shown with the Doppler frequency and the slant range. We can see that the bistatic phase term with respect to the slant range is practically invariant. Normally in SAR processing, a phase error of $\pi/8 \approx 0.4$ *radians* is acceptable. To find out the possible error from the bistatic phase term, we need to take a closer look. We therefore take the slices of the right plot given in Figure 4.1. In this way, we can observe the behavior of the bistatic phase term with the slant range, taking slices for the different Doppler frequencies.

Figure 4.2 shows the plots of the bistatic term dependency on the slant range for minimum and maximum Doppler frequencies. At the zero Doppler frequency we have practically no change, but at the Doppler frequency of 625 Hz we observe a change of the phase term of 1.5 radians over the complete slant range. If we need to have a correct compensation of the bistatic term with a maximum phase error of $\pi/8 \approx 0.4$ *radians*, then we have to divide the whole slant range into 4 blocks.

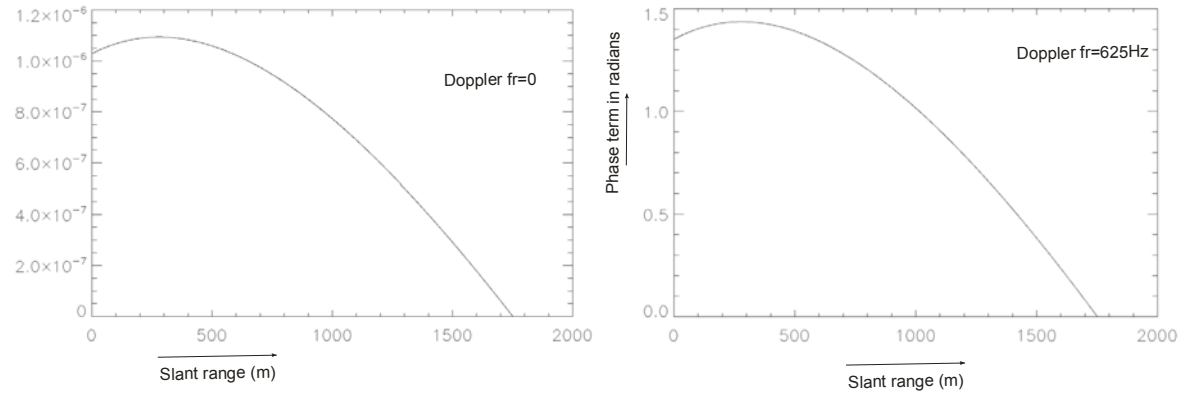


Figure 4.2. Evolution of the bistatic phase term with the slant range: left at zero Doppler frequency, right at a Doppler frequency of 625 Hz.

The compensation of the bistatic term is done in the Fourier domain, which is equivalent to the convolution in the time domain. It is well known that that convolution extends the resulting signal duration. In this respect, it is very interesting to observe the bistatic term in the range-azimuth spatial domain (in order to check the spatial extend of bistatic phase term). We generate the bistatic term tuned at the center of the slant range and convert it to a slant range-azimuth range representation.

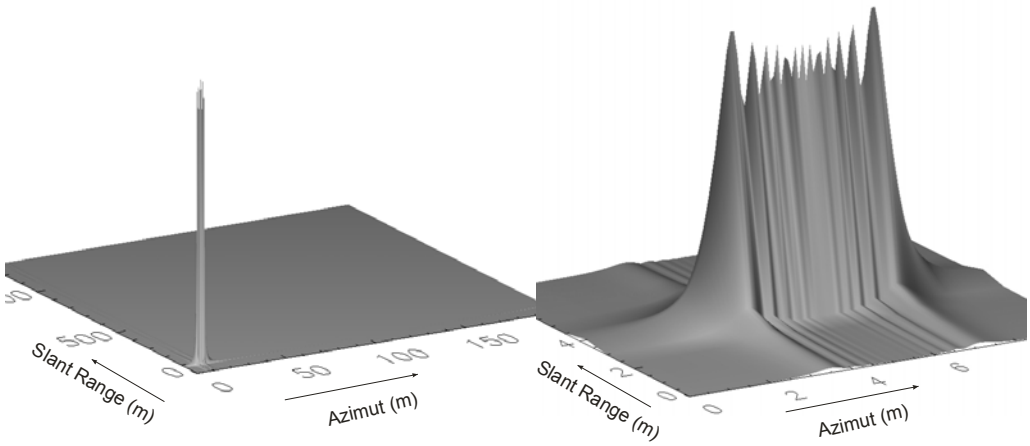


Figure 4.3. Left: the magnitude of the bistatic term for the complete scene; right: a close look of the bistatic term.

The left side of Figure 4.3 shows the bistatic term with respect to the whole scene. We observe that the bistatic phasor in spatial domain behaves as a Dirac pulse. A close look-up is shown at the right side of Figure 4.3. It is clearly seen from these two plots that the bistatic term is in fact a short operator (4 m azimuth x 2 m range) that allows it to compensate by a convolution in the range-azimuth time domain by averaging the bistatic term in range azimuth blocks. This nice feature gives us the freedom of creating range blocks that are smaller than those blocks, where the processing is done, and thus realize finer bistatic term compensation. This can be quite useful in the airborne case for high squint angles causing high Doppler frequencies.

## 4.2 Bistatic Doppler Bandwidth and Doppler Centroid

The azimuth window around the point target determines the azimuth bandwidth. From (3.32), this window is represented by $w(\tilde{\tau}-\tau_{cb})$. For convenience, we substitute $w(\tau)$ with a rectangular window, obtaining the expression $rect\left(\frac{\tilde{\tau}-\tau_{cb}}{\tau_{az}}\right)$, to be analyzed further. Here $\tau_{cb}$ is the azimuth window center. $\tau_{az}$ is the length of the window. $\tilde{\tau}$ is the bistatic point of stationary phase (PSP). All these parameters depend on the position of the PT and the configuration of the bistatic mission; the Doppler bandwidth and the Doppler centroid depend on these coordinates as well. The bistatic common PSP is determined with the formula given in (3.132). We perform some changes on the first term of $\tilde{\tau}$, which allows us to take $\tau_{0R}$ out of the fraction, thus obtaining:

$$\begin{aligned}\tilde{\tau} = \tau_{0R} + a_0 \frac{v_T{}^2 \cdot F_T\left(f,f_\tau\right)^{\frac{3}{2}}}{v_T{}^2 \cdot F_T\left(f,f_\tau\right)^{\frac{3}{2}} + a_2 v_R{}^2 \cdot F_R\left(f,f_\tau\right)^{\frac{3}{2}}} - \\ -f_\tau \cdot R_{0R}\frac{c}{2}a_2 \cdot \frac{F_R\left(f,f_\tau\right)+F_T\left(f,f_\tau\right)}{v_T{}^2 \cdot F_T\left(f,f_\tau\right)^{\frac{3}{2}} + a_2 v_R{}^2 \cdot F_R\left(f,f_\tau\right)^{\frac{3}{2}}}\end{aligned} \tag{4.3}$$

As already mentioned, the Doppler bandwidth and the Doppler centroid are determined with the rectangular window. The *rect* function is symmetric, so we can write:

$$rect\left(\frac{\tilde{\tau}-\tau_{cb}}{\tau_{az}}\right) = rect\left(-\frac{\tilde{\tau}-\tau_{cb}}{\tau_{az}}\right) \tag{4.4}$$

Then, for the argument of the *rect* function, we get:

$$\begin{aligned}\arg = \frac{1}{\tau_{az}} \cdot \left( \tau_{0R} - \tau_{cb} + a_0 \frac{v_T{}^2 \cdot F_T\left(f,f_\tau\right)^{\frac{3}{2}}}{v_T{}^2 \cdot F_T\left(f,f_\tau\right)^{\frac{3}{2}} + a_2 v_R{}^2 \cdot F_R\left(f,f_\tau\right)^{\frac{3}{2}}} - \right. \\ \left. -f_\tau \cdot R_{0R}\frac{c}{2}a_2 \frac{F_R\left(f,f_\tau\right)+F_T\left(f,f_\tau\right)}{v_T{}^2 \cdot F_T\left(f,f_\tau\right)^{\frac{3}{2}} + a_2 v_R{}^2 \cdot F_R\left(f,f_\tau\right)^{\frac{3}{2}}} \right)\end{aligned} \tag{4.5}$$

Here we introduce the next notation for the denominator:

$$N = v_T{}^2 \cdot F_T\left(f,f_\tau\right)^{\frac{3}{2}} + a_2 v_R{}^2 \cdot F_R\left(f,f_\tau\right)^{\frac{3}{2}} \tag{4.6}$$

With this notation, we rewrite (4.5) as:

$$\begin{aligned}\arg &= \frac{1}{\tau_{az}} \cdot \left( \tau_{0R} - \tau_{cb} + a_0 \frac{v_T{}^2 \cdot F_T\left(f, f_\tau\right)^{\frac{3}{2}}}{N} - f_\tau \cdot R_{0R} \frac{c}{2} a_2 \cdot \frac{F_R\left(f, f_\tau\right) + F_T\left(f, f_\tau\right)}{N} \right) \\ &= \frac{\left(\tau_{0R} - \tau_{cb}\right) \cdot N + a_0 v_T{}^2 \cdot F_T\left(f, f_\tau\right)^{\frac{3}{2}} - f_\tau \cdot R_{0R} \frac{c}{2} a_2 \cdot \left(F_R\left(f, f_\tau\right) + F_T\left(f, f_\tau\right)\right)}{\tau_{az} N}\end{aligned} \tag{4.7}$$

We need to give the above expression the shape of a Doppler frequency window:

$$rect\left( \frac{f_\tau - f_{\tau dc}}{B_{az}} \right) \tag{4.8}$$

In (4.7), we invert the numerator. We want to separate $f_\tau$ as it is given in (4.8):

$$\begin{aligned}-\arg &= \frac{f_\tau \cdot R_{0R} \frac{c}{2} \cdot a_2 \cdot \left(F_R\left(f, f_\tau\right) + F_T\left(f, f_\tau\right)\right) - \left(\tau_{0R} - \tau_{cb}\right) \cdot N + a_0 \cdot v_T{}^2 \cdot F_T\left(f, f_\tau\right)^{\frac{3}{2}}}{\tau_{az} N} \\ &= \frac{f_\tau - \frac{\left(\tau_{0R} - \tau_{cb}\right) \cdot N + a_0 v_T{}^2 \cdot F_T\left(f, f_\tau\right)^{\frac{3}{2}}}{R_{0R} \frac{c}{2} a_2 \cdot \left(F_R\left(f, f_\tau\right) + F_T\left(f, f_\tau\right)\right)}}{\frac{\tau_{az} N}{R_{0R} \frac{c}{2} a_2 \cdot \left(F_R\left(f, f_\tau\right) + F_T\left(f, f_\tau\right)\right)}}\end{aligned} \tag{4.9}$$

Thus, we can get the expressions of the Doppler centroid and the Doppler bandwidth:

$$f_{\tau dc}{}^{Bist} = \frac{\left(\tau_{0R} - \tau_{cb}\right) \cdot N + a_0 v_T{}^2 \cdot F_T\left(f, f_\tau\right)^{\frac{3}{2}}}{R_{0R} \frac{c}{2} a_2 \cdot \left(F_R\left(f, f_\tau\right) + F_T\left(f, f_\tau\right)\right)} \tag{4.10}$$

$$B_{az}{}^{Bist} = \frac{\tau_{az} N}{R_{0R} \frac{c}{2} a_2 \cdot \left(F_R\left(f, f_\tau\right) + F_T\left(f, f_\tau\right)\right)} \tag{4.11}$$

Both expressions depend on the range frequency, bistatic parameters, coordinates and the azimuth frequency itself. These expressions would be explicit without the $f_\tau$ dependency. To eliminate these dependencies on $F_R\left(f, f_\tau\right)$ and $F_T\left(f, f_\tau\right)$, the following approximations are used:

$$\begin{aligned}F_R\left(f, f_\tau\right) &= \left(f + f_0\right)^2 - \frac{f_\tau{}^2 c^2}{4 v_R{}^2} \approx \left(f + f_0\right)^2 \\ F_T\left(f, f_\tau\right) &= \left(f + f_0\right)^2 - \frac{f_\tau{}^2 c^2}{4 v_T{}^2} \simeq \left(f + f_0\right)^2\end{aligned} \tag{4.12}$$

These approximations are substituted in (4.10) and (4.11), obtaining:

$$f_{\tau_{dc}}^{Bist} = \frac{(\tau_{0R} - \tau_{cb}) \cdot \left[ v_T^2 \cdot (f + f_0)^3 + v_R^2 a_2 \cdot (f + f_0)^3 \right] + a_0 v_T^2 \cdot (f + f_0)^3}{R_{0R} \frac{c}{2} a_2 \cdot 2 \cdot (f + f_0)^2} \tag{4.13}$$

And finally, we get:

$$\begin{aligned} f_{\tau_{dc}}^{Bist} &= (f + f_0) \cdot \frac{(\tau_{0R} - \tau_{cb}) \cdot \left[ v_T^2 + v_R^2 a_2 \right] + a_0 v_T^2}{R_{0R} \frac{c}{2} a_2 2} \\ &= \frac{f + f_0}{c a_2 R_{0R}} \cdot \left[ (\tau_{0R} - \tau_{cb}) \cdot \left[ v_T^2 + v_R^2 a_2 \right] + a_0 v_T^2 \right] \\ &= \frac{f + f_0}{c} \cdot \left[ (\tau_{0R} - \tau_{cb}) \cdot \left[ \frac{v_T^2}{R_{0T}} + \frac{v_R^2}{R_{0R}} \right] + \frac{a_0 v_T^2}{R_{0T}} \right] \end{aligned} \tag{4.14}$$

Analogously, we obtain for the Doppler bandwidth:

$$\begin{aligned} B_{az}^{Bist} &= \frac{\tau_{az} N}{R_{0R} \frac{c}{2} a_2 \cdot \left( F_R(f, f_\tau) + F_T(f, f_\tau) \right)} \\ &= \frac{\tau_{az} \cdot \left[ v_T^2 \cdot (f + f_0)^3 + v_R^2 a_2 \cdot (f + f_0)^3 \right]}{R_{0R} \frac{c}{2} a_2 \cdot 2 \cdot (f + f_0)^2} \end{aligned} \tag{4.15}$$

Canceling terms on the numerator and the denominator, we get the final result together with Doppler centroid frequency:

$$\boxed{B_{az}^{Bist} = \tau_{az} \cdot (f + f_0) \cdot \frac{v_T^2 + v_R^2 a_2}{R_{0R} c a_2} = \tau_{az} \cdot \frac{f + f_0}{c} \cdot \left( \frac{v_T^2}{R_{0T}} + \frac{v_R^2}{R_{0R}} \right)}$$

$$\boxed{f_{\tau_{dc}}^{Bist} = \frac{f + f_0}{c} \cdot \left[ \tau_{0R} \cdot \frac{v_R^2}{R_{0R}} + \tau_{0T} \cdot \frac{v_T^2}{R_{0T}} - \tau_{cb} \cdot \left( \frac{v_T^2}{R_{0T}} + \frac{v_R^2}{R_{0R}} \right) \right]} \tag{4.16}$$

These expressions were used in the different stages of the processing [9],[19],[22],[23], and gave reasonable approximations.

### 4.2.1 Comparison with Doppler Frequency Results Obtained for Monostatic SAR

As already mentioned, the monostatic SAR is a special case of the bistatic SAR, where the transmitter and the receiver are located on the same carrier. (4.16) shows the Doppler bandwidth expression for bistatic configurations, and (4.14) shows the equivalent Doppler centroid expression. We would like to use these expressions to calculate the values of the Doppler bandwidth and the Doppler centroid for monostatic SAR and compare the results

with those ones already known in monostatic processing. In [24], the Doppler centroid for monostatic SAR was calculated as:

$$f_{\tau dc}{}^{mon} = \frac{2}{c \cdot R(\tau_c)} \cdot (f + f_0) \cdot (\tau_0 - \tau_c) \cdot v^2 \tag{4.17}$$

And for the monostatic Doppler bandwidth, the following expression was given:

$$B_{az}{}^{mon} = 2\tau_{az} \cdot \frac{f + f_0}{c \cdot R(\tau_c)} \cdot v^2 \tag{4.18}$$

- $f_{\tau dc}{}^{mon}$ is the monostatic Doppler centroid frequency.
- $B_{az}{}^{mon}$ is the Doppler bandwidth.
- $R(\tau_c)$ is the slant range at the center of the footprint.
- $f_0$ is the carrier frequency.
- $v$ is the sensor's velocity.
- $\tau_{az}$ is the azimuth time corresponding to the center of the footprint.

If we consider the monostatic case as a special case of bistatic SAR, then the sensors will have the same velocity and should move across the same trajectory. In this case, the transmitter's and the receiver's slant ranges at the points of closest approach will be equal for any point target: $R_{0R} = R_{0T} \cong R_0$. Besides that, velocities are equal too: $v_T = v_R = v$. The transmitter's and the receiver's azimuth times of closest approach will be also equal in the monostatic case: $\tau_{0R} = \tau_{0T}$. Hence, the bistatic parameters related to the monostatic case can be easily determined; they have simple and constant values. According to what was defined in (3.93), we have $a_0 = 0$, $a_2 = 1$ for the monostatic case, which will simplify the expression of the bistatic Doppler centroid given in (4.14):

$$f_{\tau dc}{}^{Bist} = \frac{2}{cR_{0R}} \cdot (f + f_0) \cdot (\tau_0 - \tau_c) \cdot v^2 \tag{4.19}$$

Comparing the expression for the monostatic Doppler centroid given in (4.19) with that one given in (4.17), we observe that they are nearly equivalent. The only difference is that in (4.19) we have a slant range at the PCA, and in (4.17) the slant range is taken at the center of the footprint. Taking into account the complexity of our derivations and approximations, this small difference is acceptable. In SAR derivations, the slant range very often is exchanged with the slant range at the PCA.

Analogously, we calculate the monostatic Doppler bandwidth with the formula for the bistatic Doppler bandwidth given in (4.16). After the simplifications we have:

$$B_{az}{}^{Bist} = 2\tau_{az} \cdot \frac{f + f_0}{R_{0R}c} \cdot v^2 \tag{4.20}$$

We still observe the equivalency between the (4.20) and (4.18). This was another test for our bistatic approach.

### 4.2.2 Simulation Results

The formulas derived for the bistatic Doppler centroid and the bistatic Doppler bandwidth were used often for our bistatic processing. They gave reasonable results. As a sign of that, we show here the results of two simulations: one spaceborne and one airborne.

First, we consider the spaceborne case. The parameters of the spaceborne simulation are given in Table 4.2. Because of the high squint angle, we should expect high Doppler centroids. The PRF was intentionally selected very high in order to observe the full range of Doppler frequencies without an aliasing effect.

Table 4.2. Parameters of the spaceborne bistatic simulation

| **Parameter** | **Transmitter** | **Receiver** |
|---|---|---|
| Speed of Satellites | 7300 m/s | 7500 m/s |
| Pulse Duration | 37.1us | |
| Carrier Frequency | 5.5 GHz | |
| Bandwidth | 3 MHz | |
| PRF | 7300 Hz | |
| Squint Angle | 0.3° | 0.3° |
| Off Nadir | 45° | 45° |
| Opening angle in azimuth direction | 1° | 1° |
| Opening angle in elevation | 5° | 5° |
| Max Distance with Satellites | 3080 m | |
| Min Distance with Satellites | 3000 m | |

These parameters were used for the bistatic simulation in order to generate the raw data. We then applied the Fourier transformation to these raw data. The upper plot of Figure 4.4 shows the obtained Fourier spectra of the raw data. The spectrum on the plot is a slice at the zero range frequency:

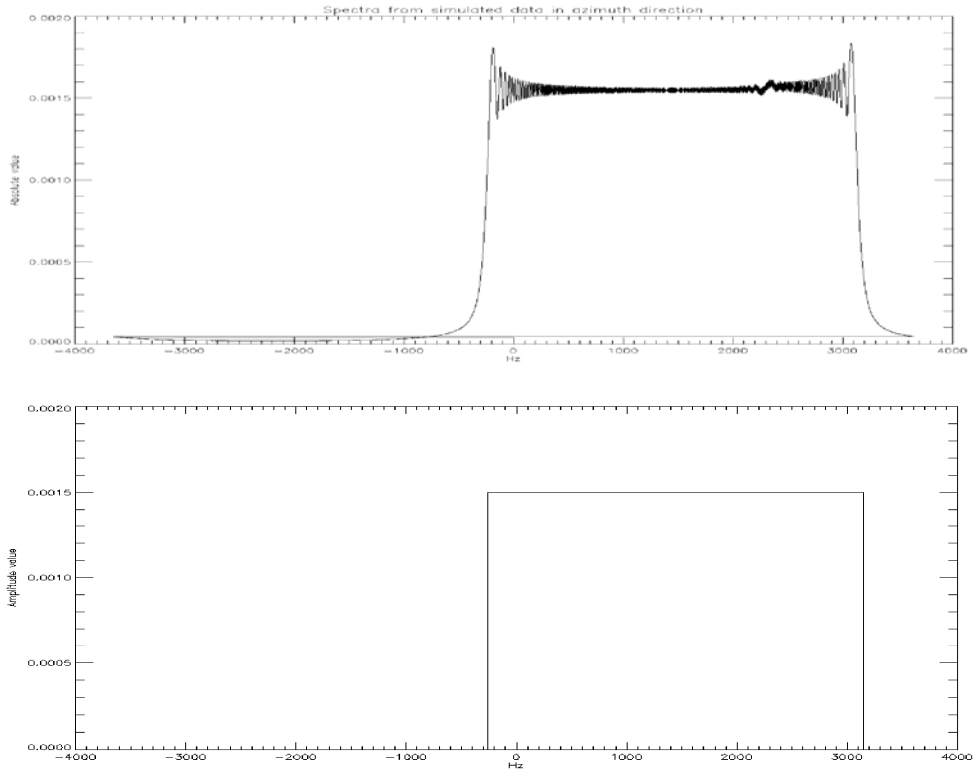


Figure 4.4. Azimuth spectrum generated from the simulated raw data

We then calculated the values of the Doppler centroid and the Doppler bandwidth using (4.14) and (4.16). For the Doppler centroid we have $f_{\tau dc}^{Bist} = 1444,9Hz$, and for the Doppler bandwidth we have $B_{az}^{Bist} = 3409.2Hz$. We have generated the rectangular window with the calculated Doppler frequency and Doppler bandwidth parameters, which are shown on the lower plot of Figure 4.4. We compare the plots given in Figure 4.4, and it is obvious that the calculated values are giving good approximations.

Now we consider the airborne case, the parameters are given in Table 4.3:

Table 4.3 Parameters of the airborne bistatic simulation

| **Parameter** | **Transmitter** | **Receiver** |
|---|---|---|
| Speed of airplanes | 98m/s | 98m/s |
| Pulse duration | 3μs | |
| Carrier Frequency | 10.17GHz | |
| Bandwidth | 20MHz | |
| PRF | 1250Hz | |
| Squint angle | 0° | 1° |
| Off Nadir angle | 42° | 52° |
| Opening angle in azimuth direction | 6° | 6° |
| Opening angle in elevation | 12° | 12° |
| Max distance between airplanes | 1029m | |
| Min distance between airplanes | 1000m | |

The upper plot of Figure 4.5 shows a slice of the azimuth spectra for the airborne experiment:

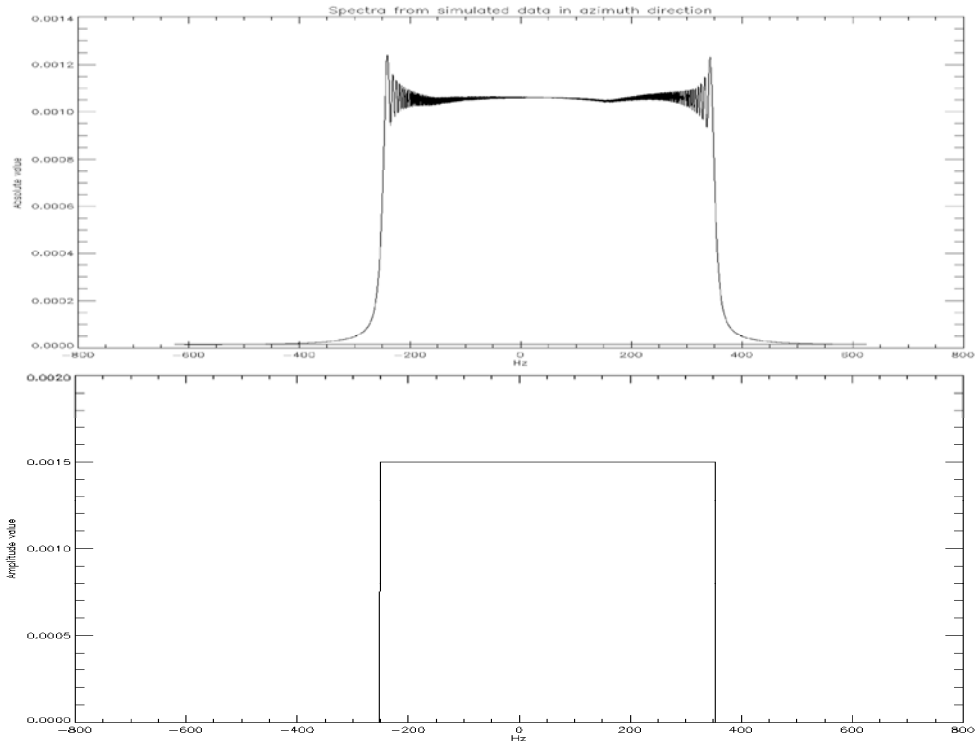


Figure 4.5. Azimuth spectrum generated from the simulated raw data

Using (4.14) and (4.16) again, we have a Doppler centroid of $f_{\tau dc}^{\ Bist} = 605,5Hz$ and a Doppler bandwidth of $B_{az}^{\ Bist} = 50.9Hz$. As the lower plot of Figure 4.5, we gave the rectangular window with calculated Doppler frequency parameters. Looking at Figure 4.5, we easily find that calculated values are in accordance with the plots.

## 4.3 Particular Cases of the Bistatic Point Target Reference Spectrum

Here we consider some particular configurations where the bistatic point target reference spectrum is simplified. We will follow the classification of the bistatic configuration given in section 2.3.

### 4.3.1 Identical Velocity Values $v_r = v_T = v_0$

By letting the velocities be equal in amplitude $v_r = v_T = v_0$, but not in direction $\vec{v}_R \neq \vec{v}_T$, some simplifications become possible.

#### 4.3.1.1 Monostatic Term

Now the quasi-monostatic term considerably simplifies and seems almost monostatic: $e^{-j\Psi_{MO}}$, where:

$$\Psi_{MO}(f, f_\tau) = \phi_T(\tilde{\tau}_T, f_\tau) + \phi_R(\tilde{\tau}_R, f_\tau) = 2\pi f_\tau \cdot \frac{\tau_{0R} + \tau_{0T}}{2} + \\ + \frac{4\pi}{c} \cdot \frac{R_{0R} + R_{0T}}{2} \cdot \sqrt{(f + f_0)^2 - f_\tau^2 \frac{c^2}{4v_0^2}} \tag{4.21}$$

which is very similar to the monostatic expression. $w(\tau - \tau_{cb})$ denotes the time extent and the center of the cut-out from the monostatic range history. But because $R_{0T}$ and $R_{0R}$ have non-linear dependences over azimuth time, we cannot think about a monostatic imaging located at the position $\left(\frac{\tau_{0R} + \tau_{0T}}{2}, \frac{R_{0R} + R_{0T}}{2}\right)$. Let's make a coordinate transformation and go to the central coordinates $(\tau_{0C}, R_{0C}) \cong \left(\frac{\tau_{0R} + \tau_{0T}}{2}, \frac{R_{0R} + R_{0T}}{2}\right)$. As we know, the receiver's parameters are chosen as the coordinates in our bistatic processing $R_{0R}$, $\tau_{0R}$, and these coordinates are determined as $(\tau_{0R}, R_{0R}) = (2\tau_{0C} - \tau_{0T}, 2R_{0C} - R_{0T})$. We have non-linear dependencies between $R_{0R}$ and $R_{0T}$, so the dependency between $R_{0R}$ over $R_{0C}$ will be non-linear as well, so we will not simplify the task at all.

The discussion above means that we cannot do bistatic processing by imagining the equivalent monostatic trajectory. Prof. Bamler came to the same conclusion in his publication [35]. He calculated the numerical transfer functions to correct the bistatic deformation. The simulations he made prove that the equivalent monostatic trajectory gives a wrong approximation in most of the bistatic configurations.

#### 4.3.1.2 Bistatic Deformation Term

The bistatic deformation term is now reduced to $e^{-j\frac{1}{2}\Psi_{BI}}$, with:

$$\Psi_{BI}\left(f,f_\tau\right)=\frac{2\pi}{c}\cdot\frac{v_0^2}{\left(f+f_0\right)^2}\cdot\frac{F_{TR}\left(f,f_\tau\right)^{\frac{3}{2}}}{R_{0R}+R_{0T}}\cdot\left(\tilde{\tau}_T-\tilde{\tau}_R\right)^2$$

$$\text{where: } \left(\tilde{\tau}_T-\tilde{\tau}_R\right)^2=\left[\tau_{0T}-\tau_{0R}-f_\tau\cdot\frac{c}{2v_0^2}\cdot\frac{R_{0T}-R_{0R}}{\sqrt{F_{TR}\left(f,f_\tau\right)}}\right]^2 \tag{4.22}$$

$$F_{T,R}\left(f,f_\tau\right)=\left(f+f_0\right)^2-f_\tau^2\frac{c^2}{4v_0^2} \tag{4.23}$$

Again, the inverse Fourier transformation turns out to be an elliptic arc in the range-azimuth time domain. As in the preceding case, this *generalized 'Smile'* changes over slant range and azimuth time, since the difference between $R_{0T}$ and $R_{0R}$ is azimuth time variant. Since for constant velocities the difference changes linearly over time, Chirp Scaling strategies to equalize the bistatic deformation term (comparable to equalize the range migration) might be thought of.

Again ignoring the convolution with the range chirp, we note that in this case the bistatic point target response can be modeled as a double convolution, the point target response of an equivalent monostatic sensor is convolved with the *generalized azimuth and range varying 'Smile'*.

#### 4.3.1.3 Amplitude Term

In the general bistatic case the amplitude term is given in (3.135). In the particular case when $v_r=v_T=v_0$, amplitude terms simplify as:

$$Amp\left(f,f_\tau,R_{0R}\right)=\frac{\left|f+f_0\right|}{F^{\frac{3}{4}}\cdot v_0\cdot\sqrt{c\cdot\left(\frac{1}{R_{0R}}+\frac{1}{R_{0T}}\right)}} \tag{4.24}$$

### 4.3.2 Identical velocity vectors $\vec{v}_T=\vec{v}_R$

Another interesting situation occurs when the transmitter and the receiver move parallel with equal velocities. This case is called the translationally invariant configuration [29].

#### 4.3.2.1 Monostatic Term

The first phasor remains unchanged.

#### 4.3.2.2 Bistatic deformation term

The bistatic deformation term essentially remains the same, except that it now is constant with respect to the azimuth time, but still range variant: $e^{-j\frac{1}{2}\Psi_{BI}}$, with:

$$\Psi_{BI}(f,f_\tau)=\frac{2\pi}{c}\cdot\frac{v_0^2}{(f+f_0)^2}\cdot\frac{F_{TR}(f,f_\tau)^{\frac{3}{2}}}{R_{0R}+R_{0T}}\cdot(\tilde{\tau}_T-\tilde{\tau}_R)^2$$
$$\text{where: } (\tilde{\tau}_T-\tilde{\tau}_R)^2=\left[\tau_{0T}-\tau_{0R}-f_\tau\cdot\frac{c}{2v_0^2}\cdot\frac{R_{0T}-R_{0R}}{\sqrt{F_{TR}(f,f_\tau)}}\right]^2 \tag{4.25}$$

$a_0=\tau_{0T}-\tau_{0R}$ is the bistatic parameter given in (3.93), constant for the complete scene; parameter $a_2$ is still range variant. As indicated before, the compensation can be accomplished in range blocks.

Again ignoring the convolution with the range chirp, we note that in this case the bistatic point target response can be modeled as a double convolution: the point target response of a monostatic equivalent sensor is convolved with the bistatic deformation term.

#### 4.3.2.3 Amplitude Term

The amplitude term has same expression as (4.24).

### 4.3.3 Constant Offset Configuration – Tandem Case

This is the case when the transmitter and the receiver follow each other with a fixed offset and the same velocity vectors. We call this a Tandem configuration. It was first considered in [27], where it was named 'Constant Offset Configuration'.

In this case, the transmitter's and the receiver's velocities are equal, and so are their slant ranges, at the point of closest approach for any point target, which will cause considerable simplifications to be discussed in the following.

#### 4.3.3.1 Quasi Monostatic Term

In Tandem Case the quasi-monostatic term becomes truly monostatic:

$$\begin{aligned}\Psi_{QM}(f,f_\tau)&=\phi_T(\tilde{\tau}_T,f_\tau)+\phi_R(\tilde{\tau}_R,f_\tau)\\&=\pi f_\tau\cdot(2\tau_{0R}+a_0)+\frac{4\pi}{c}\cdot R_{0R}\sqrt{(f+f_0)^2-f_\tau^2\frac{c^2}{4v_0^2}}\end{aligned} \tag{4.26}$$

$a_0$ expresses the difference between the azimuth times at the points of closest approach of the transmitter, and the receiver defined in (3.93). In this particular configuration, it is constant. We see from (4.26) that in this case the quasi-monostatic term is exactly a monostatic phase term. This means that in this case the focusing can be carried out by a conventional monostatic processing approach, after compensating the bistatic deformation term.

#### 4.3.3.2 Bistatic Term

The bistatic term is also relatively simple:

$$\Psi_{BI}\left(f,f_\tau\right)=\frac{\pi}{c}\cdot\frac{v_0^2}{\left(f+f_0\right)^2}\cdot\frac{F_{TR}\left(f,f_\tau\right)^{\frac{3}{2}}}{R_{0R}}\cdot\left(\tilde{\tau}_T-\tilde{\tau}_R\right)^2 \tag{4.27}$$

$$\text{where: } \left(\tilde{\tau}_T-\tilde{\tau}_R\right)^2=a_0{}^2$$

$$F_{TR}\left(f,f_\tau\right)=\left(f+f_0\right)^2-f_\tau^2\frac{c^2}{4v_0^2} \tag{4.28}$$

In the Tandem case, the baseline between the transmitter and the receiver remains constant and is equal to:

$$d=v_0a_0 \tag{4.29}$$

Substituting (4.29) in (4.27), we get:

$$\Psi_{BI}\left(f,f_\tau\right)=\frac{\pi}{c}\cdot\frac{F\left(f,f_\tau\right)^{\frac{3}{2}}}{\left(f+f_0\right)^2R_{0R}}\cdot d^2 \text{ where: } \quad \left(\tilde{\tau}_T-\tilde{\tau}_R\right)^2=a_0{}^2 \tag{4.30}$$

#### 4.3.3.3 Amplitude Term

The amplitude term given in (3.135) for general case simplifies considerably:

$$Amp\left(f,f_\tau,R_{0R}\right)=\frac{\left|f+f_0\right|}{F^{\frac{3}{4}}\cdot v_0}\cdot\sqrt{\frac{R_0}{2c}} \tag{4.31}$$

where $R_0=R_{0T}=R_{0R}$ for the Tandem case.

#### 4.3.3.4 Rocca's Smile and Point Target Reference Spectrum

Here we compare two different bistatic approaches: our bistatic approach and one of the first bistatic approaches described in [28], [29]. For the Tandem configuration, the equivalence between both approaches will be proven. The final result of both approaches will show that the bistatic processing can be converted to quasi-monostatic by initially convolving the range-compressed raw data with the bistatic deformation term.

##### *4.3.3.4.1 Rocca's Smile Expressed in our Bistatic Notation*

Fabio Rocca was the first to offer a very elegant solution for the bistatic problem [27]. It was initially done for the Tandem configuration, referred to in the original paper as the 'Stationary Offset Configuration'. To transform bistatic surveys into monostatic ones, the initial data set is first convolved with the 'Smile' operator. This 'Smile' operator has similarity with the Dip Move Out-(DMO) operator known in seismic literature. The 'Smile' was first derived with geometrical considerations and then expressed in SAR microwave terms. The term corresponding to the 'Smile' operator [27] is given as:

$$H\left(\omega,k,t_b\right)=\exp\left\{ j\left(\omega+\omega_0\right)\cdot t_b\cdot\left(1-\sqrt{1-\frac{4h^2\cdot\cos^2\vartheta}{{t_b}^2\cdot c^2}}\right)\right\} \tag{4.32}$$

- $t_b$ is the bistatic range time of *down converted* data.
- $\omega$ is the corresponding angular frequency.
- $\omega_0$ is the central angular frequency.
- $h$ is the half of the baseline between the transmitter and the receiver.
- $\vartheta$ is a dipping angle of the reflector, somehow equivalent to the squint angle of a monostatic survey.
- $k$ is the azimuth wavenumber.

It was shown in [27] that the following relation is valid:

$$\cos^2\left(\vartheta\right)=1-\frac{k^2\cdot c^2}{4\left(\omega+\omega_0\right)^2} \tag{4.33}$$

We substitute (4.33) into (4.32) and get:

$$H\left(\omega,k,t_b\right)=\exp\left\{ j\left(\omega+\omega_0\right)\cdot t_b\left(1-\sqrt{1-\frac{4h^2\cdot\left(1-\frac{k^2c^2}{4\left(\omega+\omega_0\right)^2}\right)}{{t_b}^2\cdot c^2}}\right)\right\} \tag{4.34}$$

Here we use the approximation:

$$\sqrt{1-x}=1-\frac{x}{2} \tag{4.35}$$

Of course, the approximation is correct for small values of $x$. We consider the fraction $\dfrac{4h^2\cdot\left(1-\dfrac{k^2c^2}{4(\omega+\omega_0)^2}\right)}{{t_b}^2c^2}$ given in the square root expression of (4.34). It is clear that because carrier frequencies in SAR are normally chosen to be much higher then their corresponding Doppler frequencies, the flowing relation is valid: $1\gg\dfrac{k^2c^2}{4\left(\omega+\omega_0\right)^2}$. It is clear also that $t_bc/2$ is the bistatic half slant range history and that it is much bigger than the baseline size. Hence, the term $\dfrac{4h^2}{{t_b}^2c^2}=\left(\dfrac{h}{t_bc/2}\right)^2$ is much smaller than 1. The approximation $\sqrt{1-x}=1-\dfrac{x}{2}$ is therefore applicable.

Considering the wavenumber definition, we write:

$$k=\frac{2\pi f_\tau}{v} \tag{4.36}$$

- $v$ is the velocity of the transmitter and the receiver (equal in Tandem Case).
- $f_\tau$ is the azimuth (Doppler) frequency. We take the symbol used for Doppler frequencies in our bistatic processing approach.
- $2h$ is a baseline (the distance between the transmitter and the receiver). In our approach we are naming it as $d$.
- $t_b$ is the bistatic range time, and in our approach it shows the variance of the 'Smile' operator over the different positions of the point target. As we know, the Tandem Case is azimuth time invariant and it varies only in range direction. The variance in range is expressed in our coordinates with the receiver's slant range of closest approach. So, we substitute $t_b$ with $\frac{2R_{0R}}{c}$ (in the Tandem case $R_{0R} = R_{0T}$, where $R_{0R}$ is the receiver slant range).

After this change of variables, (4.34) is transformed to:

$$H\left(\omega, k, t_b\right) = \exp\left( -j\pi d^2 \frac{\left(f_0 + f\right)^2 - \frac{f_\tau^2 c^2}{4v^2}}{2R_{0R} c \cdot \left(f + f_0\right)} \right) \tag{4.37}$$

This is the 'Rocca's Smile' expressed in the coordinates and the parameters of our bistatic approach.

#### *4.3.3.4.2 Our Approach – Bistatic Term of the Bistatic Point Target Reference Spectrum*

We return to the bistatic point target reference spectrum (BPTRS). The bistatic deformation term is given by (4.2), and it is noticeably simplified in the Tandem configuration. The transmitter's and the receiver's slant ranges are equal. The same holds for their velocities, because they move parallel with a constant offset. So, we have $R_{0R} = R_{0T}, v_T = v_R \cong v$. Therefore, according to the symbols defined in (3.60), we get $F_T = F_R \cong F$. Additionally, one of the bistatic parameters given in (3.7) is easily determined: $a_2 = 1$. The other bistatic parameter, $a_0$, expresses the azimuth time difference between the transmitter's and the receiver's points of closest approach and in our current configuration is constant and equal to the baseline: $a_2 v = const \equiv d\,(baseline)$.

After these simplifications, we have:

$$H\left(f, f_\tau, R_{0R}\right) = \exp\left( -j\pi d^2 \cdot \frac{F^{\frac{3}{2}}}{2R_{0R} \cdot c \cdot \left(f + f_0\right)^2} \right) \tag{4.38}$$

Since $f + f_0$ is a decisive value in (3.60), we use the approximation $F^{\frac{3}{2}} = F \cdot F^{\frac{1}{2}} \approx F \cdot \left(f + f_0\right)$. After substituting it in (4.38), we obtain:

$$H\left(f, f_\tau, R_{0R}\right) = \exp\left( -j\pi d^2 \cdot \frac{\left(f + f_0\right)^2 - \frac{f_\tau^2 c^2}{4v^2}}{2R_{0R}c \cdot \left(f + f_0\right)} \right) \tag{4.39}$$

This is the expression of the bistatic deformation term for the Tandem configuration derived from our approach. If we now compare (4.37) and (4.39), we see that they are absolutely identical. This proves the equivalency of the 'Rocca's Smile' and our 'Bistatic Deformation Term' Tandem ('Stationary Offset Configuration'). This is not an absolute proof that both approaches are correct, but we can say for certain that if one of them fails, then the same will happen to other one.

# 5 Constraints of Validity

The Method of the Stationary Phase (MSP) has been crucial for our derivations. Both the phase histories of the transmitter and the receiver have been expanded in a second order Taylor series around their individual points of stationary phase (MSP). Both expansions are individually valid in the vicinity of the corresponding PSP, but since the bistatic phase history is the superposition of the transmitter's and the receiver's phase histories, the natural question arise whether the superposition of the individually valid second-order Taylor series expansions is still a valid approximation of the full phase history, especially if the individual points of stationary phase are distant with respect to the azimuth time. To put it another way, the central question is: how far may the individual points of stationary phase be separated in time, so that the superposition of the two second-order Taylor series expansions around these distant points of stationary phase still remains valid?

## 5.1 Strong Terms of Validity

The first work about the bistatic constraints was given in [1].

In the derivation of the bistatic point target reference spectrum we have done the expansion of the transmitter and the receiver phase terms using Taylor series later we truncated the series after the 2nd order term. Therefore the bistatic constraints are in relation with the error introduced by these truncations. Taylor series expansion of the transmitter and the receiver slant ranges can be written as:

$$\begin{aligned} R_{T,R}(\tau) = R_{T,R}(\tilde{\tau}_{T,R}) + R^{(1)}{}_{T,R}(\tilde{\tau}_{T,R})\cdot(\tau-\tilde{\tau}_{T,R}) + \frac{1}{2!}R^{(2)}{}_{T,R}(\tilde{\tau}_{T,R})\cdot(\tau-\tilde{\tau}_{T,R})^2 + \\ + \frac{1}{3!}R^{(3)}{}_{T,R}(\tilde{\tau}_{T,R})\cdot(\tau-\tilde{\tau}_{T,R})^3 + \frac{1}{4!}\cdot R^{(4)}_{T,R}(\xi_{T,R})\cdot(\tau-\tilde{\tau}_{T,R})^4 \end{aligned} \tag{5.1}$$

where the dependencies on $R_{0T}$ and $R_{0R}$, $\tau_{0T}$ and $\tau_{0R}$ have been omitted for convenience. $\tilde{\tau}_{T,R}$ are the individual points of stationary phase of the transmitter (T) and the receiver (R). The last term in (5.1) is Lagrange form of the reminder, which sums up the higher order terms (of transmitter and receiver) according to the mean value theorem. $\xi_{T,R}$ are two different points within the intervals $(\tilde{\tau}_{T,R}, \tau)$.

The range rate errors (corresponding to the instantaneous frequency errors) of the Taylor series expansions of the transmitter (index T) and the receiver (index R) are given by:

$$e_{T,R}(\tau) = \frac{1}{2!}R^{(3)}{}_{T,R}(\tilde{\tau}_{T,R})\cdot(\tau-\tilde{\tau}_{T,R})^2 + \frac{1}{3!}\cdot R^{(4)}_{T,R}(\xi_{T,R})\cdot(\tau-\tilde{\tau}_{T,R})^3 \tag{5.2}$$

Now we require that the range rate error in the common PSP is negligible against the nominal value:

$$\left|\frac{\frac{1}{2!}R^{(3)}{}_{T,R}(\tilde{\tau}_{T,R})\cdot(\tilde{\tau}-\tilde{\tau}_{T,R}) + \frac{1}{3!}\cdot R^{(4)}_{T,R}(\xi_{T,R})\cdot(\tilde{\tau}-\tilde{\tau}_{T,R})^2}{R^{(2)}{}_{T,R}(\tilde{\tau}_{T,R})}\right| \overset{!}{<<} 1 \tag{5.3}$$

which can be guaranteed if:

$$\left|\frac{R^{(3)}{}_{T,R}\left(\tilde{\tau}_{T,R}\right)\cdot\left(\tilde{\tau}-\tilde{\tau}_{T,R}\right)}{R^{(2)}{}_{T,R}\left(\tilde{\tau}_{T,R}\right)}\right| \overset{!}{<<} 2 \tag{5.4}$$

and if the quadratic term in (5.3) is again a small denominator, then the linear term:

$$\left|\frac{R^{(4)}{}_{T,R}\left(\xi_{T,R}\right)\cdot\left(\tilde{\tau}-\tilde{\tau}_{T,R}\right)^2}{R^{(2)}{}_{T,R}\left(\tilde{\tau}_{T,R}\right)}\right| \overset{!}{<<} 3! \tag{5.5}$$

The conditions (5.4) and (5.5) are mathematically strong. If they are fulfilled, then the formula of bistatic point target reference spectrum will be valid too. However, there can be some situations when they are not holding, but the formula of bistatic point target reference spectrum is still working properly. In this sense, (5.4) and (5.5) form sufficient, but not necessary, condition.

## 5.2 Derivatives of the Slant Range at the Point of Stationary Phase

One derivative of the receiver's slant range at the point of the stationary phase is already known from (3.69). For the second derivative, we use the expression in (3.46):

$$\ddot{R}_R\left(\tau,R_{0R},\tau_{0R}\right)=-\frac{v_R{}^4}{R_R\left(\tau,R_{0R},\tau_{0R}\right)^3}\cdot\left(\tau-\tau_{0R}\right)^2+\frac{v_R{}^2}{R_R\left(\tau,R_{0R},\tau_{0R}\right)} \tag{5.6}$$

Evaluating the above on the receiver's point of stationary phase (PSP), we get:

$$\ddot{R}_R\left(\tilde{\tau}_{0R},R_{0R},\tau_{0R}\right)=\frac{v_R{}^2}{R_R\left(\tilde{\tau}_{0R},R_{0R},\tau_{0R}\right)^3}\cdot\left(-v_R{}^2\left(\tilde{\tau}_{0R}-\tau_{0R}\right)^2+R_R\left(\tilde{\tau}_{0R},R_{0R},\tau_{0R}\right)^2\right) \tag{5.7}$$

Now we exploit (3.54) and obtain the following expression for the receiver's second-order derivative at the PSP:

$$\ddot{R}_R\left(\tilde{\tau}_R\right)=\frac{v_R{}^2\cdot R_{0R}{}^2}{R_R\left(\tilde{\tau}_R\right)^3} \tag{5.8}$$

Since the bistatic configuration is symmetric, the same arguments must also hold for the transmitter, and we may also write:

$$\ddot{R}_T\left(\tilde{\tau}_T\right)=\frac{v_T{}^2\cdot R_{0T}{}^2}{R_T\left(\tilde{\tau}_T\right)^3} \tag{5.9}$$

Note that we have again used the shorthand slant range notation:

$$R_R\left(\tilde{\tau}_R\right)\cong R_R\left(\tilde{\tau}_R,R_{0R},\tau_{0R}\right),\ R_T\left(\tilde{\tau}_T\right)\cong R_T\left(\tilde{\tau}_T,R_{0T},\tau_{0T}\right) \tag{5.10}$$

For constraints given in (5.4) and (5.5), we need to determine the fourth-order derivatives of the slant ranges.

We start with (3.3) and write:

$$\begin{aligned}\dot{R}_R\left(\tau\right)\cdot R_R\left(\tau\right)&=v_R{}^2\cdot\left(\tau-\tau_{0R}\right)\\ \dot{R}_T\left(\tau\right)\cdot R_T\left(\tau\right)&=v_T{}^2\cdot\left(\tau-\tau_{0T}\right)\end{aligned} \tag{5.11}$$

We differentiate the above equations again and get:

$$\begin{aligned}\dot{R}_R(\tau)^2 + R_R(\tau)\cdot\ddot{R}_R(\tau) &= v_R{}^2\\ \dot{R}_T(\tau)^2 + R_T(\tau)\cdot\ddot{R}_T(\tau) &= v_T{}^2\end{aligned} \tag{5.12}$$

From the above we determine the second-order derivatives of the slant ranges, but this was already done in (5.9).

For the third-order term, we differentiate (5.12) again:

$$2\dot{R}_R(\tau)\cdot\ddot{R}_R(\tau) + \dot{R}_R(\tau)\cdot\ddot{R}_R(\tau) + R_R(\tau)\cdot\dddot{R}_R(\tau) = 0 \tag{5.13}$$

Reordering it, we get:

$$\dddot{R}_R(\tau) = -\frac{3\dot{R}_R(\tau)\cdot\ddot{R}_R(\tau)}{R_R(\tau)} \tag{5.14}$$

Here we substitute the expressions of $\ddot{R}_R(\tau)$ and $\dot{R}_R(\tau)$ from (5.6) and (5.11), respectively, and obtain:

$$\begin{aligned}\dddot{R}_R(\tau) &= -3\frac{v_R{}^2\cdot(\tau-\tau_{0R})}{R_R(\tau)^2}\cdot\left(-\frac{v_R{}^4}{R_R(\tau,R_{0R},\tau_{0R})^3}\cdot(\tau-\tau_{0R})^2 + \frac{v_R{}^2}{R_R(\tau,R_{0R},\tau_{0R})}\right)\\ &= -3\frac{v_R{}^4\cdot(\tau-\tau_{0R})}{R_R(\tau)^5}\cdot\left(-v_R{}^2\cdot(\tau-\tau_{0R})^2 + R_R(\tau,R_{0R},\tau_{0R})^2\right)\end{aligned} \tag{5.15}$$

We evaluate the result at the receiver's PSP and obtain:

$$\dddot{R}_R(\tilde{\tau}_R) = -3v_R{}^2\cdot\frac{\tilde{\tau}_R-\tau_{0R}}{R_R(\tilde{\tau}_R)^2}\cdot\ddot{R}_R(\tilde{\tau}_R) = -\frac{3v_R{}^4\cdot(\tilde{\tau}_R-\tau_{0R})\cdot R_{0R}{}^2}{R_R(\tilde{\tau}_R)^5} \tag{5.16}$$

For the transmitter, we have a similar expression:

$$\dddot{R}_T(\tilde{\tau}_T) = -\frac{3v_T{}^4\cdot(\tilde{\tau}_T-\tau_{0T})\cdot R_{0T}{}^2}{R_T(\tilde{\tau}_T)^5} \tag{5.17}$$

For the fourth-order derivative, we differentiate (5.13) again:

$$\dot{R}_R(\tau)\cdot\dddot{R}_R(\tau) + R_R(\tau)\cdot\ddddot{R}_R(\tau) = -3\ddot{R}_R(\tau)\cdot\ddot{R}_R(\tau) - 3\dot{R}_R(\tau)\cdot\dddot{R}_R(\tau) \tag{5.18}$$

Collecting and reordering terms, we get the expression of $\ddddot{R}_R(\tau)$:

$$\ddddot{R}_R(\tau) = \frac{-3\ddot{R}_R(\tau)^2 - 4\dot{R}_R(\tau)\cdot\dddot{R}_R(\tau)}{R_R(\tau)} \tag{5.19}$$

In (5.19) we now substitute the known lower-order derivatives, and we obtain:

$$\ddddot{R}_R(\tau) = -\frac{3v_R{}^4 R_{0R}{}^2}{R_R(\tau)^7}\cdot\left(R_{0R}{}^2 - 4v_R{}^2(\tau-\tau_{0R})^2\right) \tag{5.20}$$

Evaluating this expression at the PSP, we get:

$$\ddot{\ddot{R}}_R(\tilde{\tau}_R) = -\frac{3v_R{}^4 \cdot R_{0R}{}^2}{R_R(\tilde{\tau}_R)^7} \cdot \left( R_{0R}{}^2 - 4v_R{}^2 \cdot (\tilde{\tau}_R - \tau_{0R})^2 \right) \tag{5.21}$$

A similar expression is found for the transmitter:

$$\ddot{\ddot{R}}_T(\tilde{\tau}_T) = -\frac{3v_T{}^4 R_{0T}{}^2}{R_T(\tilde{\tau}_T)^7} \cdot \left( R_{0T}{}^2 - 4v_T{}^2 \cdot (\tilde{\tau}_T - \tau_{0T})^2 \right) \tag{5.22}$$

## 5.3 Derivation of Constraints

Now that we have determined all needed slant range derivatives at the points of stationary phase, we can go further and determine the constraints. We start with constraint (5.5). The values of the derivatives (5.8) and (5.20) are substituted in (5.5), producing:

$$\frac{1}{6} \frac{\frac{3v_T{}^4 \cdot R_{0T}{}^2}{R_T(\xi_T)^7} \cdot \left( R_{0T}{}^2 - 4v_T{}^2 \cdot (\xi_T - \tau_{0T})^2 \right) \cdot (\tilde{\tau} - \tilde{\tau}_T)^2}{\frac{v_T{}^2 \cdot R_{0T}{}^2}{R_T(\tilde{\tau}_T)^3}} \ll 1 \tag{5.23}$$

$R_T(\xi_T)^7$ is factorized as $R_T(\xi_T)^2 \cdot R_T(\xi_T)^3 \cdot R_T(\xi_T)^2$ and substituted in (5.23). We obtain:

$$\frac{1}{2} \frac{v_T{}^2 \cdot \left( R_{0T}{}^2 - 4v_T{}^2 (\xi_T - \tau_{0T})^2 \right) \cdot (\tilde{\tau} - \tilde{\tau}_T)^2}{R_T(\xi_T)^2 \cdot R_T(\xi_T)^2} \ll 1 \tag{5.24}$$

The expressions of $R_T(\tau)^2$ given in (3.3) are evaluated at $\xi_T$ and substituted in (5.24), obtaining:

$$\frac{R_{0T}{}^2 \cdot \left( 1 - \frac{4v_T{}^2 \cdot (\xi_T - \tau_{0T})^2}{R_{0T}{}^2} \right)}{R_{0T}{}^2 \cdot \left( 1 + \frac{v_T{}^2 \cdot (\xi_T - \tau_{0T})^2}{R_{0T}{}^2} \right)} \cdot \frac{v_T{}^2}{R_T(\xi_T)^2} \cdot (\tilde{\tau} - \tilde{\tau}_T)^2 \ll 2 \tag{5.25}$$

After canceling and reordering some terms, we get:

$$(\tilde{\tau} - \tilde{\tau}_T)^2 \ll 2 \cdot \frac{1 + \frac{v_T{}^2 (\xi_T - \tau_{0T})^2}{R_{0T}{}^2}}{1 - \frac{4v_T{}^2 (\xi_T - \tau_{0T})^2}{R_{0T}{}^2}} \cdot \frac{R_T(\xi_T)^2}{v_T{}^2} \tag{5.26}$$

Normally in SAR, the slant range itself is much bigger than its variation. We assume that slant ranges at $\xi_T$ and $\tau_{0T}$ are equal. Hence, in (5.26) we have further simplifications:

$$\left(\tilde{\tau}-\tilde{\tau}_T\right)^2 \ll 2\cdot\frac{1+\frac{{v_T}^2\left(\xi_T-\tau_{0T}\right)^2}{{R_{0T}}^2}}{1-\frac{4{v_T}^2\left(\xi_T-\tau_{0T}\right)^2}{{R_{0T}}^2}}\cdot\frac{{R_{0T}}^2}{{v_T}^2} \tag{5.27}$$

Normally $\frac{{v_T}^2\left(\xi_T-\tau_{0T}\right)^2}{{R_{0T}}^2}\ll 1$, and the same holds for the term in the denominator: $\frac{4{v_T}^2\left(\xi_T-\tau_{0T}\right)^2}{{R_{0T}}^2}\ll 1$. Thus, we get for the transmitter:

$$\left(\tilde{\tau}-\tilde{\tau}_T\right)^2 \ll 2\cdot\frac{{R_{0T}}^2}{{v_T}^2} \tag{5.28}$$

We take the square root from both sides and obtain:

$$\left|\tilde{\tau}-\tilde{\tau}_T\right| \ll \sqrt{2}\cdot\frac{R_{0T}}{v_T} \tag{5.29}$$

Because of symmetry of transmitter and receiver sides, we have a similar expression for the receiver:

$$\left|\tilde{\tau}-\tilde{\tau}_R\right| \ll \sqrt{2}\cdot\frac{R_{0R}}{v_R} \tag{5.30}$$

Now we continue with the second constraint given in (5.4). Using (5.4) and substituting in it the second- (5.9) and the third-order (5.17) derivatives of the slant range histories, we get:

$$\frac{\frac{3{v_T}^4\cdot\left|\tilde{\tau}_T-\tau_{0T}\right|\cdot R_{0T}^2\cdot\left|\tilde{\tau}-\tilde{\tau}_T\right|}{R_T\left(\tilde{\tau}_T\right)^5}}{\frac{{v_T}^2R_{0T}^2}{R_T\left(\tilde{\tau}_T\right)^3}} << 2 \tag{5.31}$$

By canceling the some terms in the above expression, we obtain:

$$\left|\tilde{\tau}_T-\tau_{0T}\right|\cdot\left|\tilde{\tau}-\tilde{\tau}_T\right| << \frac{2R_T\left(\tilde{\tau}_T\right)^2}{3{v_T}^2} \tag{5.32}$$

We calculate $R_T\left(\tilde{\tau}_T\right)^2$ by evaluating the expression given in (3.3) at $\tilde{\tau}_T$. We then substitute it into (5.32) to obtain:

$$\left|\tilde{\tau}_T-\tau_{0T}\right|\cdot\left|\tilde{\tau}-\tilde{\tau}_T\right| \ll \frac{2}{3}\cdot\frac{{R_{0T}}^2+{v_T}^2\left(\tilde{\tau}_T-\tau_{0T}\right)^2}{{v_T}^2} = \frac{2{R_{0T}}^2}{3{v_T}^2}+\frac{2}{3}\left(\tilde{\tau}_T-\tau_{0T}\right)^2 \tag{5.33}$$

A similar expression for the receiver is also determined:

$$\left|\tilde{\tau}_R-\tau_{0R}\right|\cdot\left|\tilde{\tau}-\tilde{\tau}_R\right| \overset{!}{<<} \frac{2}{3}\cdot\frac{R_{0R}^2+v_R^2\left(\tilde{\tau}_R-\tau_{0R}\right)^2}{v_R^2} = \frac{2R_{0R}^2}{3v_R^2}+\frac{2}{3}\left(\tilde{\tau}_R-\tau_{0R}\right)^2 \tag{5.34}$$

## 5.4 Constraints Expressed in Bistatic Parameters and Bandwidths

We have derived the constraints of validity for the given bistatic point target reference spectrum (BPTRS). The constraints are given in (5.29), (5.30), (5.33), (5.34). These constraints are very important for any bistatic mission planning and more importantly, for a given mission they allow us to analyze whether or not the BPTRS is applicable. Yet, since the stationary points expressed in equations (5.29), (5.30), (5.33), (5.34) depend on geometry and Doppler parameters, we must rewrite the constraints in terms of bandwidths and bistatic mission specific parameters. Thus, we will express the constraints given in (5.29), (5.30), (5.33), (5.34) in terms of the transmitter's and the receiver's local parameters: velocities, slant ranges and range-azimuth frequency bandwidths.

We will do the derivations for the transmitter's side. We start with (5.29) and determine $\left|\tilde{\tau}-\tilde{\tau}_T\right|$. Here, $\tilde{\tau}$ is the common bistatic point of stationary phase (PSP). It has been calculated in (3.132). We substitute it into (5.29) and modify as follows:

$$\left|\tilde{\tau}-\tilde{\tau}_T\right| = \left|\frac{\ddot{\phi}_T\left(\tilde{\tau}_T\right)\cdot\tilde{\tau}_T+\ddot{\phi}_R\left(\tilde{\tau}_R\right)\cdot\tilde{\tau}_R}{\ddot{\phi}_T\left(\tilde{\tau}_T\right)+\ddot{\phi}_R\left(\tilde{\tau}_R\right)}-\tilde{\tau}_T\right| = \left|\frac{\ddot{\phi}_R\left(\tilde{\tau}_R\right)\cdot\tilde{\tau}_R-\ddot{\phi}_R\left(\tilde{\tau}_R\right)\cdot\tilde{\tau}_T}{\ddot{\phi}_T\left(\tilde{\tau}_T\right)+\ddot{\phi}_R\left(\tilde{\tau}_R\right)}\right| = \left|\frac{\tilde{\tau}_R-\tilde{\tau}_T}{1+\dfrac{\ddot{\phi}_T\left(\tilde{\tau}_T\right)}{\ddot{\phi}_R\left(\tilde{\tau}_R\right)}}\right| \tag{5.35}$$

$\ddot{\phi}_T\left(\tilde{\tau}_T\right)$, $\ddot{\phi}_R\left(\tilde{\tau}_R\right)$ are the second-order derivatives of the transmitter's and the receiver's phase terms at their individual points of stationary phase, given in (3.72) for the receiver and in (3.117) for the transmitter.

In the further constraint derivations we use the approximations:

$$\begin{aligned} F_R\left(f,f_\tau\right) &= \left(f+f_0\right)^2-\frac{f_\tau^{\,2}c^2}{4v_R^{\,2}} \approx \left(f+f_0\right)^2 \\ F_T\left(f,f_\tau\right) &= \left(f+f_0\right)^2-\frac{f_\tau^{\,2}c^2}{4v_T^{\,2}} \simeq \left(f+f_0\right)^2 \end{aligned} \tag{5.36}$$

We assume that carrier frequency $f_0$ is much bigger then range frequency bandwidth $f$. Hence, $f+f_0$ is positive. Furthermore, the expressions of the receiver's and the transmitter's points of stationary phase are given in (3.66) and (3.107), respectively. We thus obtain the following for the numerator of (5.35):

$$\left|\tilde{\tau}_R-\tilde{\tau}_T\right| = \left|\tau_{0T}-\tau_{0R}+\frac{f_\tau c}{2\left(f+f_0\right)}\cdot\left(\frac{R_{0R}}{v_R^{\,2}}-\frac{R_{0T}}{v_T^{\,2}}\right)\right| \tag{5.37}$$

For the denominator, after using the approximation given in (5.36), we obtain:

$$1+\frac{\ddot{\phi}_T\left(\tilde{\tau}_T\right)}{\ddot{\phi}_R\left(\tilde{\tau}_R\right)} = 1+\frac{v_T^{\,2}\cdot R_{0R}}{v_R^{\,2}\cdot R_{0T}} \tag{5.38}$$

Now we insert the numerator and the denominator in (5.35):

$$\left|\tilde{\tau}-\tilde{\tau}_T\right| = \frac{\left|\tau_{0T}-\tau_{0R}+\frac{f_\tau c}{2\left(f+f_0\right)}\cdot\left(\frac{R_{0R}}{{v_R}^2}-\frac{R_{0T}}{{v_T}^2}\right)\right|}{1+\frac{{v_T}^2\cdot R_{0R}}{{v_R}^2\cdot R_{0T}}} \tag{5.39}$$

We substitute (5.39) into (5.29) and get:

$$\frac{\left|\tau_{0T}-\tau_{0R}+\frac{f_\tau c}{2\left(f+f_0\right)}\cdot\left(\frac{R_{0R}}{{v_R}^2}-\frac{R_{0T}}{{v_T}^2}\right)\right|}{1+\frac{{v_T}^2\cdot R_{0R}}{{v_R}^2\cdot R_{0T}}} \ll \sqrt{2}\,\frac{R_{0T}}{v_T} \tag{5.40}$$

In the denominator of (5.40), we factor our $\frac{R_{0T}}{{v_T}^2}$ and obtain:

$$\frac{\left|\tau_{0T}-\tau_{0R}+\frac{f_\tau c}{2\left(f+f_0\right)}\cdot\left(\frac{R_{0R}}{{v_R}^2}-\frac{R_{0T}}{{v_T}^2}\right)\right|}{\frac{{v_T}^2}{R_{0T}}\cdot\left(\frac{R_{0R}}{{v_R}^2}+\frac{R_{0T}}{{v_T}^2}\right)} \ll \sqrt{2}\,\frac{R_{0T}}{v_T} \tag{5.41}$$

We multiply both sides of (5.41) with $\frac{{v_T}^2}{R_{0T}}$ and get:

$$\frac{\left|\tau_{0T}-\tau_{0R}+\frac{f_\tau c}{2\left(f+f_0\right)}\cdot\left(\frac{R_{0R}}{{v_R}^2}-\frac{R_{0T}}{{v_T}^2}\right)\right|}{\frac{R_{0R}}{{v_R}^2}+\frac{R_{0T}}{{v_T}^2}} \ll \sqrt{2}v_T \tag{5.42}$$

We can get similar inequality for the receiver:

$$\frac{\left|\tau_{0R}-\tau_{0T}+\frac{f_\tau c}{2\left(f+f_0\right)}\cdot\left(-\frac{R_{0R}}{{v_R}^2}+\frac{R_{0T}}{{v_T}^2}\right)\right|}{\frac{R_{0R}}{{v_R}^2}+\frac{R_{0T}}{{v_T}^2}} \ll \sqrt{2}v_R \tag{5.43}$$

Now we continue with the constraint given in (5.33). We divide both sides by $\left|\tilde{\tau}_T-\tau_{0T}\right|$ and get:

$$\left|\tilde{\tau}-\tilde{\tau}_T\right| \ll \frac{2{R_{0T}}^2}{3{v_T}^2\cdot\left|\tilde{\tau}_T-\tau_{0T}\right|}+\frac{2}{3}\left|\tilde{\tau}_T-\tau_{0T}\right| \tag{5.44}$$

On the right side of (5.44), we have the variable $\left|\tilde{\tau}_T-\tau_{0T}\right|$. This is the modulus of the azimuth time difference between the receiver's point of closet approach and PSP. This time difference can be determined from (3.107) as:

$$\left|\tilde{\tau}_T - \tau_{0T}\right| = \left|\frac{f_\tau c R_{0T}}{2v_T^2\left(f+f_0\right)}\right| = \frac{\left|f_\tau\right|\cdot c\cdot R_{0T}}{2v_T^2\cdot\left(f+f_0\right)} \tag{5.45}$$

Substituting (5.45) and (5.39) into (5.44), we obtain:

$$\frac{\left|\tau_{0T} - \tau_{0R} + \frac{f_\tau c}{2\left(f+f_0\right)}\cdot\left(\frac{R_{0R}}{{v_R}^2} - \frac{R_{0T}}{{v_T}^2}\right)\right|}{\frac{{v_T}^2}{R_{0T}}\cdot\left(\frac{R_{0R}}{{v_R}^2} + \frac{R_{0T}}{{v_T}^2}\right)} << \frac{2{R_{0T}}^2}{3{v_T}^2}\cdot\frac{2v_T^2\cdot\left(f+f_0\right)}{\left|f_\tau\right| c R_{0T}} + \frac{2}{3}\frac{\left|f_\tau\right| c R_{0T}}{2v_T^2\cdot\left(f+f_0\right)} \tag{5.46}$$

Now we multiply both side of (5.46) with $\frac{{v_T}^2}{R_{0T}}$ and get:

$$\frac{\left|\tau_{0T} - \tau_{0R} + \frac{f_\tau c}{2\left(f+f_0\right)}\cdot\left(\frac{R_{0R}}{{v_R}^2} - \frac{R_{0T}}{{v_T}^2}\right)\right|}{\frac{R_{0R}}{{v_R}^2} + \frac{R_{0T}}{{v_T}^2}} << \frac{4}{3}\frac{v_T^2\left(f+f_0\right)}{\left|f_\tau\right|\cdot c} + \frac{1}{3}\frac{\left|f_\tau\right| c}{\left(f+f_0\right)} \tag{5.47}$$

Because of the symmetry of transmitter and receiver sides, we have a similar inequality for the receiver:

$$\frac{\left|-\tau_{0T} + \tau_{0R} + \frac{f_\tau c}{2\left(f+f_0\right)}\cdot\left(-\frac{R_{0R}}{{v_R}^2} + \frac{R_{0T}}{{v_T}^2}\right)\right|}{\frac{R_{0R}}{{v_R}^2} + \frac{R_{0T}}{{v_T}^2}} << \frac{4}{3}\frac{v_R^2\cdot\left(f+f_0\right)}{\left|f_\tau\right|\cdot c} + \frac{1}{3}\frac{\left|f_\tau\right|\cdot c}{\left(f+f_0\right)} \tag{5.48}$$

In the left sides of inequalities (5.42), (5.47), we have same term. Therefore, the question naturally arises as to whether we can change these two constraints into one. To answer this question we should consider the ratio:

$$Ratio_T = \frac{\frac{4}{3}\frac{v_T^2\cdot\left(f+f_0\right)}{\left|f_\tau\right|\cdot c} + \frac{1}{3}\frac{\left|f_\tau\right|\cdot c}{\left(f+f_0\right)}}{\sqrt{2}v_T} \tag{5.49}$$

If the $Ratio_T$ always stays bigger or smaller than 1 for a given bistatic mission, then we can change the two inequalities (5.42) and (5.47) with one inequality. We have done research in this respect and found out that this is not a case. For example, we calculate $Ratio_T$ with the following parameters:

Table 5.1. Parameters for bistatic scenario

| **Parameter** | **Transmitter** |
|---|---|
| Speed of airplane $v_T$ | 98m/s |
| Frequency $f + f_0 \approx f_0$ | 1:10GHz |
| Doppler frequency range | 200:1200Hz |

The change of $Ratio_T$ with respect to Range and Doppler frequency is shown on the left side of Figure 5.1. Please note that $Ratio_T$ is bigger than 1 at some regions, and at some

regions is smaller than 1. It is better visible on the right side of Figure 5.1, where we have shown a cutout of the plot on the left for the range frequency 1GHz. We are therefore obliged to keep both constraints (5.42), (5.47) for the transmitter. It is obvious that that the same is valid for the receiver. In summary, we have two inequalities (5.42), (5.47) for the transmitter and two inequalities (5.43) and (5.48) for the receiver.

Now, to make it better visible, we divide all four inequalities (5.42), (5.47), (5.43), (5.48) with their individual right sides. Everywhere on the right side we get 1. Everywhere in the inequalities we will have $....<<1$. We have done many simulations and observed that $....<<1$ could be changed to $...<0.4$, forming a properly sufficient condition for bistatic constraints.

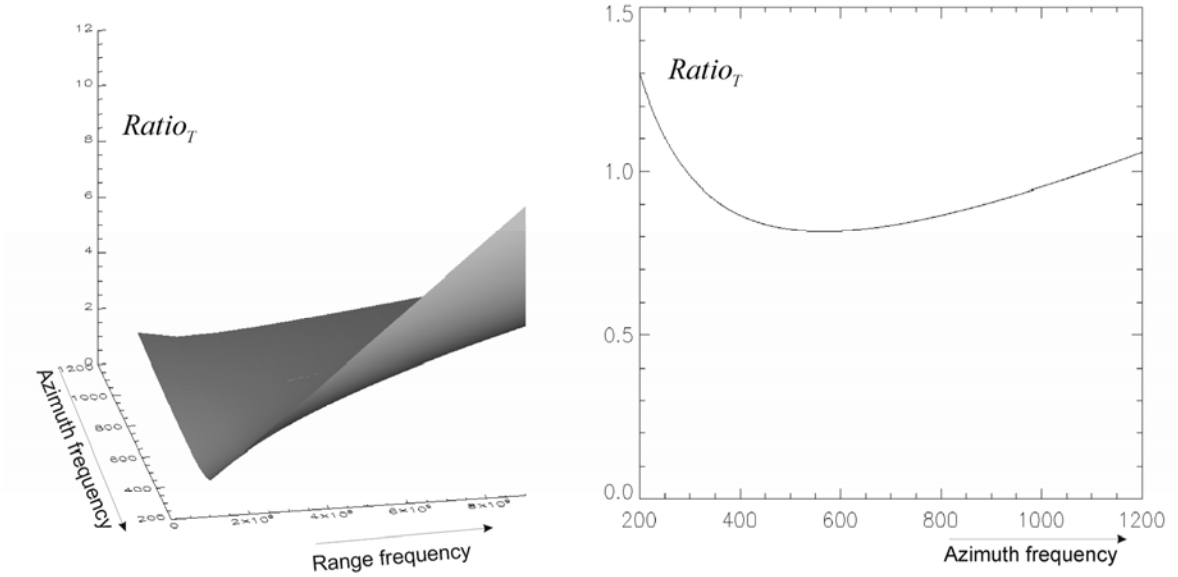


Figure 5.1, $Ratio_T$ with respect to Range and Doppler frequencies on the left plot; cutout of the plot on the left at the fixed range frequency 1GHz;

Summarizing, we collect all four constraints together:

$$L_{1T}=\frac{\left|\tau_{0T}-\tau_{0R}+\frac{f_\tau c}{2\left(f+f_0\right)}\cdot\left(\frac{R_{0R}}{v_R{}^2}-\frac{R_{0T}}{v_T{}^2}\right)\right|}{0.4\cdot\left(\frac{R_{0R}}{v_R{}^2}+\frac{R_{0T}}{v_T{}^2}\right)\cdot\left(\frac{4}{3}\frac{v_T^2\cdot\left(f+f_0\right)}{\left|f_\tau\right|\cdot c}+\frac{1}{3}\frac{\left|f_\tau\right|\cdot c}{\left(f+f_0\right)}\right)}<1$$

$$L_{1R}=\frac{\left|\tau_{0R}-\tau_{0R}+\frac{f_\tau c}{2\left(f+f_0\right)}\cdot\left(-\frac{R_{0R}}{v_R{}^2}+\frac{R_{0T}}{v_T{}^2}\right)\right|}{0.4\cdot\left(\frac{R_{0R}}{v_R{}^2}+\frac{R_{0T}}{v_T{}^2}\right)\cdot\left(\frac{4}{3}\frac{v_R^2\cdot\left(f+f_0\right)}{\left|f_\tau\right|\cdot c}+\frac{1}{3}\frac{\left|f_\tau\right|\cdot c}{\left(f+f_0\right)}\right)}<1 \qquad (5.50)$$

$$L_{2T}=\frac{\left|\tau_{0T}-\tau_{0R}+\frac{f_\tau c}{2\left(f+f_0\right)}\cdot\left(\frac{R_{0R}}{v_R{}^2}-\frac{R_{0T}}{v_T{}^2}\right)\right|}{0.4\cdot\sqrt{2}v_T\cdot\left(\frac{R_{0R}}{v_R{}^2}+\frac{R_{0T}}{v_T{}^2}\right)}<1$$

$$L_{2R} = \frac{\left| \tau_{0R} - \tau_{0T} + \frac{f_\tau c}{2\left(f + f_0\right)} \cdot \left( -\frac{R_{0R}}{{v_R}^2} + \frac{R_{0T}}{{v_T}^2} \right) \right|}{0.4 \cdot \sqrt{2} v_R \cdot \left( \frac{R_{0R}}{{v_R}^2} + \frac{R_{0T}}{{v_T}^2} \right)} < 1$$

$\tau_{0T} - \tau_{0R}$ is the azimuth time difference at the transmitter's and the receiver' points of closest approach. It was determined by using vectorial calculations and is given in (3.93). $f_\tau$ is the azimuth frequency, determining the azimuth frequency range. $f + f_0$ is the range frequency, determining the actual range frequency interval. In addition to the above constraints we have the velocities and slant ranges of the transmitter and the receiver. In order to process the bistatic raw data, we should carefully select the frequency bands, bistatic geometry and bistatic parameters.

## 5.5 Interpreting the Bistatic Constraints

For the validity of the bistatic point target reference spectrum (BPTRS), we have derived the four constraints given in (5.50). The constraints bind together the transmitter's and the receiver's velocities, their slant ranges and range and Doppler frequencies. Here we consider the result of these constraints using parameters used in conventional SAR missions.

First we consider the Tandem configuration. In the Tandem case, $R_{0R} = R_{0T} \cong R_0$ and $v_{0R} = v_{0T} \cong v_0$. The constraints given in (5.50) are further simplified:

$$\begin{aligned} L_{1T} = L_{1R} &= \frac{\left|\tau_{0T} - \tau_{0R}\right|}{\frac{2 \cdot 0.4 \cdot R_0}{v^2} \cdot \left( \frac{4}{3} \frac{v^2 \cdot \left(f + f_0\right)}{\left|f_\tau\right| \cdot c} + \frac{1}{3} \frac{\left|f_\tau\right| c}{\left(f + f_0\right)} \right)} < 1 \\ L_{2T} = L_{2R} &= \frac{\left|\tau_{0T} - \tau_{0R}\right|}{2 \cdot 0.4 \cdot \sqrt{2} \frac{R_0}{v}} < 1 \text{ where } \left|\tau_{0T} - \tau_{0R}\right| = \left|a_0\right| \end{aligned} \tag{5.51}$$

Now we evaluate above for airborne case with parameters given in Table 5.2.

Table 5.2. Parameters for airborne simulation

| **Parameter** | **Transmitter/Receiver** |
|---|---|
| Speed of airplane $v$ | 100m/s |
| Slant Range $R_0$ | 5000m |
| Carrier Frequency $f + f_0 \approx f_0$ | 1GHz |
| Doppler frequency range | -1200Hz : 1200Hz |

We have evaluated both constraints for the transmitter and the receiver and observed that for this particular case the constraint $L_{1T} = L_{1R}$ is stronger than $L_{2T} = L_{2R}$.

The dependency of $\left|\tau_{0T} - \tau_{0R}\right| = \left|a_0\right|$ with respect to $f_\tau$ is shown on the left side of Figure 5.2. We can observe that $\left|a_0\right|$ should be selected at less than 10s. In the Tandem case, the time separation of 10s corresponds to the baseline $d = \left|a_0\right| \cdot v = 10s * 100m/s = 1000m$. If the

carrier frequency increases, then the baseline calculated from the constraint becomes also bigger.

Now we consider spaceborne case with parameters given in Table 5.3.

Table 5.3. Parameters for spaceborne simulation

| **Parameter** | **Transmitter/Receiver** |
|---|---|
| Speed of satellite $v$ | 8000m/s |
| Slant Range $R_0$ | 200km |
| Carrier Frequency $f + f_0 \approx f_0$ | 1GHz |
| Doppler frequency range | -2200Hz : 2200Hz |

The results are shown in the right side of Figure 5.2. It is obvious that $|a_0|$ should be less than 100s. Time separation of 100s in a spaceborne Tandem case corresponds to the baseline $d = 100s * 8000m/s = 800km$.

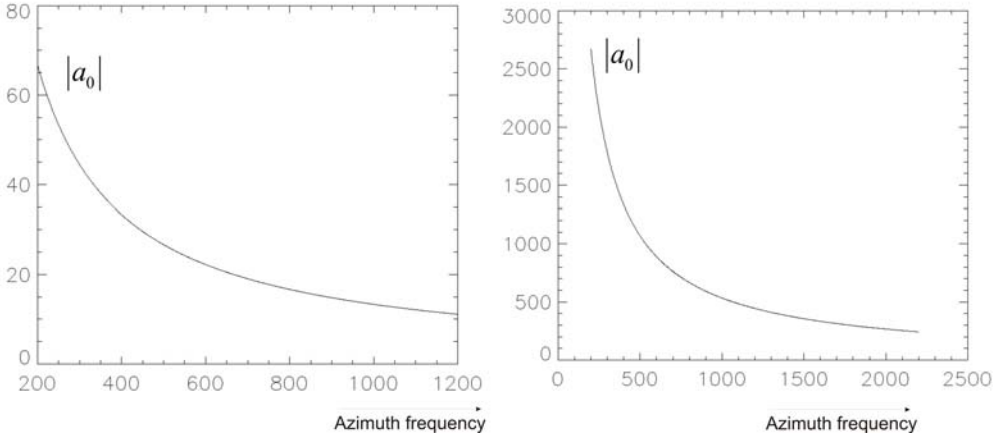


Figure 5.2. Tandem case $|\tau_{0T} - \tau_{0R}| = |a_0|$ with respect to $|f_\tau|$

## 5.6 Numerical Values of the Bistatic Constraints for Different Simulations

### 5.6.1 Translationally Invariant Case

Now we consider a particular airborne translationally invariant SAR configuration with parameters given in Table 5.4. We simulated this configuration using the parameters similar to the real bistatic experiment described in section 8.3.4.

The airplanes move with equal velocities on parallel tracks in a way such that $|\tau_{0T} - \tau_{0R}| = |a_0| = 0$. We simplify the bistatic constraints given in (5.50) and obtain:

$$L_{1T} = L_{1R} = \frac{\left| \frac{f_\tau c}{2(f+f_0)} \cdot (R_{0R} - R_{0T}) \right|}{0.4 \cdot (R_{0R} + R_{0T}) \cdot \left( \frac{4}{3} \frac{v^2 \cdot (f+f_0)}{|f_\tau| \cdot c} + \frac{1}{3} \frac{|f_\tau| \cdot c}{(f+f_0)} \right)} < 1 \qquad (5.52)$$

$$L_{2T} = L_{2R} = \frac{\left| \frac{f_\tau c}{2(f+f_0)} \cdot (R_{0R} - R_{0T}) \right|}{(R_{0R} + R_{0T}) \cdot \sqrt{2} \cdot 0.4v} < 1$$

Table 5.4. Parameters of airborne translationally invariant case

| Parameter | Transmitter | Receiver |
|---|---|---|
| Speed of airplanes | 110m/s | 110m/s |
| Pulse duration | 3.0μs | |
| Carrier Frequency | 10.13GHz | |
| Bandwidth | 100MHz | |
| Squint angle | 0° | 0° |
| Off Nadir angle | 55° | 57° |
| Opening angle in azimuth direction | 1.8° | 1.8° |
| Opening angle in elevation | 8° | 8° |
| PRF | 1250Hz | |
| Distance between airplanes (constant) | 1000m | |

Bistatic constraints given in (5.50) are strongly dependent on the Doppler bandwidth. Opposite to range frequency, azimuth frequency range depends on the particular bistatic geometry and on the position of the bistatic point target. In the general bistatic case, it is azimuth time variant. The derivation of the bistatic Doppler centroid and the Doppler bandwidth was performed in section 4.2 (derivations are based on the work given in [2]).

As mentioned above, $|\tau_{0T} - \tau_{0R}| = |a_0| = 0$. Additionally, because the squint angles of the transmitter and the receiver are zero, $\tau_{0R}$ coincides with the azimuth time at the center of the bistatic footprint $\tau_{cb}$. Therefore, using (4.16), we obtain:

$$\begin{aligned} B_{az}^{Bist} &= \tau_{az} \cdot \frac{f+f_0}{c} \cdot v^2 \cdot \left( \frac{1}{R_{0T}} + \frac{1}{R_{0R}} \right) \\ f_{\tau_{dc}}^{Bist} &= \frac{f+f_0}{c} \cdot \left[ 0 \cdot \left( \frac{v_T^{\,2}}{R_{0T}} + \frac{v_R^{\,2}}{R_{0R}} \right) + \frac{0 \cdot v_T^{\,2}}{R_{0T}} \right] = 0 \end{aligned} \tag{5.53}$$

We have generated the scene consisting of 5 point targets allocated in azimuth direction with distance separation of 100m. By calculating the Doppler bandwidths using (5.53) we obtain the results given in Table 5.5. We use the Doppler bandwidths given in Table 5.5 and evaluate the bistatic constraints given in (5.52) for each point target. On the left side of Figure 5.3 the parameter $L_{1T} = L_{1R}$ with respect to the estimated Doppler frequency range is shown for each point target. Both constraint parameters are much less than one.

Table 5.5. Doppler bandwidths for 5 point targets

| Point Target | Doppler Bandwidth |
|---|---|
| PT1 | 219.09Hz |
| PT2 | 219.34Hz |
| PT3 | 219.49Hz |
| PT4 | 219.74Hz |
| PT5 | 219.88Hz |

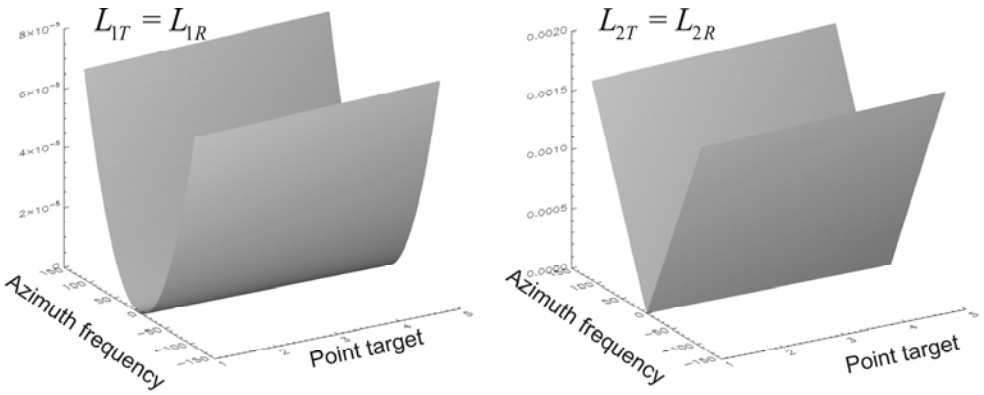


Figure 5.3. Bistatic constraints for translationally invariant case: left with have $L_{1T} = L_{1R}$ constraint parameter and $L_{2T} = L_{2R}$ on right side

The validity of the constraints is demonstrated by focusing the scene with BPTRS, matching it to different point targets.

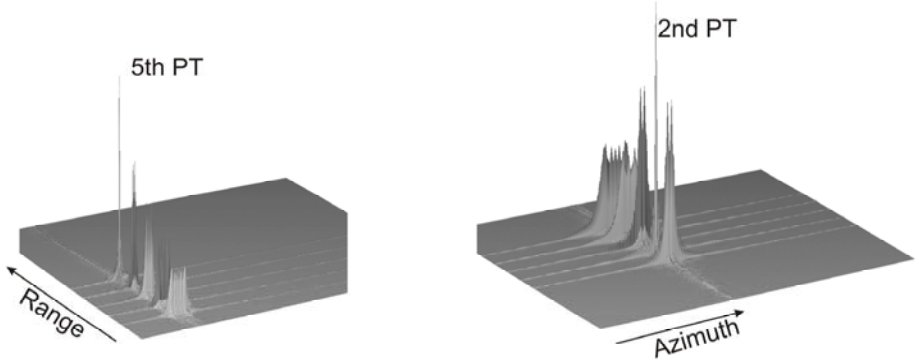


Figure 5.4. Focused scene with bistatic point target reference spectrum matched to 5th and 2nd point targets

The left side of Figure 5.4 shows the focusing result for the 5th point target, and on the right we have the result for the 2nd PT.

### 5.6.2 Hybrid Bistatic Experiment

In the next simulation we consider very extreme bistatic configuration. This is the hybrid bistatic experiment. It uses a satellite as the transmitter and an airplane as the receiver. It was described in detail in section 2.4.1. The parameters of this experiment are given in Table 5.6.

In this experiment, we have a big difference between the transmitter and the receiver velocities and the slant ranges. The velocity of the transmitter is 76 times bigger than for the receiver, and the altitudes differ by a magnitude of about 170. Because of these factors, we have a bistatic mission where the focusing is a big challenge. In the case of the hybrid mission, the complete integration time is 3s. The azimuth time difference $a_0 = \tau_{0T} - \tau_{0R}$,

constant in translationally invariant configurations, changes in this case very quickly along the azimuth direction.

Table 5.6. Parameters of hybrid bistatic experiment

| **Parameter** | **Transmitter** | **Receiver** |
|---|---|---|
| Speed | 7600m/s | 100m/s |
| Pulse duration | 3.0μs | |
| Carrier Frequency | 9.65GHz | |
| Bandwidth | 100MHz | |
| PRF | 2500Hz | |
| Altitude | 514km | ≈3000m |

If we fix the satellite and the airplane antenna steering angles constant, we will have a very small bistatic scene extension. To solve this problem, we propose using the azimuth variant angle steering for both transmitting and receiving antennas. The steering allows us to increase the bistatic scene in azimuth direction till 1200m.

We have generated the scene with 7x7 point targets with 200m separation in azimuth direction (parallel to the trajectories of the transmitter and the receiver) and 100m separation in range direction. This kind of allocation practically covers the almost whole bistatic swath.

We have generated the hybrid simulation and calculated different parameters used in bistatic constraints. Doppler frequencies and different bistatic parameters are shown in the following tables. Doppler centroids are given in Table 5.7 and Doppler bandwidths in Table 5.8. They were calculated using (4.16). Even though Doppler bandwidths are nearly the same, because of the big variation of the Doppler centroids, we have complete azimuth bandwidth close to 6KHz.

Table 5.7. Doppler centroids of 7x7 point targets

| | | | | | | |
|---|---|---|---|---|---|---|
| 2651.8 | 1668.5 | 685.3 | 0.0 | -610.0 | -1220.1 | -1830.1 |
| 2577.4 | 1621.7 | 666.1 | 0.7 | -592.2 | -1185.9 | -1778.8 |
| 2511.1 | 1580.4 | 649.0 | 0.7 | -577.9 | -1155.8 | -1734.4 |
| 2451.3 | 1542.3 | 634.1 | 0.7 | -564.1 | -1129.7 | -1694.5 |
| 2395.7 | 1508.2 | 620.6 | 0.7 | -552.3 | -1105.5 | -1658.6 |
| 2344.4 | 1476.4 | 608.5 | 0.7 | -541.2 | -1083.1 | -1625.8 |
| 2296.4 | 1446.3 | 597.0 | 1.4 | -531.3 | -1063.5 | -1595.6 |

Table 5.8. Doppler bandwidths of 7x7 point targets

| | | | | | | |
|---|---|---|---|---|---|---|
| 768.4 | 762.5 | 761.0 | 761.7 | 767.7 | 775.8 | 788.4 |
| 758.0 | 757.2 | 758.7 | 764.6 | 773.5 | 786.0 | 802.3 |
| 749.8 | 752.0 | 757.2 | 766.8 | 779.3 | 794.8 | 813.3 |
| 742.5 | 747.6 | 756.5 | 768.3 | 783.8 | 802.2 | 824.3 |
| 735.9 | 744.0 | 755.1 | 769.8 | 788.2 | 808.8 | 833.2 |
| 729.4 | 741.2 | 754.4 | 771.3 | 791.2 | 814.8 | 840.5 |
| 725.1 | 738.3 | 753.8 | 772.9 | 794.2 | 820.0 | 847.9 |

Table 5.9. $a_0$ - parameters of 7x7 point targets

| | | | | | | |
|---|---|---|---|---|---|---|
| -2.8 | -0.8 | 1.1 | 0.0 | -1.9 | -3.9 | -5.9 |
| -2.8 | -0.8 | 1.1 | 0.0 | -1.9 | -3.9 | -5.9 |
| -2.8 | -0.8 | 1.1 | 0.0 | -1.9 | -3.9 | -5.9 |
| -2.8 | -0.8 | 1.1 | 0.0 | -1.9 | -3.9 | -5.9 |
| -2.8 | -0.8 | 1.1 | 0.0 | -1.9 | -3.9 | -5.9 |
| -2.8 | -0.8 | 1.1 | 0.0 | -1.9 | -3.9 | -5.9 |
| -2.8 | -0.8 | 1.1 | 0.0 | -1.9 | -3.9 | -5.9 |

Table 5.10. $a_2$ - bistatic parameters of 7x7 point targets

| | | | | | | |
|---|---|---|---|---|---|---|
| 188.0 | 188.0 | 188.0 | 188.0 | 188.0 | 188.0 | 188.0 |
| 182.8 | 182.8 | 182.8 | 182.8 | 182.8 | 182.8 | 182.8 |
| 177.8 | 177.8 | 177.8 | 177.8 | 177.8 | 177.8 | 177.8 |
| 173.1 | 173.1 | 173.1 | 173.1 | 173.1 | 173.1 | 173.1 |
| 168.6 | 168.6 | 168.6 | 168.6 | 168.6 | 168.6 | 168.6 |
| 164.4 | 164.4 | 164.4 | 164.4 | 164.4 | 164.4 | 164.4 |
| 160.3 | 160.3 | 160.3 | 160.3 | 160.3 | 160.3 | 160.3 |

Table 5.11. $R_{0R}$ - receiver slant ranges of 7x7 point targets

| | | | | | | |
|---|---|---|---|---|---|---|
| 3450.0 | 3450.0 | 3450.0 | 3450.0 | 3450.0 | 3450.0 | 3450.0 |
| 3550.0 | 3550.0 | 3550.0 | 3550.0 | 3550.0 | 3550.0 | 3550.0 |
| 3650.0 | 3650.0 | 3650.0 | 3650.0 | 3650.0 | 3650.0 | 3650.0 |
| 3750.0 | 3750.0 | 3750.0 | 3750.0 | 3750.0 | 3750.0 | 3750.0 |
| 3850.0 | 3850.0 | 3850.0 | 3850.0 | 3850.0 | 3850.0 | 3850.0 |
| 3950.0 | 3950.0 | 3950.0 | 3950.0 | 3950.0 | 3950.0 | 3950.0 |
| 4050.0 | 4050.0 | 4050.0 | 4050.0 | 4050.0 | 4050.0 | 4050.0 |

Table 5.12. $R_{0T}$ - transmitter slant ranges of 7x7 point targets

| | | | | | | |
|---|---|---|---|---|---|---|
| 648911.02 | 648911.02 | 648911.02 | 648911.02 | 648911.02 | 648911.02 | 648911.02 |
| 649029.67 | 649029.67 | 649029.67 | 649029.67 | 649029.67 | 649029.67 | 649029.67 |
| 649140.22 | 649140.22 | 649140.22 | 649140.22 | 649140.22 | 649140.22 | 649140.22 |
| 649244.64 | 649244.64 | 649244.64 | 649244.64 | 649244.64 | 649244.64 | 649244.64 |
| 649344.22 | 649344.22 | 649344.22 | 649344.22 | 649344.22 | 649344.22 | 649344.22 |
| 649439.90 | 649439.90 | 649439.90 | 649439.90 | 649439.90 | 649439.90 | 649439.90 |
| 649532.34 | 649532.34 | 649532.34 | 649532.34 | 649532.34 | 649532.34 | 649532.34 |

Bistatic parameters $a_0$ and $a_2$ are given in Table 5.9 and Table 5.10 correspondingly. The transmitter and the receiver slant ranges at the point of closest approach are given in Table 5.11 and Table 5.12.

Now we calculate the bistatic constraints according to (5.50). The transmitter constraint $L_{1T}$ for the point targets 7x7 (totally 49) is shown in Figure 5.5 on axis ‘Z’.

On the ‘X’ axis, the numerical value of each row is depicted. It changes from 0 to 6, which corresponds to the first 1-7 rows. Different columns are shown on different plots of Figure 5.5. Because of space, we have plotted only 1-6 columns. On the ‘Y’ axis, the Doppler frequency is given. For point targets located in the same column, the Doppler frequency does not change too much. However, during a move from one column to another, the azimuth frequency bandwidth has a big variation. The change of the Doppler frequency for columns and rows is shown in Figure 5.6.

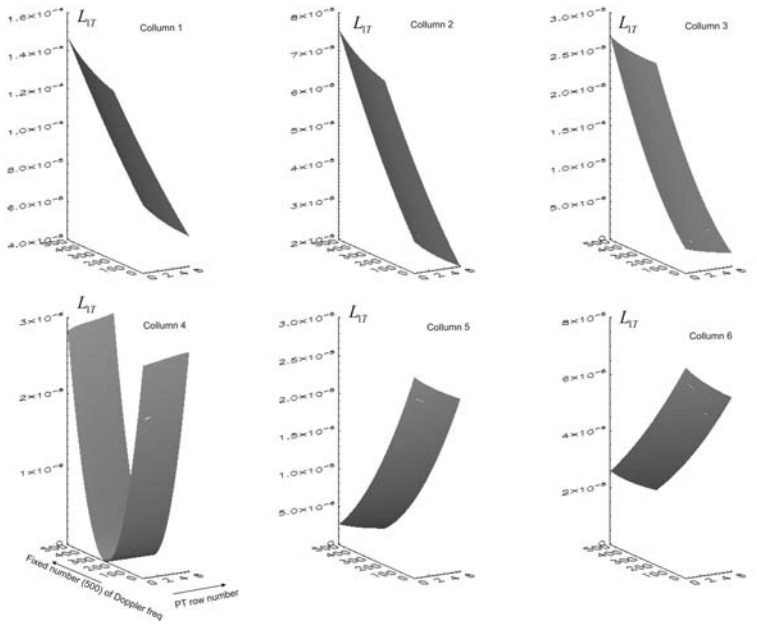


Figure 5.5. $L_{1T}$ bistatic constraint parameter of 7x6 point targets

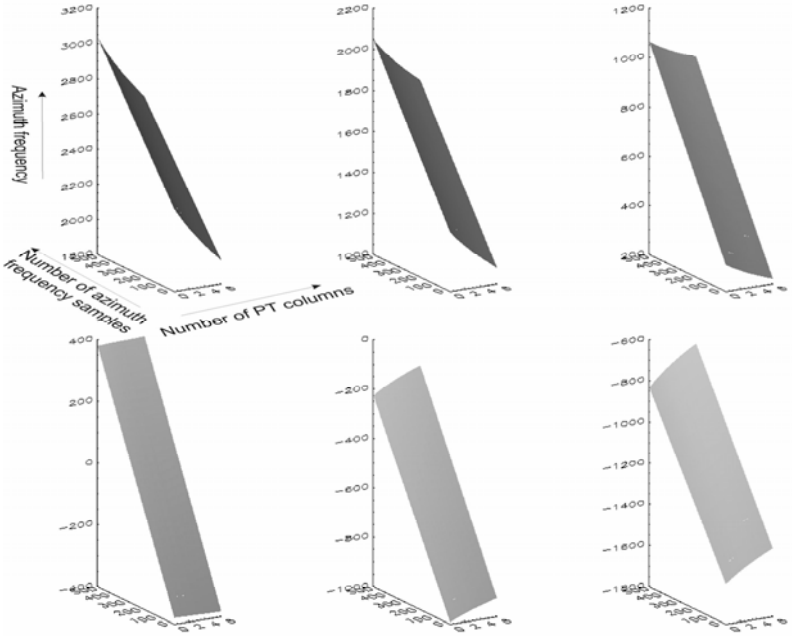


Figure 5.6. Real Doppler frequency range of 7x6 point targets

In Figure 5.5, we observe that the values of $L_{1T}$ are much smaller than 1. So, this particular bistatic constraint holds. Next we calculate the $L_{2T}$ parameter, shown in Figure 5.7. We can observe that the values of $L_{2T}$ also do not violate the bistatic constraints, because they are less than one.

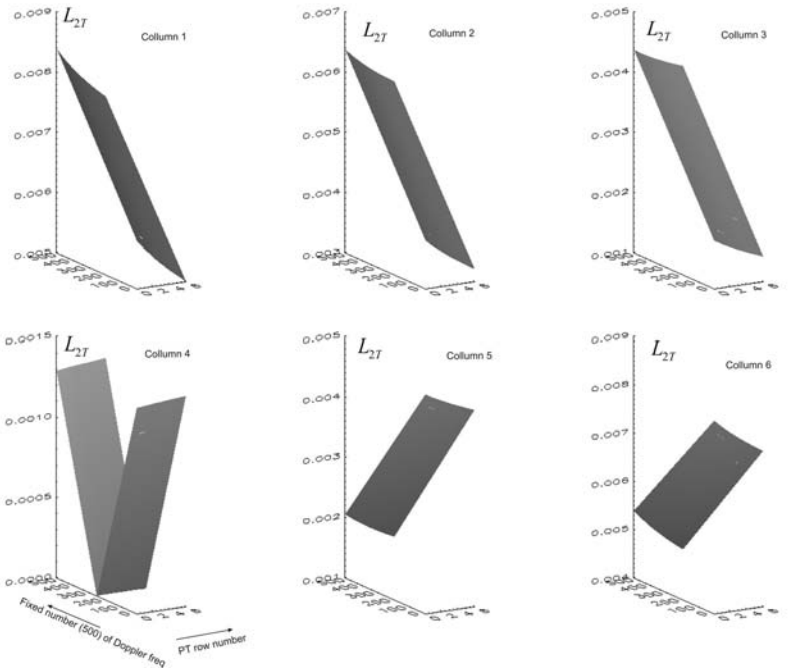


Figure 5.7. $L_{2T}$ bistatic constraint parameter for 7x6 point targets

We now perform the calculations for the receiver. The values of the $L_{1R}$ and $L_{2R}$ parameters are shown respectively in Figure 5.8 and in Figure 5.9.

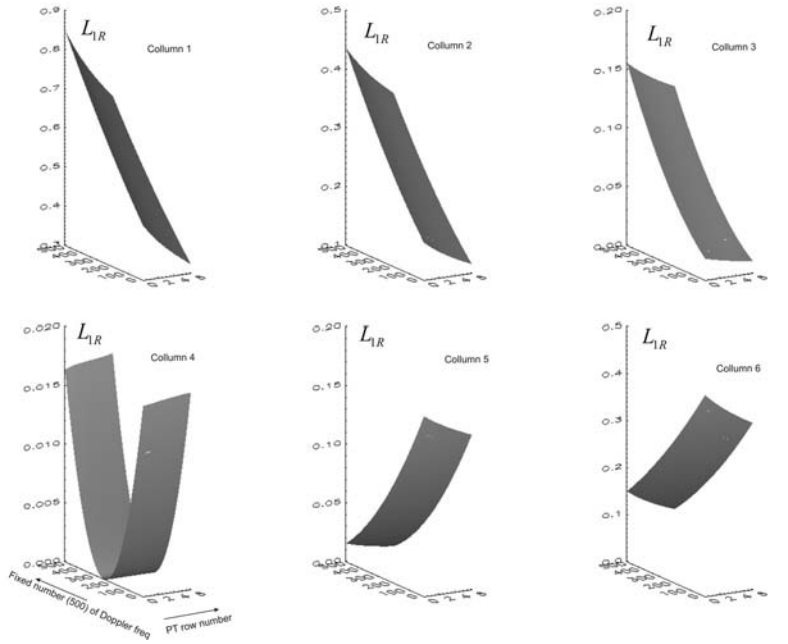


Figure 5.8. $L_{1R}$ bistatic constraint parameter of 7x6 point targets

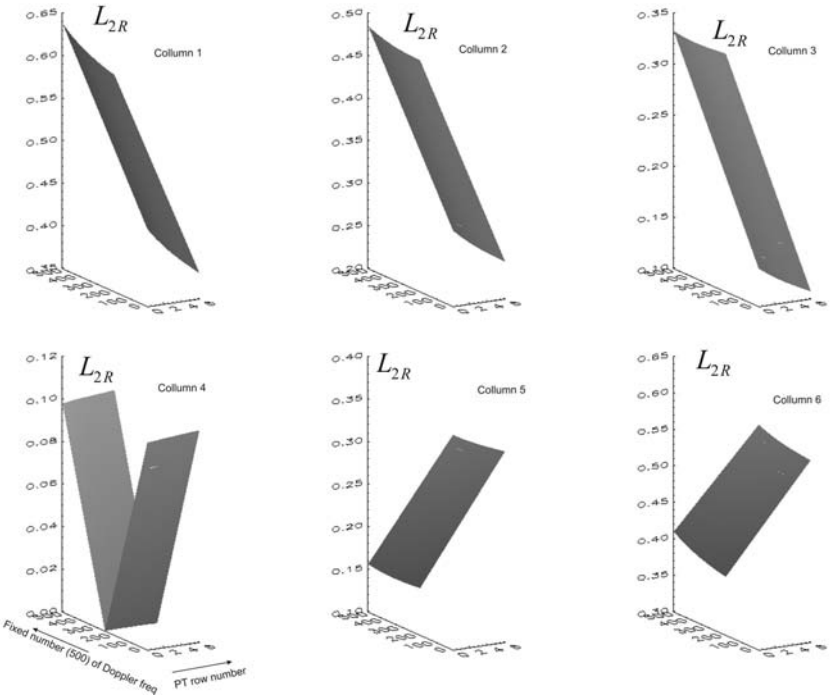


Figure 5.9. $L_{2R}$ bistatic constraint parameter of 7x6 point targets

The parameters $L_{1R}$ and $L_{2R}$ for some point targets are bigger than 1, which breaks our bistatic constraints. As mentioned in the beginning, our bistatic constraints are sufficient, but not necessary, conditions. Therefore, we cannot claim that the bistatic point target reference spectrum fails for the hybrid case. In the scope of this thesis we could not perfectly focus the simulated scene for a hybrid mission using the BPTRS. Work in this area is going on.

# 6 Checking the Validity of the Bistatic Point Target Reference Spectrum by Simulations

We derived the bistatic point target reference spectrum (BPTRS) in chapter 3. The Method of the Stationary Phase (MSP) was applied for the derivation, a necessary step in order to transform the point target response from azimuth time to the Fourier domain. This method is thoroughly explained in Appendix A. MSP itself is an approximation, and we additionally expanded the bistatic phase terms in second order Taylor expansion. These approximations limit the validity of the point target reference spectrum. In chapter 4 we gave the constraints of validity for the BPTRS. In total, we have derived three constraints: two separate constraints for the transmitter and for the receiver parameters, and one additional constraint binding the transmitter's and the receiver's slant ranges and velocities.

The best way of verifying the suitability of the BPTRS is by showing the focusing results, which we will do in this chapter, using simulated bistatic raw data.

## 6.1 Checking the Validity for Single Point Target

The bistatic simulator was implemented in IDL[1]. We can use different parameters (typical for bistatic configurations) in the simulator: trajectories of the remote sensors, their velocities, positions of the point targets and the steering angles of the transmitter and the receiver beams. Any type of signal can be selected as the transmitted signal. In SAR, a linear frequency-modulated signal (chirp signal) is normally used. With the simulation we generate the bistatic raw data for different configurations. In addition, all parameters (such as slant ranges, values of the parameters $a_0, a_2$ given in (3.93) and necessary for our bistatic approach, etc.) are determined from the simulator. The simulation principle realized by the IDL program is shown in Figure 6.2.

The trajectories of the transmitter and the receiver are assumed here to be straight lines. It is also possible for the simulator to generate arbitrary trajectories.

In the first approximation, the footprints are quadrilaterals[2]. The vertexes of the footprints are determined by calculating the offset with the half of the opening angles in the range and azimuth direction. The beam center direction is determined with the squint and the off-nadir angles.

We follow the conventional definition of squint and off-nadir angle. The definitions can be visualized by taking the transmitter's movement as an example. Supposing a situation where the remote sensor (in this case, the transmitter) moves across a straight line with a constant velocity vector $\vec{v}_T$ (as shown in Figure 6.1), the coordinates of the point target are described with the receiver's coordinates $R_{0R,}\tau_{0R}$. The line A-PT is parallel to the sensor's trajectory crossing the point target. Point B is the instantaneous position of the sensor, and O is the projection of the point B onto the illuminated scene. The line A-B is perpendicular to the trajectory of the sensor. The resulting angle O-B-A is called the off-nadir angle and is denoted with $\beta$, and the angle A-B-PT is called the squint angle and is denoted with $\Psi$.

[1] Interactive Data Language

[2] In geometry, a **quadrilateral** is a polygon with four sides and four vertices

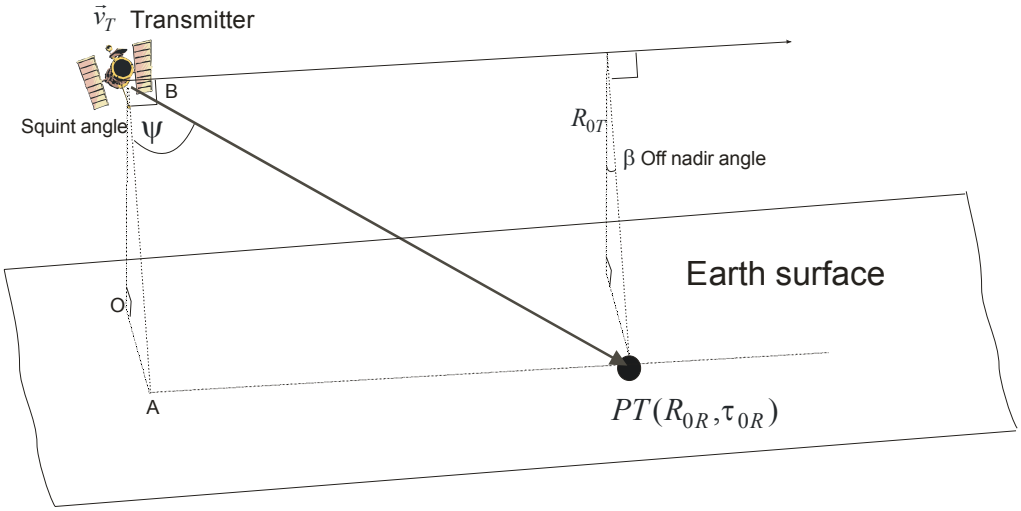


Figure 6.1. Geometry of the sensor's illumination

The simulation principle realized by the bistatic simulator is shown in Figure 6.2. The footprint of the transmitter is given in green, and that of the receiver is in red. The intersection of all footprints gives the common bistatic footprint. For each time instant, we determine whether or not the point target is within the common bistatic footprint. For this purpose, we measure the common azimuth window (the time when the PT is seen transmitting and receiving sensor).

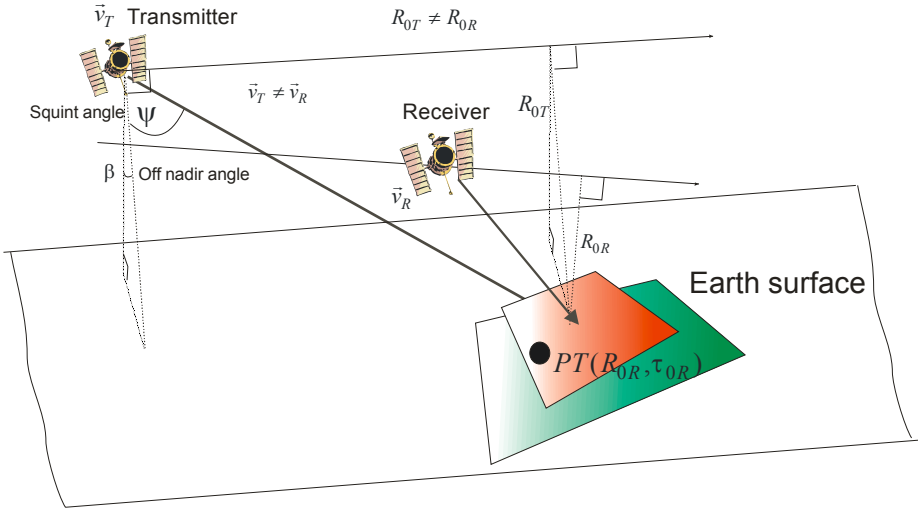


Figure 6.2. Simulation Principle

At each time instant we determine whether the PT is inside the common bistatic footprint. We check if the PT is within the footprint of the transmitter and the receiver simultaneously. This is done using vectors. The footprint of the transmitter with the PT inside is given in Figure 6.3. For the vectors $\vec{A}$ and $\vec{B}$, the inner product is defined as:

$$\vec{A} \cdot \vec{B} = \left|\vec{A}\right| \cdot \left|\vec{B}\right| \cdot \cos\beta \tag{6.1}$$

where $\beta$ is the angle between these two vectors. The quadrilateral footprints are just an approximation of the real footprint, which are of more or less elliptical shape. We have

selected this representation only for simplicity in order to generate the correct steering of the beam. Because the quadrilaterals are approximations of the real footprint, we can assume that all four angles are smaller than 180° ($0 \le \beta < 180°$). If we then take two vectors that coincide with two neighboring sides, the angle between them can be uniquely determined from (6.1). First we check whether the PT is within the angle 2-1-4. This is done by calculating the angles 2-1-PT and PT-1-4 and comparing them with 2-1-4. The angles are calculated by determining the corresponding vectors and by using (6.1). If both the 2-1-PT and PT-1-4 angles are smaller than 2-1-4, then PT is inside the 2-1-4 angle. Similarly, we check to see if the PT is inside the angle 1-2-3 at the same time; if this is the case, we conclude that the PT is inside the quadrilateral 1-2-3-4.

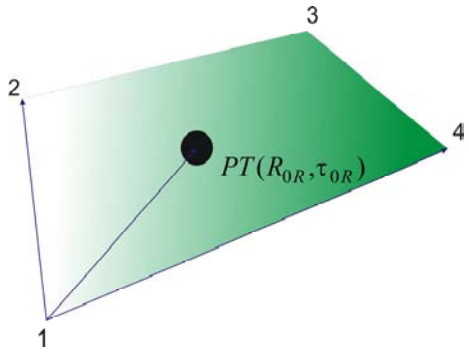


Figure 6.3. Point target inside of the transmitter's footprint

For each time instant we check whether the PT is inside of the transmitter and the receiver footprints. We also calculate the instantaneous positions of the transmitting and receiving sensors and determine their slant ranges. The sum of the transmitter's and the receiver's slant ranges corresponds to the signal travel time necessary to cover the path from transmitter-point to target-receiver. Then, the azimuth time variant delay is calculated as:

$$t_0\left(\tau, R_{0R}, \tau_{0R}\right) = \frac{R_R + R_T}{c} \tag{6.2}$$

Finally, we determine the bistatic point target response for a single PT by means of:

$$g_l\left(t, \tau, R_{0R}, \tau_{0R}\right) = \sigma\left(R_{0R}, \tau_{0R}\right) \cdot w\left(\tau - \tau_{cb}\right) \cdot s_l\left(t - t_0\left(\tau, R_{0R}, \tau_{0R}\right)\right) \cdot e^{-j2\pi f_0 \cdot t_0\left(\tau, R_{0R}, \tau_{0R}\right)} \tag{6.3}$$

- $t$ is the range time, $\tau$ is the azimuth time.
- $R_{0R}, \tau_{0R}$ are the receiver coordinates.
- $\sigma\left(R_{0R}, \tau_{0R}\right)$ is the backscattering coefficient, which is assumed to be real.
- $w\left(\tau - \tau_{cb}\right)$ is the common bistatic azimuth time window.
- $s_l$ is the transmitted chirp signal in the low-pass domain.
- $f_0$ is the carrier frequency.
- $t_0\left(\tau, R_{0R}, \tau_{0R}\right)$ is the complete bistatic time delay including both delay times: from the transmitter to the PT and from PT to the receiver. It depends on the location of PT and on the azimuth time.
- $\tau_{cb}$ is the bistatic azimuth window center. We know the footprints of the transmitter and the receiver. We therefore determine the start and end time of their intersection.

We later distribute groups of PTs at different locations in the scene. We determine their individual responses and add them together. In this way we obtain the raw SAR data of the complete scene.

### 6.1.1 Airborne Case

We demonstrate the functionality of the bistatic simulator by one particular simulation, an airborne bistatic experiment with parameters given on Table 6.1:

Table 6.1. Parameters of the airborne simulation

| **Parameter** | **Transmitter** | **Receiver** |
|---|---|---|
| Speed of airplanes | 98 m/s | 98 m/s |
| Pulse duration | 3 μs | |
| Carrier Frequency | 10.17 GHz | |
| Bandwidth | 20 MHz | |
| PRF | 1250 Hz | |
| Squint angle | 0° | 0° |
| Off Nadir angle | 42° | 52° |
| Opening angle in azimuth direction | 6° | 6° |
| Opening angle in elevation | 12° | 12° |
| Max distance between airplanes | 1029 m | |
| Min distance between airplanes | 1000 m | |
| Distance of closest approach | 3893 m | 4603 m |

The transmitter and the receiver move with equal velocities, but their tracks are not parallel. The fact that the tracks are not parallel is obvious from Table 6.1, since the distance between the transmitter and the receiver changes during flight time.

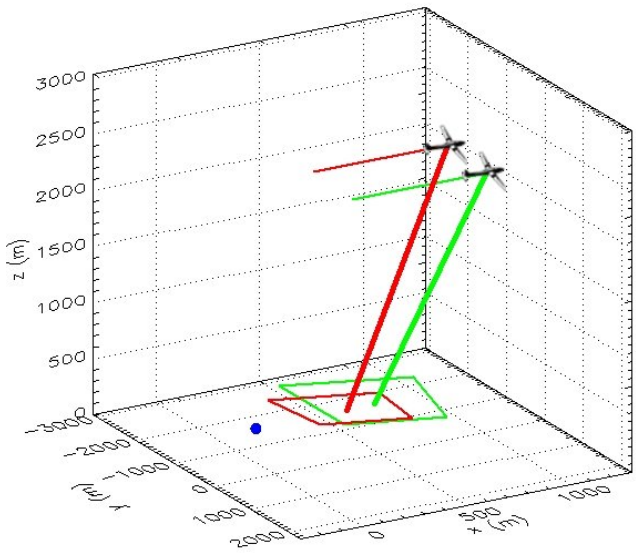


Figure 6.4. 3D view of the airborne simulation

Figure 6.4 shows the 3D view of the simulation. The transmitter's path and its footprint are given in green, and the receiver's path and its footprint are in red. The point target is indicated in blue. We check whether the PT is simultaneously within the footprints of the transmitter and the receiver. In this way we find the common bistatic window that

determines the azimuth bandwidth. As a first test, SAR raw data set corresponding to a single PT was simulated and focused by means of the BPTRS. Since in this case we are talking only about a single PT, the focusing can be understood as correlation of the raw data with the bistatic point target response. The correlation is implemented by FFT techniques. We transform the raw data for the single PT into the Fourier domain. The real parts of the response and the spectrum for the simulated PT are displayed in Figure 6.5:

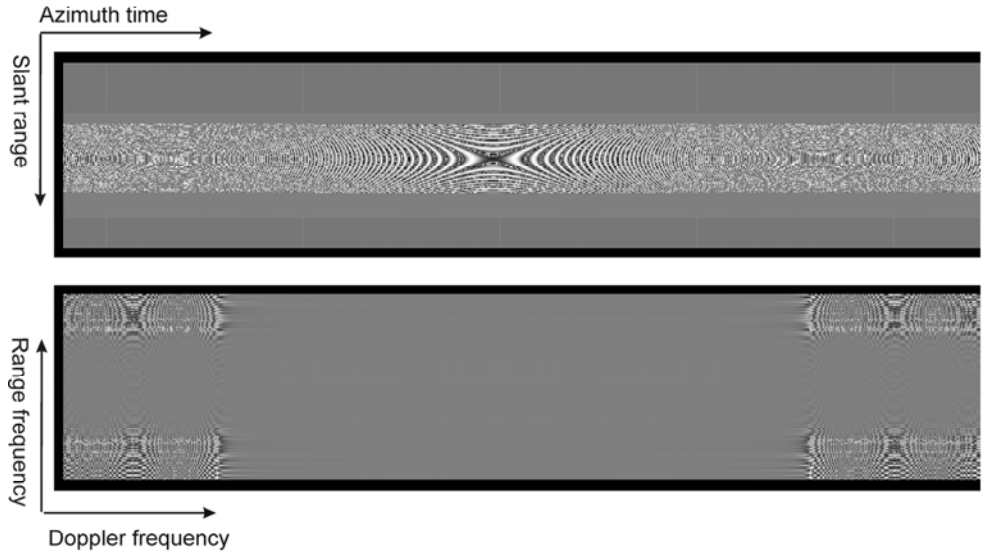


Figure 6.5. Time domain response (top) and the spectrum (bottom) of the single point target

The point target reference spectrum is generated with the expression given in (3.136). We then multiply the spectrum corresponding to the raw data by the complex conjugate of the BPTRS. The result is back-transformed to the time domain, and we obtain the focused result for the single PT.

Initially, to be sure that our simulation is running correctly, we only compared two different spectra: one generated by the expression of the BPTRS, and another corresponding to the raw data.

In Figure 6.6, we can see the absolute values of the spectrum generated by a single PT corresponding to the raw data (lower plot) and to the point target reference spectrum (upper plot). Both results are given in the range frequency direction, and the cut of the 2D spectrum was taken at the zero Doppler frequency. The results are very similar, since they have the same frequency range and are equivalent to the bandwidth given in Table 6.1.

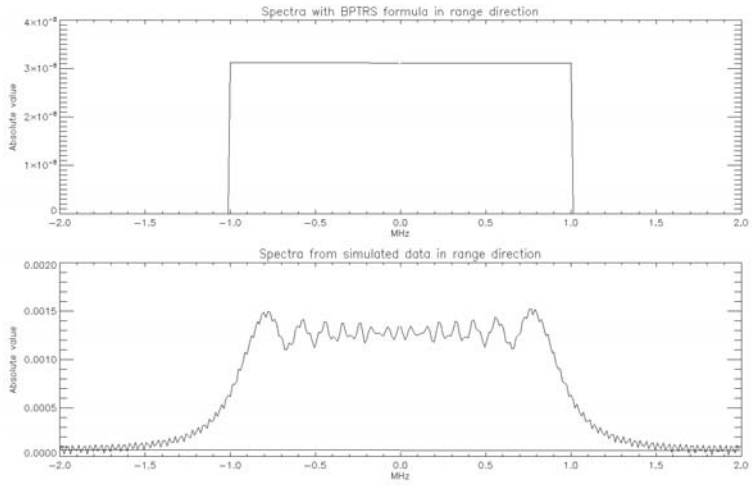


Figure 6.6. Comparison of the range spectra – upper plot: generated by the point target reference spectrum; lower plot: created by the raw data

A similar cut of the 2D spectrum was made in the azimuth direction. This case is always more interesting, because we often have in the azimuth direction an offset corresponding to a Doppler centroid.

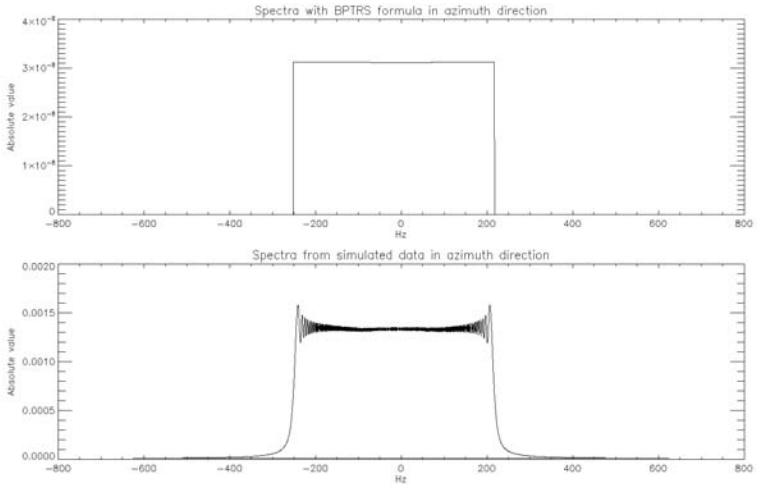


Figure 6.7. Comparison of the Doppler spectra – upper plot: generated by the bistatic point target reference spectrum; lower plot: created from the raw data

Figure 6.7 represents the absolute value of the spectrum generated from the BPTRS (lower plot) and the spectrum created using our bistatic formula (upper plot). We observe that both plots show the same bandwidth in the azimuth direction and have the same small negative frequency offset (bistatic Doppler centroid).

In Figure 6.8 we show the focusing result for a single PT. The left column is the focusing result obtained with the BPTRS. /A/ shows a closer look, and /B/ is the result for the complete scene. For comparison, we also tried to focus the raw data with the monostatic point target reference spectrum given in (6.4):

$$G_l^{MO}\left(f,f_\tau,R_0,\tau_0\right)=S_l\left(f\right)\cdot\sigma\left(R_0,\tau_0\right)\cdot rect\left(\frac{f-f_c}{B_{az}}\right)\cdot\sqrt{\frac{cR_0}{2}}\cdot\frac{1}{v}\cdot$$
$$\cdot\frac{f+f_0}{\left[\left(f+f_0\right)^2-\frac{f_\tau^2c^2}{4v^2}\right]^{\frac{3}{4}}}\cdot e^{-j\pi/4}\cdot e^{-j2\pi f_\tau\tau_0}\cdot e^{-j\pi\frac{R_0}{c}\sqrt{\left(f+f_0\right)^2-\frac{f_\tau^2c^2}{4v^2}}} \tag{6.4}$$

The symbols have the following meanings:

- $f_c$ is the monostatic Doppler centroid frequency.
- $B_{az}$ is the monostatic Doppler bandwidth.
- $R\left(\tau_c\right)$ is the slant range at the footprint center.
- $f_0$ is the carrier frequency.
- $v$ is the sensor velocity in the monostatic case.

The result is shown on the right column of the same image. /C/ presents a closer view of the focusing result with the monostatic point target reference spectrum, and /D/ is the result of the complete scene. By means of the bistatic formula, we have a clearly focused result, whereas when we apply the monostatic formula we get a result blurred both in range and azimuth directions.

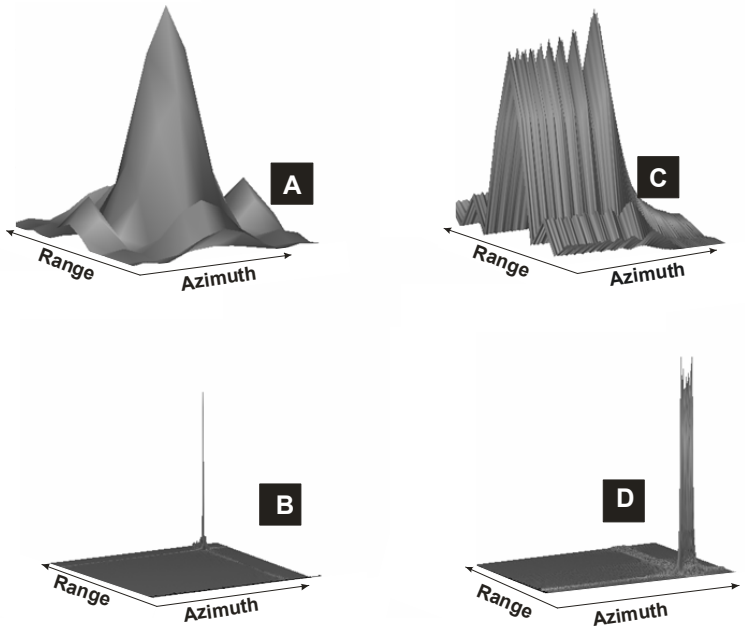


Figure 6.8. Left side: focusing with the bistatic formula, magnitude of the focusing result - /A/: a closer look and /B/: the complete scene; right: focusing with the monostatic formula – /C/: a closer look and /D/: the complete scene

### 6.1.2 Spaceborne Case

Next, we perform a spaceborne experiment. The satellites move at different velocities, and their tracks are not parallel. Table 6.2 shows the parameters of the simulation:

Table 6.2. Parameters of the spaceborne bistatic simulation

| **Parameter** | **Transmitter** | **Receiver** |
|---|---|---|
| Speed of Satellites | 7300 m/s | 7500 m/s |
| Pulse Duration | 37.1 us | |
| Carrier Frequency | 5.5 GHz | |
| Bandwidth | 3 MHz | |
| PRF | 7300 Hz | |
| Squint Angle | 0.3° | 0.3° |
| Off Nadir | 45° | 45° |
| Opening angle in azimuth direction | 1° | 1° |
| Opening angle in elevation | 5° | 5° |
| Max Distance between Satellites | 3080 m | |
| Min Distance between Satellites | 3000m | |
| Distance of Closest Approach | 284 km | 286 km |

The distance between satellites is changing, so we are dealing with a typical general case (the definition is given in section 2.3). The top part of Figure 6.9 shows the real part of the point target response; the bottom part displays the real part of the spectrum. We can observe a considerable Doppler shift, corresponding to the squint angles of the satellites:

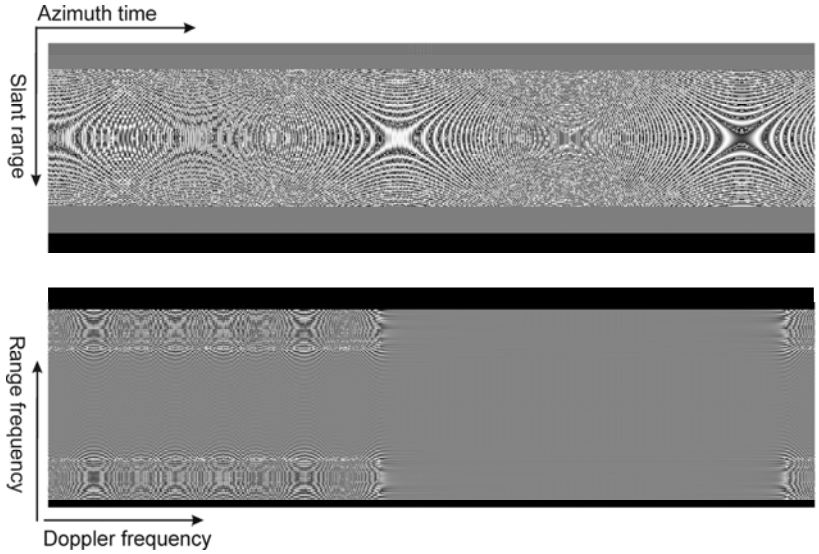


Figure 6.9. Real part of the response (top) and real part of the spectrum (bottom)

As in the airborne case, we have compared the spectral components for the signals generated from the BPTRS with those created directly from the simulated raw data. Figure 6.10 shows the result of this comparison. The upper plot shows the spectrum generated from the BPTRS, and the lower plot shows the spectra corresponding to the simulated data. Both plots are in the range frequency direction. The observable bandwidth of the signal is around 3MHz, which corresponds to the bandwidth given in Table 6.2.

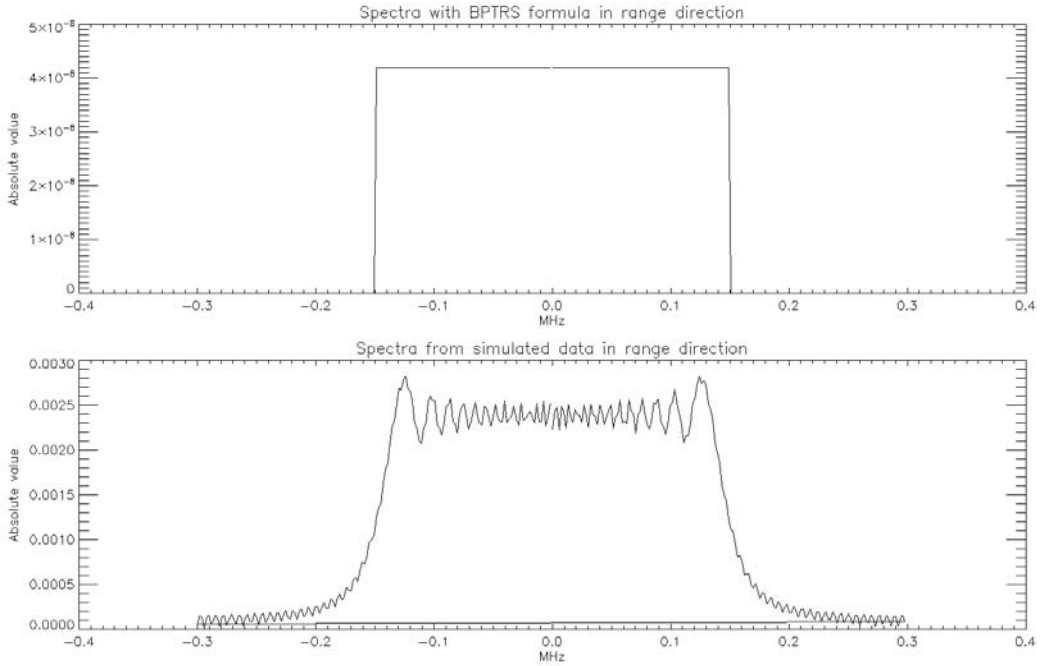


Figure 6.10. Comparison of the range spectra – upper plot: generated by the point target reference spectrum; lower plot: created from the raw data

The same kind of comparison is done in the Doppler frequency direction. The results are shown in Figure 6.11. The upper plot shows the absolute value of the spectrum obtained from the BPTRS, and the lower plot shows the spectrum created from the simulated raw data. The results are very similar, and they are in agreement with the parameters of the simulation. We have obtained a Doppler frequency offset of around 1000 Hz, which corresponds to the satellite's squint angle of 0.3°. The azimuth bandwidth is around 2500 Hz.

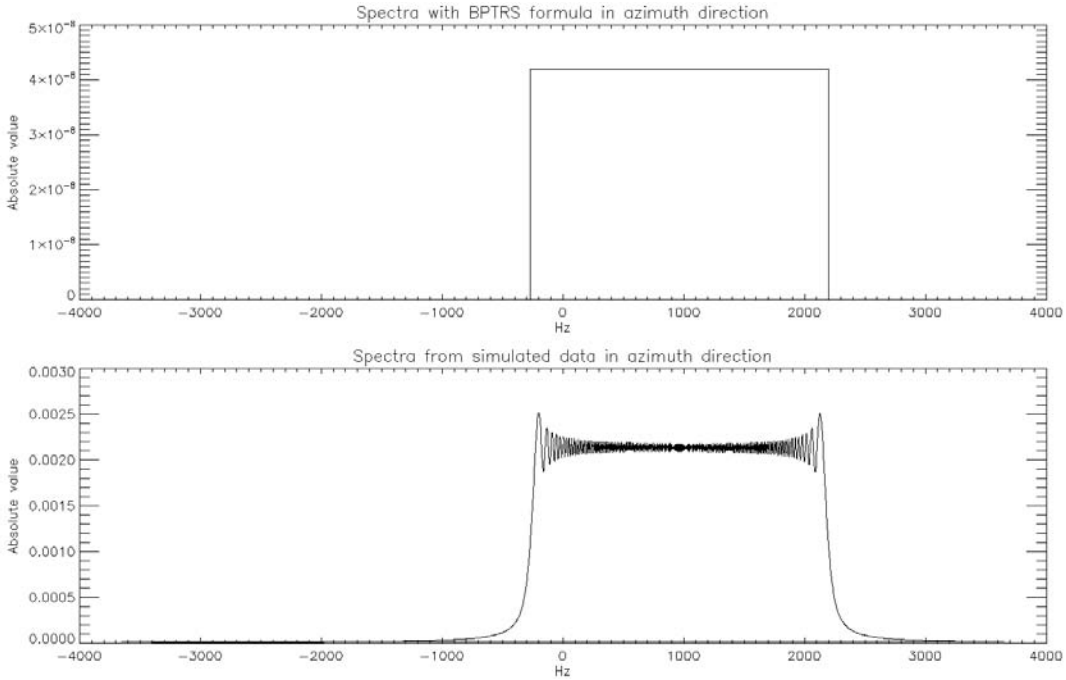


Figure 6.11. Comparison of the Doppler spectra – upper plot: generated by the bistatic point target reference spectrum; lower plot: created from the raw data

In Figure 6.12, we visualize the results of the focusing of a single PT, but this time for the spaceborne case. /A/ gives a closer look and /B/ the complete scene. Processing results using the monostatic formula are shown on /C/ and /D/, where /C/ is a closer look and /D/ is the complete scene. Various configurations were considered, all of them showing extremely well-focused results.

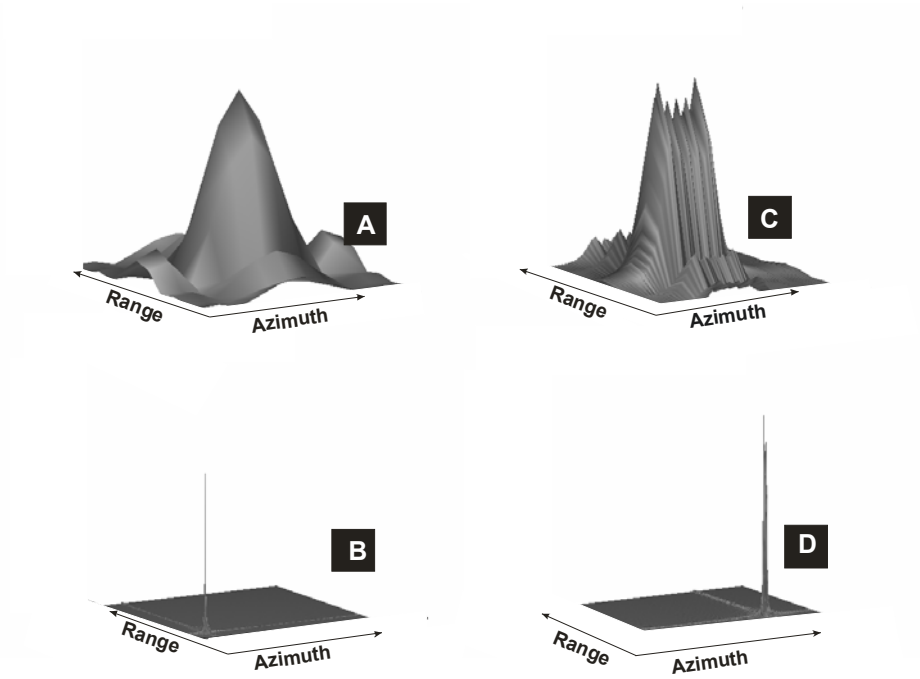


Figure 6.12. Focusing with the bistatic formula – /A/ close look and /B/ complete scene; focusing with monostatic formula – /C/ close look and /D/ complete scene

## 6.2 Focusing Groups of Point Targets with the Bistatic Point Target Reference Spectrum

It is not possible to apply the bistatic point target reference spectrum (BPTRS) directly to focus the complete scene, as was done for a single point target. In principle, the range migration curve is different for the different PTs, and therefore the focusing should be done by taking into account the individual location of each PT. But in some configurations (for example in Tandem and translationally invariant configurations) the PTs across the line parallel to the azimuth direction will experience the constant range hyperbolas and can be focused with the same reference function.

### 6.2.1 Point Targets along the Azimuth Direction

As a start, we consider the translationally invariant case (airplanes flying on parallel trajectories with equal velocities). On the illuminated area, four PTs in azimuth direction are located parallel to the flight path, and the separation between them is 100 m.

Figure 6.13 shows the location of the target point, the receiver's and the transmitter's trajectories and their footprints on the ground plane:

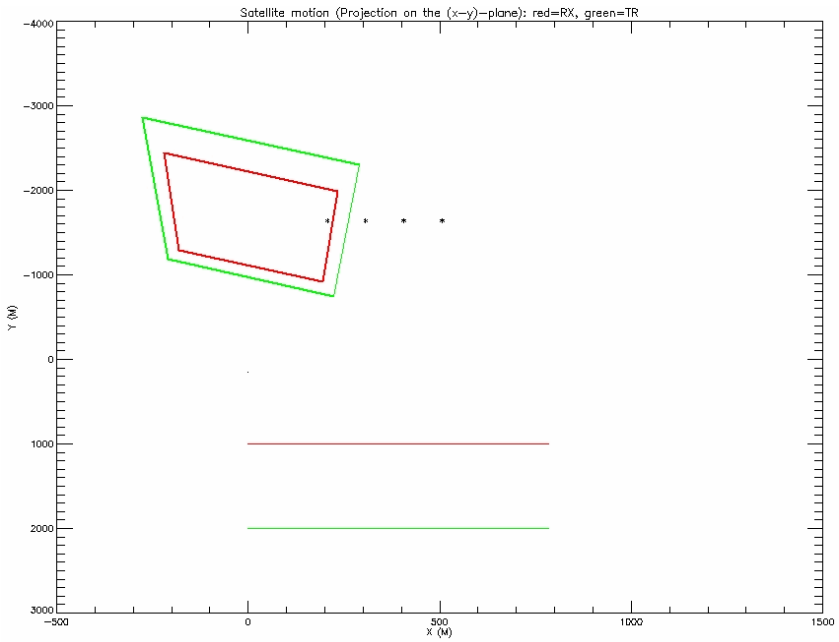


Figure 6.13. Translationally invariant case, PTs are located across the azimuth direction

This is an airborne experiment, the parameters for are shown in Table 6.3.

Table 6.3. Parameters of the translationally invariant configuration, airborne case

| **Parameter** | **Transmitter** | **Receiver** |
|---|---|---|
| Speed of Satellites | 98 m/s | 98 m/s |
| Pulse Duration | 3 us | |
| Carrier Frequency | 10.17 GHz | |
| Bandwidth | 20 MHz | |
| PRF | 1250 Hz | |
| Squint Angle | 90° | 90° |
| Off Nadir Angle | 52° | 42° |
| Opening angle in azimuth direction | 6° | 6° |
| Opening angle in elevation | 12° | 12° |
| Distance of Closest Approach | 4599 m | 3893 m |
| a0 | 0 s | |
| a2 | 1.18 | |

The SAR raw data were generated by simulation. The bistatic reference function is azimuth time invariant, and it is the same for all four PTs since the slant ranges of these PTs are identical. So, instead of applying the complete focusing approach, we focus all PTs in the same way as it was done for a single PT. The raw data spectrum is multiplied with the complex conjugate of the first PT spectrum; this is another way to check the reference function's validity concerning distributed targets in the azimuth direction. It should be noted that verifying the reference function's validity has a crucial importance, since it will be the basis for the development of the processing algorithms for complete scenes in the next chapters.

Figure 6.14 shows the focusing results. /A/ and /B/ are the result obtained with the bistatic reference function, /A/ showing the complete scene and /B/ presenting a closer look. For comparison, we have done the processing with the monostatic reference function, shown as /C/ and /D/. /C/ is the complete scene and /D/ shows the corresponding closer look. For the simulation above, we measured the distances between the PTs and got a value of 100 m, which corresponds with the reality. We may thus note that the approach has not only focused the PTs correctly, but that it also locates the focusing results in the correct positions.

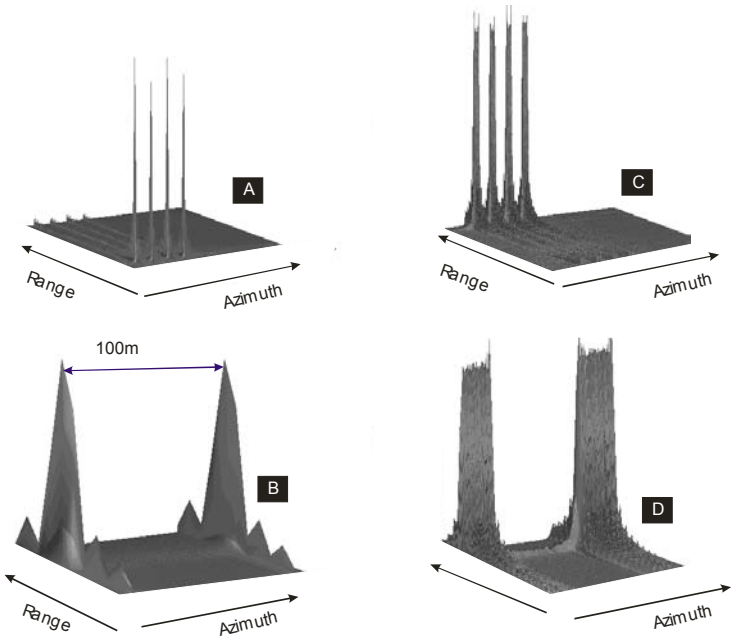


Figure 6.14. Focusing with the bistatic reference function – /A/ complete scene, /B/ closer look for only two point targets; Focusing with the monostatic reference function – /C/ complete scene, /D/ close look only for two point targets

## 6.2.2 Point Targets Distributed in the Range Direction

The next test will have the same airborne parameters given in 6.2.1, but in this case, the point targets are deployed in range direction with a separation of 100m. Of course now the PTs, because of their different location, have different reference functions (due to the different range curvatures); hence, we cannot expect the focusing with one reference function to be successful. It will be interesting to see how the focusing quality will be degraded by the mismatch of the reference function:

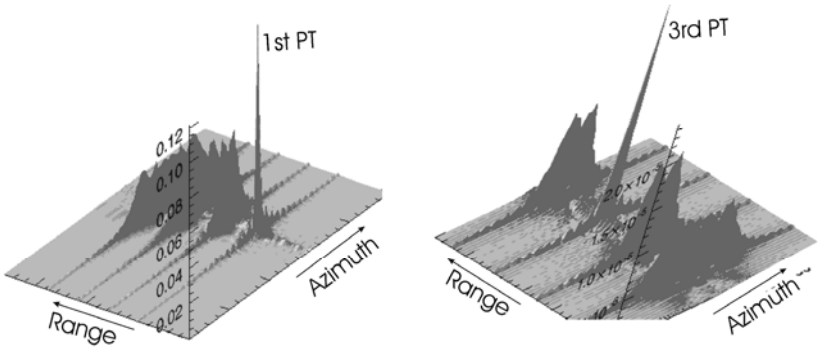


Figure 6.15. Focusing with BPTRS tuned to 1st PT (left) and to 3rd PT (right)

First, we performed the focusing by multiplying the complex spectrum with the complex conjugate of the bistatic reference spectrum tuned to the first PT. The result is shown on the left side of Figure 6.15: 1st PT is correctly focused, but other PTs are defocused, which is to be expected. For each focused PT, we have calculated the location of the range line. We observed that all range lines correspond to the location of PTs. The reference function range is then adjusted to the 3rd PT, and the focusing is carried out again. This result is shown on the right side of Figure 6.15. The reference function is still valid and works properly if it is tuned to the correct reference range. Nevertheless, it is obvious that the focusing of complete scenes implies dealing with the range dependent value of the reference function.

# 7 Extension to Focusing of Complete Scenes

Until now we have mainly considered the focusing of individual point targets (PT) and groups of spatially separated PTs. The validity of the bistatic reference function was demonstrated by means of simulated raw data. We saw that, by using the bistatic reference function tuned to a given range, we can focus all PTs at that range, while all other PTs with different ranges are defocused.

Now we extend the focusing ability from a single and a group of PTs to the focusing of complete scenes.

## 7.1 Monostatic Focusing Approach

Our bistatic processor will use the modules from the monostatic processor. Therefore we first explain the steps of monostatic approach developed at ZESS [3],[4].

In the last two decades, algorithms in the frequency domain have become quite popular. The reason is that they only use forward and backward FFTs and chirp multiplications, thus avoiding any interpolation. These features increase the processing efficiency and quality. Our monostatic processor based on the Inverse Scaling (IS) FFT is one of the kind of algorithms mentioned above, first developed in [3]. The Inverse Scaling processor will be considered in more detail later.

## 7.2 Monostatic Point Target Reference Spectrum

In the monostatic case, the transmitter and the receiver are located on the same moving platform. The received backscattered signal is described with a range-dependent delay:

$$t_v\left(\tau, R_0, \tau_0\right) = \frac{2R\left(\tau, R_0, \tau_0\right)}{c} \tag{7.1}$$

$R_0$ is the slant range at the point of closest approach, and $\tau_0$ is the azimuth time when this point is reached.

The received signal is:

$$g_l\left(t, \tau, R_0, \tau_0\right) = \sigma\left(R_0, \tau_0\right) \cdot w\left(\tau - \tau_c\right) \cdot s_l\left(t - t_v\left(\tau, R_0, \tau_0\right)\right) e^{-j2\pi f_0 \cdot t_v\left(\tau, R_0, \tau_0\right)} \tag{7.2}$$

For determining the backscattering coefficient spectrum, we need to take the Fourier transform twice for both fast and slow time variables:

$$G_l\left(f, f_\tau, R_0, \tau_0\right) = \mathbb{F}_t \mathbb{F}_\tau \left\{ g_l\left(t, \tau, R_0, \tau_0\right) \right\} \tag{7.3}$$

The expression above works to solve the double integral:

$$G_l\left(f, f_\tau, R_0, \tau_0\right) = \int_{-\infty}^{\infty} \int_{-\infty}^{\infty} \sigma\left(R_0, \tau_0\right) \cdot w\left(\tau - \tau_c\right) \cdot s_l\left(t - t_v\left(\tau, R_0, \tau_0\right)\right) \cdot e^{-j2\pi f_0 \cdot t_v\left(\tau, R_0, \tau_0\right)} \cdot e^{-j2\pi f t} \cdot e^{-j2\pi f_\tau \tau} dt d\tau \tag{7.4}$$

After solving the integral, the 2D point target reference spectrum of the received signal scattered at the location $\left(R_0, \tau_0\right)$ is obtained. In [4] it was shown that this spectrum is given by:

$$G_l^{MO}\left(f,f_\tau,R_0,\tau_0\right)=\sigma\left(R_0,\tau_0\right)\cdot S_l\left(f\right)\cdot rect\left(\frac{f-f_c}{B_{az}}\right)\cdot\sqrt{\frac{cR_0}{2}}\cdot\frac{1}{v}\cdot$$
$$\cdot\frac{f+f_0}{\left(\left(f+f_0\right)^2-\frac{f_\tau^2c^2}{4v^2}\right)^{\frac{3}{4}}}\cdot e^{-j\pi/4}\cdot e^{-j2\pi f_\tau\tau_0}\cdot e^{-j\pi\frac{R_0}{c}\sqrt{\left(f+f_0\right)^2-\frac{f_\tau^2c^2}{4v^2}}} \tag{7.5}$$

- $f_c$ is the monostatic Doppler centroid frequency.
- $B_{az}$ is the monostatic Doppler bandwidth.
- $R_0$ is the slant range at the point of closest approach.
- $f_0$ is the carrier frequency.
- $v$ is the sensor velocity.

The detailed derivation of this formula is given in [24].

If the locations of the transmitting and the receiving sensors coincide, then the bistatic configuration converges to a monostatic constellation. Indeed, it was shown in section 3.9 that the monostatic reference spectrum is a special case of the bistatic point target reference spectrum.

## 7.3 Spectrum of the Complete Scene

The expression (7.5) indicates the monostatic point target reference spectrum.

The backscattering coefficient for the whole scene can be represented as the convolution of the scene brightness distribution with the Dirac function. as follows:

$$\sigma\left(R,\tau\right)=\sigma\left(R_0,\tau_0\right)**\delta\left(R,\tau\right)=\int_{-\infty}^{\infty}\int_{-\infty}^{\infty}\sigma\left(R_0,\tau_0\right)\cdot\delta\left(R-R_0,\tau-\tau_0\right)dR_0d\tau_0 \tag{7.6}$$

The point target (PT) located at $\left(R_0,\tau_0\right)$ and having a backscattering coefficient of $\sigma\left(R_0,\tau_0\right)\cdot\delta\left(R-R_0,\tau-\tau_0\right)$ produces the reference spectrum $G_l^{MO}\left(f,f_\tau,R_0,\tau_0\right)$ given in (7.5). Hence the backscattering coefficient for the whole scene $\sigma\left(R,\tau\right)$ will have the following correspondence:

$$\sigma\left(R,\tau\right)\rightarrow SAR\,scene\rightarrow\int_{-\infty}^{\infty}\int_{-\infty}^{\infty}G_l^{MO}\left(f,f_\tau,R_0,\tau_0\right)dR_0d\tau_0 \tag{7.7}$$

To determine the spectrum of the complete scene, the monostatic point target reference spectrum must be integrated over all point targets illuminated by the antenna:

$$W\left(f,f_\tau\right)=\iint G_l^{MO}\left(f,f_\tau,R_0,\tau_0\right)dR_0d\tau_0 \tag{7.8}$$

We do the range compression, assuming that $S_l(f)\cdot S_l^*(f)=rect\left(\frac{f}{B_r}\right)$ and compensate the amplitude term. The integral above is converted to:

$$W'(f,f_\tau)=rect\left(\frac{f}{B_r}\right)\cdot\int\int\sqrt{R_0}\cdot\sigma(R_0,\tau_0)\cdot e^{-j2\pi f_\tau\tau_0}e^{-j\pi\frac{R_0}{c}\sqrt{(f+f_0)^2-\frac{f_\tau^2c^2}{4v^2}}}dR_0d\tau_0 \tag{7.9}$$

The integration over $\tau_0$ is equivalent to the Fourier transform, which is straightforward for this variable.

The slant range is substituted by the minimum distance plus the extension:

$$R_0=R_{0(\min)}+r \tag{7.10}$$

In addition, we approximate in inner amplitude factor $\sqrt{R_0}\approx\sqrt{R_{0(\min)}}$. This can be done because the change of the slant range compared to the slant range itself is very small. After the substitution in the integral, we obtain:

$$\begin{aligned}W'(f,f_\tau)=&\sqrt{R_{0(\min)}}e^{-j\pi\frac{R_{0(\min)}}{c}\sqrt{(f+f_0)^2-\frac{f_\tau^2c^2}{4v^2}}}\cdot rect\left(\frac{f}{B_r}\right)\cdot\\&\cdot\int\int\sigma\left(R_{0(\min)}+r,f_\tau\right)e^{-j\pi\frac{r}{c}\sqrt{(f+f_0)^2-\frac{f_\tau^2c^2}{4v^2}}}dr\end{aligned} \tag{7.11}$$

Here we introduce the notation:

$$f_r(f,f_\tau)=\frac{2}{c}\sqrt{(f+f_0)^2-\frac{f_\tau^2c^2}{4v^2}} \tag{7.12}$$

This shorthand notation is inserted into (7.11), and we get:

$$\begin{aligned}W'(f,f_\tau)=&\sqrt{R_{0(\min)}}e^{-j2\pi R_{0(\min)}\cdot f_r(f,f_\tau)}\cdot rect\left(\frac{f}{B_r}\right)\cdot\\&\cdot\int\int\sigma\left(R_{0(\min)}+r,f_\tau\right)e^{-j2\pi rf_r(f,f_\tau)}dr\end{aligned} \tag{7.13}$$

The integral given in (7.13) is a Fourier integral. Using the shifting property of the Fourier transformation, we obtain:

$$\begin{aligned}W'(f,f_\tau)&=\sqrt{R_{0(\min)}}\cdot e^{-j2\pi R_{0(\min)}f_r(f,f_\tau)}\cdot\sigma(f_r(f,f_\tau),f_\tau)\cdot e^{j2\pi R_{0(\min)}\cdot f_r(f,f_\tau)}\cdot rect\left(\frac{f}{B_r}\right)\\&=\sqrt{R_{0(\min)}}\cdot\sigma(f_r(f,f_\tau),f_\tau)\cdot rect\left(\frac{f}{B_r}\right)\\&=\sqrt{R_{0(\min)}}\cdot\sigma\left(\frac{2}{c}\sqrt{(f+f_0)^2-\frac{f_\tau^2c^2}{4v^2}},f_\tau\right)\cdot rect\left(\frac{f}{B_r}\right)\end{aligned} \tag{7.14}$$

The result is meaningful as follows: the complete spectrum contains the spectrum of the backscattering coefficient, but this backscattering spectrum is not the one we are looking for. It is a scaled replica of the backscattering spectrum, where the scaling of the range frequency is given in terms of square root expression in (7.12).

## 7.4 First Compression Transfer Function

Here we introduce the first compression function. It contains the complex conjugate of the chirp signal spectrum and the inverted amplitude term. Therefore, it performs the range compression and the amplitude term compensation.

$$H_1\left(f, f_\tau, R_0, \tau_0\right) = S_l\left(f\right)^* \cdot \frac{\left(\left(f+f_0\right)^2 - \frac{f_\tau^2 c^2}{4v^2}\right)^{\frac{3}{4}}}{f+f_0} \cdot e^{-j\pi/4} \cdot v \cdot \sqrt{\frac{2}{c}} \cdot \sqrt{R_{0(\min)}} \tag{7.15}$$

After applying this transfer function to the raw data spectrum (7.8), we have:

$$\begin{aligned} W'\left(f, f_\tau\right) &= W\left(f, f_\tau\right) \cdot H_1\left(f, f_\tau, R_m\right) \\ &= \sigma\left(f_r\left(f, f_\tau\right), f_\tau\right) \cdot rect\left(\frac{f_\tau - f_c}{B_{az}}\right) \cdot rect\left(\frac{f}{B_r}\right) \end{aligned} \tag{7.16}$$

The result given in (7.16) is very important. We multiply the spectrum of the raw data with $H_1\left(f, f_\tau, R_0, \tau_0\right)$, and the resulting spectrum is the scaled replica of the backscattering coefficient spectrum. Our aim is to compensate this scaling and to determine the backscattering coefficient $\sigma\left(R_0, \tau_0\right)$ for the whole scene. At a first look we could think that this task is very trivial, and that we would only need to perform the backtransformation of $\sigma\left(f_r\left(f, f_\tau\right), f_\tau\right)$ into the time domain.

The problem is that $\sigma\left(f_r\left(f, f_\tau\right), f_\tau\right) = \sigma\left(\frac{2}{c}\sqrt{\left(f+f_0\right)^2 - \frac{f_\tau^2 c^2}{4v^2}}, f_\tau\right)$ is a backscattering spectrum containing nonlinear range frequency scaling. The next step will be, then, the azimuth compression in order to return to the normal range frequency.

## 7.5 Statement of the Nonlinear Frequency Scaling Problem

The spectrum of a point target depends directly on its position. Thus the compression function for each point target (PT) is different. A PT located at a distance $R_{01}$ has to be compressed with a different transfer function than one located at a distance $R_{02}$. If we do focusing of the complete scene with the same transfer function, then only the PTs located at the correct distance will be focused correctly; all other PTs will be blurred at different levels. The received signal in SAR is the superposition of infinitely many PTs within the antenna footprint. Each PT of the SAR scene has its own slant range at the point of closest approach $R_0$ and thus creates a location-dependant contribution in the 2D total spectrum. To compress the SAR scene correctly, it is necessary to take care of each PT individually. However, this care should be done with an analytical solution.

In section 7.4, we showed that after the first transfer function $H_1(f, f_\tau, R_0, \tau_0)$, we got the spectrum of the backscattering coefficient $\sigma\left(f_r(f, f_\tau), f_\tau\right)$, which is still scaled in range frequency direction. The aim is to cancel the scaling and obtain the backscattering coefficient spectrum $\sigma(f, f_\tau)$. The problem is the type of scaling we experience here. Range frequency depends *nonlinearly* on range and azimuth frequencies:

$$\sigma(f_r, f_\tau) = \sigma\left(\frac{2}{c}\sqrt{(f+f_0)^2 - \frac{f_\tau^2 c^2}{4v^2}}, f_\tau\right) \tag{7.17}$$

## 7.6 Scaled Spectrum

First we consider the trivial case in which we have the scaling of the spectrum with a constant scaling factor.

Let's consider the scaled spectrum $G(f)$, which is the scaled version of the $S(f)$ spectrum:

$$G(f) = S(a \cdot f) \tag{7.18}$$

The backtransformation is implemented by a Fourier integral:

$$g(f) = \int_{-\infty}^{\infty} S(a \cdot f) e^{j2\pi f \cdot t} df \tag{7.19}$$

Here we introduce the substitution $f' = a \cdot f$, and we get:

$$g(f) = \frac{1}{a} \cdot \int_{-\infty}^{\infty} S(f') \cdot e^{j2\pi f' \cdot \frac{t}{a}} df = \frac{1}{a} \cdot s\left(\frac{t}{a}\right) \tag{7.20}$$

This means that the signal corresponding to the scaled spectrum is an inversely scaled time signal. In monostatic SAR processing (discussed above), we have to compensate the frequency scaling so that we obtain the signal in the time domain without any scaling. Papoulis proposed a method to solve the scaling problem [34]. His algorithm uses chirp multiplications and forward and inverse Fourier transformations. The result of the algorithm is a scaling compensated spectrum. Rather than removing the scaling and then transforming back from frequency to space domain, we will develop a direct approach, where the scaling is removed as a part of back transformation.

We reconsider the result of (7.19), but now multiply the scaled spectrum by a factor of $e^{j2\pi afi}$ instead of $e^{j2\pi fi}$. We then proceed with the integration and get a different result:

$$g'(t) = \int_{-\infty}^{\infty} S(a \cdot f) \cdot e^{j2\pi a \cdot f \cdot t} df \tag{7.21}$$

By introducing the change $f' = a \cdot f$, we have:

$$g'(t) = \frac{1}{|a|} \cdot \int_{-\infty}^{\infty} S(f') \cdot e^{j2\pi f' \cdot t} df' = \frac{1}{|a|} \cdot s(t) \tag{7.22}$$

With the result above, we can use the following expression to solve the problem of the scaled spectrum:

$$s(t) = |a| \cdot \int_{-\infty}^{\infty} S(a \cdot f) \cdot e^{j2\pi a \cdot f \cdot t} df \tag{7.23}$$

## 7.7 Inverse Scaled Fourier Transformation

(7.23) looks similar to the Fourier integral, but it has an additional scaling coefficient in the phasor. We can expand this phasor as:

$$e^{j2\pi a \cdot f \cdot t} = e^{j2\pi a \cdot t^2} \cdot e^{j2\pi a \cdot f^2} \cdot e^{-j\pi a \cdot (t-f)^2} \tag{7.24}$$

After the expansion, we obtain the following:

$$s(t) = |a| \cdot \int_{-\infty}^{\infty} S(a \cdot f) \cdot e^{j\pi a t^2} \cdot e^{j\pi a f^2} \cdot e^{-j\pi a \cdot (t-f)^2} df \tag{7.25}$$

We take the phasor $e^{j\pi a t^2}$ out of the integral, since it is invariant with regard to $f$:

$$s(t) = |a| \cdot e^{j\pi a \cdot t^2} \cdot \int_{-\infty}^{\infty} S(a \cdot f) \cdot e^{j\pi a \cdot f^2} \cdot e^{-j\pi a \cdot (t-f)^2} df \tag{7.26}$$

The integral above can be understood as the convolution of two signals: $S(a \cdot f) \cdot e^{j\pi a \cdot f^2}$ and $e^{j\pi a \cdot f^2}$.

The final result is rewritten as:

$$s(t) = |a| \cdot e^{j\pi a t^2} \cdot \left( \left\{ S(a \cdot f) \cdot e^{j\pi a f^2} \right\} * e^{j\pi a \cdot f^2} \right) \tag{7.27}$$

The very surprising result of the equation above is that the desired scaling compensated signal in the time domain can be achieved by first multiplying the scaled spectrum with $e^{j\pi a \cdot f^2}$, then performing the convolution in the frequency domain and finally multiplying the result with the time chirp $|a| \cdot e^{j\pi a \cdot t^2}$.

The whole transformation is known as the Scaled Inverse (SI) Fourier transformation. It was first introduced by R. Lanari in [63]. In the discrete implementation, we need the direct and the inverse FFTs and the chirp multiplications, so the implementation is straightforward:

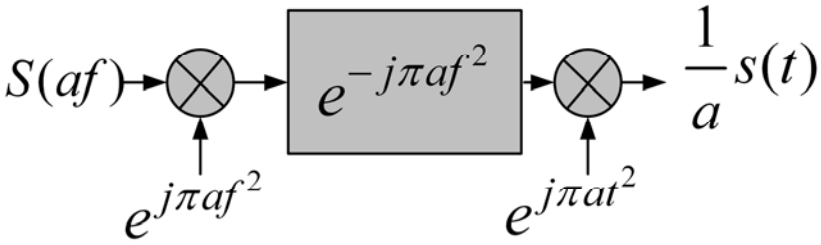


Figure 7.1. Inverse Scaled Fourier Transformation

The implementation above works for continuous signals, but in discrete implementation it is necessary to introduce some normalization factors. $f$ and $t$ could be any variable, but in our case they are time and frequency, respectively, and their corresponding dimensions are (s) and (Hz). In [4], the following implementation for the normalization is proposed:

$$e^{j2\pi a\cdot(f_u t_u)\cdot\frac{f}{f_u}\cdot\frac{t}{t_u}} = e^{j\pi a\cdot(f_u\cdot t_u)\cdot\left[\frac{t}{t_u}\right]^2} e^{ja(f_u\cdot t_u)\cdot\left[\frac{f}{f_u}\right]^2} e^{-j\pi a(f_u\cdot t_u)\cdot\left(\frac{t}{t_u}-\frac{f}{f_u}\right)^2} \tag{7.28}$$

The frequency and time sampling units are expressed as $f_u$ and $t_u$, respectively. For the continuous case, the integral implementation (7.27) is the integration of continuous signals.

Furthermore, we know that the scaling coefficient of the chirp signal determines the bandwidth by means of the expression $B = a \cdot T$, where $a$ is the scaling coefficient and $T$ is the duration of the signal. Therefore, a long-term signal will have a higher bandwidth and may suffer an undersampling problem in the Fourier domain during the discrete implementation.

Another important factor to be taken into account is the extension of the signal in both time and frequency domains. The convolution in Fourier domain is equivalent to the multiplication in time domain, and vice versa. The convolution extends the duration of the resulting signal, which has to be taken into account by performing appropriate zero padding.

## 7.8 Approximation of the Scaled Range Frequency Term

We discussed in section 7.7 how to perform the scaling. The solution is only known for the linear case, but the backscattering coefficient given in (7.17) is a nonlinearly scaled spectrum. The range frequency depends nonlinearly on the range and azimuth frequencies.

As an approximation, we linearize the problem by means of a Taylor expansion:

$$f(x) = f(x_0) + \dot{f}(x_0)\cdot(x - x_0) + \frac{1}{2}\ddot{f}(x_0)\cdot(x - x_0)^2 + .. \tag{7.29}$$

We do a second-order Taylor expansion for $f_r(f, f_\tau) = \frac{2}{c}\sqrt{(f + f_0)^2 - \frac{f_\tau^2 c^2}{4v^2}}$ with respect to the range frequency. But before we do that, a small modification of $f_r(f, f_\tau)$ is done by taking $f_0$ out of the square root:

$$f_r(f, f_\tau) = \frac{2}{c}\sqrt{(f + f_0)^2 - \frac{f_\tau^2 c^2}{4v^2}} = \frac{2}{c} f_0 \sqrt{\left(1 + \frac{f}{f_0}\right)^2 - \frac{f_\tau^2 c^2}{4v^2 f_0^2}} \tag{7.30}$$

The zero-order term of the Taylor expansion is calculated as:

$$f_r\left(f=0,f_\tau\right)=\frac{2}{c}f_0\sqrt{1-\frac{f_\tau^{\,2}c^2}{4v^2f_0^{\,2}}} \tag{7.31}$$

We then have for the first-order term:

$$\dot{f}_r\left(f,f_\tau\right)=\frac{2}{c}f_0\left.\frac{\left(1+\frac{f}{f_0}\right)\frac{1}{f_0}}{\sqrt{\left(1+\frac{f}{f_0}\right)^2-\frac{f_\tau^{\,2}c^2}{4v^2f_0^{\,2}}}}\right|_{f=0}=\frac{2}{c}\frac{1}{\sqrt{1-\frac{f_\tau^{\,2}c^2}{4v^2f_0^{\,2}}}} \tag{7.32}$$

Hence, the square root frequency term is expressed as:

$$f_r\left(f,f_\tau\right)=\frac{2}{c}\sqrt{\left(f+f_0\right)^2-\frac{f_\tau^{\,2}c^2}{4v^2}}=\frac{2}{c}f_0\sqrt{1-\frac{f_\tau^{\,2}c^2}{4v^2f_0^{\,2}}}+\frac{2}{c}\frac{f}{\sqrt{1-\frac{f_\tau^{\,2}c^2}{4v^2f_0^{\,2}}}} \tag{7.33}$$

The nonlinear frequency term is linearized with respect to the range frequency $f$. Here, the following abbreviations are introduced:

$$a\left(f_\tau\right)=\frac{2}{c}\frac{1}{\sqrt{1-\frac{f_\tau^{\,2}c^2}{4v^2f_0^{\,2}}}} \tag{7.34}$$

and

$$b\left(f_\tau\right)=\frac{2}{c}\sqrt{1-\frac{f_\tau^{\,2}c^2}{4v^2f_0^{\,2}}} \tag{7.35}$$

With these notations, we can rewrite the term $f_r\left(f,f_\tau\right)$ as:

$$f_r\left(f,f_\tau\right)=\frac{2}{c}\cdot\sqrt{\left(f+f_0\right)^2-\frac{f_\tau^{\,2}c^2}{4v^2}}\cong a\left(f_\tau\right)\cdot f+b\left(f_\tau\right)\cdot f_0 \tag{7.36}$$

Now, we insert (7.35) into (7.17). The nonlinear scaled backscattering spectrum is converted to a linear scaled one, as follows:

$$\sigma\left(f_r,f_\tau\right)=\sigma\left(\frac{2}{c}\cdot\sqrt{\left(f+f_0\right)^2-\frac{f_\tau^{\,2}c^2}{4v^2}},f_\tau\right)=\sigma\left(a\left(f_\tau\right)\cdot f+b\left(f_\tau\right)\cdot f_0,f_\tau\right) \tag{7.37}$$

We already know from section 7.7 how to perform the scaling of a linear spectrum with the Inverse Scaling approach. The only problem left is the constant shift of the frequency, which is easy to compensate and will be addressed next.

## 7.9 Compensation of the Initial Time Delay

In SAR, the scattered signal comes with a delay $t_0$, which is why the data are recorded after this delay. Because of the shifting property of the Fourier transformation, the delay in the time domain is equivalent to a multiplication by the phasor $e^{-j2\pi(f+f_0)\cdot t_0}$:

$$W''(f,f_\tau)=W'(f,f_\tau)e^{-j2\pi(f+f_0)\cdot t_0}=\sigma\left(a(f_\tau)\cdot f+b(f_\tau)\cdot f_0,f_\tau\right) \tag{7.38}$$

## 7.10 Transformation into the Range Distance Domain

The expression (7.38) shows the backscattering spectrum scaled in the frequency domain. This scaling in the frequency domain implies an inverse scaling in the time domain. After getting rid of the scaling, we will obtain the result in the range time - azimuth time which should be rescaled into the range distance - azimuth distance coordinates. We represent the whole slant range as the sum of the minimum slant range distance $R_0(\min)$, plus a change varable:

$$R_0=R_{0(\min)}+r \tag{7.39}$$

As an initial point, we take the point target backscattering spectrum, which is scaled and shifted in the range direction $\sigma\left(a(f_\tau)\cdot f+b(f_\tau)\cdot f_0,f_\tau\right)$. We notice that we do not have scaling in the azimuth direction. Hence, we write:

$$\sigma\left(a(f_\tau)f+b(f_\tau)f_0,f_\tau\right)=\mathbb{F}_{\tau\to f_\tau}\left\{\int_{-\infty}^{+\infty}\sigma(r,\tau)e^{-j2\pi\sigma\left(a(f_\tau)\cdot f+b(f_\tau)\cdot f_0,f_\tau\right)}dr\right\} \tag{7.40}$$

To simplify the derivations, we only consider the 1D case, fixing the value of the azimuth frequency $f_\tau$. For the given azimuth frequency, the range scaling coefficient and the shift are constant:

$$\sigma\left(a(f_\tau)\cdot f+b(f_\tau)\cdot f_0,f_\tau\right)=\sigma_{f_\tau}\left(a\cdot f+b\cdot f_0\right) \tag{7.41}$$

The backscattering coefficient in the slant range is determined as the inverse Fourier integral:

$$\sigma_{f_\tau}(R_0)=\mathbb{F}^{-1}\left\{\sigma_{f_\tau}(f)\right\}=\int_{-\infty}^{\infty}\sigma_{f_\tau}(v)\cdot e^{j2\pi v\cdot R_0}dv \tag{7.42}$$

Here we introduce the substitution $av=u$:

$$\sigma_{f_\tau}(R_0)=|a|\cdot\int_{-\infty}^{\infty}\sigma_{f_\tau}(a\cdot u)\cdot e^{j2\pi a\cdot u\cdot R_0}du \tag{7.43}$$

With the further substitution $u=x+\dfrac{b}{a}f_0$, we get:

$$\sigma_{f_\tau}(R_0)=|a|\cdot\int_{-\infty}^{\infty}\sigma_{f_\tau}(a\cdot x+b\cdot f_0)\cdot e^{j2\pi(a\cdot x+b\cdot f_0)\cdot R_0}dx \tag{7.44}$$

We factor out the invariant phasor from the integral:

$$\sigma_{f_\tau}\left(R_0\right)=\left|a\right|\cdot e^{j2\pi b f_0 R_0}\cdot\int_{-\infty}^{\infty}\sigma_{f_\tau}\left(a\cdot x+b\cdot f_0\right)\cdot e^{j2\pi a\cdot x\cdot R_0}dx \tag{7.45}$$

Here, we make a new substitution $f=x$ and get:

$$\sigma_{f_\tau}\left(R_0\right)=\left|a\right|\cdot e^{j2\pi b f_0 R_0}\cdot\int_{-\infty}^{\infty}\sigma_{f_\tau}\left(a\cdot f+b\cdot f_0\right)\cdot e^{j2\pi a\cdot f\cdot R_0}df \tag{7.46}$$

The desired backscattering expression for the range distance - azimuth frequency domain is then given as:

$$\sigma\left(R_0,f_\tau\right)=\left|a\left(f_\tau\right)\right|\cdot e^{j2\pi b\left(f_\tau\right)f_0 R_0}\cdot\int_{-\infty}^{\infty}\sigma_{f_\tau}\left(a\left(f_\tau\right)\cdot f+b\left(f_\tau\right)\cdot f_0\right)\cdot e^{j2\pi\cdot a\left(f_\tau\right)\cdot f\cdot R_0}df \tag{7.47}$$

The equation above is valid for the complete slant range. We represent the slant range as $R_0=r+R_{0(\min)}$. $R_{0(\min)}$ is the minimal slant range. We insert the new value of $R_0$ in (7.47) and obtain:

$$\begin{aligned}\sigma\left(R_{0(\min)}+r,f_\tau\right)=&\left|a\left(f_\tau\right)\right|\cdot e^{j2\pi b\left(f_\tau\right)\cdot f_0\cdot\left(R_{0(\min)}+r\right)}\cdot\\&\cdot\int_{-\infty}^{\infty}\sigma_{f_\tau}\left(a\left(f_\tau\right)\cdot f+b\left(f_\tau\right)\cdot f_0\right)e^{j2\pi a\left(f_\tau\right)\cdot f\cdot\left(R_{0(\min)}+r\right)}df\end{aligned} \tag{7.48}$$

## 7.11 Representation of the Complete Processor

As already discussed in section 7.9, the raw data needs to be shifted with an initial time delay according to (7.38). In the Fourier domain, this delay is equivalent to the phasor $e^{-j2\pi\left(f+f_0\right)t_0}$.

$$\begin{aligned}\sigma\left(R_{0(\min)}+r,f_\tau\right)=&\left|a\left(f_\tau\right)\right|\cdot e^{j2\pi b\left(f_\tau\right)\cdot f_0\cdot\left(R_{0(\min)}+r\right)}\cdot\\&\cdot\int_{-\infty}^{\infty}\sigma_{f_\tau}\left(a\left(f_\tau\right)\cdot f+b\left(f_\tau\right)\cdot f_0\right)\cdot e^{j2\pi\left(f+f_0\right)t_0}\cdot e^{j2\pi\cdot a\left(f_\tau\right)\cdot f\cdot\left(R_{0(\min)}+r\right)}df\end{aligned} \tag{7.49}$$

We reorder the above integral and take out the terms that are invariant with the range frequency:

$$\begin{aligned}\sigma\left(R_{0(\min)}+r,f_\tau\right)=&\left|a\left(f_\tau\right)\right|\cdot e^{j2\pi\cdot b\left(f_\tau\right)\cdot\left(R_{0(\min)}+r\right)f_0}\cdot e^{-j2\pi f_0 t_0}\cdot\\&\cdot\int_{-\infty}^{\infty}\sigma_{f_\tau}\left(a\left(f_\tau\right)\cdot f+b\left(f_\tau\right)\cdot f_0\right)\cdot e^{-j2\pi f t_0}\cdot e^{j2\pi\cdot a\left(f_\tau\right)\cdot f\cdot\left(R_{0(\min)}+r\right)}df\end{aligned} \tag{7.50}$$

Because $t_0$ is the minimal delay, it has a direct connection to the slant range with relation $t_0=\dfrac{2R_{0(\min)}}{c}$. We insert this relation into (7.50) and get:

$$\sigma\left(R_{0(\min)}+r,f_\tau\right)=\left|a\left(f_\tau\right)\right|\cdot e^{j2\pi f_0\cdot R_{0(\min)}\cdot\left(b(f_\tau)-\frac{2}{c}\right)}\cdot e^{-j2\pi f_0\cdot b(f_\tau)}\cdot \\ \cdot\int_{-\infty}^{\infty}W'\left(f,f_\tau\right)\cdot e^{-j2\pi f\cdot\left(\frac{2}{c}-a(f_\tau)\right)\cdot R_{0(\min)}}\cdot e^{j2\pi\cdot a(f_\tau)\cdot f\cdot r}df \tag{7.51}$$

$W'\left(f,f_\tau\right)$ is the ranged compressed raw data given in (7.9). Here we introduce two important transfer functions:

$$H_2\left(f,f_\tau\right)=e^{-j2\pi f\cdot\left(\frac{2}{c}-a(f_\tau)\right)\cdot R_{0(\min)}} \tag{7.52}$$

$$H_3\left(f,f_\tau\right)=\cdot e^{j2\pi f_0 R_{0(\min)}\cdot\left(b(f_\tau)-\frac{2}{c}\right)}e^{-j2\pi f_0\cdot b(f_\tau)}=\left|a\left(f_\tau\right)\right|\cdot e^{j2\pi\cdot b(f_\tau)\cdot\left(R_{0(\min)}+r\right)\cdot f_0}\cdot e^{-j2\pi f_0\cdot t_0} \tag{7.53}$$

Substituting these notations into (7.51) we obtain:

$$\sigma\left(R_{0(\min)}+r,f_\tau\right)=H_3\left(f,f_\tau\right)\cdot\int_{-\infty}^{\infty}W'\left(f,f_\tau\right)\cdot H_2\left(f,f_\tau\right)\cdot e^{j2\pi\cdot a(f_\tau)\cdot f\cdot r}df \tag{7.54}$$

Equation (7.54) is the final expression that represents the principal algorithm to perform monostatic processing.

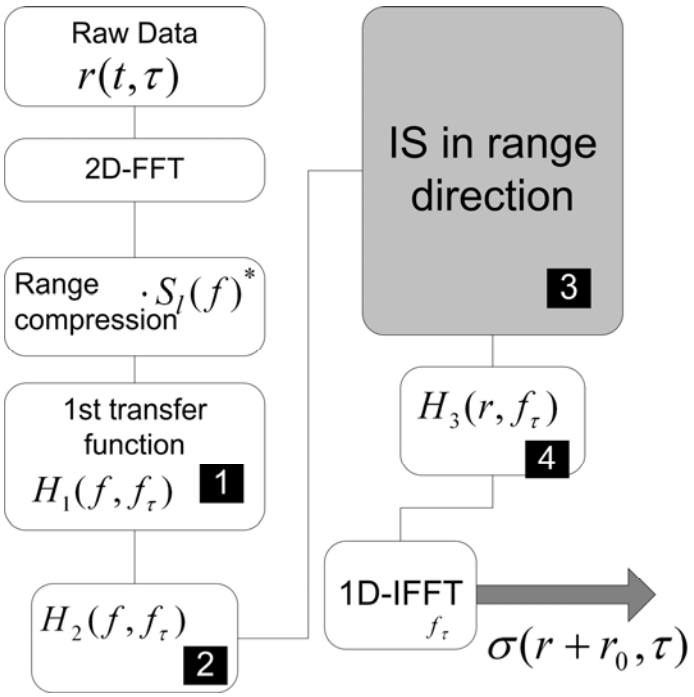


Figure 7.2. Monostatic algorithm based on the Inverse Scaling

The algorithm is presented in Figure 7.2. The initial raw data is first transformed into the range frequency - azimuth frequency domain. It is then range-compressed. The secondary range compression is done only if necessary. The compensation of the amplitude term is done with the transfer function $H_1\left(f,f_\tau,R_{0(\min)}\right)$. The results are multiplied by the $H_2\left(f,f_\tau\right)$ function. The next block is the Inverse Scaling module. It performs the inverse scaling of range frequency by means of the Inverse Scaling FFT algorithm. The outcome

signal is given in the range distance - Doppler frequency domain, and it is multiplied by the $H_3(r, f_\tau)$ transfer function. The last IFFT for the azimuth frequency brings us the desired result: the backscattering coefficient in the range distance azimuth time domain.

## 7.12 Inverse Scaling Approach - from Continuous to Discrete Implementation

### 7.12.1 Discrete Implementation of Inverse Scaling FFT

One of the most important modules of the Inverse Scaling monostatic processor is the one where the range frequency dependency on the azimuth frequency is compensated. In [3], the discrete implementation of the Inverse Scaling was given, and it is done according to the following diagram:

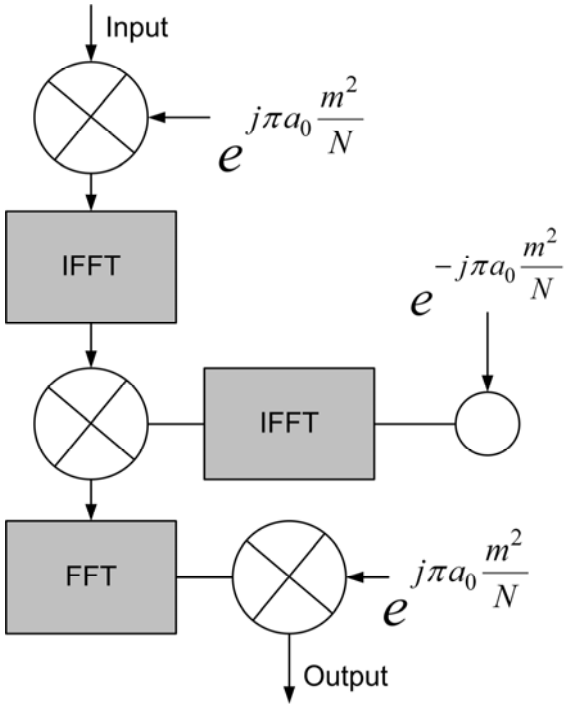


Figure 7.3. Discrete implementation of the Inverse Scaling approach

In the diagram the new symbol $a_0$ was used, which is defined as $a_0 = a(f_\tau) \cdot \frac{c}{2}$. $N$ is the amount of samples of the signal, and $m$ is the sample number. This kind of implementation is very efficient and relatively easy, but it does not take into account the extensions of the signals in the time and frequency domains at different stages of the algorithm. This causes an erroneous result of the algorithm when the scaling coefficient strongly deviates from 1. This is often the case in SAR, especially in an airborne configuration. We observed that the scaling coefficient in the range frequency direction sometimes reaches 1.03. In the following section, we will consider the novel solution of these problems developed in the scope of this work.

### 7.12.2 Some Ideas about a Correct Implementation of Inverse Scaling Approach

We redraw the diagram given in Figure 7.1 by adding some intermediate annotation:

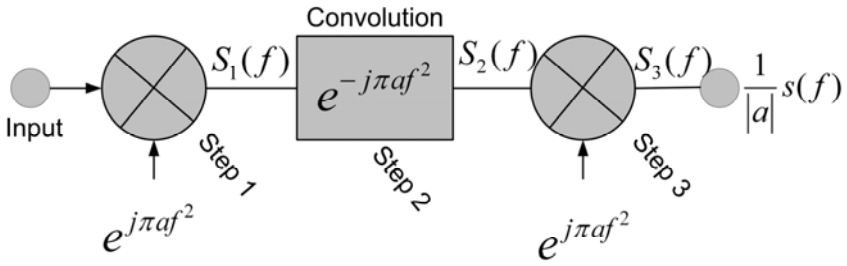


Figure 7.4. Continuous implementation of the Inverse Scaling approach with some notations

It is well known that any convolution extends the duration of the obtained signals. The first step is the multiplication in the frequency domain, which can be understood as the convolution in the time domain. After the first step, the bandwidth should not change, but the time duration will be extended. This extension must be determined.

To resolve this, we introduce the appropriate parameters of all three chips and then analyze the algorithm given in Figure 7.5 more carefully. As opposed to Figure 7.4, in Figure 7.5 we realized the convolution using the FFT technique. We bring two components of the convolution into the time domain, multiply them and then do the Fourier transformation:

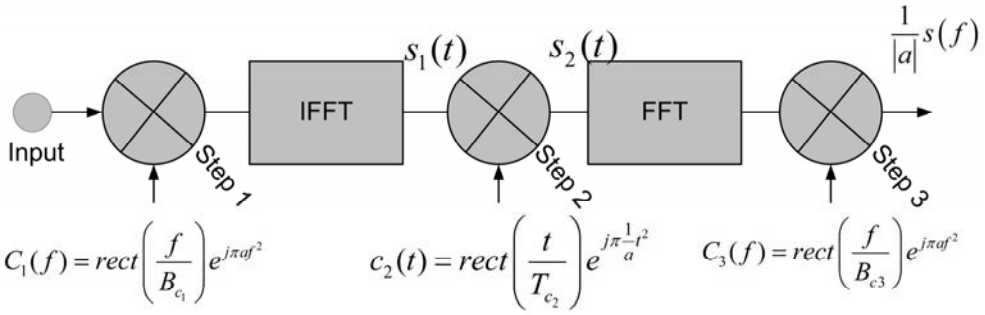


Figure 7.5. Schematic diagram of the discrete implementation of the Inverse Scaling algorithm

The following symbols are used in the subsequent figures:

$\Delta f$ is the bandwidth of the input signal.

$T_0$ is the time extent (duration) of the input signal.

$B_{c_{1,2,3}}$ are the bandwidths of the corresponding chirps $C_{1,2,3}(f)$.

$T_{c_{1,2,3}}$ are the time durations of the corresponding chirps $c_{1,2,3}(t)$.

$T_{1ext,2ext,3ext}$ are the time extensions at each step of the algorithm.

$f_{1ext,2ext,3ext}$ are the bandwidth extensions at each step of the algorithm.

$T_{1,2,3}$ are the complete time extent after the corresponding step.

$\Delta f_{1,2,3}$ are the complete signal bandwidths after the corresponding step.

*Step 1*

The first chirp multiplication is done in the frequency domain. It keeps the frequency bandwidth unchanged. Hence, the bandwidth of the chirp and the output signal after step 1 are equal to the bandwidth of the input signal $S(a \cdot f)$. Therefore, we write:

$$B_{c_1} = \Delta f \tag{7.55}$$

First we calculate the duration of the chirp $C_1(f)$. Generally for the time and frequency chirps the following relation is valid:

$$rect\left(\frac{t}{T}\right) \cdot e^{j\pi a t^2} \circ\!\!-\!\!\bullet \frac{1}{\sqrt{a}} \cdot rect\left(\frac{f}{aT}\right) \cdot e^{-j\pi \frac{1}{a} f^2} \cdot e^{j\frac{\pi}{4}} \tag{7.56}$$

According to (7.56), we can determine the time chirp corresponding to the $C_1(f)$ frequency chirp as:

$$c_1(t) = c_{1_0} rect\left(\frac{t}{T_{1c}}\right) e^{-j\pi \frac{1}{a} t^2} \tag{7.57}$$

$T_{1c}$ is the time duration of the chirp $c_1(t)$. It will be equal to the size of the time extension $T_{1ext}$ at step 1.

The bandwidth of the first chirp is known from (7.55), and it has a direct relation with the time duration. Hence, we calculate the duration of the first chirp as:

$$\frac{1}{|a|} \cdot T_{c_1} = B_{c_1} = \Delta f \tag{7.58}$$

Now we determine $T_{1ext}$ from (7.58) as:

$$\boxed{T_{1ext} = T_{c_1} = |a| \cdot B_{c_1} = |a| \cdot \Delta f} \tag{7.59}$$

*Step 2*

Now we calculate the necessary time and frequency extensions after the step 2 in Figure 7.4.

After step 2, we have: $s_2(t) = s_1(t) \cdot c_2(t)$. This operation is performed in the time domain, so it will not change the time duration, but it extends the frequency bandwidth of the result. For time duration at the end of step 2, we can write:

$$\boxed{T_2 = T_0 + T_{1ext} = T_0 + \Delta f \cdot |a|} \tag{7.60}$$

where $T_0$ is the time duration of the input signal.

For the frequency bandwidth of the second chirp $C_2(f)$, we have:

$$B_{c_2} = T_2 \cdot \frac{1}{|a|} = \frac{1}{|a|} \cdot \left(T_0 + \Delta f \cdot |a|\right) = \frac{T_0}{|a|} + \Delta f \tag{7.61}$$

It represents the size of the frequency extension after step 2. Hence, we have $f_{2ext} = B_{c_2}$. The complete frequency bandwidth after step 2 is obtained as:

$$\Delta f_2 = f_{2ext} + \Delta f = \frac{T_0}{|a|} + \Delta f + \Delta f = \frac{T_0}{|a|} + 2\Delta f \tag{7.62}$$

*Step 3*

The last step is multiplication with the chirp in the frequency domain. It keeps the frequency bandwidth unchanged, but it extends the time duration of the outcoming signal.

The parameters of the last chirp are the bandwidth:

$$B_{c_3} = \Delta f_2 = \frac{T_0}{|a|} + 2\Delta f \tag{7.63}$$

and the time extension (calculated as the time duration of the last chirp $\frac{T_{c_3}}{|a|} = B_{c_3}$):

$$T_{3ext} = T_{c_3} = T_0 + 2\Delta f \cdot |a| \tag{7.64}$$

The complete time duration after step 3 is:

$$T_3 = T_2 + T_{3ext} = T_0 + \Delta f \cdot |a| + T_0 + 2\Delta f \cdot |a| = 2T_0 + 3\Delta f \cdot |a| \tag{7.65}$$

### 7.12.3 The Corrected Discrete Implementation of the Inverse Scaling FFT Algorithm

In the previous section, we discussed the ideas about the correct discrete implementation of the Inverse Scaling approach. Here, we perform more detailed calculations of the time and the frequency extensions done at the different steps.

We assume that at the input we have a scaled signal $S(a \cdot f)$ with a bandwidth $\Delta f$ and time duration $T_0$. The initial signal consists of $N_0$ samples. In Figure 7.4, the discrete implementation of the Inverse Scaling algorithm is shown. The first step is the multiplication with the frequency domain chirp. We denote the time extension as $T_{1ext}$.

In the Inverse Scaling algorithm, $t$ and $f$ can be any variables, but when we consider them as time and the frequency, we should take into account their dimensions (s) and (Hz). Standardization is therefore necessary. In [4], standardization was implemented according to (7.28). That kind of normalization can be used only when the time and the bandwidth extensions of the signals at the different steps of the algorithm are not taken into account. In the previous section, we showed that all three steps of the Inverse Scaling algorithm cause either time or frequency extension. Here, we propose a different solution:

*Step 1*

We fix the scaling coefficient during the whole processing as.

$$\tilde{a}_0 = a_0 \cdot \frac{t_e}{f_e} \tag{7.66}$$

$t_e$ is the initial sampling time, with measuring unit $[t_e] = s$;

$f_e$ is the corresponding initial frequency sample width, with unit $[f_e] = Hz$;

The first frequency chirp has a shape:

$$c_1(f) = rect\left(\frac{f}{B_{c_1}}\right) \cdot e^{j\pi\tilde{a}_0 f^2} \tag{7.67}$$

Because we need to extend the time duration after step 1, we generate the first chirp in the time domain. We extend it with the size of the initial time extent of the input signal and finally apply FFT.

The first chirp in time domain is given as:

$$c_1(t) = \sqrt{\tilde{a}_0} \cdot rect\left(\frac{t}{T_{1ext}}\right) \cdot e^{-j\pi\frac{1}{\tilde{a}_0}\cdot t^2} = \sqrt{\tilde{a}_0} \cdot rect\left(\frac{t}{T_{1ext}}\right) \cdot e^{-j\pi\frac{1}{a_0\cdot\frac{t_e}{f_e}}\cdot t^2} \tag{7.68}$$

We observe that, because of the new scaling coefficient (7.55), the chirps are dimensionless in both the time and the frequency domains. This is a necessary condition for the correct implementation of the algorithm.

We calculate the necessary time extension according to (7.58) as:

$$\frac{\tilde{a}_0}{T_{1ext}} = \frac{1}{\Delta f} \tag{7.69}$$

$T_{1ext}$ is found from the above as:

$$T_{1ext} = \tilde{a}_0 \cdot \Delta f = \frac{t_e}{f_e} \cdot a_0 \cdot \Delta f = a_0 \cdot T_0 = a_0 \cdot t_e \cdot N_0 \tag{7.70}$$

In the time domain, zero padding is done with size $T_{1ext}$. The corresponding number of the extended samples is determined as:

$$N_1 = N_0 + N_{1ext} = N_0 \cdot (1 + a_0) \tag{7.71}$$

where $N_1$ is the number of the total time samples after the first time extension.

*Step 2*

In the next step, we do the convolution in the frequency domain, which extends the frequency bandwidth but keeps the time extent unchanged. We generate a chirp in frequency domain and extend it with the bandwidth of the convolution partner $S_1(f)$ according to Figure 7.4. We then apply IFFT, multiply with $s_1(t)$ as shown in Figure 7.5 and do forward FFT. In this way we realize the convolution with FFT techniques.

The second chip in the frequency domain is given as:

$$c_2(f) = rect\left(\frac{f}{B_{c_2}}\right) \cdot e^{-j\pi\tilde{a}_0 \cdot f^2} \tag{7.72}$$

The bandwidth extension is calculated from (7.61):

$$f_{2ext} = B_{c_2} = \frac{T_1}{t_e} = \frac{T_0 + T_{1ext}}{t_e} = \frac{t_e \cdot (N_0 + N_{1ext})}{\tilde{a}_0} \tag{7.73}$$

Using (7.73), we determine the bandwidth of $S_2(f)$ after step 2:

$$f_2 = f_{2ext} + \Delta f \tag{7.74}$$

The extension in the frequency domain causes the extension of the number of the samples:

$$N_2 = N_1 + N_{2ext} \tag{7.75}$$

The change of the number of the samples in the frequency domain from $N_1$ to $N_2$ causes the change of time sampling with ratio $\frac{N_1}{N_2}$.

*Step 3*

As a last step, we multiply $S_2(f)$ with the frequency chirp:

$$c_3(f) = rect\left(\frac{f}{B_{c_3}}\right) \cdot e^{j\pi\tilde{a}_0 \cdot f^2} = rect\left(\frac{f}{\Delta f_2}\right) \cdot e^{j\pi\tilde{a}_0 \cdot f^2} \tag{7.76}$$

This extends the time signal. At the end of step 2, we ended with FFT. Therefore, if it was continuous implementation, we would think that we are in frequency domain. Since we are realizing a discrete algorithm, we look to the outcome as a time signal.

We observed that the time extension in the last step caused different focusing problems. Hence, we keep the time duration at step 3 unchanged, equal to the outcome from step 2.

We generate the last chirp in the time domain according to Figure 7.5 and then convert it into the frequency domain. The corresponding chirp in the time domain is:

$$c_3(t) = \sqrt{\tilde{a}_0} \cdot rect\left(\frac{t}{T_1}\right) \cdot e^{-j\pi\frac{1}{\tilde{a}_0} \cdot t^2} \tag{7.77}$$

Now we need to find out the effect of the algorithm on the input signal. We consider the point target initially located at the position $t_e n$. The new location of this PT after the end of the algorithm can be calculated as:

$$t_e \cdot n = f_{e2} \cdot n_{new} \cdot \tilde{a}_0 \tag{7.78}$$

$f_{e_2}$ is the frequency unit width at the end of the algorithm, calculated as:

$$f_{e_2} = \frac{N_0}{N_1} \cdot f_e \tag{7.79}$$

$n_{new}$ is the new location of the PT. We substitute the expressions of (7.66) and (7.78) into (7.79) and obtain:

$$t_e \cdot n = \frac{N_0}{N_1} \cdot n_{new} \cdot f_e \cdot a_0 \cdot \frac{t_e}{f_e} = \frac{N_0}{N_1} \cdot n_{new} \cdot a_0 \cdot t_e \tag{7.80}$$

The actual scaling factor is the ratio of the original and the new location of PT. We therefore write:

$$a_{act} = \frac{n}{n_{new}} = \frac{N_0 \cdot a_0}{N_1} = \frac{N_0 \cdot a_0}{N_0 + N_0 \cdot a_0} = \frac{a_0}{1 + a_0} \tag{7.81}$$

$a_{act}$ is the actual scaling coefficient. Since $a_0$ is a positive number, the actual scaling factor will always be smaller than 1. Therefore, scaling implementation given in (7.81) is not always useful.

We propose a different solution: in SAR, scaling factor $a_0$ is normally close to 1. Therefore, instead of extending the signal after the first step with $aT_0$, we extend it with $bT_0$, where $b$ is some fixed factor (close to1). After this modification, we recalculate the final scaling factor as:

$$a_{act} = \frac{N_0 \cdot a_0}{N_0 + N_0 \cdot b} = \frac{a_0}{1+b} \tag{7.82}$$

If the scaling with a factor $a_{act}$ is desired, we start the algorithm with the initial factor calculated as:

$$a_0 = a_{act} \cdot (1+b) \tag{7.83}$$

For example, in case of requiring a scaling of 0.9, we modify the scaling coefficient at the input as $a_0 = 0.9 \cdot (1+1) = 1.8$.

The modified algorithm works better when the values of $b$ and $a_0$ are close to each other. In our applications, we used the values of $b$ in the range (1.0:1.5), producing correct results.

### 7.12.4 Inverse Scaling Algorithm – Simulated Result

Now we will demonstrate the performance of the corrected Inverse Scaling algorithm. We have generated a 2D signal. In one direction, we have sampling with a frequency of 1250Hz. We distributed the point targets in this direction with a separation of 500, 1000, 1500, 2000 and 2500 samples. By increasing the distance, the magnitude was increased as well; this was done intentionally to distinguish the correct direction at the end of the algorithm. We see the initial allocation of all PTs in Figure 7.6:

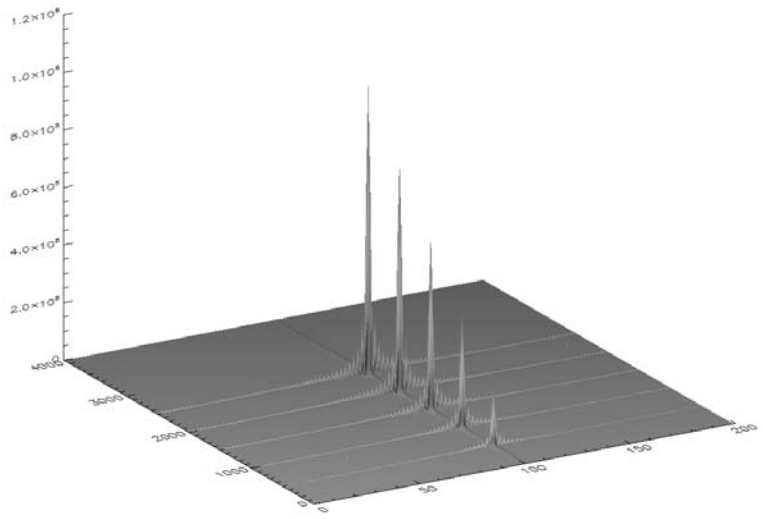

Figure 7.6. Original scene: 5 point targets in one direction with a separation of 500 samples

We desire to perform the frequency scaling with factor 1.1, but only in one direction. We keep the second direction of the 2D signal unchanged. If we compensate the scaling with the normal Inverse Scaling algorithm, without taking into account time and frequency extensions, we end up with a wrong result shown in Figure 7.7. The PTs are reallocated at wrong places and, furthermore, they are duplicated.

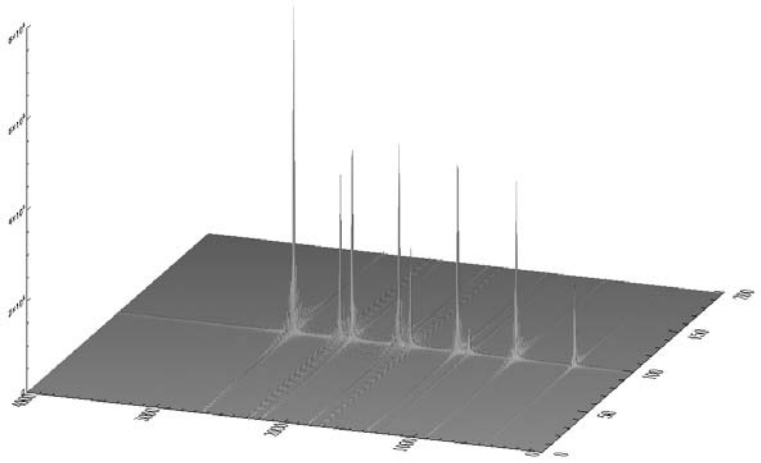

Figure 7.7. Wrong result after the normal Inverse Scaling algorithm

We have completely different results after performing the scaling with the modified Inverse Scaling algorithm described in 7.12.3. The result is shown in Figure 7.8:

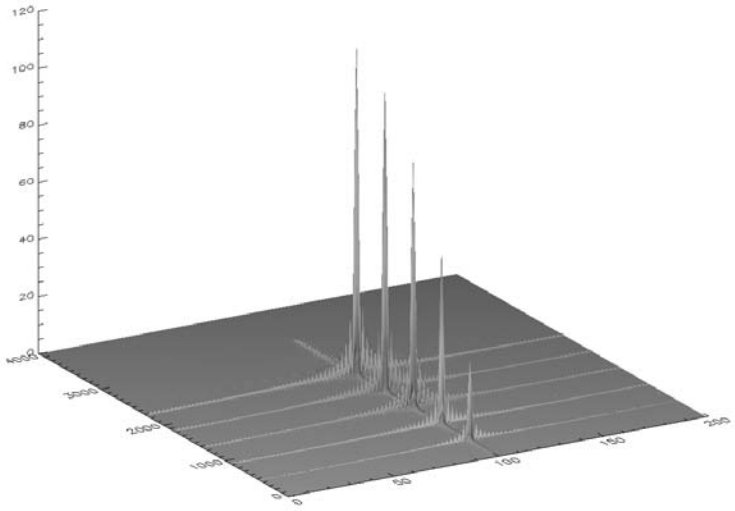


Figure 7.8. Result after the correct Inverse Scaling algorithm

Now all PTs are well focused and correctly located. For example, the 5$^{th}$ PT was initially located at sample number 2500. After the scaling, the new location of the 5$^{th}$ PT becomes 2272, as seen in Figure 7.8. Hence, the algorithm does correct scaling according to the actual scaling factor $2500/1.1 \approx 2272$ .

## 7.13 Chirp Scaling Algorithm

In section 7.12, we developed the Inverse Scaling algorithm. In this algorithm (see Figure 7.1), the final result is in time domain. Very often we have a situation requiring the result in frequency domain. Remarking the task, we have a scaled spectrum at the input, and we would like to have a scaling compensated spectrum at the output.

We have experienced this situation during the processing of the bistatic general case, where the bistatic processing becomes truly azimuth time dependent [9]. This dependency is the cause of the azimuth frequency scaling in addition to range scaling. In the initial implementations, we used the Inverse Scaling algorithm. It was later substituted with the Chirp Scaling (CS) approach. With the Chirp Scaling algorithm, after compensating the range frequency scaling, we still stay in range frequency domain; that is a benefit, because we save extra FFT as compared with the Inverse Scaling algorithm.

Originally, the Chirp Scaling algorithm was derived in [34]. In [4] a duality between the Chirp Scaling and the Inverse Scaling approaches was proven. The detailed derivation of the Chirp Scaling algorithm, including the discrete implementation, is given in Appendix B. We should note that both Inverse Scaling and Chirp Scaling algorithms can be easily reversed from the given to the inverse domains. For example, if we apply the inverse Fourier transformation to the Inverse Scaling algorithm shown in Figure 7.1, then all multiplications will be changed with the convolutions (but in the opposite domain), and all convolutions with the multiplications. Finally, we will get the scaled time signal as the input and the scaled spectrum as the output. Similar reversion is possible for the Chirp Scaling algorithm.

# 8 Processing for different Bistatic SAR Configurations

In the previous chapters, we derived the bistatic point target reference spectrum. We demonstrated the validity of this bistatic point target reference spectrum on a single point target and on a group of point targets. In this chapter, we extend the processing solution to complete SAR scenes. We develop the bistatic processing algorithms for configurations with an increasing complexity, such as the Tandem case, the translationally invariant case and the general case.

The bistatic formula is the key instruction for our bistatic processing: for bistatic processing, the raw data has to be initially convolved with the bistatic deformation term, the behavior of which was analyzed in section 3.6. The simulations show that the variation of the bistatic phase term with respect to the range is small in comparison to the monostatic phase term. Hence, we may compensate it in range blocks.

## 8.1 Aim of the Bistatic Processing

In the previous chapters, we derived the bistatic point target reference spectrum (BPTRS), giving its constraints of validity. Its correctness was demonstrated with the result of different simulations on a single point target and on a group of point targets.

We later detailed our monostatic focusing approach. It is based on the Inverse Scaling and the Chirp Scaling approaches. We used some modules of the monostatic processor for the bistatic processing, so this description was necessary.

Our aim is to develop the bistatic processing algorithm, which will be analytical and able to process the complete scene.

The raw data in SAR is a sum of reflected signals from all PTs. Hence, the spectrum of the raw data can be expressed as a double integral:

$$W(f,f_\tau)=\int\int G_l(f,f_\tau,R_{0R},\tau_{0R})\,dR_{0R}d\tau_{0R} \tag{8.1}$$

$G_l(f,f_\tau,R_{0R},\tau_{0R})$ is the BPTRS for the PT at the position $R_{0R},\tau_{0R}$. The focusing should invert the integral given in (8.1) and extract the bistatic backscattering coefficient for the whole scene $\sigma(R_{0R},\tau_{0R})$.

From the BPTRS spectrum given in (3.136), it is clear for the general case that the BPTRS is range as well as azimuth time variant. This makes the bistatic focusing for arbitrary configurations a problem that is not trivial. Furthermore, all time variant parameters in the BPTRS need to be expressed in terms of the receiver's relative coordinates $(R_{0R},\tau_{0R})$, $R_{0R}$ being receiver's slant range at the point of closest approach, and $\tau_{0R}$ the azimuth time at the point of closest approach.

In the following, we consider some particular bistatic configurations and give the appropriate processing solutions.

## 8.2 Tandem Configuration

### 8.2.1 Theoretical Derivation of the Processing Algorithm

In the Tandem case, the transmitter and the receiver follow each other on the same track with a constant offset. This case was described in detail in section 2.3. The quasi-monostatic term given in (4.1) becomes a monostatic term and is given as:

$$\Psi_{QM}\left(f,f_\tau\right)=\pi\left(2\tau_{0R}+a_0\right)\cdot f_\tau+\frac{4\pi}{c}R_{0R}\cdot F^{1/2} \tag{8.2}$$

The bistatic term given in (4.2) also experience simplifications as in (4.30):

$$\Psi_{BI}\left(f,f_\tau\right)=\frac{\pi d^2\cdot F\left(f,f_\tau\right)^{\frac{3}{2}}}{c\left(f+f_0\right)^2\cdot R_{0R}} \tag{8.3}$$

where:

- $a_0=\tau_{0T}-\tau_{0R}$ is a bistatic parameter, expressing the azimuth time difference of the point of closest approach (PCA).
- $d$ is a baseline between transmitter and receiver, constant in Tandem case.

$F^{\frac{1}{2}}\left(f,f_\tau\right)$ has following expression:

$$F^{\frac{1}{2}}\left(f,f_\tau\right)=\sqrt{\left(f+f_0\right)^2-\frac{f_\tau^{\,2}c^2}{4v^2}} \tag{8.4}$$

which is a particular case of $F_{R,T}{}^{\frac{1}{2}}\left(f,f_\tau\right)$ given in (3.60) for equal velocities $v_T=v_R=v$.

The bistatic deformation term strongly depends on $d$. Both bistatic and monostatic terms vary only with respect to slant range and are invariant with respect to azimuth time. Based on that observation, for the spaceborne case, we can linearize (8.3):

$$\frac{1}{R_{0R}}\approx\frac{1}{R_{0R(\min)}}-\frac{r}{R_{0R\,(\min)}^{\,2}}\quad\text{where: } R_{0R}=R_{0R(\min)}+r \tag{8.5}$$

After the previous modification, we combine the bistatic and the monostatic phase terms. In the airborne case, the bistatic deformation term is simply averaged and compensated blockwise in the range direction. The number of blocks that are necessary to perform a correct compensation of the bistatic term depends on the speed of change of the bistatic deformation. This question was considered in detail in section 3.6. After the compensation, the bistatic focusing task is transformed to a modified monostatic processor.

The spectrum of received bistatic SAR raw data can be calculated as the double integral over the individual BPTRS:

$$W\left(f,f_\tau\right)=\int\int G_l\left(f,f_\tau,R_{0R},\tau_{0R}\right)dR_{0R}d\tau_{0R} \tag{8.6}$$

$G_l$ is the BPTRS given in (3.136). We substitute (3.136) inside (8.6) and use the monostatic and the bistatic phase term descriptions from (8.2), (8.3) and obtain:

$$W(f,f_\tau)=\int\int\sigma(R_{0R},\tau_{0R})\cdot w(\tilde{\tau}-\tau_{cb})\cdot S_l(f)\cdot\frac{\sqrt{2\pi}}{\sqrt{\ddot{\phi}_T(\tilde{\tau}_T)+\ddot{\phi}_R(\tilde{\tau}_R)}}$$
$$\cdot e^{-j\pi(2\tau_{0R}+a_0)\cdot f_\tau-j\frac{4\pi}{c}R_{0R}F^{1/2}}\cdot e^{-j\frac{1}{2}\frac{\pi d^2F(f,f_\tau)^{\frac{3}{2}}}{c(f+f_0)^2R_{0R}}}dR_{0R}d\tau_{0R} \tag{8.7}$$

For each block, the bistatic term and the amplitude terms are substituted by their averaged values in the range block. Amplitude term for the Tandem case was calculated in (4.31). We use an approximation in $F^{\frac{1}{2}}(f,f_\tau)=\sqrt{(f+f_0)^2-\frac{f_\tau^2c^2}{4v^2}}$, ignoring $\frac{f_\tau^2c^2}{4v^2}$, and obtain $F^{\frac{1}{2}}(f,f_\tau)=|f+f_0|$. We substitute it inside (4.31) and get:

$$Amp(f,f_\tau,R_{0R})=\frac{|f+f_0|}{F^{\frac{3}{4}}\cdot v}\cdot\sqrt{\frac{R_{0R}}{2c}}=\frac{1}{v}\cdot\sqrt{\frac{R_{0R}}{2c|f+f_0|}} \tag{8.8}$$

The averaged value of $Amp(f,f_\tau,R_{0R})$ in the slant range block is abbreviated as $Amp(f,f_\tau)_{aver}$.

$$\boxed{Amp_{aver}(f,f_\tau)=\frac{1}{v_0}\cdot\sqrt{\frac{R_{0R(aver)}}{2c|f+f_0|}}} \tag{8.9}$$

$R_{0(aver)}$ is the averaged value of receiver slant range in each range block.

Similarly, we do averaging of bistatic phase terms given in (8.3) and obtain the transfer function to compensate the bistatic deformation:

$$\boxed{H_1(f,f_\tau)=e^{j\frac{\pi d^2\cdot F(f,f_\tau)^{\frac{3}{2}}}{2c(f+f_0)^2\cdot R_{0R(aver)}}}} \tag{8.10}$$

The averaged bistatic term and amplitude term do not depend on $R_{0R}$. Hence, they are factored out of the integral (8.7). Then, we compensate the terms outside the integral by multiplying them with their complex conjugates. Range chirp spectrum is also factored out because it only depends on $f$. We obtain the following simplifications:

$$W'(f,f_\tau)=\int\int\sigma(R_{0R},\tau_{0R})\cdot e^{-j2\pi f_\tau\tau_{0R}}\cdot e^{-j\pi f_\tau a_0}\cdot e^{-j\frac{4\pi}{c}R_{0R}F^{1/2}}dR_{0R}d\tau_{0R} \tag{8.11}$$

where:

$$W'(f,f_\tau)=\frac{W(f,f_\tau)\cdot S_l^*(f)\cdot(BistaticTerm)^*}{Amp_{aver}}=\frac{W(f,f_\tau)\cdot S_l^*(f)}{Amp_{aver}}\cdot H_1(f,f_\tau) \tag{8.12}$$

In the Tandem case, $\tau_{0T}-\tau_{0R}=a_0=const$. We take the constant phasor containing $a_0$ out of the integral (8.11) and obtain:

$$W''(f,f_\tau)=\int\int\sigma(R_{0R},\tau_{0R})\cdot e^{-j2\pi f_\tau\tau_{0R}}\cdot e^{-j\frac{4\pi}{c}R_{0R}\cdot F^{1/2}}dR_{0R}d\tau_{0R} \tag{8.13}$$

where:

$$W''(f,f_\tau)=W(f,f_\tau)'\cdot e^{j\pi f_\tau a_0} \tag{8.14}$$

We make an additional abbreviation:

$$\boxed{H_2(f_\tau)=e^{j\pi f_\tau\cdot a_0}} \tag{8.15}$$

In chapter 7, we solved an integral similar to (8.13), where we considered monostatic processing. We have solved it with the Inverse Scaling algorithm.

Here we introduce two extra transfer functions:

$$\boxed{H_3(f,f_\tau)=e^{-j2\pi f\cdot(t_0-a(f_\tau)\cdot R_{0R(\min)})}} \tag{8.16}$$

$$\boxed{H_4(r,f_\tau)=|a(f_\tau)|\cdot e^{j2\pi f_0\cdot(r+R_{0R(\min)})\cdot b(f_\tau)}e^{-j2\pi f_0\cdot t_0}} \tag{8.17}$$

In the above two notations are introduced:

$$\boxed{a(f_\tau)=\frac{2}{c}\cdot\frac{1}{\sqrt{1-\frac{f_\tau^2c^2}{4v^2f_0^2}}},\ b(f_\tau)=\frac{2}{c}\cdot\sqrt{1-\frac{f_\tau^2c^2}{4v^2f_0^2}}} \tag{8.18}$$

The block diagram of the processing algorithm for Tandem case is shown in Figure 8.1.

Major blocks of the processor given in Figure 8.1 could be explained in a following way:

1) 2D signal is transformed into the range frequency azimuth frequency domain by double directional FFT.
2) This module performs range compression. It is done by convolving the raw data with the complex conjugate of the transmitted chirp. This convolution is implemented by the FFT techniques.
3) The amplitude term is compensated by averaging it in the range blocks and dividing the signal on averaged value of $Amp_{aver}(f,f_\tau)$, given in (8.9).
4) In this module we compensate the bistatic term given in (8.10). We average it in respect to slant range and compensate it by multiplying the 2D signal with the $H_1$ function.
5) Here we do a multiplication with $H_2$ transfer functions. The $H_2$ function compensates the time shift corresponding to $\tau_{0T}-\tau_{0R}=a_0$.
6) We multiply the signal with $H_3$, given in (8.16). It brings our processing reference range to the minimal receiver slant range $R_{0R(\min)}$.
7) This module performs the range frequency inverse scaling. Hence, it eliminates the azimuth frequency dependent range scaling. The detailed derivation of the correct discrete implementation of the Inverse Scaling algorithm is given in section 7.12. After the step 8, the result is in slant range - azimuth frequency domain;
8) We multiply the result with transfer function $H_4$, given in (8.17);

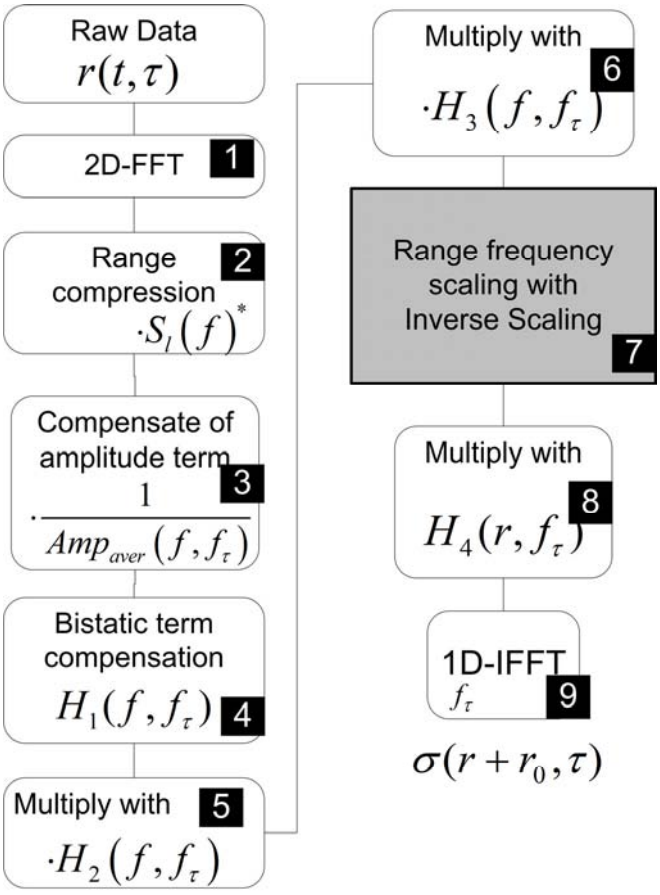


Figure 8.1. Tandem configuration processor

9) This step is the last step of the Tandem case processor. It performs one-dimensional IFFT onto the azimuth frequency. The final result is in slant range - azimuth time domains.

We should note that the Tandem case is the only bistatic configuration that can be processed using a monostatic algorithm, but only after compensating the bistatic deformation term. The rest of the configurations require more complicated processors.

### 8.2.2 Spaceborne Simulation

We will demonstrate the validity of our processor for the Tandem configuration by means of some simulations.

Table 8.1. Spaceborne Tandem case

| **Parameter** | **Transmitter** | **Receiver** |
|---|---|---|
| Speed of satellites | 7000 m/s | 7000 m/s |
| Pulse duration | 8.5 μs | |
| Carrier Frequency | 5.16 GHz | |
| Bandwidth | 40 MHz | |
| PRF | 2500 Hz | |
| Squint angle | 0.1° | -0.1° |
| Off-Nadir angle | 45° | 45° |
| Opening angle in azimuth direction | 0.5° | 0.5° |
| Opening angle in elevation | 5° | 5° |
| Distance between satellites (constant) | 1000 m | |
| Distance of closest approach of PT1/PT2 | 315 km/325 km | |

Table 8.1 shows the parameters of particular spaceborne simulation, and Figure 8.2 presents the corresponding focusing results. The scene consists of 2 PTs separated by 10 km in range direction.

The magnitudes of the 1st PT and 2nd PT were deliberately chosen different to distinguish the correct positions after the processing. The distance between the focused peaks is in accordance with the simulated placement.

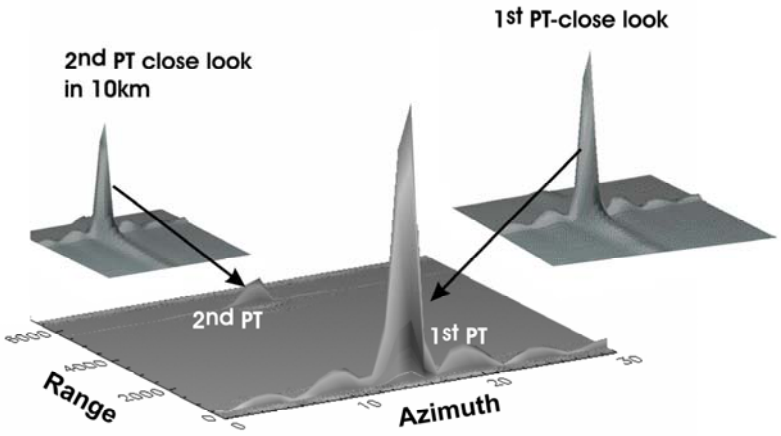


Figure 8.2. Results of the focusing for the spaceborne Tandem case

### 8.2.3 Airborne Simulation

Next we proceed with an airborne simulation, with the parameters given in Table 8.2. The airplanes follow each other with a constant baseline of 500 m. The scene consists of 10 point targets located on the vertexes of a 2x5 matrix (where 2 is the number of range columns and 5 is the number of azimuth rows). They have a separation in the azimuth direction of 10 m (resolution is 0.3 m), while the separation in the range direction is 100 m (with a resolution of 1.5 m).

Table 8.2. Airborne Tandem Case

| **Parameter** | **Transmitter** | **Receiver** |
|---|---|---|
| Speed of airplanes | 98 m/s | 98 m/s |
| Pulse duration | 3 μs | |
| Carrier Frequency | 10.13 GHz | |
| Bandwidth | 100 MHz | |
| PRF | 125 0Hz | |
| Squint angle | 2° | -2° |
| Off-Nadir angle | 55° | 55° |
| Opening angle in azimuth direction | 3° | 3° |
| Opening angle in elevation | 7° | 7° |
| Distance between airplanes (constant) | 500 m | |
| Distance of closest approach of PT1-PT5(m) | 6519.2<br>6319.2<br>6119.2<br>5919.2<br>5719.2 | |

The focusing result for this particular configuration is shown in Figure 8.3. The PTs are correctly focused, and the distances calculated from the focused result are identical to initial given values.

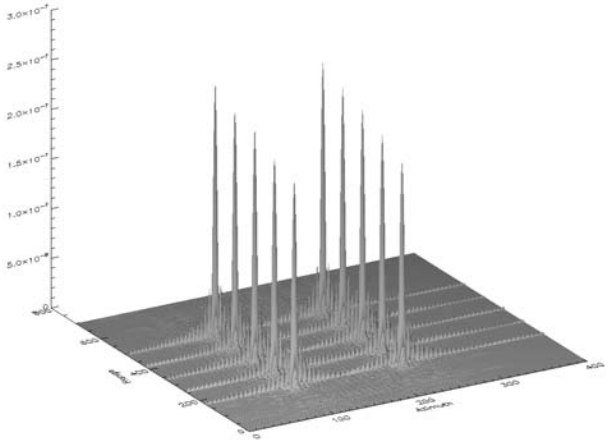

Figure 8.3. Results of the focusing for the airborne Tandem case

## 8.3 Translationally Invariant Configuration

### 8.3.1 Theoretical Derivation of the Processing Algorithm

Another very important bistatic constellation is the translationally invariant (TI) configuration, where the transmitter and the receiver move on parallel tracks with equal velocities. This constellation was described in section 2.3. The bistatic point target reference spectrum (BPTRS) still only depends on the slant range and is invariant with respect to the azimuth time. After some rearrangements in (4.1) and (4.2), we end up with the BPTRS that shows quasi-monostatic and a bistatic phase terms, given in (8.19) and (8.20) respectively:

$$\Psi_{QM}\left(f,f_\tau\right)=\pi\left(2\tau_{0R}+a_0\right)\cdot f_\tau+\frac{4\pi}{c}\frac{R_{0R}+R_{0T}}{2}\cdot F^{\frac{1}{2}} \tag{8.19}$$

$$\Psi_{BI}\left(f,f_\tau\right)=\frac{2\pi}{c}\frac{v^2}{\left(f+f_0\right)^2}\cdot\frac{F^{\frac{3}{2}}}{R_{0R}+R_{0T}}\cdot\left(a_0-f_\tau\frac{c}{2v^2}\frac{R_{0T}-R_{0R}}{F^{\frac{1}{2}}}\right)^2 \tag{8.20}$$

Careful observation of (8.19) and (8.20) makes it clear that basically two problems must be solved: the compensation of bistatic term and expression of $R_{0T}$ in terms of $R_{0R}$.

While in the Tandem case the bistatic acquisition can be understood as a monostatic one located at the middle of the baseline, the situation is different for the translationally invariant case. This can be easily seen from (8.19), where the phases are expressed in terms of $\left(R_{0R}+R_{0T}\right)/2$, and not in terms of $R_{0R}$. We propose a range blockwise processing leading to a modified translationally invariant Inverse Scaling algorithm.

Again, the spectrum of the received bistatic SAR raw data can be calculated as the double integral over the individual BPTRS:

$$W\left(f,f_\tau\right)=\int\int G_l\left(f,f_\tau,R_{0R},\tau_{0R}\right)dR_{0R}d\tau_{0R} \tag{8.21}$$

$G_l$ is the BPTRS given in (3.136). The bistatic preprocessing is done in range blocks. For each block, the bistatic term and the amplitude correction factors are substituted by their averaged values over the range block.

Amplitude term for translationally invariant case was calculated in (4.24). Amplitude term is not as vital as other terms of BPTRS. Hence, we use approximation in $F^{\frac{1}{2}}(f,f_\tau)=\sqrt{(f+f_0)^2-\frac{f_\tau^2 c^2}{4v^2}}$ and ignore $\frac{f_\tau^2 c^2}{4v^2}$ inside the square root, obtaining $F^{\frac{1}{2}}(f,f_\tau)=|f+f_0|$. We substitute this simple form of $F$ inside (4.24) and get:

$$Amp(f,f_\tau,R_{0R})=\frac{|f+f_0|}{F^{\frac{3}{4}}\cdot v_0\cdot\sqrt{c\cdot\left(\frac{1}{R_{0R}}+\frac{1}{R_{0T}}\right)}}=\frac{1}{v}\sqrt{\frac{f+f_0}{c\cdot\left(\frac{1}{R_{0R}}+\frac{1}{R_{0T}}\right)}} \tag{8.22}$$

We use averaged value of $Amp(f,f_\tau,R_{0R})$ over the slant range $R_{0R}$ and abbreviate it as $Amp(f,f_\tau)_{aver}$:

$$Amp_{aver}(f,f_\tau)=\frac{1}{v}\sqrt{\frac{f+f_0}{c\cdot\left(\frac{1}{R_{0R(aver)}}+\frac{1}{R_{0T(aver)}}\right)}} \tag{8.23}$$

where $R_{0Raver}$,($R_{0Taver}$) is the averaged value of the receiver (transmitter) slant range in each block. The same kind of averaging is done for bistatic phase term given in (8.20), and we obtain the transfer function to compensate the bistatic term:

$$H_1(f,f_\tau)=e^{j\frac{\pi}{c}\cdot\frac{v^2\cdot F^{3/2}}{(f+f_0)^2\cdot(R_{0T}+R_{0R})_{(aver)}}\cdot\left(a_0-f_\tau\cdot\frac{c\cdot(R_{0T(aver)}-R_{0R(aver)})}{2v^2F^{1/2}}\right)^2} \tag{8.24}$$

Since these terms are invariant over the integrands $R_{0R}$, $\tau_{0R}$, they are taken out of the integral given in (8.21). The range chirp spectrum is also factored out, because it only depends on $f$. We compensate the terms outside the integral by multiplying them with their complex conjugates. We end up with following simplifications:

$$W'(f,f_\tau)=\int\int\sigma(R_{0R},\tau_{0R})e^{-j\pi f_\tau(\tau_{0R}+\tau_{0T})}\cdot e^{-j\frac{2\pi}{c}(R_{0R}+R_{0T})F^{\frac{1}{2}}}dR_{0R}d\tau_{0R} \tag{8.25}$$

where:

$$W'(f,f_\tau)=\frac{W(f,f_\tau)\cdot S_l^*(f)\cdot(Bistatic\_term)^*}{Amp_{aver}}=\frac{W(f,f_\tau)\cdot S_l^*(f)}{Amp_{aver}}\cdot H_1(f,f_\tau) \tag{8.26}$$

In the translationally invariant case, the time interval between the transmitter's and the receiver's individual points of closest approach is constant, so we have:

$$\tau_{0T}-\tau_{0R}=a_0=const \tag{8.27}$$

We take the constant phasor containing $a_0$ out of the integral in (8.25), thus obtaining:

$$W''(f,f_\tau)=\int\int\sigma(R_{0R},\tau_{0R})\cdot e^{-j2\pi f_\tau\cdot\tau_{0R}}\cdot e^{-j\frac{2\pi}{c}(R_{0R}+R_{0T})\cdot F^{\frac{1}{2}}}dR_{0R}d\tau_{0R} \tag{8.28}$$

where:

$$W''(f,f_\tau)=W(f,f_\tau)'\cdot e^{j\pi f_\tau\cdot a_0} \tag{8.29}$$

We make an abbreviation:

$$\boxed{H_2(f_\tau)=e^{j\pi f_\tau\cdot a_0}} \tag{8.30}$$

Now we do the integration in (8.28) over $\tau_{0R}$. It is a Fourier integral with respect to the slow time, and we obtain:

$$W''(f,f_\tau)=\int\sigma(R_{0R},f_\tau)\cdot e^{-j\frac{2\pi}{c}(R_{0R}+R_{0T})\cdot F^{\frac{1}{2}}}dR_{0R} \tag{8.31}$$

In order to solve the remaining integral, we need to express $R_{0T}$ in terms of $R_{0R}$. To interpret this as a Fourier integral, as a first approximation we express $R_{0T}$ over $R_{0R}$ by means of a linear regression:

$$R_{0T}=b+a\cdot R_{0R} \tag{8.32}$$

This result is substituted in (8.31). Because $b$ is a constant of the linear regression, the term $e^{-j\frac{4\pi}{c}\frac{b}{2}F_T^{\frac{1}{2}}}$ is also factored out of the integral.

We obtain:

$$W''(f,f_\tau)=e^{-j\frac{4\pi}{c}\frac{b}{2}F^{\frac{1}{2}}}\int\sigma(R_{0R},f_\tau)\cdot e^{-j\frac{2\pi}{c}R_{0R}(1+a)F^{\frac{1}{2}}}dR_{0R} \tag{8.33}$$

We make further abbreviation:

$$\boxed{H_3(f,f_\tau)=\left(e^{-j\frac{4\pi}{c}\frac{b}{2}\cdot F^{\frac{1}{2}}}\right)^*=e^{j\frac{2\pi}{c}b\cdot F^{\frac{1}{2}}}} \tag{8.34}$$

By using this abbreviation in (8.33), we get:

$$W'''(f,f_\tau)=\int\sigma(R_{0R},f_\tau)\cdot e^{-j\frac{2\pi}{c}R_{0R}\cdot(1+a)\cdot F^{\frac{1}{2}}}dR_{0R} \tag{8.35}$$

where:

$$W'''(f,f_\tau)=W''(f,f_\tau)\cdot H_3(f,f_\tau) \tag{8.36}$$

Integral (8.35) looks like Fourier integral with respect to $R_{0R}$, but the $\frac{1}{c}R_{0R}(1+a)\cdot\sqrt{(f+f_0)^2-\frac{f_\tau^2c^2}{4v^2}}$ factor in the phasor causes the scaling of range frequency. The difficulty of the integral (8.35) is the non-linear nature of the scaling. We solved a similar problem in section 7.1. There, $F^{\frac{1}{2}}$ containing a nonlinear dependency over the range frequency $f$ is expanded in a first order Taylor series. We bring only the result:

$$F^{\frac{1}{2}} = \frac{f}{\sqrt{1-\frac{f_\tau^2 c^2}{4v^2 f_0^2}}} + f_0 \cdot \sqrt{1-\frac{f_\tau^2 c^2}{4v^2 f_0^2}} \tag{8.37}$$

We substitute the expression above into the integral expression given in (8.35), thus obtaining:

$$W'''(f, f_\tau) = \int \sigma(R_{0R}, f_\tau) \cdot e^{-j2\pi R_{0R}\left(a(f_\tau)\cdot f + b(f_\tau)\cdot f_0\right)} dR_{0R} \tag{8.38}$$

In the above, the following shorthand notation is introduced:

$$a(f_\tau) = \frac{1}{c}(1+a) \cdot \frac{1}{\sqrt{1-\frac{f_\tau^2 c^2}{4v^2 f_0^2}}},\ b(f_\tau) = \frac{1}{c}(1+a) \cdot \sqrt{1-\frac{f_\tau^2 c^2}{4v^2 f_0^2}} \tag{8.39}$$

(8.38) shows a Fourier integral over the slant range $R_{0R}$. The integration gives the backscattering coefficient spectrum scaled in range direction. But now the scaling is linear:

$$W'''(f, f_\tau) = \sigma\left(a(f_\tau)\cdot f + b(f_\tau)\cdot f_0, f_\tau\right) \tag{8.40}$$

The relation above is very promising. It connects the spectrum of the raw data (which is known) with the backscattering coefficient spectrum. We only need to convert the backscattering coefficient to the space domain and obtain $\sigma(R_{0R}, \tau_{0R})$. The expression of the backscattering coefficient spectrum $\sigma\left(a(f_\tau)\cdot f + b(f_\tau)\cdot f_0, f_\tau\right)$ is scaled. $a(f_\tau)$ is the range scaling factor, and $b(f_\tau)$ is the range frequency shift. Both depend on the azimuth frequency $f_\tau$.

In section 7.7, we already considered a similar task and compensated the range scaling by means of:

$$\sigma(R_{0R}, f_\tau) = \left|a(f_\tau)\right| \cdot e^{j2\pi b(f_\tau)\cdot f_0 R_{0R}} \cdot \int \sigma\left(a(f_\tau)\cdot f + f_0 \cdot b(f_\tau), f_\tau\right) \cdot e^{j2\pi a(f_\tau)\cdot f \cdot R_{0R}} df \tag{8.41}$$

We represent the slant range as:

$$R_{0R} = R_{0R(\min)} + r \tag{8.42}$$

Now we shift (8.41) to the minimal slant range distance $R_{0R(\min)}$ and obtain:

$$\begin{aligned}\sigma\left(r + R_{0R(\min)}, f_\tau\right) = \left|a(f_\tau)\right| \cdot e^{j2\pi\left(r+R_{0R(\min)}\right)\cdot b(f_\tau) f_0} \cdot \\ \int \sigma\left(a(f_\tau)\cdot f + f_0 \cdot b(f_\tau), f_\tau\right) e^{j2\pi a(f_\tau)\cdot f \cdot \left(r+R_{0R(\min)}\right)} df\end{aligned} \tag{8.43}$$

Real SAR data come with some delay $t_0$, so the acquisition starts after this delay. The shift in the time domain is equivalent to the rotation of the signal in the frequency domain with the term $e^{-j2\pi(f+f_0)t_0}$, where $t_0 = \frac{\left(R_{0R} + R_{0T}\right)_{(\min)}}{c}$.

After inserting this phase term in (8.43), and doing some reordering, we obtain:

$$\sigma\left(r+R_{0R(\min)},f_\tau\right)=\left|a\left(f_\tau\right)\right|\cdot e^{j2\pi f_0\cdot b\left(f_\tau\right)\cdot\left(r+R_{0R(\min)}\right)}e^{-j2\pi f_0 t_0}\cdot \\ \cdot\int\sigma\left(a\left(f_\tau\right)\cdot f+f_0\cdot b\left(f_\tau\right),f_\tau\right)\cdot e^{-j2\pi f\left(t_0-a\left(f_\tau\right)\cdot R_{0R(\min)}\right)}\cdot e^{j2\pi r\cdot f\cdot a\left(f_\tau\right)}df \tag{8.44}$$

We introduce here two additional transfer functions:

$$H_4\left(f,f_\tau\right)=e^{-j2\pi f\cdot\left(t_0-a\left(f_\tau\right)\cdot R_{0R(\min)}\right)} \tag{8.45}$$

$$H_5\left(r,f_\tau\right)=\left|a\left(f_\tau\right)\right|\cdot e^{j2\pi f_0\cdot\left(r+R_{0R(\min)}\right)\cdot b\left(f_\tau\right)}e^{-j2\pi f_0\cdot t_0} \tag{8.46}$$

$R_{0R(\min)}$, ($R_{0T(\min)}$) is the smallest value of the receiver (transmitter) slant range in the particular range block;

With these abbreviations, we rewrite (8.44) as:

$$\sigma\left(r+R_{0R(\min)},f_\tau\right)=H_3\left(r,f_\tau\right)\cdot\int\sigma\left(a_{ra}\cdot f+f_0\cdot b_{ra},f_\tau\right)\cdot H_2\left(f,f_\tau\right)\cdot e^{j2\pi r\cdot f\cdot a_{ra}}df \tag{8.47}$$

(8.47) instructs how to carry out the bistatic processing algorithm in the translationally invariant case.

The important modules of the translationally invariant algorithm are presented in Figure 8.4:

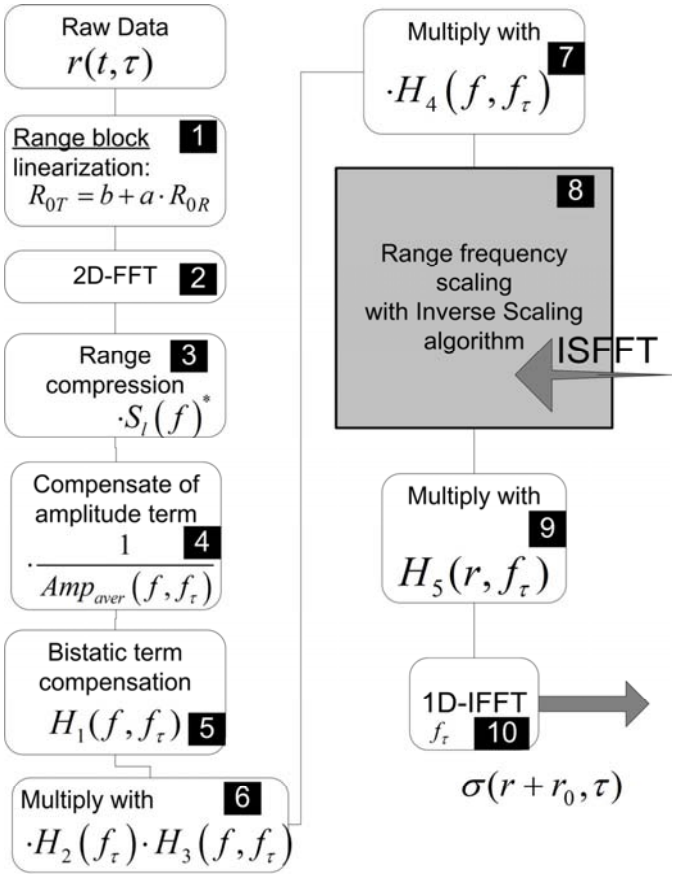


Figure 8.4. Block diagram of modified translationally invariant Inverse Scaled algorithm

The bistatic processor for translationally invariant case consists of the following blocks:

1) In this module, we generate the range blocks and we perform a linearization of the transmitter slant range $R_{0T}$ in respect with $R_{0R}$ in each block.
2) The 2D signal is transformed into the range frequency azimuth frequency domains by the double directional FFT.
3) We do a range compression;
4) The amplitude term is compensated by averaging it in each range block and dividing the signal on the averaged term $Amp_{aver}\left(f, f_\tau\right)$, given in (8.23).
5) In this module, we compensate the bistatic deformation. It is done by canceling the bistatic term given in (8.24). In the translationally invariant case, the bistatic term is azimuth time invariant. In addition, $\tau_{0T} - \tau_{0R} = a_0$ is constant along the whole scene. We average the bistatic term with respect to slant ranges and compensate the bistatic term by multiplying the 2D signal with $H_1$ function.
6) We do a multiplication with $H_2$ and $H_3$ transfer functions. The $H_2$ function compensates a time shift of $\tau_{0T} - \tau_{0R} = a_0$, and the $H_3$ function is the product of parameter $b$, coming from the linear regression.
7) We multiply the signal with $H_4$, given in (8.47), which brings our processing reference range to the minimal receiver slant range $R_{0R(\min)}$.
8) This module performs the range frequency inverse scaling. Hence, it eliminates the azimuth frequency dependent range scaling. The detailed derivation of the correct discrete implementation of Inverse Scaling algorithm is given in section 7.12 . After step 8, the result is in slant range - azimuth frequency domains;
9) We multiply the result with the transfer function $H_5$ given in (8.46);
10) The last step performs one-dimensional IFFT on azimuth frequency. The final result is on slant range - azimuth time domains.

Actually, the modules containing the multiplications with $H_1$, $H_2$, $H_3$ and $H_4$ could be combined as one single step. We separate them to better understand the steps of the processor. Additionally, we still have the freedom of creating the range blocks with a size smaller than the size of the blocks, where the processing is done, and thus performing a finer compensation of the bistatic term. This can be quite useful in the airborne case, as was shown in section 4.1.2.1.

The bistatic processor has been applied to both simulated and real bistatic SAR data.

### 8.3.2 Results Obtained with Simulated Raw Data – Spaceborne Case

Starting with simulated raw data, we consider a spaceborne experiment. For the simulation, we consider a scene consisting of 5 PTs with a separation of 1 km in the range direction. The magnitude of the PTs is weighted (the brightness varies linearly over the slant range).

Some of the parameters are given in Table 8.3. The satellites move parallel with equal velocities and with a baseline of 1 km. the amplitudes of the point targets were deliberately chosen independently in order to better observe the positions of PTs. Figure 8.5 shows the focusing result after applying the bistatic algorithm. Each PT is correctly focused and correctly located.

Table 8.3. Spaceborne translationally invariant case

| Parameter | Transmitter | Receiver |
|---|---|---|
| Speed of satellites | 7000 m/s | 7000 m/s |
| Pulse duration | 8.5 μs | |
| Carrier Frequency | 5.16 GHz | |
| Bandwidth | 40 MHz | |
| PRF | 2500 Hz | |
| Squint angle | 0.0° | 0.0° |
| Off-Nadir angle | 45° | 45° |
| Opening angle in azimuth direction | 0.5° | 0.5° |
| Opening angle in elevation | 6° | 6° |
| Distance between satellites (constant) | 1000 m | |
| Distance of closest approach of PT1-PT5 (km) | 321.7 | 321.0 |
| | 322.7 | 322.0 |
| | 323.7 | 323.0 |
| | 324.7 | 324.0 |
| | 325.7 | 325.0 |

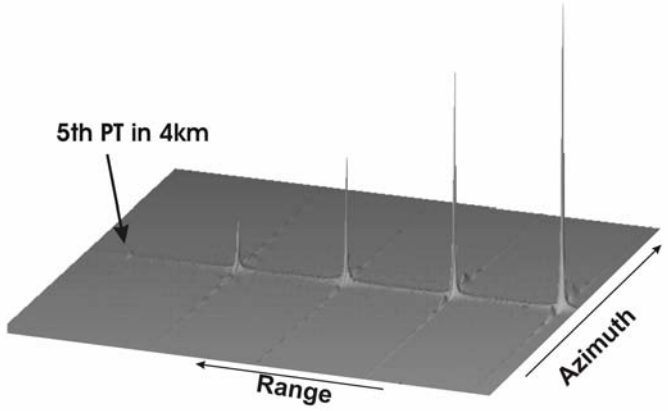


Figure 8.5. Results of the focusing for the spaceborne translationally invariant case

### 8.3.3 Results Obtained with Simulated Raw Data – Airborne Case

The next test we perform is an airborne experiment. The SAR scene consists of 20 point targets allocated at a 2x5 matrix (where 2 is the number of range columns and 5 is the number of azimuth rows). The separation between the PTs is 10 m in azimuth direction and 100 m in range direction. The parameters of the simulation are given in

Table 8.4. In the airborne case, as compared to the spaceborne case, the scaling coefficient strongly differs from 1. The maximum value of the scaling coefficient in the spaceborne case is 1.001, while in the airborne configuration the scaling factor approaches 1.03.

Table 8.4. Airborne translationally invariant case

| Parameter | Transmitter | Receiver |
|---|---|---|
| Speed of satellites | 110 m/s | 110 m/s |
| Pulse duration | 3.0 μs | |
| Carrier Frequency | 10.13 GHz | |
| Bandwidth | 100 MHz | |
| PRF | 1250 Hz | |
| Squint angle | 0.0° | 0.0° |
| Off-Nadir angle | 57° | 55° |
| Opening angle in azimuth direction | 1.8° | 1.8° |

| | | |
|---|---|---|
| Opening angle in elevation | 8° | 8° |
| Distance between satellites (constant) | 1000 m | |

After doing the processing by using the short version of the Inverse Scaling approach given in section 7.12.1 (it does not take into account the time and the frequency extension), we obtain an erroneous focusing result as shown in Figure 8.6.

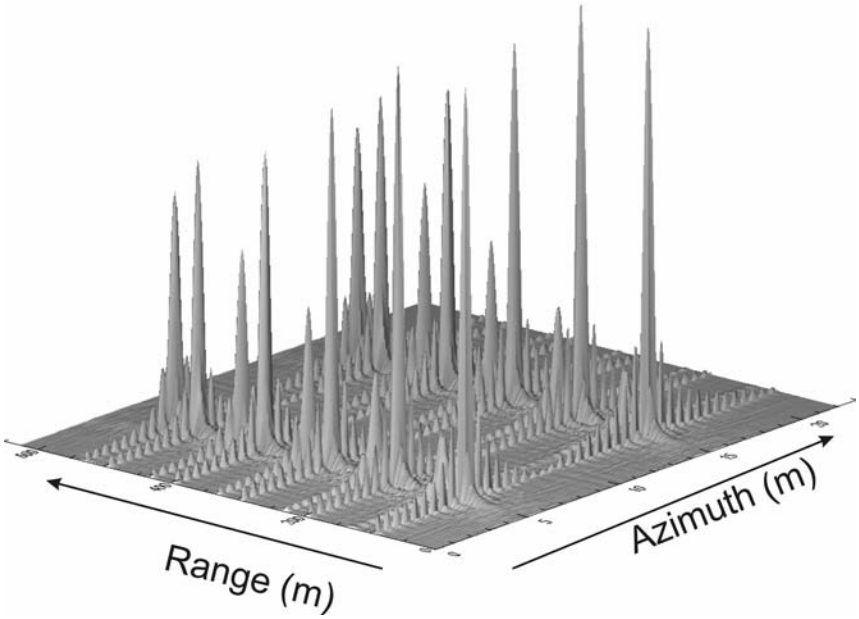


Figure 8.6. Results of the focusing for the airborne translationally invariant case – focusing with the short Inverse Scaling module

We observe that in the range direction we get 10 PTs instead of 5. This kind of wrong result was predicted already in section 7.12.2. The source of the error was the wrong implementation of the Inverse Scaling algorithm (it does not take into account the extensions of the signal at the different steps of the algorithm).

After applying the corrected Inverse Scaling module developed in section 7.12.2, we obtain correct focusing result, as shown in Figure 8.7.

A closer view of this result is displayed in Figure 8.8 , where the upper part shows the azimuth direction and the lower part shows the range direction. The distance between the range columns is calculated from the simulation result and has a value of 10 m. It corresponds to the initial allocation of the PTs. The distance between the first and the last azimuth row is equal to 400 m, which is also true.

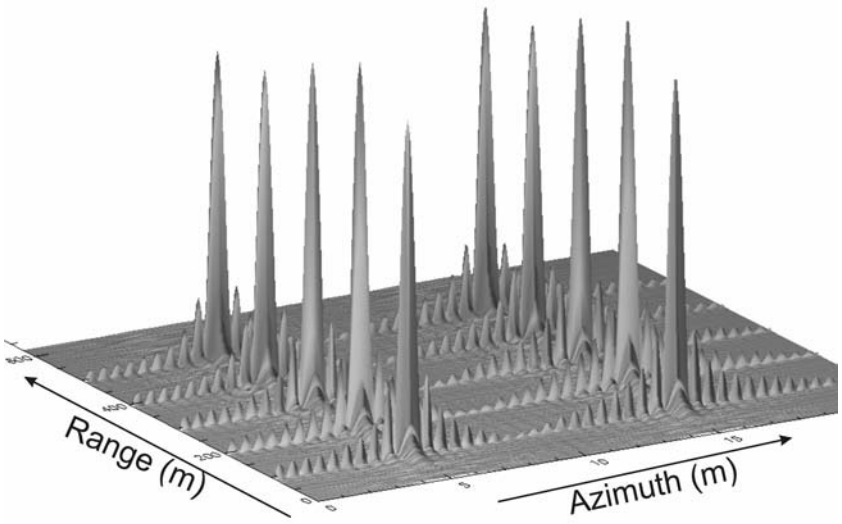


Figure 8.7. Results of the focusing for the airborne translationally invariant case – Focusing with the corrected Inverse Scaling module

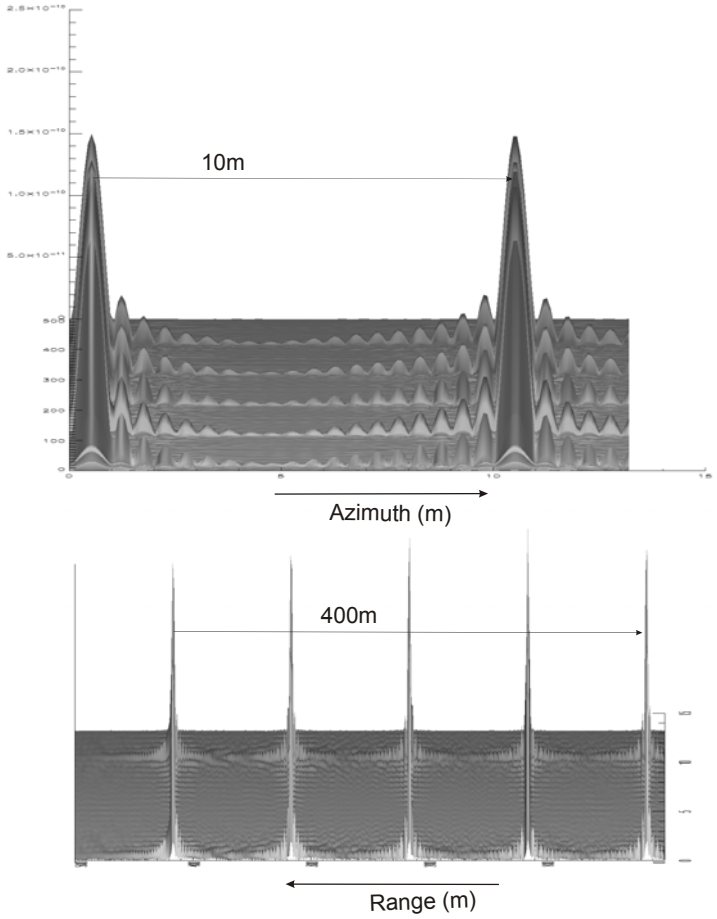


Figure 8.8. Closer look of the previous results: the upper part represents the azimuth direction; the lower part represents the range direction

### 8.3.4 Results Obtained with Real Bistatic SAR Data

As the next step, we applied our bistatic processor to raw data of a real bistatic experiment. The detailed description of the experiment and the obtained results can be found in [19]-[21]. The data were acquired by FGAN[1]'s PAMIR (mounted on a Transall C-160) and AER-II (mounted on a Do-228), shown in Figure 8.9. The data were provided as part of our collaboration in bistatic SAR. The SAR sensors operate in the X-band sharing a common bandwidth of 300 MHz.

Because of wind and some other reasons, it was not possible to maintain an exact parallel track of the airplanes. Hence, this experiment cannot be considered as a purely translationally invariant configuration. The bistatic parameter turned out to be crucial for the bistatic processing [19]-[21].


Figure 8.9 FGAN's transmitter on Do-228 (left) and receiver on Transall-C160 (right)

The positions of the airplanes were estimated with the Kalman filter by fusing GPS[2] with INS[3] measurements. The bistatic parameter estimation ($a_0, a_2, v_T, v_R$) improved the image quality considerably, as we can see in Figure 8.9 in a cut-out of the focused result, which shows the city of Oberndorf (Lech), Germany.

[1] German research establishment for applied natural sciences
[2] Global Positioning and Navigation System
[3] Inertial Navigation System

Figure 8.10. Bistatic SAR image of Oberndorf (Lech), vertically – azimuth direction

## 8.4 Focusing for General Case

### 8.4.1 Theoretical Derivation of the Processing Algorithm

The general case (GC) is given when transmitter and receiver are mounted on different platforms and move on non-parallel trajectories with different velocities. The processing becomes additionally azimuth time dependent. Compared with the bistatic configurations we have seen until now, this azimuth time variance is an additional problem, and it is the cause of the high processing complexity. We will see in the following that the azimuth time dependency causes a scaling of the azimuth frequency. The problem will be solved using the 2D Inverse Scaling algorithm.

The spectrum of the received raw data is given in form of the following integral:

$$W\left(f,f_\tau\right)=\int\int G_l\left(f,f_\tau,R_{0R},\tau_{0R}\right)\cdot dR_{0R}d\tau_{0R} \tag{8.48}$$

$G_l$ is the bistatic point target reference spectrum given in (3.136).

The quasi-monostatic term for the general case according to (4.1) has the following form:

$$\Psi_{QM}\left(f,f_\tau\right)=\pi f_\tau\left(\tau_{0R}+\tau_{0T}\right)+2\pi\frac{R_{0R}}{c}\cdot F_R^{\frac{1}{2}}+2\pi\frac{R_{0T}}{c}\cdot F_T^{\frac{1}{2}} \tag{8.49}$$

The bistatic pre-processing is done blockwise in the range-azimuth blocks. For each block, the amplitude correction factors are substituted by averaged values over range and azimuth time.

Amplitude term for the general case was calculated in (3.135). We additionally use approximation in $F^{\frac{1}{2}}(f,f_\tau)=\sqrt{(f+f_0)^2-\frac{f_\tau^{\,2}c^2}{4v^2}}$, ignoring $\frac{f_\tau^{\,2}c^2}{4v^2}$.

$$F^{\frac{1}{2}}(f,f_\tau)=|f+f_0| \tag{8.50}$$

We substitute $F$ inside (3.135) and obtain:

$$Amp(f,f_\tau,R_{0R},\tau_{0R})=\frac{|f+f_0|}{\sqrt{c\cdot\left(\frac{F_R^{\frac{3}{2}}\cdot v_R^{\,2}}{R_{0R}}+\frac{F_T^{\frac{3}{2}}\cdot v_T^{\,2}}{R_{0T}}\right)}} \tag{8.51}$$

The average value of $Amp(f,f_\tau,R_{0R})$ over the slant range $R_{0R}$ is abbreviated as $Amp(f,f_\tau)_{aver}$:

$$Amp_{aver}(f,f_\tau)=\sqrt{\frac{f+f_0}{c\cdot\left(\frac{v_R^{\,2}}{R_{0R(aver)}}+\frac{v_T^{\,2}}{R_{0T(aver)}}\right)}} \tag{8.52}$$

The averaged amplitude term is invariant over the integrands $R_{0R}$ and $\tau_{0R}$, and we take them out of the integral in (8.48). We do same for the bistatic term. It is averaged for the transmitter and receiver slant ranges and additionally for parameter $a_0$.

$$H_1(f,f_\tau)=\exp\left\{-j\frac{\pi}{c}\cdot\frac{1}{\frac{R_{0R(aver)}}{F_R(f,f_\tau)^{\frac{3}{2}}\cdot v_R^{\,2}}+\frac{R_{0T(aver)}}{F_T(f,f_\tau)^{\frac{3}{2}}\cdot v_T^{\,2}}}\cdot\left[a_{0(aver)}-\frac{f_\tau c}{2}\cdot\left[\frac{R_{0T(aver)}}{v^2{}_T\cdot F_T^{\frac{1}{2}}(f,f_\tau)}-\frac{R_{0R(aver)}}{v_R^{\,2}\cdot F_R^{\frac{1}{2}}(f,f_\tau)}\right]\right]^2\right\} \tag{8.53}$$

The range chirp spectrum is also factored out because it only depends on $f$. This integral then takes on the simple form:

$$W'(f,f_\tau)=\int\int\sigma(R_{0R},\tau_{0R})\cdot e^{-j\pi f_\tau\cdot(\tau_{0R}+\tau_{0T})}\cdot e^{-j2\pi\frac{R_{0R}}{c}\cdot F_R^{\frac{1}{2}}-j2\pi\frac{R_{0T}}{c}\cdot F_T^{\frac{1}{2}}}dR_{0R}d\tau_{0R} \tag{8.54}$$

where:

$$W'(f,f_\tau)=\frac{W(f,f_\tau)\cdot S_l^*(f)\cdot(Bistatic\_term)^*}{Amplitude\_term}=\frac{W(f,f_\tau)\cdot S_l^*(f)}{Amp_{(aver)}(f,f_\tau)}\cdot H_1(f,f_\tau) \tag{8.55}$$

In order to solve the integral (8.54), we must express the pair $(R_{0T},\tau_{0T})$ in terms of $(R_{0R},\tau_{0R})$. Generally these relations are not linear, but as a first approximation, we express $R_{0T}$ and $\tau_{0T}$ over $R_{0R}$ and $\tau_{0R}$ in terms of bilinear regressions:

$$\begin{aligned}\tau_{0T}&=h_{11}+h_{12}\cdot R_{0R}+h_{13}\cdot\tau_{0R}\\ R_{0T}&=h_{21}+h_{22}\cdot R_{0R}+h_{23}\cdot\tau_{0R}\end{aligned} \tag{8.56}$$

We substitute these results in (8.54). Because $h_{11}$ and $h_{21}$ are linear regression constants, the terms $e^{-j\pi f_\tau h_{11}}$ and $e^{-j\frac{2\pi}{c}h_{21}F_T^{\frac{1}{2}}}$ are also factored out of the integral. Thus equation (8.54) is further simplified:

$$W''(f,f_\tau)=\iint\sigma(R_{0R},\tau_{0R})\cdot e^{\underbrace{-j2\pi\tau_{0R}\left(f_\tau\frac{1+h_{13}}{2}+\frac{h_{23}}{c}\cdot F_T^{\frac{1}{2}}\right)}_{bracket\,1}}\cdot e^{\underbrace{-j2\pi R_{0R}\left(\frac{1}{c}F_R^{\frac{1}{2}}+\frac{h_{22}}{c}\cdot F_T^{\frac{1}{2}}+\frac{f_\tau h_{12}}{2}\right)}_{bracket\,2}}dR_{0R}d\tau_{0R} \tag{8.57}$$

where:

$$W''(f,f_\tau)=W'(f,f_\tau)\cdot\left(e^{-j\pi f_\tau h_{11}}\right)^*\cdot\left(e^{-j\frac{2\pi}{c}h_{21}\cdot F_T^{\frac{1}{2}}}\right)^* \tag{8.58}$$

We make an abbreviation:

$$H_2(f,f_\tau)=\cdot\left(e^{-j\pi f_\tau\cdot h_{11}}\right)^*\cdot\left(e^{-j\frac{2\pi}{c}h_{21}\cdot F_T^{\frac{1}{2}}}\right)^*=e^{-j\pi f_\tau\cdot h_{11}-j\frac{2\pi}{c}h_{21}\cdot F_T^{\frac{1}{2}}} \tag{8.59}$$

We substitute (8.59) into (8.58) and obtain:

$$W''(f,f_\tau)=W'(f,f_\tau)\cdot H_2(f,f_\tau) \tag{8.60}$$

The next idea in the course of our derivation is to express the integral (8.57) term $F_T^{\frac{1}{2}}$ (bracket 1) in linear terms of $f_\tau$. The expansions are done by the Taylor series.

Considering the first exponential bracket in (8.545), we truncate the Taylor series expansion after the linear term:

$$F_T^{\frac{1}{2}}(f,f_\tau)\approx F_T^{\frac{1}{2}}{}_{(f_\tau=0)}+\frac{\partial}{\partial f_\tau}F_T^{\frac{1}{2}}{}_{(f_\tau=0)}\cdot f_\tau \tag{8.61}$$

Using the definition given at (3.60), we expand $F_T^{\frac{1}{2}}(f,f_\tau)=\sqrt{(f+f_0)^2-\frac{f_\tau c^2}{4v_R{}^2}}$ with respect to $f_\tau$. At first we determine the zero order term $F_T^{\frac{1}{2}}{}_{(f_\tau=0)}$ of the Taylor series:

$$F_T^{\frac{1}{2}}(f_\tau)_{f_\tau=0} = f + f_0 \tag{8.62}$$

The first order derivative of $F_T^{\frac{1}{2}}$ at zero Doppler vanishes:

$$\left.\frac{\partial F_T^{\frac{1}{2}}(f_\tau)}{\partial f_\tau}\right|_{f_\tau=0} = 0 \tag{8.63}$$

We therefore determine the $F_T^{\frac{1}{2}}$ term as a first-order Taylor expansion:

$$F_T^{\frac{1}{2}}(f_\tau) \approx f + f_0 \tag{8.64}$$

We see that $F_T^{\frac{1}{2}}(f_\tau)$ given in (8.64) is invariant with respect to Doppler frequency $f_\tau$.

Next we express $F_T^{\frac{1}{2}}$, $F_R^{\frac{1}{2}}$ (bracket 2) in linear terms over $f$. Analogously, we expand $F_T^{\frac{1}{2}}$ and $F_R^{\frac{1}{2}}$ in the second bracket, but now with respect to $f$. We have already accomplished this in section 7.8. Here we give the final result:

$$F_{R,T}^{\frac{1}{2}} \approx \frac{f}{\sqrt{1-\frac{f_\tau^2 c^2}{4 v_{R,T}^2 f_0^2}}} + f_0 \cdot \sqrt{1-\frac{f_\tau^2 c^2}{4 v_{R,T}^2 f_0^2}} \tag{8.65}$$

(8.64) and (8.65) are substituted in (8.57). After reorganizing, we have:

$$W''(f, f_\tau) = \int\int \sigma(R_{0R}, \tau_{0R}) \cdot e^{-2j\pi\tau_{0R}\cdot(a_{az} f_\tau + b_{az})} \cdot e^{-2j\pi R_{0R}\cdot(a_{ra} f + b_{ra} f_0)} dR_{0R} d\tau_{0R} \tag{8.66}$$

In the above, the following shorthand notation was used:

$$\begin{aligned}
&a_{az} = \frac{1+h_{13}}{2},\ b_{az} = \frac{h_{23}}{c}\cdot(f+f_0) \\
&a_{ra} = \frac{1}{c}a_{0R} + \frac{h_{22}}{c}\cdot a_{0T},\ b_{ra} = \frac{1}{c}b_{0R} + \frac{h_{22}}{c}\cdot b_{0T} + \frac{f_\tau h_{12}}{2 f_0} \\
&a_{0R,T} = \frac{1}{\sqrt{1-\frac{f_\tau^2 c^2}{4 v_{R,T}^2 f_0^2}}},\ b_{0R,T} = \sqrt{1-\frac{f_\tau^2 c^2}{4 v_{R,T}^2 f_0^2}}
\end{aligned} \tag{8.67}$$

Now the 2D Fourier integral interpretation of (8.66) leads to a backscattering coefficient spectrum that is scaled and shifted in both the range and the azimuth frequency directions:

$$W''(f, f_\tau) = \sigma(a_{ra}\cdot f + b_{ra}\cdot f_0, a_{az}\cdot f_\tau + b_{az}) \tag{8.68}$$

$a_{ra}$ and $a_{az}$ are scaling factors in range and azimuth frequency direction, respectively. $b_{ra}$ and $b_{az}$ are range and azimuth frequency shifts.

The final aim is to express the backscattering coefficient $\sigma(r,\tau)$, compensating the scaling and the shifting factors for both directions.

From (8.67) it is interesting to note that:

- The scaling factor and the shifting of the range frequency depend on the azimuth frequency $f_\tau$.
- The scaling factor of the azimuth frequency in the first-order approximation is constant, but the shift depends on the range frequency $f$.

These observations allow us to separate the scaling compensation steps. First, we compensate the scaling and the shifting with respect to range, and then the constant azimuth scaling and range frequency dependent shifts are corrected. We use Inverse Scaling (section 7.12) or Chirp Scaling approaches (Appendix B) to eliminate the scaling in both directions.

First, the compensation of the scaling in range direction is performed. We introduce the abbreviation:

$$\tilde{f}_\tau = a_{az} \cdot f_\tau + b_{az} \tag{8.69}$$

We have already discussed in section 7.11 how to compensate the range frequency scaling:

$$\sigma\left(R_{0R}, \tilde{f}_\tau\right) = |a_{ra}| \cdot e^{j2\pi b_{ra} \cdot f_0 \cdot R_{0R}} \cdot \int \sigma\left(a_{ra} \cdot f + f_0 \cdot b_{ra}, \tilde{f}_\tau\right) e^{j2\pi a_{ra} \cdot f \cdot R_{0R}} df \tag{8.70}$$

Now we let:

$$R_{0R} = R_{0R(\min)} + r \tag{8.71}$$

We shift (8.70) to the minimal slant range distance $R_{0R(\min)}$. This shift is realized in the following way:

$$\sigma\left(r + R_{0R(\min)}, \tilde{f}_\tau\right) = |a_{ra}| \cdot e^{j2\pi\left(r+R_{0R(\min)}\right) \cdot b_{ra} \cdot f_0} \cdot \int \sigma\left(a_{ra} \cdot f + f_0 \cdot b_{ra}, \tilde{f}_\tau\right) \cdot e^{j2\pi a_{ra} \cdot f \cdot \left(r+R_{0R(\min)}\right)} df \tag{8.72}$$

Real SAR data come with some delay $t_0$, so acquisition starts after this time. This delay needs compensation. The shifting in the time domain is equivalent to a rotation of the signal in the frequency domain with the term: $e^{-j2\pi(f+f_0)\cdot t_0}$, where $t_0 = \dfrac{\left(R_{0R} + R_{0T}\right)_{(\min)}}{c}$.

We insert this phase term in (8.72), and after reordering obtain:

$$\begin{aligned} \sigma\left(r + R_{0R(\min)}, \tilde{f}_\tau\right) = |a_{ra}| \cdot e^{j2\pi f_0 b_{ra} \cdot \left(r+R_{0R(\min)}\right)} \cdot e^{-j2\pi f_0 \cdot t_0} \cdot \\ \cdot \int \sigma\left(a_{ra} \cdot f + f_0 \cdot b_{ra}, \tilde{f}_\tau\right) \cdot e^{-j2\pi f\left(t_0 - a_{ra} \cdot R_{0R(\min)}\right)} e^{j2\pi r f \cdot a_{ra}} df \end{aligned} \tag{8.73}$$

At this stage, we introduce some further notations:

$$\boxed{\begin{aligned} H_{3ra}(f, f_\tau) &= e^{-j2\pi f \cdot \left(t_0 - a_{ra} R_{0R(\min)}\right)} \\ H_{4ra}(f, \tau) &= |a_{ra}| \cdot e^{j2\pi f_0 b_{ra} \cdot \left(r+R_{0R(\min)}\right)} \cdot e^{-j2\pi f_0 t_0} \end{aligned}} \tag{8.74}$$

With these notations, we can rewrite (8.73) as:

$$\sigma\left(r+R_{0R(\min)},\tilde{f}_\tau\right)=H_{4ra}\left(r,\tilde{f}_\tau\right)\cdot \cdot\int\sigma\left(a_{ra}\cdot f+f_0\cdot b_{ra},\tilde{f}_\tau\right)\cdot H_{3ra}\left(f,\tilde{f}_\tau\right)\cdot e^{j2\pi rf\cdot a_{ra}}df \tag{8.75}$$

Equation (8.75) suggests the implementation of the range scaling algorithm. First, the scaled spectrum is multiplied by $H_{3ra}\left(f,\tilde{f}_\tau\right)$. Then, the scaling factor is taken out from the range frequency and the overall result is multiplied by $H_{4ra}\left(r,\tilde{f}_\tau\right)$. At this stage, the 2D signal is slant range - scaled azimuth frequency domains.

In the next step, we compensate the scaling and the shifting in the azimuth direction. As a preprocessing, the signal is converted from slant range to range frequency domain. This is necessary because Inverse Scaling algorithm requires 2D signal in range frequency - azimuth frequency domains at the input.

$$\sigma\left(f,\tau_{0R}\right)=\left|a_{az}\right|\cdot e^{j2\pi\tau_{0R}\cdot b_{az}}\cdot\int\sigma\left(f,a_{az}\cdot f_\tau+b_{az}\right)\cdot e^{j2\pi a_{az}\cdot f_\tau\cdot\tau_{0R}}df_\tau \tag{8.76}$$

The azimuth time is expressed as the sum of the initial time $\tau_{st}$ in each block and a remainder:

$$\tau_{0R}=\tau_{st}+\tau \tag{8.77}$$

Therefore, after shifting (8.76), we have:

$$\sigma\left(f,\tau+\tau_{st}\right)=\left|a_{az}\right|\cdot e^{j2\pi\cdot(\tau+\tau_{st})\cdot b_{az}}\cdot\int\sigma\left(f,a_{az}\cdot f_\tau+b_{az}\right)\cdot e^{j2\pi a_{az}\cdot f_\tau\cdot(\tau+\tau_{st})}df_\tau \tag{8.78}$$

Since the acquisition starts at $\tau_0$, we have an additional phasor inside the integral:

$$\sigma\left(f,\tau+\tau_{st}\right)=\left|a_{az}\right|\cdot e^{j2\pi\cdot(\tau+\tau_{st})\cdot b_{az}}\cdot \cdot\int\sigma\left(f,a_{az}\cdot f_\tau+b_{az}\right)\cdot e^{j2\pi a_{az}\cdot f_\tau\cdot(\tau+\tau_{st})}\cdot e^{-j2\pi f_\tau\cdot\tau_0}df_\tau \tag{8.79}$$

We regroup the phase terms inside the integral and obtain:

$$\sigma\left(f,\tau+\tau_{st}\right)=\left|a_{az}\right|\cdot e^{j2\pi\cdot(\tau+\tau_{st})\cdot b_{az}}\cdot \cdot\int\sigma\left(f,a_{az}\cdot f_\tau+b_{az}\right)\cdot e^{j2\pi f_\tau\cdot(a_{az}\cdot\tau_{st}-\tau_0)}\cdot e^{j2\pi f_\tau\cdot\tau}df_\tau \tag{8.80}$$

Here we introduce some further abbreviations:

$$\boxed{\begin{aligned}H_{3az}\left(f,f_\tau\right)&=e^{j2\pi\cdot f_\tau\cdot(a_{az}\cdot\tau_{st}-\tau_0)}\\H_{4az}\left(f,\tau\right)&=\left|a_{az}\right|\cdot e^{j2\pi\cdot b_{az}\cdot(\tau+\tau_{st})}\end{aligned}} \tag{8.81}$$

And therefore get:

$$\sigma\left(f,\tau+\tau_{st}\right)=H_{4az}\cdot\int\sigma\left(f,a_{az}\cdot f_\tau+b_{az}\right)\cdot H_{3az}\cdot e^{j2\pi f_\tau\cdot\tau}df_\tau \tag{8.82}$$

The scaling in azimuth direction is performed similarly to the scaling in range direction: the azimuth scaled spectrum is first multiplied by $H_{3az}\left(f,f_\tau\right)$, the scaling is then

compensated with Inverse Scaling approach and the outcoming result is multiplied by $H_{4az}(f,\tau)$.

Focusing the algorithm for a general case is shown in Figure 8.11. The processor uses some modules from the translationally invariant algorithm given in Figure 8.4.

1) In this module, we divide the bistatic scene on range-azimuth blocks. The processing is made in each block separately. The translationally invariant case scene was divided only on range blocks. As compared with the translationally invariant case, case processing is in general azimuth time variant. Therefore, division also in azimuth direction is necessary. In each block, bilinear regression is made according to (8.56). The regression coefficients $\begin{matrix} h_{11}, h_{12}, h_{13} \\ h_{21}, h_{22}, h_{23} \end{matrix}$ depend on particular bistatic geometry and stay constant during the block processing.
2) The 2D signal is transformed into the range frequency - azimuth frequency domain by double directional FFT.
3) In this module, range compression is realized.
4) The amplitude term is compensated by averaging it in the range - azimuth blocks and dividing the signal by the averaged term of $Amp_{aver}(f, f_\tau)$, given in (8.52).
5) We compensate the bistatic term. We average it with respect to slant ranges and azimuth times of the closest approach for the transmitter and the receiver and compensate it by multiplying with the $H_1$ function given in (8.53).
6) We multiply with the transfer function $H_2$.
7) We do a multiplication with $H_{3ra}$, which brings our processing reference range to the minimal receiver slant range $R_{0R(\min)}$.
8) In this block we perform a range frequency scaling with Inverse Scaling approach. It eliminates the azimuth frequency dependent range scaling. In Figure 8.11, to save a space, we didn't display steps of the Inverse Scaling algorithm. It is given in detail in section 7.12.
9) We multiply with the transfer function $H_{4ra}$ given in (8.74);
10) The signal after step 9 is in slant range - azimuth frequency domains. In the range direction, the scaling is already taken out. The remaining scaling is in the azimuth frequency direction. Steps 11, 12, 13 solve this problem. In 10, we convert slant range into the range frequency domain.
11) We multiply the 2D spectrum with $H_{3az}$.
12) We cancel scaling in azimuth frequency direction.
13) We multiply the signal with $H_{4az}$.
14) We perform a one-dimensional IFFT of azimuth frequency. The final result is slant range - azimuth time domains.

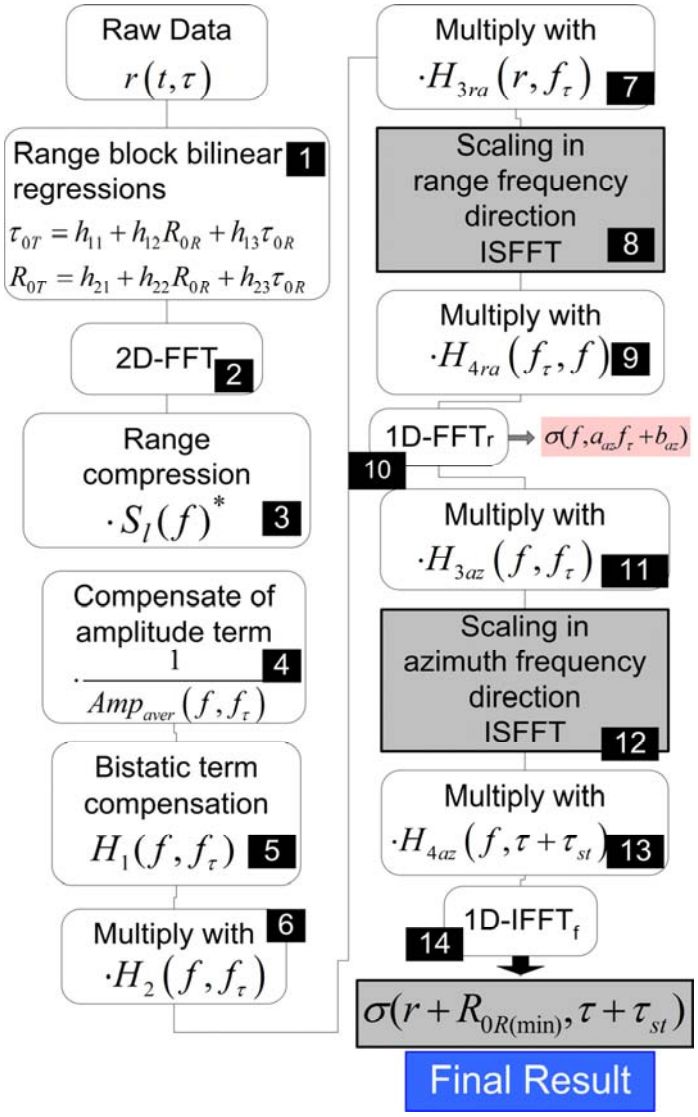


Figure 8.11. General case processing block diagram

### 8.4.2 Simulation Results

To demonstrate the validity of the general bistatic algorithm, we conducted a further simulation with the spaceborne parameters given in Table 8.5. The satellites have different velocity vectors (the absolute values are different and they move on non-parallel tracks).

The scene consisted of 15 PTs located on the vertexes of a 5x3 matrix (where 5 is the number of range columns and 3 is the number of azimuth rows), with a separation in each direction of 1 km.

After compensating the range scaling and the shifting, the PTs seem correctly focused (Figure 8.12), but a closer look shows incorrect displacements (Figure 8.13, Stage 1). In observing Figure 8.12, it should be kept in mind that the azimuth scaling factors still have not been compensated. The figure also shows a closer view of the first azimuth row. At the azimuth distance of 5 km, the PTs show a range walk of 35 m (the range resolution is 7 m). So, we experience a wrong range positioning due to the uncompensated azimuth shifts.

Table 8.5. Parameters of spaceborne general case

| **Parameter** | **Transmitter** | **Receiver** |
|---|---|---|
| Speed of satellites | 7000 m/s | 7100 m/s |
| Pulse duration | 8.5 μs | |
| Carrier Frequency | 5.16 GHz | |
| Bandwidth | 20 MHz | |
| PRF | 1800 Hz | |
| Squint angle | 0.0° | 0.0° |
| Off-Nadir angle | 45° | 45° |
| Max distance between satellites | 4874 m | |
| Min distance between satellites | 5100 m | |

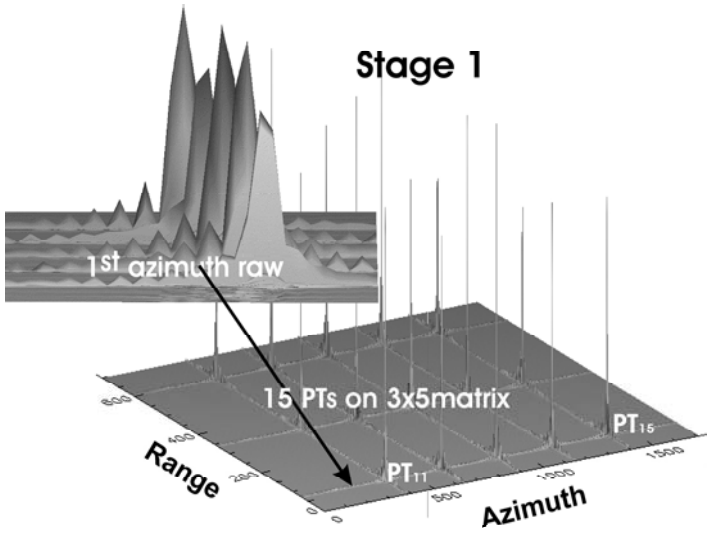


Figure 8.12. Focusing of 15 PTs after compensating the range scaling

Furthermore, as a drawback of the still uncompensated azimuth scaling, the PTs are incorrectly located with respect to the azimuth direction: the distance between the $PT_{11}$ (first row, first column) and $PT_{15}$ (first row, fifth column) is 3966 m instead of 4000 m (the expected value).

As the next step, the azimuth scaling and the shifting are compensated. After getting rid of the azimuth scaling, the PTs look as shown in Figure 8.13, Stage 2. Finally, we cancel the azimuth shifting. Now all PTs move to their correct positions, as displayed in Figure 8.13, Stage 3. Figure 8.14 shows the final result of the 2D range-azimuth bistatic focusing together with the first azimuth row and the first range column.

Analyzing the first range column and the first azimuth row of Figure 8.14, we see that now all PTs are arranged in perfectly straight lines. There is no more range or azimuth walk present. Furthermore, all the PTs are quite nicely focused, finally demonstrating the validity of the approach.

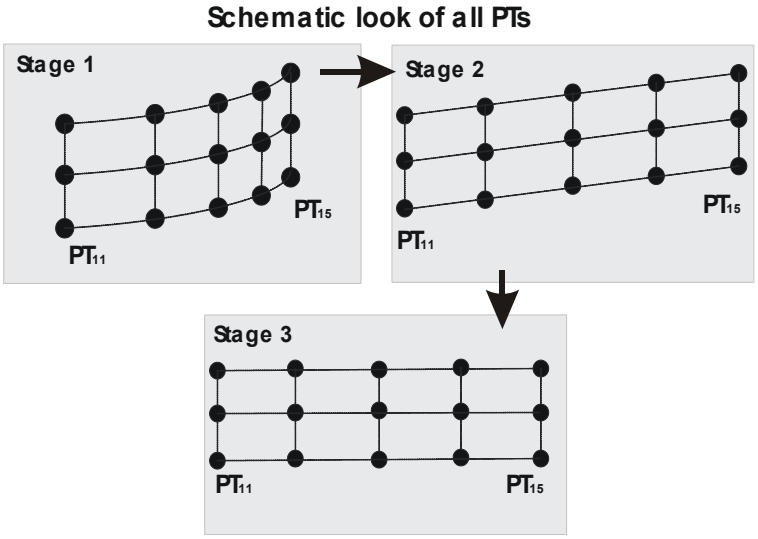


Figure 8.13. Location of all PTs at different stages of the processing: Stage 1 – result after compensating range frequency scaling and shifts; Stage 2 – result after compensating additionally azimuth frequency scaling; Stage 3 – final result after additionally compensating azimuth frequency shifts

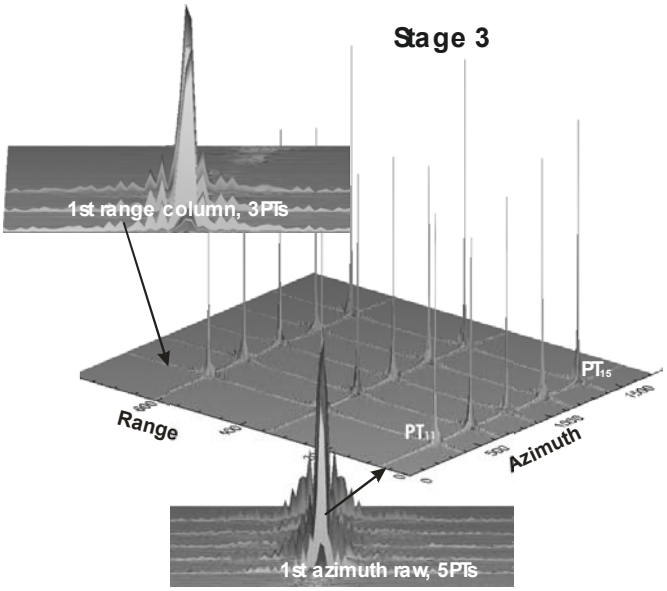


Figure 8.14. Final result of the bistatic focusing for the general case

# 9 Processing Quality Measurements

In this chapter, we evaluate our bistatic processing algorithms. Different SAR algorithms perform the processing with different techniques and accuracy. The resolution obtained from one algorithm can be different from the resolution from one to other.

In addition, in any particular algorithm the range migration curve changes according to the positions of the point targets, therefore the precision of the algorithm is position dependent. In our conventional monostatic approach, the reference point has a minimal slant range. We should then expect the best focusing result for the point targets located at the minimal slant range. The same holds in the bistatic case.

In the Chirp Scaling algorithm [41], the reference point is located at the center of the swath. Therefore, the PTs located at this center are better focused.

To check the quality of our processor, we generate the PTs at different locations on the scene. We analyze the focusing quality of these PTs after the end of the bistatic processing algorithm. For the focused PTs, we measure parameters such as the impulse response width (resolution), maximum peak, Peak Side Lobe Ratio (PSLR), Integrated Side Lobe Ratio (ISLR), etc. To calculate these parameters, we need to make a correct cut of the 2D focused point target.

## 9.1 Directions of the Azimuth and the Range Lines

In the monostatic strip mode case, the azimuth direction is directly related to the flight path. Therefore, the definition of the azimuth and the range directions is well known for the monostatic case. In the bistatic case, the analogous definition of the range and the azimuth directions is not valid, because they depend on the trajectories of the transmitter and the receiver, which normally not coincide. Hence, the direction in the bistatic case can be arbitrary, depending on the bistatic modeling and on the individual processor. In [33], some work to define the bistatic azimuth and range directions was made, and the appropriate resolution estimates were calculated. Instead of the azimuth direction, the ‘lateral’ direction was used for the bistatic case.

In the following, we do not derive the theoretical azimuth and the range resolutions; we measure them directly from the processing result. We tried different methods to determine the directions of the 2D point spread function, but the best results were obtained by using the Radon transformation. For a description and theoretical derivations of the Radon transformation, see Appendix C.

## 9.2 The Range and the Azimuth Lines in our Bistatic Processing

We used the Radon transformation to detect the directions of the range and the azimuth lines of the processed point targets by means of the implementation available in IDL[1].

We checked out the quality of our bistatic processor for different configurations: the Tandem configuration (for both the airborne and the spaceborne case), and the translationally invariant case and the (spaceborne) general case. The Radon transformation was precise enough to determine the range and the azimuth directions. Sometimes the line was not clearly structured, because most of the energy was concentrated on the main peak. In such situations, we used upsampling. The interpolation was made by zero padding in the frequency domain. In all computations, we generated the bistatic scene with PTs allocated at

[1] Interactive Data Language

the vertexes of a 2x5 matrix (being 2 the number of range columns and 5 the number of azimuth lines). Figure 9.1 shows the result of the Radon transformation for one particular simulation, the spaceborne Tandem configuration. The peaks located at the middle of the image, close to 90°, correspond to the angles of the azimuth lines. A very close look gives exact value of this angle. At the beginning and the end of the image, we have peaks located at 0° and 180°, which correspond to the angles of the two range lines.

In most of the simulations done before now, we got the azimuth line parallel to the flight trajectory of the receiver track and the range line perpendicular to the azimuth line. Only for the airborne case of the Tandem configuration do we obtain a 0.5° offset from the range perpendicular direction. We visualize this result in detail in Figure 9.2. In the lower part, we have all 2x5 PTs projected on the ground plane. The top left image represents a closer view of the single PT. It is obvious that the range angle is not exactly perpendicular to the azimuth line. The exact angle was calculated by the Radon transformation, and it has a value of 0.5°. The peak on the top right of image corresponds to a value of 0.5°, and it is shifted to the left from the 0° line.

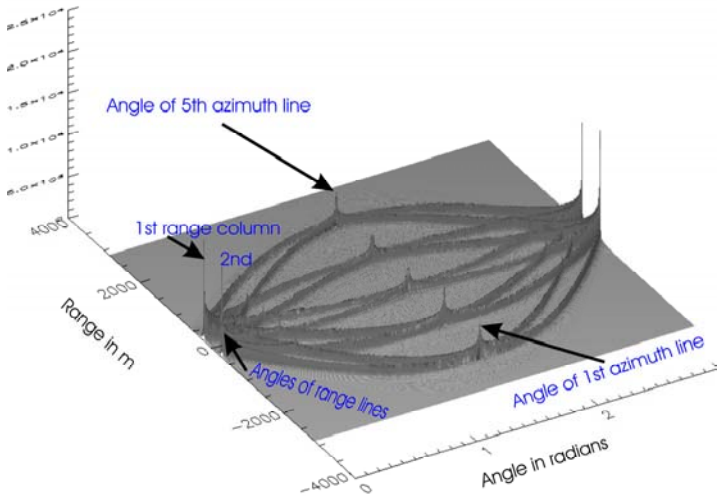


Figure 9.1, Radon transformation of a 2x5 focused image

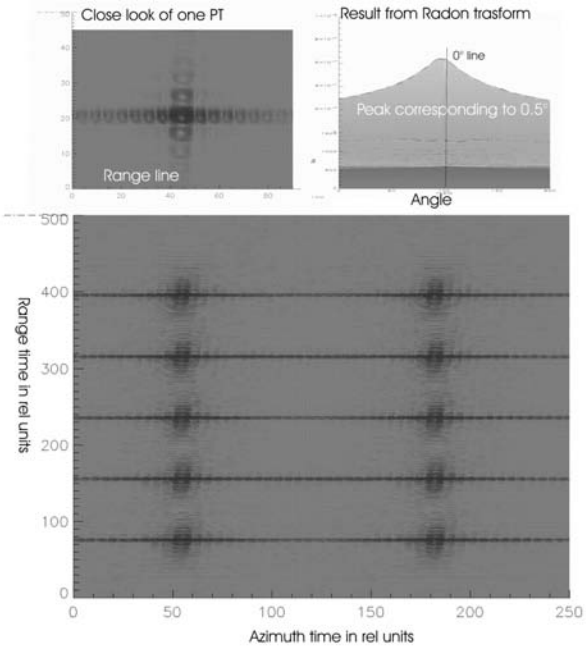


Figure 9.2. Range lines with an offset of 0.5° from the vertical line

## 9.3 SAR Image Quality Measurements Based on Simulations

After determining the correct azimuth and the range direction, we now return to the focused image quality parameters. The individual peaks are sliced over the correct range and azimuth directions. We then calculate the following parameters for the different PTs: the resolution (in both the range and the azimuth directions) at the maximum peak, the integrated side lobe ratio (ISLR) and the peak side lobe ratio (PSLR). The geometric registration was checked as well.

Normally, the resolution is associated with a main peak's width of 3dB. Here, the width of the peak is calculated as the standard deviation of a random variable. We normalize the main lobe of the focused PT, thinking about it as power density function of a random variable. The variance of a random variable can be calculated as the second moment by means of:

$$\sigma^2 = \frac{\int f(t)\cdot(t-\mu)^2\,dt}{\int f(t)\cdot dt} \tag{9.1}$$

$\mu$ is the mean of the random variable. $f(t)$ corresponds to the normalized main lobe.

With a uniform antenna and the reference function weightings, the width of the main lobe response can be expressed in terms of the spatial resolution $\delta$ by the following relation:

$$L = 2.258\cdot\delta \tag{9.2}$$

$L$ is the width of the main lobe.

The Integrated Side Lobe Ratio (ISLR) is defined as the ratio of the side lobes energy to the main lobe energy (analogy with Sinc function Figure 9.3) in the system response of a PT. Mathematically, in the 1D case, the ISLR is given by:

$$ISLR = \frac{\int_{-\infty}^{-\frac{L}{2}} |f(x)|^2\,dx + \int_{\frac{L}{2}}^{\infty} |f(x)|^2\,dx}{\int_{-\frac{L}{2}}^{\frac{L}{2}} |f(x)|^2\,dx} \tag{9.3}$$

$f(x)$ is the amplitude system response to a PT.

In SAR literature the Peak Side Lobe Ratio (PSLR) is defined as the ratio of the maximums of the main lob and the most strong side lobe. In this work PSLR we define as the ratio of the energies of the side lobe to the main lobe.

$$PSLR = \frac{\int_{\frac{L}{2}}^{L} |f(x)|^2\,dx}{\int_{-\frac{L}{2}}^{\frac{L}{2}} |f(x)|^2\,dx} \tag{9.4}$$

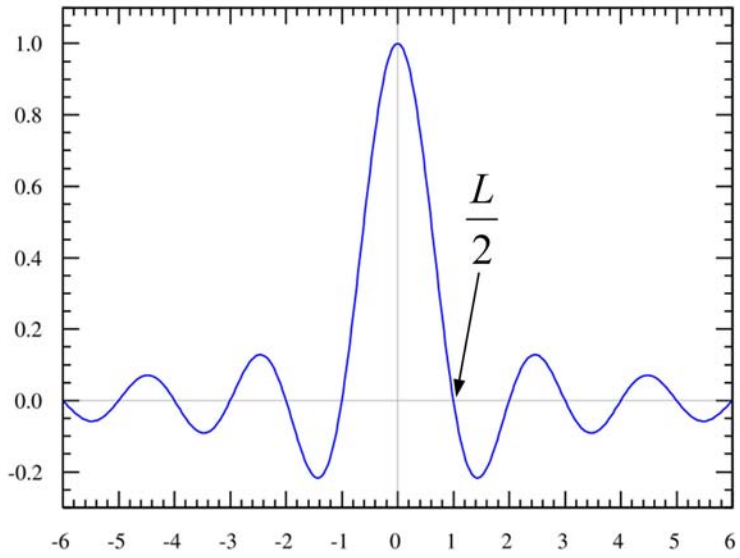


Figure 9.3. Sinc function

The ISLR, the PSLR and the spatial resolution of the SAR system will be affected by introducing a weighting of the antenna reference functions. Indeed, the ISLR and the PSLR are very sensitive to phase errors within the system.

Table 9.1 shows the calculated processing parameters for different configurations in the azimuth direction. Table 9.2 shows similar results, but in the range direction.

For all the configurations, the maximum change in the azimuth resolution was 1.7%. The maximum difference of the ISLR between the first and the second points is 0.8 dB. The maximum difference of the PSLR in the azimuth direction is 2.3dB.

The error in the geometrical registration was quite small in the both directions, so we do not consider it here.

Table 9.1. Calculated processing quality parameters (azimuth direction)

| | Velocity (m/s) | Altitude (km) | BW (MHz) | PRF (Hz) | Az. Resol. (m) | Az. ISLR (dB) | Az. PSLR (dB) | $Peak_{MAX}$ (Norm) |
|---|---|---|---|---|---|---|---|---|
| **Tandem Case (Spaceborne)** | | | | | | | | |
| 1st PT | $V_t=V_r=$ 7000 | 225 | 40 | 2500 | 5.1 | -12.2 | -17.1 | 0.8 |
| 2nd PT (at 4 km) | | | | | 5.1 | -12.2 | -19.3 | 0.5 |
| **Tandem Case (Airborne)** | | | | | | | | |
| 1st PT | $V_t=V_r=$ 98 | 3 | 100 | 1250 | 0.4 | -10.8 | -16.2 | 1.0 |
| 2nd PT (at 400 m) | | | | | 0.4 | -10.0 | -15.8 | 0.9 |
| **Translationally Invariant Case (Spaceborne)** | | | | | | | | |
| 1st PT | $V_t=V_r=$ 7000 | 225 | 40 | 2500 | 5.7 | -13.3 | -20.6 | 0.8 |
| 5nd PT (at 4 km) | | | | | 5.8 | -13.3 | -20.7 | 0.6 |
| **Translationally Invariant Case (Airborne)** | | | | | | | | |
| 1st PT | $V_t=V_r=$ 110 | 3.5 | 100 | 1250 | 0.5 | -10.1 | -15.4 | 0.9 |
| 2nd PT (at 400 m) | | | | | 0.5 | -10.3 | -15.5 | 0.8 |
| **General Case (Spaceborne)** | | | | | | | | |
| $PT_{11}$ | $V_t$=7100 $V_r$=7000 | 300 | 20 | 1800 | 8.6 | -10.7 | -17.1 | 0.9 |
| $PT_{53}$ (at 1 km) | | | | | 8.6 | -9.8 | -14.9 | 0.8 |

In the range direction, the maximum change of the ISLR is 0.9 dB, and the change of the PSLR is 2 dB. The change in the resolution had a limit of 6%.

Processing for the general case is the most challenging and complicated. It contains the scaling steps in both range and azimuth directions. We obtained slightly worse focusing results in this case. The parameters of PT5x3 are not very pleasing. We can observe from Table 9.2 that the change in range direction for ISLR is general case is nearly 5dB, and the value of ISLR in this case is far from an excellent result.

It should be mentioned that the error comes partially from the simulation itself. The reason is that we consider the idealistic model. The PTs in a far range are longer in the beamwidth. Therefore, they experience the bigger resolution than the PTs in the near range. We do not consider the attenuation factor in our processor.

Table 9.2. Calculated processing quality parameters (range direction)

| | Velocity (m/s) | Altitude (km) | BW (MHz) | PRF (Hz) | Az. Resol. (m) | Az. ISLR (dB) | Az. PSLR (dB) | $Peak_{MAX}$ (Norm) |
|---|---|---|---|---|---|---|---|---|
| **Tandem Case (Spaceborne)** | | | | | | | | |
| 1st PT | $V_t=V_r=$ 7000 | 225 | 40 | 2500 | 7.6 | -11.7 | -16.5 | 0.8 |
| 2nd PT (at 4 km) | | | | | 8.2 | -10.4 | -16.4 | 0.5 |
| **Tandem Case (Airborne)** | | | | | | | | |
| 1st PT | $V_t=V_r=$ 98 | 3 | 100 | 1250 | 2.1 | -12.1 | -17.5 | 1.0 |
| 2nd PT (at 400 m) | | | | | 2.1 | -12.4 | -18.4 | 0.9 |
| **Translationally Invariant Case (Spaceborne)** | | | | | | | | |
| 1st PT | $V_t=V_r=$ 7000 | 225 | 40 | 2500 | 6.4 | -11.1 | -17.0 | 0.8 |
| 5nd PT (at 4 km) | | | | | 6.8 | -10.0 | -16.1 | 0.6 |
| **Translationally Invariant Case (Airborne)** | | | | | | | | |
| 2nd PT (at 400 m) | $V_t=V_r=$ 110 | 3.5 | 100 | 1250 | 2.5 | -10.9 | -16.6 | 0.9 |
| 2nd PT (at 400 m) | | | | | 2.6 | -10.6 | -15.9 | 0.8 |
| **General Case (Spaceborne)** | | | | | | | | |
| $PT_{11}$ | $V_t$=7100 $V_r$=7000 | 300 | 20 | 1800 | 11.0 | -11.8 | -18.1 | 0.9 |
| $PT_{53}$ (at 1 km) | | | | | 13.2 | -6.4 | -11.2 | 0.8 |

# 10 2D-Inverse Scaled Fourier Transformation for Bistatic SAR

In this chapter we consider the Inverse Scaled Fourier Transformation in two or more dimensions. The concept was first presented in [7]. The transformation directly transforms back a frequency-scaled spectrum into the non-scaled corresponding counterpart in the space-time domain. Hence it is applicable to those imaging processes where the spectrum of the acquired data is a frequency-scaled replica of the radar brightness spectrum, such as mono- and bistatic focusing applications. The transformation makes use of a quadratic form extension of the Bluenstein formula, also known as the Chirped Z-Transform.

Monostatic SAR data focusing can be carried out by filtering the data in the 2D frequency domain, either applying a change of variables often referred to as Stolt interpolation [62] or using Chirp Scaling techniques [41], or by directly applying an Inverse Scaled Fourier Transformation [62], [3], [4], transforming the counterpart to the space-time domain. This Inverse Scaled FFT can be realized by chirp multiplications in both the time and frequency domain. While the scaling in the monostatic case only affects the range frequency, in the bistatic case the scaling affects both frequency axes: the range frequency and the azimuth (Doppler frequency). Even if the scaling factors of both the range and the azimuth frequencies are not directly coupled, thus allowing the scaling to be removed in two individual steps, the combination of the two individual rescaling operations in one higher dimensional rescaling step is conceptually preferable, especially if the discrete implementation is considered. The derivations are given for 2D signals, but due to the vector matrix notation, they are not restricted to 2D. The first coordinate in the space-time domain refers to the range time, and the second one denotes the azimuth time.

## 10.1 Focusing and Inverse Scaled Fourier Transformation

The Fourier integral interpretation of the range-compressed bistatic raw data spectrum [9] leads to a backscattering coefficient spectrum that is scaled and shifted in both the range and the azimuth frequency directions (section 8.4, (8.68)):

$$W\left(f,f_\tau\right)=\sigma\left(a_{ra}\cdot f+b_{ra}\cdot f_0,a_{az}\cdot f_\tau+b_{az}\right) \tag{10.1}$$

$a_{ra}$ and $a_{az}$ are the scaling factors in the range and the azimuth frequency directions, respectively. $b_{ra}$ and $b_{az}$ are the range and the azimuth frequency shifts. The final aim is to express the backscattering coefficient $\sigma\left(r,\tau\right)$, compensating the scaling and the shifting factors for both directions.

In section 8.4 it was shown that:

- The scaling factor and the shifting of the range frequency depend on the azimuth frequency $f_\tau$.
- The scaling factor of the azimuth frequency in the 1st order approximation is constant, but the shifting depends on the range frequency $f$.

Introducing vectorial notation $\underline{f}=\left[f,f_\tau\right]^T$, we rewrite (10.1) as:

$$\begin{aligned} &W\left(\underline{f}\right)=\sigma\left(A\cdot\underline{f}+\underline{f}_{off}\right)\\ &where:\\ &A=\begin{bmatrix} a_{11} & a_{12}\\ a_{21} & a_{22}\end{bmatrix} \text{ and } \underline{f}_{off}=\begin{bmatrix} b_{ra}\cdot f_0\\ b_{az}\end{bmatrix}\end{aligned} \tag{10.2}$$

Having $a_{11}=a_{ra}$, $a_{22}=a_{az}$, $a_{12}=a_{21}=0$, $A$ becomes a diagonal matrix, indicating that the scaling might also be removed by two 1D Inverse Scaling algorithm, as is done in section 8.4.

If $w(\underline{t})$ and $W\left(\underline{f}\right)$ now form a conventional Fourier transform pair $W\left(\underline{f}\right)\bullet\!\!-^{IFT}\!\!\circ w(\underline{t})$, $\underline{t}=\left[t_r,t_\tau\right]^T$ being the space-time counterpart of f, and assuming $A$ to be invertible, then $w(\underline{t})$ will be given by:

$$\begin{aligned} w(\underline{t}) &= \exp\left\{j2\pi\left[A^{-1}\underline{f}_{off}\right]^T\cdot\underline{t}\right\}\cdot\mathbb{F}^{-1}_{|\underline{f}\to\underline{t}}\left\{\sigma\left(A\cdot\underline{f}\right)\right\}\\ &= \exp\left\{j2\pi\left[A^{-1}\underline{f}_{off}\right]^T\cdot\underline{t}\right\}\cdot\frac{1}{\left|\det\left(A\right)\right|}\cdot\sigma\left(A^{-1T}\cdot\underline{t}\right)\end{aligned} \tag{10.3}$$

yielding an inversely time-scaled replica of the reflectivity of the scene, which is not the focused image that we want. Conceptually, (10.3) allows us to define the Inverse Scaled Fourier Transformation by specifying its desired output:

$$\begin{aligned} \tilde{w}(\underline{t}) &= \exp\left\{j2\pi\left[A^{-1}\underline{f}_{off}\right]^T\cdot\underline{t}\right\}\cdot ScF^{-1}_{|\underline{f}\to\underline{t}}\left\{\sigma\left(A\cdot\underline{f}\right)\right\}\\ &= \exp\left\{j2\pi\left[A^{-1}\underline{f}_{off}\right]^T\cdot\underline{t}\right\}\cdot\frac{1}{\left|\det\left(A\right)\right|}\cdot\sigma\left(\underline{t}\right)\end{aligned} \tag{10.4}$$

saying that the Inverse Scaled Fourier Transformation applied to a scaled spectrum yields its non-scaled counterpart in the space-time domain:

$$Sc\mathbb{F}^{-1}_{|\underline{f}\to\underline{t}}\left\{\sigma\left(A\cdot\underline{f}\right)\right\}=\frac{1}{\left|\det\left(A\right)\right|}\cdot\sigma\left(\underline{t}\right) \tag{10.5}$$

## 10.2 Complex Quadratic Forms and Chirps

Consider the complex time frequency signal $c\left(\underline{t},\underline{f}\right)$ given by:

$$c\left(\underline{t},\underline{f}\right)=\exp\left\{-j\pi\left(\underline{t}-\underline{f}\right)^T\cdot A^T\cdot\left(\underline{t}-\underline{f}\right)\right\} \tag{10.6}$$

where $A$ is a quadratic, not necessarily symmetric, but invertible matrix. Let $S\left(A\cdot\underline{f}\right)$ be some scaled spectrum, so we can consider the following integral:

$$\begin{aligned}\tilde{s}(\underline{t}) &= \exp\left\{j\pi\cdot\underline{t}^T A^T\underline{t}\right\}\cdot\int_{-\infty}^{\infty}\left[S(A\underline{f})\cdot\exp\left\{j\pi\cdot\underline{f}^T A^T\underline{f}\right\}\right]\cdot c(\underline{t},\underline{f})\,d\underline{f}\\ &= \exp\left\{j\pi\cdot\underline{t}^T A^T\underline{t}\right\}\cdot\left[\left[S(A\underline{t})\cdot\exp\left\{j\pi\cdot\underline{t}^T A^T\underline{t}\right\}\right]*\exp\left\{-j\pi\cdot\underline{t}^T A^T\underline{t}\right\}\right]\end{aligned} \tag{10.7}$$

(10.7) indicates that the integral in the frequency domain can be interpreted as a convolution in the time domain. Now we analyze the integral in detail. Substituting (10.6) into (10.7), and factoring out the quadratic form in the exponential term, we obtain (after cancelling some terms):

$$\tilde{s}(\underline{t}) = \int_{-\infty}^{\infty} S(A\underline{f})\cdot\exp\left\{-j2\pi\cdot\underline{f}^T A^T\underline{t}\right\}d\underline{f} = \int_{-\infty}^{\infty} S(A\underline{f})\cdot\exp\left\{-j2\pi\cdot(A\underline{f})^T\cdot\underline{t}\right\}d\underline{f} \tag{10.8}$$

Substituting $\underline{u} = A\cdot\underline{f}$ and $d\underline{u} = |\det(A)|\cdot d\underline{f}$, we get:

$$\tilde{s}(\underline{t}) = \frac{1}{|\det(A)|}\cdot\int_{-\infty}^{\infty} S(\underline{u})\cdot\exp\left\{-j2\pi\cdot\underline{u}^T\cdot\underline{t}\right\}d\underline{u} = \frac{1}{|\det(A)|}\cdot s(\underline{t}) = Sc\mathbb{F}^1_{\underline{f}\to\underline{t}}\left\{S(A\underline{f})\right\} \tag{10.9}$$

Now combining (10.7) and (10.9), we obtain the meaningful result:

$$\begin{aligned}\frac{1}{|\det(A)|}\cdot s(\underline{t}) = Sc\mathbb{F}^1_{\underline{f}\to\underline{t}}\left\{S(A\underline{f})\right\} &= \exp\left\{j\pi\cdot\underline{t}^T A^T\underline{t}\right\}\cdot\\ \cdot\left[\left[S(A\underline{t})\cdot\exp\left\{j\pi\cdot\underline{t}^T A^T\underline{t}\right\}\right]*\exp\left\{-j\pi\cdot\underline{t}^T A^T\underline{t}\right\}\right]&\end{aligned} \tag{10.10}$$

The expression above means that the Inverse Scaled Fourier Transformation can be realized by a sequence of a chirp multiplication in the frequency domain, a chirp convolution in the frequency domain and a chirp multiplication in the time domain. It should be mentioned that in this case we need multidimensional chirps, opposite to the chirps discussed in sections 7.12 for the Inverse Scaled approach.

Now, substituting the independent variable $\underline{t}$ by $\underline{f}$, we obtain a block diagram description of (10.10), displayed in Figure 10.1:

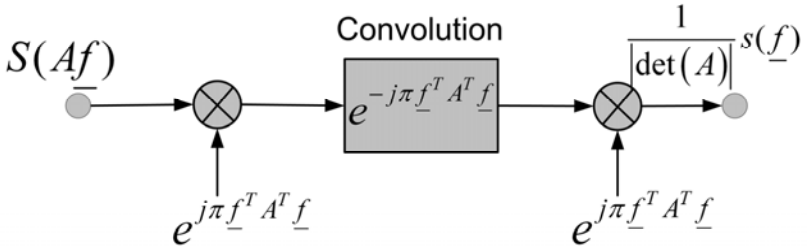


Figure 10.1. Inverse Scaled Fourier transformation with chirps

Figure 10.1 and (10.10) may be understood as a generalisation of the 1D Inverse Scaling approach discussed in section 7.12 for the high dimensional case.

## 10.3 Implementation and Results

The 2D scaling procedure has not yet been applied to the general case [12]. As a first test, we applied the 2D scaling procedure to a set of simulated PTs. The targets are arranged in a 45° line, where the outer target is located at the point $(n_r = 500, n_\tau = 500)$:

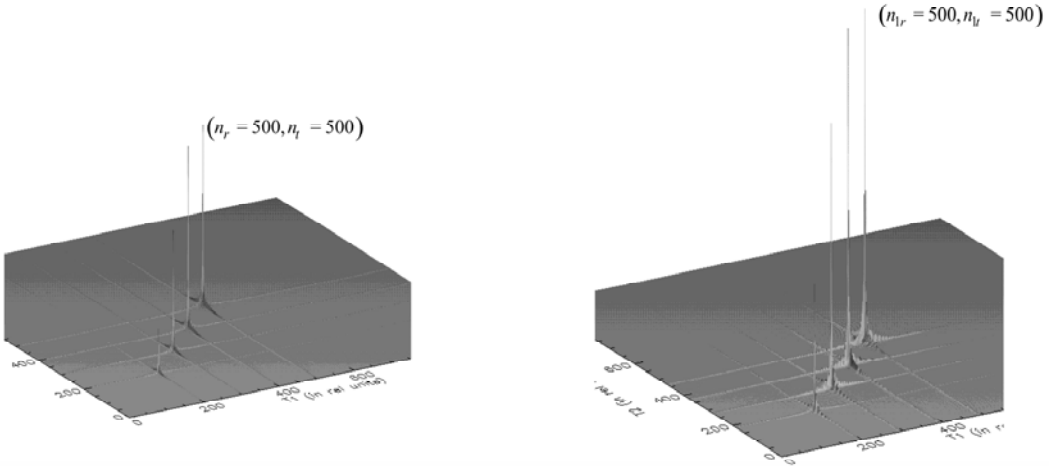


Figure 10.2. 2D Inverse Scaling approach

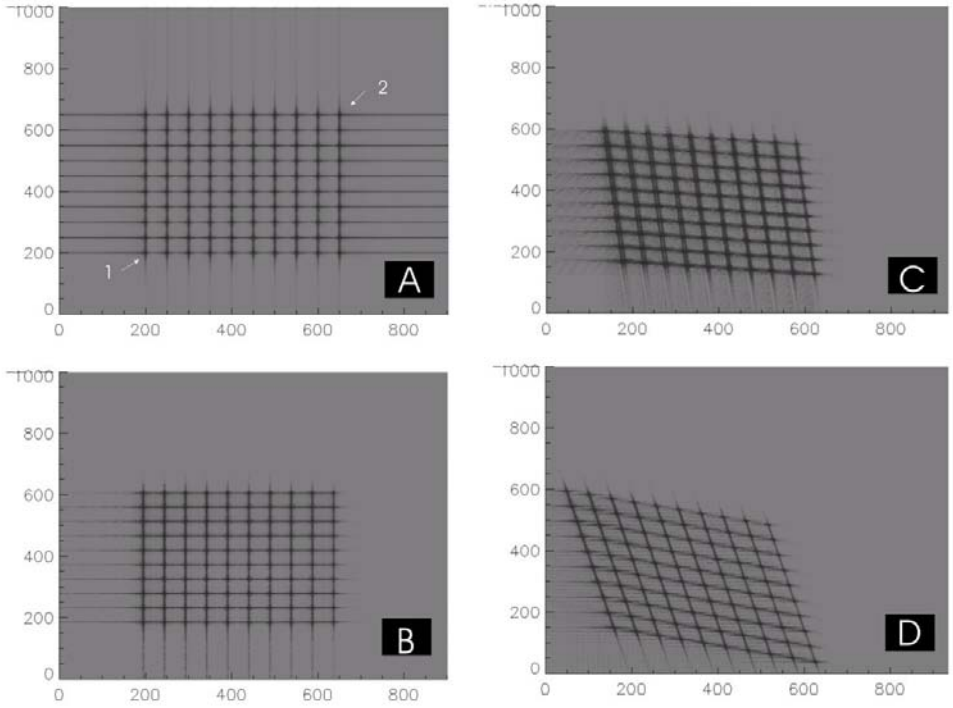


Figure 10.3. 2D Inverse Scaling approach

On the left side of Figure 10.2, we have the simulated PTs. The amplitudes were deliberately set up separately in order to identify the PTs after the end of the Inverse Scaling algorithm. We assume that the image spectrum undergoes a scaling of $(a_r = 1.02, a_\tau = 1.07)$. The right side of Figure 10.2 shows the result after the Inverse Scaling. The outer point is located exactly at $(n_{1r} = 490 = 500/1.02,\ n_{1\tau} = 468 = 500/1.07)$, which proves that the procedure works properly. The determinant of the scaling matrix is not equal to 1, which causes amplitude scaling of the unscaled image.

The next test we perform uses the scaling matrix $A$ with only diagonal terms. We distributed 100 PTs with a separation of 50 samples in both the horizontal and the vertical direction, as visible in part A in Figure 10.3. First, we apply a scaling by means of the

diagonal matrix $A = \begin{pmatrix} a_{11} = 1.02 & a_{12} = 0 \\ a_{21} = 0 & a_{22} = 1.07 \end{pmatrix}$. The result in the time domain is shown in /B/. The first PT shown in A was originally located at the position (200,200), and the second PT was at (650,650). After the scaling, we have new locations of the PTs: the first PT is now located at (196=200/1.02, 186=200/1.07), and the second PT is at (637=650/1.02, 607=650/1.07). Both values are in good agreement with the simulation results. Next, we applied the scaling matrix $A = \begin{pmatrix} a_{11} = 1.02 & a_{12} = 0 \\ a_{21} = 0.2 & a_{22} = 1.07 \end{pmatrix}$, but only with one non-vanishing off-diagonal element. The result is shown in C. We see now that, in addition to scaling, we have a skewing of the image. We got similar results with the scaling matrix $A = \begin{pmatrix} a_{11} = 1.02 & a_{12} = 0.3 \\ a_{21} = 0.2 & a_{22} = 1.07 \end{pmatrix}$, as we see in /D/. In the case of a scaling with non-vanishing off-diagonal terms, we do not have direct relations between the time and the frequency scaling, as we have in the 1D case. Therefore, the results with non-diagonal terms are slightly difficult to interpret.

# 11 Results and Summary

In this doctoral work we have considered the bistatic SAR focusing problem.

While the processing of conventional monostatic SAR data has been studied thoroughly, bistatic processing is an issue of interesting research.

In this work, we have given the first analytical approximated solution for the most difficult bistatic general case configuration.

Our bistatic approach is based on a point target reference spectrum derived at our research institute; we gave a detailed derivation of this bistatic point target reference spectrum and explained it thoroughly. The result of the bistatic formula is an instruction for the processing: the bistatic focusing is converted to a quasi-monostatic processor by first convolving the range-compressed raw data with the bistatic phase term. This convolution can be implemented in the time domain very easily only because of the nature of the bistatic term. The different simulations show that the bistatic deformation term is a short and slowly varying operator. These facts allow realization of the convolution in the time domain by averaging the bistatic term in range azimuth blocks.

Based on the bistatic formula, we gave some approximate expressions of the bistatic azimuth bandwidth and Doppler centroid frequencies. These formulas were later used in the bistatic processing, and they gave perfect results.

The derivation of the bistatic point target reference spectrum is complex and mathematically lengthy; as an approximation, the Method of Stationary Phase was used. The use of this method in the monostatic case is straightforward, but in the bistatic case, the bistatic point of stationary phase is difficult to determine. Additionally, the range history in the bistatic case loses the hyperbolic shape that we had in the monostatic case, becoming a flat-top hyperbola. Therefore, the Method of the Stationary Phase had to be applied very carefully. Hence, we derived four constraints for the validity of the bistatic formula. Two of them were obtained for the transmitter side and two for the receiver side. The bistatic constraints are expressed in terms of the range and azimuth frequencies, the receiver's and transmitter's velocities and slant ranges. The results of the constraints were demonstrated by considering particular bistatic configurations.

Later, the correctness of the bistatic of formula was demonstrated with a bistatic simulator implemented in IDL. We were able to generate the raw data for an arbitrary bistatic configuration and determine all the necessary parameters for the bistatic processing. Initially, we generated the raw data for the scenes only with a single point target and groups of point targets and later focused with our bistatic formula, yielding excellent results: all point targets were correctly focused and positioned at the correct locations.

The focusing of groups of point targets was extended for the whole scene. In the beginning, we considered the azimuth invariant configurations: the Tandem case and the translationally invariant case. Focusing solution for the Tandem case was completed analytically for the spaceborne case. The airborne case was carried out by compensating the averaged bistatic term in range blocks. It should be noted that only the Tandem case can be transformed to the conventional monostatic processing after compensating the bistatic term.

In the translational invariant configuration, we tested the algorithm by simulation and with real bistatic data from an FGAN bistatic experiment. The data were acquired by FGAN's PAMIR (mounted on a Transall C-160) and AER-II (mounted on a Do-228) SAR systems. These data were provided as part of the collaboration on bistatic SAR. Because of the wind and some other reasons, it was not possible to maintain the parallel tracks of the airplanes. Hence, this experiment cannot be considered as a purely translationally invariant configuration. Bistatic parameter tuning turned out to be crucial for the bistatic processing. The positions of the airplanes were estimated by means of the Kalman filter by fusing GPS

with INS measurements. The bistatic parameter estimation improved the image quality considerably.

In the very general bistatic case, the processing became truly azimuth variant, which caused an additional scaling in the azimuth direction. We implemented two directional scaling algorithms in IDL, which initially compensated the frequency scaling in range and in azimuth. For the algorithm of the general case, we used some modules of the inverse scaling approach similar to the chirp scaling algorithm, which only uses chirp multiplications and convolutions. Hence, it was easy to implement for the discrete case. However, it is well known that the convolution causes the extension of the resulting signal, so a modified Inverse Scaling algorithm was implemented in IDL, where we considered the time and the frequency extensions. The performance of the modified Inverse Scaling algorithm was validated by some simulations on groups of point targets. The simulations proved the correctness of our general case processing algorithm. At the end of the processing, all point targets were located in the correct positions.

The quality of the bistatic processing algorithm were checked by calculating the image quality parameters like resolution, peak side lob ratio, integrated side lob ratio, peak maximums for both range and azimuth directions. These directions were calculated by applying the Radon transformation. We observed that our processors for different bistatic cases performed perfectly and gave excellent image quality parameters.

In the future, the sequence of the scaling in the range and the azimuth directions will be changed with a real 2D scaling approach. To address this, we gave the mathematical derivation of a 2D Inverse Scaling approach (it is the generalization of the 1D Inverse Scaling algorithm) and showed some processing results on some simulations.

# Appendix

# A Method of the Stationary Phase

## A.1 General Derivation

Very often we deal with integrals with fast oscillating integrands. In this situation, the Method of the Stationary Phase (MSP) can be applied. We follow the derivation given in [5].

We consider the asymptotic behavior of the following Fourier integral:

$$N(k)=\int_a^b f(t)\cdot e^{jk\cdot\mu(t)}dt \tag{11.1}$$

## A.2 Case when μ(t) has no Extrema within the Interval (a≤t≤b)

Having no maximums or minimums means that $\mu'(t)\neq 0$ within the interval. Therefore, the phase term is continuously increasing or decreasing. We solve the integral given in (11.2) by the integration by parts:

$$\begin{aligned} N(k)&=\int_a^b f(t)\cdot e^{jk\cdot\mu(t)}dt=\int_a^b f(t)\cdot\frac{d}{dt}\frac{e^{jk\cdot\mu(t)}}{jk\mu'(t)}dt \\ &=\left[\frac{f(t)}{jk\cdot\mu'(t)}\cdot e^{jk\cdot\mu(t)}\right]_a^b-\frac{1}{jk}\cdot\int_a^b\frac{d}{dt}\left(\frac{f(t)}{\mu'(t)}\right)\cdot e^{jk\cdot\mu(t)}dt \\ &=\frac{f(b)}{jk\cdot\mu'(b)}\cdot e^{jk\cdot\mu(b)}-\frac{f(a)}{jk\cdot\mu'(a)}\cdot e^{jk\cdot\mu(a)}-\frac{1}{jk}\cdot\int_a^b g(t)\cdot e^{jk\cdot\mu(t)}dt \end{aligned} \tag{11.2}$$

In the above, we have introduced an abbreviation $g(t)=\frac{d}{dt}\left(\frac{f(t)}{\mu'(t)}\right)$. Because of $\mu'(t)\neq 0$, the function $g(t)$ will have no singularities and will not limit to $\infty$.

Now we determine the integral $\int_a^b g(t)\cdot e^{jk\cdot\mu(t)}dt$ given in the right side of (11.2):

$$\begin{aligned} \int_a^b g(t)\cdot e^{jk\cdot\mu(t)}dt&=\int_a^b\frac{g(t)}{jk\cdot\mu'(t)}\frac{d}{dt}e^{jk\cdot\mu(t)}\,dt \\ &=\frac{1}{jk}\left(\frac{g(b)}{\mu'(b)}\cdot e^{jk\cdot\mu(b)}-\frac{g(a)}{\mu'(a)}\cdot e^{jk\cdot\mu(a)}\right)-\frac{1}{jk}\int_a^b\frac{d}{dt}\left(\frac{g(t)}{\mu'(t)}\right)\cdot e^{jk\cdot\mu(t)}dt \\ &=o\left(k^{-1}\right) \end{aligned} \tag{11.3}$$

It is obvious that the integral above vanishes asymptotically. Taking into account the result of (11.3), we obtain for $N(k)$:

$$N(k)=\frac{1}{jk}\cdot\left(\frac{f(b)}{\mu'(b)}\cdot e^{jk\cdot\mu(b)}-\frac{f(a)}{\mu'(a)}\cdot e^{jk\cdot\mu(a)}\right)+o\left(k^{-1}\right) \tag{11.4}$$

The result of (11.4) is equivalent to the following:

$$\boxed{\lim_{k\to\infty} N(k) = O\left(k^{-1}\right)} \tag{11.5}$$

Hence, the spectrum of function with non-stationary phase has asymptotical behavor at infinity.

## A.3 Case when μ(t) has Maximum or Minimum within the Interval (a≤t≤b)

Having an extremum means that at some point $t_0$ $\mu'(t_0) = 0$. This point is called the Point of Stationary Phase (PSP). In the vicinity of extrema $t_0$, the phase changes very slowly. Also, because of the maximum/minimum condition, we can demand that $\mu''(\mathrm{t}_0) \neq 0$. We additionally assume the rate of change of frequency is very high, which is equivalent to $\left|\mu''(t_0)\right|$. In this case, the peak at point of stationary phase will be sharp.

We proceed with calculation of the Fourier integral $N(k)$ by dividing the complete interval of integration into three parts. One part covers the interval in the vicinity of the PSP:

$$\begin{aligned} N(k) &= \int_a^b f(t)\cdot e^{jk\cdot\mu(t)}dt \\ &= \int_a^{t_0-\varepsilon} f(t)\cdot e^{jk\cdot\mu(t)}dt + \int_{t_0-\varepsilon}^{t_0+\varepsilon} f(t)\cdot e^{jk\cdot\mu(t)}dt + \int_{t_0+\varepsilon}^{b} f(t)\cdot e^{jk\cdot\mu(t)}dt \\ &= O\left(k^{-1}\right) \quad + \quad \int_{t_0-\varepsilon}^{t_0+\varepsilon} f(t)\cdot e^{jk\cdot\mu(t)}dt \quad + \quad O\left(k^{-1}\right) \end{aligned} \tag{11.6}$$

In the interval of the integral $\int_a^{t_0-\varepsilon} f(t)\cdot e^{jk\cdot\mu(t)}dt$, we do not have PSPs. Therefore, according to the result of (11.5), it will be asymptotically vanishing. The same is valid for the third integral in (11.6). Hence, we can write:

$$\boxed{N(k) = \int_{t_0-\varepsilon}^{t_0+\varepsilon} f(t)\cdot e^{jk\cdot\mu(t)}dt + O\left(k^{-1}\right)} \tag{11.7}$$

We still have one integral left to determine. We do the Taylor series expansion of the phase function $\mu(t)$ in a vicinity of PSP:

$$\mu(t) = \mu(t_0) + \frac{\mu''(t_0)}{2}\cdot(t-t_0)^2 \ldots \tag{11.8}$$

In the extension above, the first-order term is not available because it is zero at PSP. We substitute the quadratic term of (11.8) into (11.7) and obtain:

$$N(k)=\int_{t_0-\varepsilon}^{t_0+\varepsilon} f(t)\cdot e^{jk\cdot\mu(t)}dt\cong\int_{t_0-\varepsilon}^{t_0+\varepsilon} f(t)\cdot e^{jk\left[\mu(t_0)+\frac{\mu''(t_0)}{2}\cdot(t-t_0)^2\right]}dt$$
$$=e^{jk\cdot\mu(t_0)}\cdot\int_{t_0-\varepsilon}^{t_0+\varepsilon} f(t)\cdot e^{jk\frac{\mu''(t_0)}{2}\cdot(t-t_0)^2}\,dt \tag{11.9}$$

To proceed with our calculation, we introduce an approximation and change the Gaussian distribution with a Dirac function.

$$\delta(t)=\lim_{\sigma\to 0}\frac{1}{\sqrt{\pi}}\cdot\frac{1}{\sigma}\cdot e^{-\frac{t^2}{\sigma^2}} \tag{11.10}$$

We do a substitution $\sigma^2=\sigma_0{}^2\cdot j$ and get:

$$\delta(t)=\lim_{\sigma_0\to 0}\frac{1}{\sqrt{\pi}}\cdot\frac{1}{\sqrt{j}\cdot\sigma_0}\cdot e^{j\frac{t^2}{\sigma_0{}^2}} \tag{11.11}$$

Therefore, for the infinitesimally small values of $\sigma_0$, we can write:

$$\delta(t)\cong\frac{1}{\sqrt{\pi}}\cdot\frac{1}{\sqrt{j}\cdot\sigma_0}\cdot e^{j\frac{t^2}{\sigma_0{}^2}} \tag{11.12}$$

Now we make a change of variables:

$$\frac{k}{2}\cdot\mu''(t_0)=\frac{1}{\sigma_0{}^2}\quad\Leftrightarrow\quad\sigma_0=\sqrt{\frac{2}{k\cdot\mu''(t_0)}} \tag{11.13}$$

In the above, we assumed that $|\mu''(t_0)|$ is very large, which guarantees that $\sigma_0$ is very small.

Now we rewrite (11.10) as:

$$\delta(t)\cong\frac{1}{\sqrt{\pi}}\cdot\frac{1}{\sqrt{j}}\cdot\frac{\sqrt{k\cdot\mu''(t_0)}}{\sqrt{2}}\cdot e^{j\cdot\frac{t^2}{2}\cdot k\cdot\mu''(t_0)}\Leftrightarrow e^{j\cdot\frac{t^2}{2}\cdot k\cdot\mu''(t_0)}\cong\delta(t)\cdot\frac{\sqrt{j}\cdot\sqrt{2}\cdot\sqrt{\pi}}{\sqrt{k\cdot\mu''(t_0)}} \tag{11.14}$$

The result of (11.14) is substituted into (11.9), thus obtaining:

$$\int_{t_0-\varepsilon}^{t_0+\varepsilon} f(t)\cdot e^{jk\frac{\mu''(t_0)}{2}\cdot(t-t_0)^2}\,dt=\int_{t_0-\varepsilon}^{t_0+\varepsilon} f(t)\cdot e^{j\frac{(t-t_0)^2}{\sigma_0^2}}\,dt=\sqrt{\pi}\cdot\sqrt{j}\cdot\sigma_0\cdot\int_{t_0-\varepsilon}^{t_0+\varepsilon} f(t)\cdot\underbrace{\frac{e^{j\frac{(t-t_0)^2}{\sigma_0^2}}}{\sqrt{\pi}\cdot\sqrt{j}\cdot\sigma_0}}_{\cong\delta(t-t_0)}\,dt \tag{11.15}$$

In the above, we resubstitute the result of (11.14) and obtain:

$$\int_{t_0-\varepsilon}^{t_0+\varepsilon} f(t)\cdot e^{jk\frac{\mu''(t_0)}{2}\cdot(t-t_0)^2}\,dt\cong\sqrt{\pi}\cdot\sqrt{j}\cdot\sigma_0\cdot\int_{t_0-\varepsilon}^{t_0+\varepsilon} f(t)\cdot\delta(t-t_0)\,dt \tag{11.16}$$

With the additional substitution $t-t_0=u$, we obtain:

$$\int_{t_0-\varepsilon}^{t_0+\varepsilon} f(t)\cdot e^{jk\frac{\mu''(t_0)}{2}\cdot(t-t_0)^2}\,dt\cong\sqrt{\pi}\cdot\sqrt{j}\cdot\sigma_0\cdot\int_{-\varepsilon}^{\varepsilon} f(u+t_0)\cdot\delta(u)\,du \tag{11.17}$$

From the definition of Dirac function, we can write $\int_{-\varepsilon}^{\varepsilon} s(u)\cdot\delta(u)\,du = s(0)$. Using this property, we modify (11.17) as:

$$\int_{t_0-\varepsilon}^{t_0+\varepsilon} f(t)\cdot e^{jk\frac{\mu''(t_0)}{2}\cdot(t-t_0)^2}\,dt \cong \sqrt{\pi}\cdot\sqrt{j}\cdot\sigma_0\cdot f(t_0) = \sqrt{2\pi}\cdot\sqrt{j}\cdot\frac{1}{\sqrt{k\cdot\mu''(t_0)}}\cdot f(t_0) \tag{11.18}$$

The final result is summarized as:

$$N(k) = \int_a^b f(t)\cdot e^{jk\mu(t)}dt = \int_{-\infty}^{\infty} rect\left(\frac{t-\frac{a+b}{2}}{b-a}\right)\cdot f(t)\cdot e^{jk\cdot\mu(t)}dt$$

$$\cong \sqrt{\pi}\cdot\sqrt{j}\cdot\sqrt{2}\cdot\frac{e^{jk\cdot\mu(t_0)}}{\sqrt{k\cdot\mu''(t_0)}}\cdot f(t_0)\cdot rect\left(\frac{t_0-\frac{a+b}{2}}{b-a}\right)+O\left(k^{-1}\right) \tag{11.19}$$

$$with \quad t_0: \quad \mu'(t_0)=0, \quad \mu''(t_0)\neq 0$$

Interpretation: the spectrum of a high-speed oscillating phasor can be estimated only by knowing the phase term and its second derivative at the point of stationary phase.

## A.4 Example – Chirp Signal

As an example of a function with an oscillating phase, we consider a chirp signal:

$$f(t) = rect\left(\frac{t}{T}\right)\cdot e^{j\pi k_r t^2} \tag{11.20}$$

The frequency of this signal is linearly modulated.

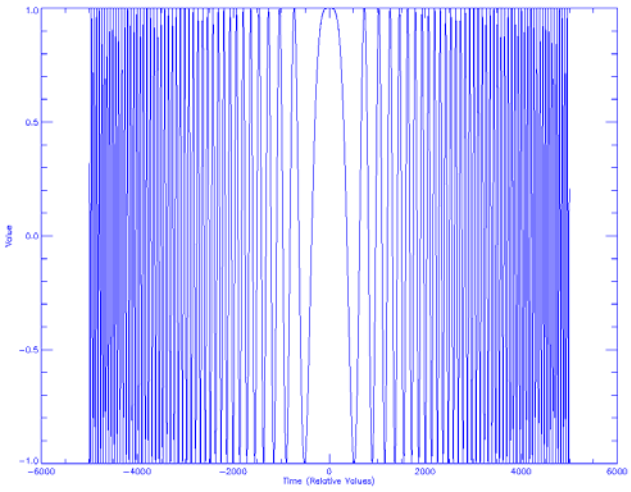


Figure 11.1. Real part of the chirp signal in time domain

Figure 11.1 shows the real part of the chirp signal that is centered at the origin. We observe that the phase is nearly constant at the zero time, but it changes very fast distancing the origin.

The Fourier transformation of the chirp can be calculated as:

$$F(f)=\int_{-\infty}^{\infty} rect\left(\frac{t}{T}\right)\cdot e^{j\pi k_r t^2}\cdot e^{-j2\pi ft}dt=\int_{-\frac{T}{2}}^{\frac{T}{2}}\underbrace{e^{j2\pi f\cdot\left(-t+\frac{k_r}{2}\cdot\frac{t^2}{f}\right)}}_{e^{jk\mu(t)}}dt \tag{11.21}$$

We make a substitution $k=2\pi f;\quad \mu(t)=\frac{k_r}{2}\cdot\frac{t^2}{f}-t$ and end up with expression similar to (11.1). (11.21) is a Fresnel type of integral, and it can be found in most of mathematical books.

Here we solve it by means of the method of stationary phase:

$$\begin{aligned}F(f)&=\int_{-\frac{T}{2}}^{\frac{T}{2}} e^{-j2\pi f\cdot t}\cdot e^{j\pi k_r\cdot t^2}dt=\int_{-\infty}^{\infty} rect\left(\frac{t}{T}\right)\cdot e^{-j2\pi f\cdot t}\cdot e^{j\pi k_r\cdot t^2}dt\\&=\int_{-\infty}^{\infty} rect\left(\frac{t}{T}\right)\cdot e^{-j2\pi f\cdot\left(t-\frac{k_r}{2}\cdot\frac{t^2}{f}\right)}dt\end{aligned} \tag{11.22}$$

The integral above is similar to (11.19). Hence, we can use the method of stationary phase. At first, comparing (11.22) and (11.19), we make relations:

$$\mu'(t)=1-\frac{k_r\cdot t}{f}\Rightarrow\mu'(t_0)=1-\frac{k_r\cdot t_0}{f}=0\Leftrightarrow t_0=\frac{f}{k_r} \tag{11.23}$$

Now we calculate the phase term at the point of stationary phase as:

$$\mu(t_0)=t_0-\frac{k_r\cdot t_0^{\,2}}{2f}=\frac{f}{k_r}-\frac{k_r\cdot f^2}{2f\cdot k_r^{\,2}}=\frac{f}{k_r}\cdot\left(1-\frac{1}{2}\right)=\frac{f}{2k_r} \tag{11.24}$$

We should remember that the method of stationary phase can be applied if the phase term's second derivative at point of closest approach is not zero and has big values. The first condition is fulfilled because $\mu''(t_0)=-\frac{k_r}{f}\neq 0$. The second condition is satisfied if $k_r$ is selected big enough. The chirp sweep rates used in the communication field and in radar applications are normally selected to be high. We apply the method of stationary phase on (11.22) and get:

$$\begin{aligned}F(f)&\cong\sqrt{\pi}\cdot\sqrt{j}\cdot\sqrt{2}\cdot\frac{e^{-j2\pi f\cdot\frac{f}{2k_r}}}{\sqrt{(-2\pi f)\cdot\left(-\frac{k_r}{f}\right)}}\cdot rect\left(\frac{\frac{f}{k_r}}{T}\right)=\sqrt{j}\cdot\frac{1}{\sqrt{k_r}}\cdot e^{-j\pi\cdot\frac{f^2}{k_r}}\cdot rect\left(\frac{f}{k_r\cdot T}\right)\\&=\frac{1}{\sqrt{k_r}}\cdot e^{-j\pi\left(\frac{f^2}{k_r}-\frac{1}{4}\right)}\cdot rect\left(\frac{f}{k_r\cdot T}\right)\end{aligned} \tag{11.25}$$

Therefore, the spectrum of the chirp signal is determined as:

$$f(t)=rect\left(\frac{t}{T}\right)\cdot e^{j\pi k_r t^2}\circ\!\!-\!\!\bullet\, F(f)\cong\frac{1}{\sqrt{k_r}}\cdot e^{-j\pi\frac{f^2}{k_r}}\cdot rect\left(\frac{f}{k_r\cdot T}\right)\cdot e^{j\frac{\pi}{4}} \tag{11.26}$$

This is a nice feature of chip signal: it is a chirp in both time and frequency domains. The real part of the chirp spectrum is shown in Figure 11.2:

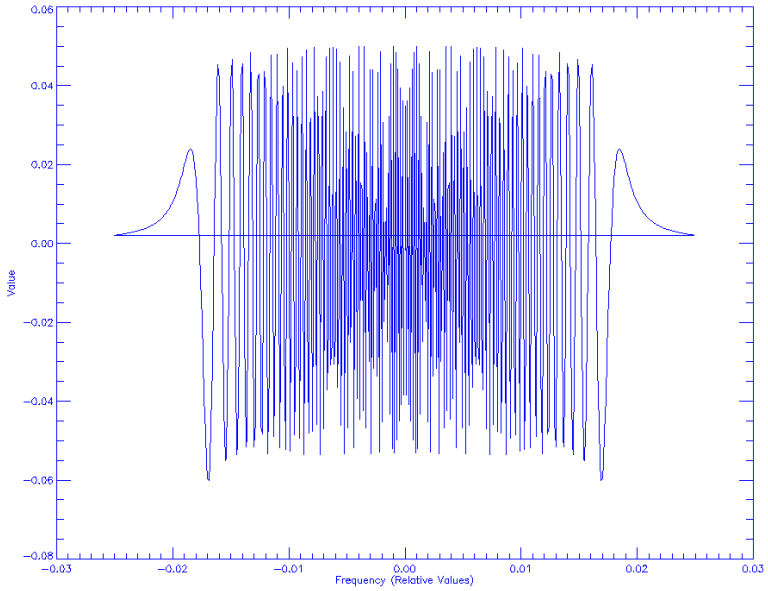


Figure 11.2. Real part of the chirp spectrum

# B Chirp Scaling Algorithm

## B.1 Continuous Implementation

Here we follow the derivation of the Chirp Scaling algorithm [6]. The block diagram of the Chirp Scaling approach is displayed in Figure 11.3.

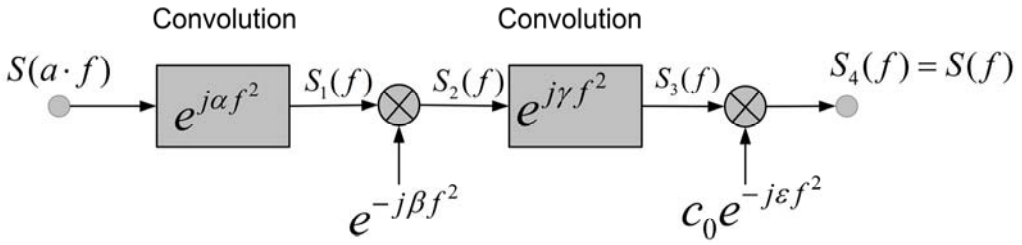


Figure 11.3. Chirp Scaling algorithm in the continuous implementation

It contains the chirp multiplications and convolutions. These chirps have different sweep rates. During the derivation, we will observe that there are some binding relations between these chirp sweep rates.

$S_1(f)$ is the result of the convolution of the input scaled spectrum $S(a_0 f)$ with $e^{j\alpha f^2}$. Therefore, we can write:

$$S_1(f)=\int_{-\infty}^{\infty} S(a\cdot x)\cdot e^{j\alpha\cdot(f-x)^2}dx = e^{j\alpha f^2}\cdot\int_{-\infty}^{\infty} S(a\cdot x)\cdot e^{j\alpha\cdot x^2}\cdot e^{-j2\alpha\cdot x\cdot f}dx \tag{11.27}$$

For the signal $S_2(f)$, we have:

$$S_2(f)=S_1(f)\cdot e^{-j\beta f^2}=e^{j(\alpha-\beta)f^2}\cdot\int_{-\infty}^{\infty} S(a\cdot x)e^{j\alpha x^2}\cdot e^{-j2\alpha x f}dx \tag{11.28}$$

$S_3(f)$ is the convolution of $S_2(f)$ with the chirp $e^{j\gamma f^2}$, so we write:

$$S_3(f)=S_2(f)*e^{j\gamma f^2}=\int_{-\infty}^{\infty} e^{j(\alpha-\beta)\cdot z^2}\cdot\int_{-\infty}^{\infty} S(a\cdot x)\cdot e^{j\alpha x^2}\cdot e^{-j2\alpha xz}\cdot e^{j\gamma\cdot(f-z)^2}dxdz \tag{11.29}$$

We bring the phasor $e^{j(\alpha-\beta)z^2}$ inside the double integral by grouping some phasors, and we obtain:

$$\begin{aligned} S_3(f)&=\int_{-\infty}^{\infty}\int_{-\infty}^{\infty} S(a\cdot x)\cdot e^{j\alpha\cdot x^2}\cdot e^{-j2\alpha\cdot x\cdot z}\cdot e^{j\gamma\cdot f^2}\cdot e^{j\gamma\cdot z^2}\cdot e^{-j2\gamma fz}\cdot e^{j(\alpha-\beta)\cdot z^2}dxdz \\ &=\int_{-\infty}^{\infty} S(a\cdot x)\cdot e^{j\alpha\cdot x^2}\cdot e^{j\gamma f^2}\cdot\int_{-\infty}^{\infty} e^{j(\alpha-\beta+\gamma)\cdot z^2}\cdot e^{-j2(\alpha x+\gamma f)\cdot z}dxdz \end{aligned} \tag{11.30}$$

Now we evaluate the internal integral:

$$I=\int_{-\infty}^{\infty} e^{j(\alpha-\beta+\gamma)\cdot z^2}\cdot e^{-j2(\alpha x+\gamma f)\cdot z}dz \tag{11.31}$$

Until now we did not impose any constraint on the chirp sweep rates. Hence, we have freedom to select them arbitrarily. To force the phasor $e^{j(\alpha-\beta+\gamma)\cdot z^2}$ to vanish, we assume that the following relation holds:

$$\alpha - \beta + \gamma = 0 \tag{11.32}$$

We substitute (11.32) into (11.31) and obtain:

$$I = \int_{-\infty}^{\infty} e^{-j2(\alpha x + \gamma f)\cdot z} dz \tag{11.33}$$

Here we introduce a new variable, $f' = \frac{1}{\pi}(\alpha x + \gamma f)$, and rewrite (11.33) as:

$$I = \int_{-\infty}^{\infty} e^{-j2\pi f' z} dz \tag{11.34}$$

This integral is a Fourier transformation of the unitary function $f(z) = 1$. It is known that the inverse Fourier pair of the unit function is Dirac function. We therefore write:

$$I = \int_{-\infty}^{\infty} e^{-j2\pi f' z} dz = \delta(f') \tag{11.35}$$

Now we resubstitute $f' = \frac{1}{\pi}(\alpha x + \gamma f)$ into (11.35) and get:

$$I = \delta\left\{\frac{1}{\pi}(\alpha x + \gamma f)\right\} = \left|\frac{\pi}{\alpha}\right| \cdot \delta\left(x + \frac{\gamma}{\alpha} f\right) \tag{11.36}$$

In the above, the scaling property of Dirac function was used:

$$\delta(\alpha \cdot x) = \frac{1}{|\alpha|} \cdot \delta(x) \tag{11.37}$$

Now we substitute the result of (11.36) into (11.30), obtaining:

$$\begin{aligned} S_3(f) &= \int_{-\infty}^{\infty} S(a \cdot x) e^{j\alpha x^2} e^{j\gamma f^2} = \left|\frac{\pi}{\alpha}\right| \cdot \delta\left(x + \frac{\gamma}{\alpha} \cdot f\right) dx \\ &= \left|\frac{\pi}{\alpha}\right| S\left(-a\frac{\gamma}{\alpha} \cdot f\right) \cdot e^{j\alpha\left(\frac{\gamma}{\alpha} f\right)^2} \cdot e^{j\gamma f^2} \end{aligned} \tag{11.38}$$

Here we introduce another dependency between the chirp sweep rates:

$$-a\frac{\gamma}{\alpha} = 1 \tag{11.39}$$

which is equivalent to:

$$\frac{\alpha}{\gamma} = -a \tag{11.40}$$

We insert (11.40) into (11.38) and obtain:

$$S_3(f) = \left|\frac{\pi}{\alpha}\right| \cdot S(f) \cdot e^{j\alpha \cdot \left(\frac{\gamma^2}{\alpha} + \gamma\right) \cdot f^2} \tag{11.41}$$

Looking at the algorithm in Figure 11.3, we note that only one step – multiplication by the frequency chirp $c_0 e^{-j\varepsilon f^2}$ is necessary for the final result:

$$S_4(f) = S_3(f)\cdot c_0 \cdot e^{-j\varepsilon f^2} = c_0 \left|\frac{\pi}{\alpha}\right| \cdot S(f) \cdot e^{j\alpha\cdot\left(\frac{\gamma^2}{\alpha}+\gamma\right)\cdot f^2} \cdot e^{-j\varepsilon\cdot f^2} = \\ = c_0 \left|\frac{\pi}{\alpha}\right| \cdot S(f) \cdot e^{j\left(\frac{\gamma^2}{\alpha}+\gamma-\varepsilon\right)\cdot f^2} = ! = S(f) \tag{11.42}$$

Looking at (11.42), it is natural to introduce two new relations:

$$c_0 = \left|\frac{\alpha}{\pi}\right| \tag{11.43}$$

and

$$\varepsilon = \frac{\gamma^2}{\alpha} + \gamma = \frac{\gamma\cdot\beta}{\alpha} \tag{11.44}$$

We calculate the third chirp rate using (11.40) as:

$$\gamma = -\frac{\alpha}{a} \tag{11.45}$$

The second chirp rate $\beta$ is obtained from (11.32) as:

$$\beta = \alpha - \frac{\alpha}{a} = \alpha\cdot\left(1-\frac{1}{a}\right) \tag{11.46}$$

The expression of the fourth chirp rate $\varepsilon$ is determined from (11.44) and using (11.46):

$$\varepsilon = \gamma\frac{\beta}{\alpha} = -\frac{\frac{\alpha}{a}\cdot\alpha\cdot\left(1-\frac{1}{a}\right)}{\alpha} = \alpha\cdot\left(\frac{1}{a^2}-\frac{1}{a}\right) \tag{11.47}$$

As the summary, we collect all the chirp factors together:

$$\boxed{\begin{array}{l} \alpha = \textit{freely selected} \\ \beta = \alpha\cdot\left(1-\frac{1}{a}\right),\ \gamma = -\frac{\alpha}{a},\ \ c_0 = \left|\frac{\alpha}{\pi}\right| \\ \varepsilon = \gamma\cdot\frac{\beta}{\alpha} = -\frac{\frac{\alpha}{a}\cdot\alpha\cdot\left(1-\frac{1}{a}\right)}{\alpha} = \alpha\cdot\left(\frac{1}{a^2}-\frac{1}{a}\right) \end{array}} \tag{11.48}$$

The chirp rates above show the dependence on both the scaling factor $a_0$ (given) and the first chirp rate $\alpha$ (freely selected).

The nice fact that the first chirp rate can be arbitrarily selected is seized by the SAR processors [38], [39]. Their first chirp rate $\alpha$ is chosen equal to the negative value of the transmitted chirp sweep rate. Then, the first convolution in Figure 11.3 becomes equivalent to the range compression, which has to be done anyway. Hence, one convolution is omitted from the processing, which increases the efficiency of the algorithm.

## B.2 Discrete Implementation of the Chirp Scaling Algorithm

We discussed in appendix B.1 the continuous implementation of the Chirp Scaling algorithm. Here, we consider its discrete realization. As already mentioned, we have freedom to select the first chirp rate $\alpha$ arbitrarily. For simplicity, we make substitution: $\alpha \to \pi\alpha$. Then, the chirp rates shown in Figure 11.3 are slightly modified (as shown in Figure 11.4):

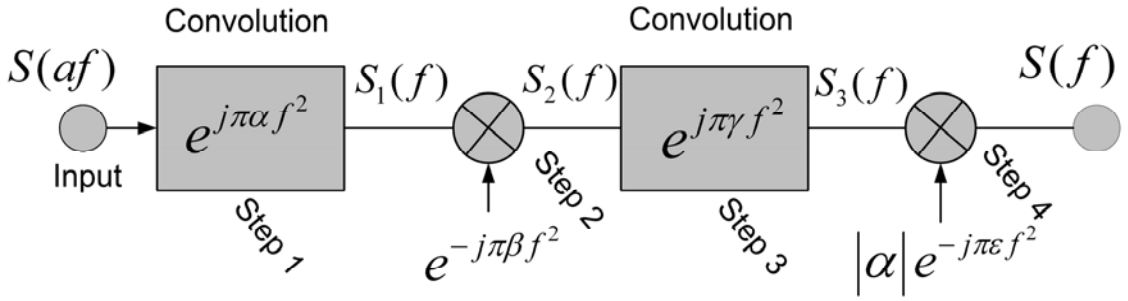


Figure 11.4. Modified continuous implementation of the Chirp Scaling algorithm

All chirp rates have changed by a factor of $\pi$. Nevertheless, all relations given in (11.48) remain unchanged.

The algorithm consists of chirp multiplications and convolutions. The convolutions are carried out by FFT techniques, as was done in the Inverse Scaling algorithm. Figure 11.5 shows the discrete implementation of the Chirp Scaling algorithm:

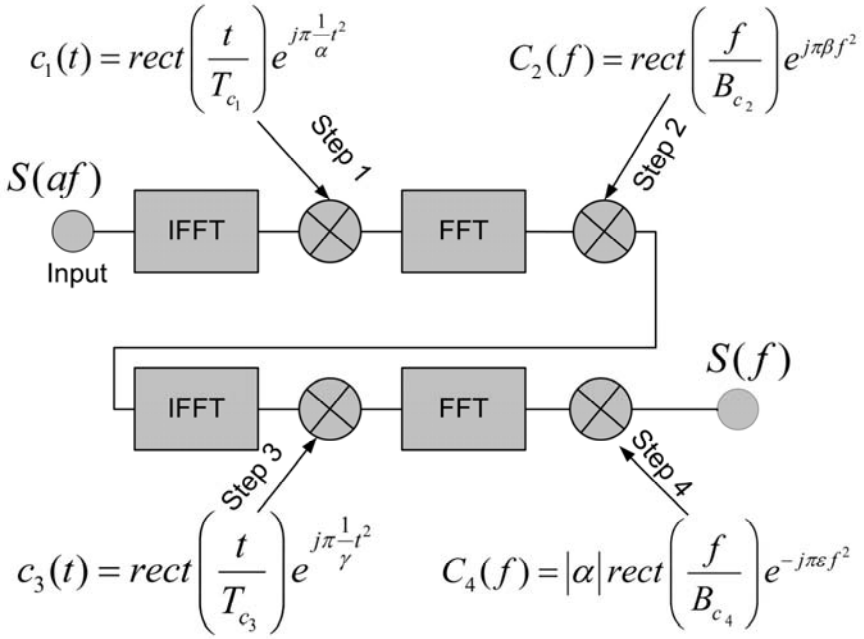


Figure 11.5. Discrete implementation of Chirp Scaling algorithm

Symbols used:

$\Delta f$ is the bandwidth of the input signal.

$T_0$ is the time extent (duration) of the input signal.

$B_{c_{1,2,3,4}}$ are the bandwidths of the corresponding chirps $C_{1,2,3,4}(f)$.

$T_{c_{1,2,3,4}}$ are the time durations of the chirps $c_{1,2,3,4}(t)$.

$T_{1ext,2ext,3ext,4ext}$ are the time extensions at corresponding steps of the algorithm.

$f_{1ext,2ext,3ext,4ext}$ are the equivalent bandwidth extensions.

$T_{1,2,3,4}$ are the equivalent complete time extents.

$\Delta f_{1,2,3,4}$ are the full signal bandwidths.

*Step 1*

Step 1 performs the convolution with the chirp $e^{j\pi\alpha f^2}$. Hence, it extends the bandwidth, but keeps the signal duration unchanged. We calculate the bandwidth of the first chirp $rect\left(\frac{f}{B_{c_1}}\right)\cdot e^{-j\pi\alpha f^2}$. This bandwidth equals to the size of frequency extension $f_{1ext}$ after the step 1:

$$f_{1ext} = B_{c_1} = \frac{T_0}{\alpha} \tag{11.49}$$

Hence, the final extended frequency bandwidth after the step 1 is obtained as:

$$\boxed{\Delta f_1 = \Delta f + f_{1ext}} \tag{11.50}$$

*Step 2*

Here we multiply $S_1(f)$ with $e^{-j\pi\beta f^2}$. Step 2 extends the time and keeps the frequency bandwidth unchanged. Time domain chirp equivalent to $e^{-j\pi\beta f^2}$ can be written as $\sqrt{\beta}\cdot rect\left(\frac{t}{T_{c_2}}\right)\cdot e^{j\pi\frac{1}{\beta}t^2}$. Therefore, the time extension is obtained as:

$$T_{2ext} = T_{c_2} = \beta\cdot\Delta f_1 = \beta\cdot\left(\Delta f + f_{1ext}\right) \tag{11.51}$$

The total time duration after step 2 is given as:

$$\boxed{T_2 = T_1 + T_{2ext} = T_0 + T_{2ext}} \tag{11.52}$$

The frequency bandwidth stays unchanged:

$$\boxed{\Delta f_2 = \Delta f_1 = \Delta f + f_{1ext}} \tag{11.53}$$

*Step 3*

This step contains the convolution of $S_2(f)$ with chirp $e^{j\pi\gamma f^2}$. Thus it does not extend the time:

$$T_{3ext} = 0 \tag{11.54}$$

The total time extent after step 3 is:

$$\boxed{T_3 = T_2 + T_{3ext} = T_2 = T_0 + T_{2ext}} \tag{11.55}$$

The frequency extension after step 3 is calculated as:

$$f_{3ext} = B_{c_3} = \frac{T_2}{\gamma} \tag{11.56}$$

The final frequency bandwidth after the step 3 is given as:

$$\Delta f_3 = \Delta f_2 + f_{3ext} = f_2 + \frac{T_2}{\gamma} \tag{11.57}$$

*Step 4*

The final step is a multiplication of $S_3(f)$ with $|\alpha| \cdot e^{-j\pi\varepsilon f^2}$. It does not change the frequency bandwidth, but it extends the time. The time extension is calculated as:

$$T_{4ext} = T_{c_4} = \varepsilon \cdot f_3 = \varepsilon \cdot \Delta f \cdot (f_2 + f_{3ext}) \tag{11.58}$$

The chirp is generated in the time domain as $\frac{|\alpha|}{\sqrt{\varepsilon}} \cdot rect\left(\frac{t}{T_{4ext}}\right) \cdot e^{j\pi\frac{1}{\varepsilon}t^2}$ and then converted into the frequency domain. For the unchanged bandwidth, we write:

$$\Delta f_4 = \Delta f_3 = \Delta f_2 + f_{3ext} \tag{11.59}$$

## B.3 Standardization of the Chirp Scaling Algorithm

In case of discrete implementation, because we deal with the frequency and the time, we should take care of the standardization like it was done in case of the Inverse Scaling algorithm. Suppose the following:

$t_e$ is the initial sampling time measured in $[s]$.

$f_e$ is the corresponding frequency unit width measured in $[Hz]$.

$N_0$ is the number of initial discrete signal samples.

$\Delta f$ is the bandwidth of the input signal and can be calculated as $\Delta f = \frac{1}{N_0 t_e}$.

We know that the factor $\alpha$ can be freely selected in the algorithm. We introduce a modified scaling factor $\tilde{\alpha}$:

$$\tilde{\alpha} = \alpha \cdot T_e^2 \cdot N_0 \tag{11.60}$$

$\tilde{\alpha}$, given in (11.60), has a dimension of $s^2$, which solves the standardization problem in the future derivations.

*Step 1*

We calculate the values of the time and the frequency extensions after step 1 using (11.49), (11.50). For the complete frequency bandwidth after step 1, we have:

$$\Delta f_1 = \frac{1}{t_e} + \frac{1}{\tilde{\alpha} t_e} = \frac{1}{t_e} \cdot \left(1 + \frac{1}{\tilde{\alpha}}\right) \tag{11.61}$$

And for the time extent, we can write:

$$T_1 = t_e \cdot N_0 \tag{11.62}$$

*Step 2*

At step 2 we use (11.52) and obtain the complete time extent:

$$\begin{aligned} T_2 &= t_e \cdot N_0 + \tilde{\alpha} \cdot t_e^{\,2} \cdot N_0 \cdot \left(1-\frac{1}{a}\right) \cdot \left(\frac{1}{t_e}+\frac{1}{\tilde{\alpha} t_e}\right) \\ &= t_e \cdot N_0 + t_e \cdot N_0 \cdot \left(1-\frac{1}{a}\right) \cdot \left(1+\tilde{\alpha}\right) \end{aligned} \tag{11.63}$$

Using (11.53), we calculate the equivalent frequency bandwidth after step 2 as:

$$\Delta f_2 = \frac{1}{t_e} + \frac{t_e \cdot N_0}{\alpha} = \frac{1}{t_e} + \frac{t_e \cdot N_0}{t_e^{\,2} \cdot N_0 \cdot \tilde{\alpha}} = \frac{1}{t_e} \cdot \left(1+\frac{1}{\tilde{\alpha}}\right) \tag{11.64}$$

*Step 3*

After step 3, using (11.56) and (11.57), we can easily determine the complete frequency bandwidth as:

$$\begin{aligned} \Delta f_3 &= \frac{1}{t_e} + \frac{t_e N_0}{t_e^{\,2} N_0 \tilde{\alpha}} + \frac{a}{t_e^{\,2} N_0 \tilde{\alpha}} \cdot \left[ t_e N_0 + \tilde{\alpha} t_e^{\,2} N_0 \left(1-\frac{1}{a}\right) \cdot \left(\frac{1}{t_e} + \frac{t_e N_0}{t_e^{\,2} N_0 \tilde{\alpha}}\right) \right] \\ &= \frac{1}{t_e} + \frac{1}{\tilde{\alpha} t_e} + \frac{a}{t_e^{\,2} N_0 \tilde{\alpha}} \cdot \left[ t_e N_0 + t_e N_0 \left(1-\frac{1}{a}\right) \cdot \left(1+\tilde{\alpha}\right) \right] \\ &= \frac{1}{t_e} \cdot \left(1 + \frac{1}{\tilde{\alpha}} + \frac{a}{\tilde{\alpha}} + \frac{a}{\tilde{\alpha}} \cdot \left(1-\frac{1}{a}\right) \cdot \left(1+\tilde{\alpha}\right)\right) \end{aligned} \tag{11.65}$$

We simplify the above equation and obtain:

$$\Delta f_3 = \frac{1}{t_e} \cdot \left(1 + \frac{1}{\tilde{\alpha}} + \frac{a}{\tilde{\alpha}} + \left(a-1\right) \cdot \left(1+\frac{1}{\tilde{\alpha}}\right)\right) \tag{11.66}$$

Considering (11.55), the time extent is calculated as:

$$\begin{aligned} T_3 &= t_e \cdot N_0 + \tilde{\alpha} \cdot t_e^{\,2} \cdot N_0 \cdot \left(1-\frac{1}{a}\right) \cdot \left(\frac{1}{t_e} + \frac{t_e \cdot N_0}{\tilde{\alpha} \cdot t_e^{\,2} \cdot N_0}\right) \\ &= t_e \cdot N_0 + t_e \cdot N_0 \cdot \left(1-\frac{1}{a}\right) \cdot \left(1+\tilde{\alpha}\right) \end{aligned} \tag{11.67}$$

*Step 4*

At step 4, we use (11.57), (11.58) and obtain the final frequency bandwidth:

$$\Delta f_4 = \Delta f_3 = \frac{1}{t_e} \cdot \left(1 + \frac{1}{\tilde{\alpha}} + \frac{a}{\tilde{\alpha}} + \left(a-1\right) \cdot \left(1+\frac{1}{\tilde{\alpha}}\right)\right) \tag{11.68}$$

The complete time extent is determined using the equation (11.58):

$$\begin{aligned} T_4 &= t_e \cdot N_0 + t_e \cdot N_0 \cdot \left(1-\frac{1}{a}\right) \cdot \left(1+\tilde{\alpha}\right) + \tilde{\alpha} \cdot t_e^{\,2} \cdot N_0 \cdot \left(\frac{1}{a^2}-\frac{1}{a}\right) \cdot \left(1 + \frac{1}{\tilde{\alpha}} + \frac{a}{\tilde{\alpha}} + \left(1+\frac{1}{\tilde{\alpha}}\right) \cdot \left(a-1\right)\right) \\ &= t_e N_0 \left[ 1 + \left(1-\frac{1}{a}\right) \cdot \left(1+\tilde{\alpha}\right) + \left(\frac{1}{a^2}-\frac{1}{a}\right) \cdot \left(\tilde{\alpha} + a + 1 + \left(1+\tilde{\alpha}\right) \cdot \left(a-1\right)\right) \right] \end{aligned} \tag{11.69}$$

At the end of the algorithm, the bandwidth of the signal is resized by the scaling factor. Therefore, the actual scaling factor is calculated as:

$$a_{act} = \frac{\Delta f_4}{\Delta f} = 1 + \frac{1}{\tilde{\alpha}} + \frac{a}{\tilde{\alpha}} + (a-1)\cdot\left(1 + \frac{1}{\tilde{\alpha}}\right) \tag{11.70}$$

Appropriately selecting $\tilde{\alpha}$ and $a$ factors, we can obtain the necessary scaling effect.

## B.4 Chirp Scaling algorithm –simulated result

To verify the validity of the Chirp Scaling algorithm we simulate a very extreme case, where the scaling is required with the scaling coefficient equal to 0.5. We have experienced this kind of situation in the processing of the hybrid bistatic configuration described in section 2.4.1. In this case, the azimuth time variance of the bistatic processing causes the scaling of the azimuth frequency with a factor of the 0.5. The compensation of a big scaling was impossible to achieve by the Inverse Scaling approach. Additionally, after the azimuth scaling we needed to stay in the frequency domain, so the Chirp Scaling algorithm was more preferable.

In one direction we have a sampling with a frequency of 8000 Hz, and six point targets are distributed at the positions 300, 800, 1300, 1500, 2500 and 5000, visible in Figure 11.6:

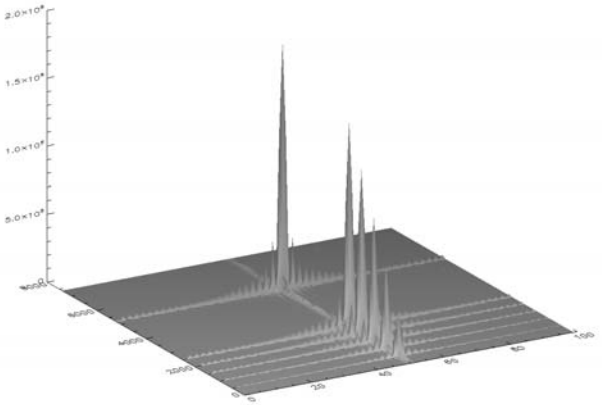

Figure 11.6. Initial location of the point targets

The magnitudes of the PTs are intentionally increased for better observation of the processing effect.

In Figure 11.7, we have the result after applying the Chirp Scaling algorithm. All PTs are focused correctly and allocated at the correct positions. The algorithm is quite complex and long. In order to decrease the processing time, we slightly simplify the algorithm by using some approximations. These approximations cause an error on the magnitude of the last PT, but it is actually not a big problem. At the beginning of most of the processing algorithms, the zeros are padded to the end of the scene in order to perform a correct convolution. Therefore, the erroneous result in the end of the scene can be ignored, because at the location of the last PT we have zeros anyway.

The position of the last PT after the end of the Chirp Scaling algorithm is calculated as:

$$\begin{aligned} Nnew &= Nold \cdot \frac{timeSamplingUnitOld}{timeSamplingUnitNew} \cdot \frac{1}{scalingFactor} \\ &= 5000 \cdot 0.50 \cdot \frac{1}{0.5} = 5000.06 \end{aligned} \tag{11.71}$$

*Nnew* is the new position of the PT and *Nold* is the old position.
*timeSamplingUnitOld* is the initial sampling time and *timeSamplingUnitNew* is the sampling time at the and of the processing.
*scalingFactor* is the required scaling factor.

This result is in good accordance to the real allocation of the 6th PT given in Figure 11.6:

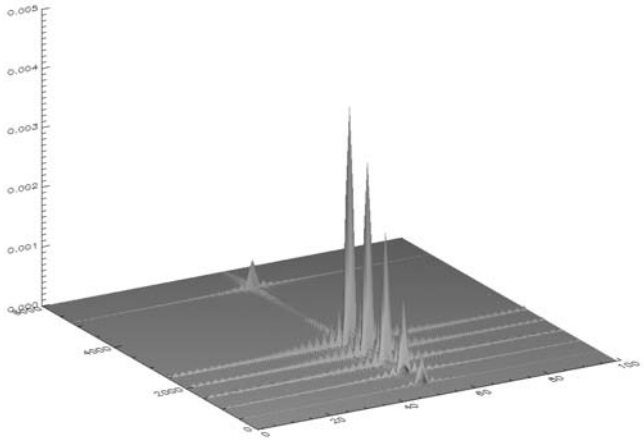

Figure 11.7. The result after the Chirp Scaling algorithm

# C Radon Transformation

The Radon transformation [36] converts lines from the Cartesian coordinates into points in the polar domain. Suppose that we have a 2D function $u(x_1, x_2)$ and we are looking for the parallel projection of $u(x_1, x_2)$ along the direction $T$. The parallel projection of a 2D signal can be understood as a convolution with a Dirac line perpendicular to the line of projection, as seen in Figure 11.8.

Now we convert Dirac line to polar coordinates:

$$\delta(\mathbf{g}\cdot\mathbf{x}) = \delta(R)\cdot 1(T) \tag{11.72}$$

$\mathbf{g}$ is a unit vector normal to the Dirac line. The 2D signal $u(x_1, x_2)$ in polar coordinates is given as: $u_\varphi(R,T) = u(x_1, x_2)$. The result of the convolution of the Dirac line with $u_\varphi(R,T)$ is a parallel projection, and we abbreviate it as $u_p(R,T)$:

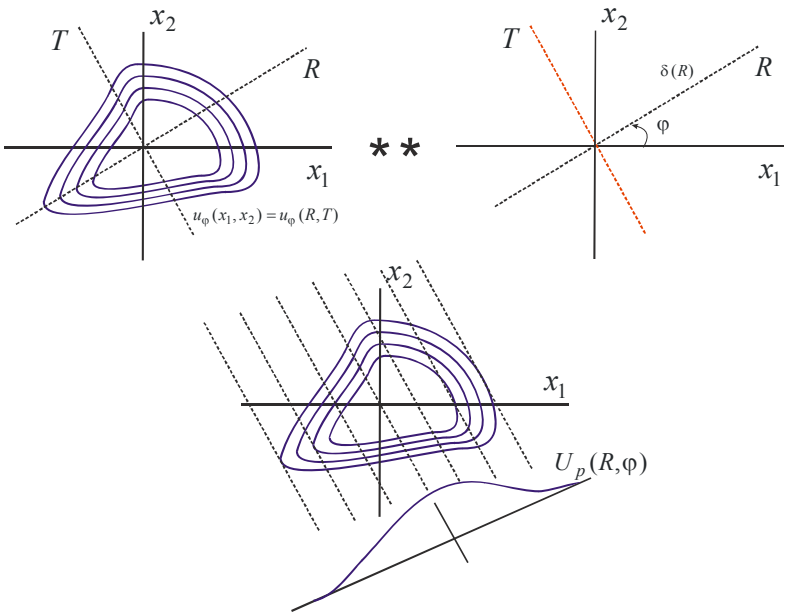


Figure 11.8. Parallel projections of a 2D signal by the convolution with the Dirac line

Using (11.72) we express the parallel projections using the line integral in the polar coordinates:

$$u_p(R,\varphi) = \int_{-\infty}^{\infty} u_\varphi(R,T)\cdot dT = u_\varphi(R,T) ** \delta(R) \tag{11.73}$$

The integral given in (11.78) expresses the Radon transformation. It was first introduced in [61]. The Radon transformation calculates the integrals over the lines and then gives the result in polar coordinates. It is widely used in the X-Ray tomography.

## C.1 Central Slice Theorem

Very often, the Radon transformation is associated with the Central Slice theorem. Generally for any 1D signal, we can write:

$$\int_{-\infty}^{\infty} u(t)\,dt = U(0) \tag{11.74}$$

This property comes directly from the Fourier integral after inserting the value $f = 0$. (11.74) can be generalized for the multidimensional functions:

$$\int_{-\infty}^{\infty} u(\mathbf{x})\,d\mathbf{x} = U(\mathbf{0}) \tag{11.75}$$

where $\mathbf{0} = (0,0,...,0)^T$ is a null vector.

(11.75) was obtained after the integration of all the variables of the multidimensional function.

It is interesting to find out what kind of result we will get if we perform the integration with only some variables and then do projection across the rest of the variables. We consider this task for 2D functions. We use $R,T$ polar coordinates as shown in Figure 11.8. We abbreviate the frequency axes as $f_R, f_T$. They are oriented in the same way as $R,T$ axes. We calculate the Fourier spectrum as:

$$u(x_1,x_2) =: u_\varphi(R,T) \circ\!\!-\!\!\bullet\, U_\varphi(f_R,f_T) := U(f_1,f_2) \tag{11.76}$$

which is equivalent to:

$$U_\varphi(f_R,f_T) = \int_{-\infty}^{\infty}\int_{-\infty}^{\infty} u_\varphi(R,T)\,e^{-j2\pi(R\cdot f_R + T\cdot f_T)}\,dR\,dT \tag{11.77}$$

By setting $f_T = 0$, we get

$$U_p(f_R,\varphi) = \int_{-\infty}^{\infty}\left[\int_{-\infty}^{\infty} u_\varphi(R,T)\,dT\right]\cdot e^{-j2\pi R\cdot f_R}\,dR = \int_{-\infty}^{\infty} u_p(R,\varphi)\cdot e^{-j2\pi R\cdot f_R}\,dR \tag{11.78}$$

$U_p(f_R,\varphi)$ is the slice of 2D spectrum at the origin and taken on $\varphi$ direction. ($u_p(R,\varphi)$ is the projection of the 2D function $u(x_1,x_2)$ in direction $T$ evaluated across the $R$ axes).

The equation above represents the Central Slice theorem. We write it in another way:

$$\boxed{\int_{-\infty}^{\infty} u_\varphi(R,T)\,dT = u_p(R,\varphi) \;\circ\!\!-\!\!\bullet\; U_p(f_R,\varphi) = U_\varphi(f_R,f_T=0)} \tag{11.79}$$

The Central Slice theorem can be formulated in the following way: the spectrum of the projected signal can be calculated by taking the slice of original signal spectrum; the slice is taken at the origin and at the perpendicular to the projection direction.

## C.2 Another Interpretation of Central Slice Theorem – Fourier Spectrum of Dirac points, Dirac lines and Dirac planes

Generally for 1D signals, the following correspondence is valid:

$$\delta(t) \circ\!\!-\!\!\bullet\, 1 \;\; and \;\; 1 \circ\!\!-\!\!\bullet\, \delta(f) \tag{11.80}$$

We use the shifting property of Fourier transformation and write:

$$\delta(t-t_0) \circ\!\leftrightarrow\!\bullet\; e^{-j2\pi t_0 f} \quad and \quad e^{j2\pi f_0 t} \circ\!\leftrightarrow\!\bullet\; \delta(f-f_0) \tag{11.81}$$

In the multidimensional case with separable variables, the Fourier transformation is calculated by separating the variables. Hence, for a multidimensional Dirac point with separable variables, the following is valid:

$$\delta(\mathbf{x}) = \delta(x_1)\cdot\delta(x_2)\cdot\ldots\delta(x_n) \circ\!\leftrightarrow\!\bullet\; 1(f_1)\cdot 1(f_2)\cdot\ldots 1(f_n) = 1 \tag{11.82}$$

For a multidimensional Dirac point, we have the analogue of the 1D expression:

$$\delta(\mathbf{x}-\mathbf{x}_0) \circ\!\leftrightarrow\!\bullet\; e^{-2\pi \mathbf{x}_0\cdot\mathbf{f}} \tag{11.83}$$

Now we return to the 2D case. For the Dirac lines within a plane, we have:

$$\delta(x_1) = \delta(x_1)\cdot 1(x_2) \circ\!\leftrightarrow\!\bullet\; 1(f_1)\cdot\delta(f_2) \tag{11.84}$$

The expression (11.84) can be visualized graphically, as shown in Figure 11.9:

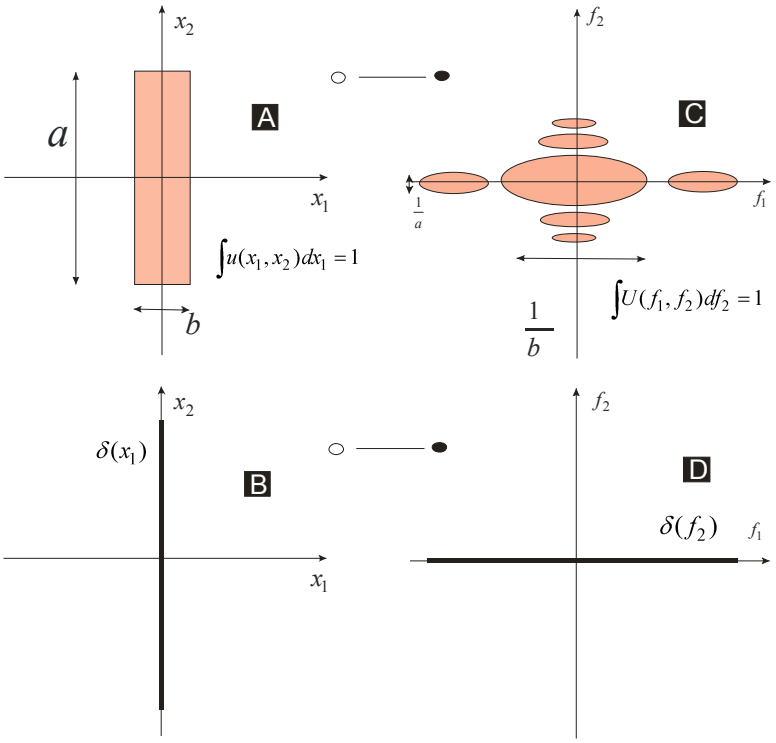


Figure 11.9. Fourier transform of a Dirac line in 2D space

The Dirac line can be interpreted as a rectangle with one side going to zero; this rectangle is displayed in /A/. We consider the case when the side $b$ vanishes and another side increases to infinity keeping the underling area constant. In the limiting case, we will obtain a Dirac line as shown in /B/. Now we observe the corresponding scenario in the Fourier domain. The spectrum corresponding to the rectangle is a 2D $si$ function shown in /C/. Generally, it is known that the time scaling causes an inverse scaling in frequency domain. Therefore, the spectrum in /C/ will be stretched horizontally; in a limit case, the function $\frac{si\left(\frac{\pi f}{\varepsilon}\right)}{\varepsilon}$ (when $\varepsilon \to 0$) approaches the $\delta(f)$ function. Hence, the time domain Dirac line

will be transformed as well to the Dirac line in frequency domain as shown in /D/. Time and frequency Dirac lines will be orthogonal to each other.

As discussed above, the parallel projection of 2D signal can be considered as a convolution with a Dirac line. This convolution in time domain is equivalent to a multiplication in frequency domain by the Dirac line. Therefore a multiplication by a frequency Dirac line will be equivalent to a slice of a spectrum at the origin. That is why Radon transformation is often associated with the multidimensional Central Slice theorem.

# References

[1] O. Loffeld, H. Nies, V. Peters, S. Knedlik, ‘Models and Useful Relations for Bistatic SAR Processing’, *IEEE Transactions on Geoscience and Remote Sensing,* Vol. 42, No. 10, Oct 2004

[2] O. Loffeld, H. Nies, U. Gebhardt, V. Peters, S. Knedlik, ‘Bistatic SAR - Some Reflections on Rocca's Smile’, *Proc. EUSAR04, European Conference on Synthetic Aperture Radar,* Ulm, Germany, May 2004

[3] O. Loffeld, A. Hein, ‘SAR Processing by ‘Inverse Scaled Fourier Transformation’, Proc. EUSAR96, *European Conference on Synthetic Aperture Radar*, Königswinter, Germany, 1996

[4] O. Loffeld, F. Schneider, A. Hein, ‘Focusing SAR images by Inverse Scaled Fourier Transformation’, *Proc. International Conference on Signal Processing and Communication*, Las Palmas, Gran Canaria, 1998

[5] O. Loffeld, ‘Allgemaine Nachrichtentechnik’, Vorlesung, Script of Communication Engineering, Siegen, 2002

[6] O. Loffeld, ‘Derivation of Chirp Scaling Algorithm’, ZESS, Siegen, 2004, unpublished notes

[7] O. Loffeld, K. Natroshvili, H. Nies, U. Gebhardt, S. Knedlik, A. Medrano Ortiz, A. Amankwah, ‘2D-Scaled Inverse Fourier Transformation for Bistatic SAR’, *European Conference on Synthetic Aperture Radar,* Dresden, Germany, 2006

[8] O. Loffeld, ‘Bistatic SAR Processing and Rocca´s Smile, Invited Talk,’ presented at *4th DLR/CNES Workshop ‘Methods and Techniques for meter resolution’*, Munich, Germany, 2003

[9] K. Natroshvili, O. Loffeld, H. Nies, A. Medrano Ortiz, ‘First Steps to Bistatic Focusing’, *Proc. IGARSS05, International Geoscience and Remote Sensing Symposium*, Seoul, Korea, 2005

[10] K. Natroshvili, O. Loffeld, H. Nies, ‘Focusing of Arbitrary Bistatic SAR Configurations’, *European Conference on Synthetic Aperture Radar,* Dresden, Germany, 2006

[11] K. Natroshvili, O. Loffeld, ‘Comparison of Bistatic SAR Focusing Approaches’, EUSAR06, *European Conference on Synthetic Aperture Radar,* Dresden, Germany, 2006

[12] K. Natroshvili, O. Loffeld, H. Nies, A. Medrano Ortiz,, S. Knedlik, 'Focusing of General Bistatic SAR configuration data with 2D Inverse Scaled FFT', *IEEE Transactions in Geoscience and Remote Sensing*, Vol. 44, No 10, Oct 2006

[13] K. Natroshvili, T. Müller, 'Spatial Channel Modeling for Mobile Application in Frequency Range 100-800MHz', Daimler Research Center, internal report, Ulm, Nov 2004

[14] K. Natroshvili, T. Müller, 'DOA in Frequency Range 200-800MHz with MUSIC Algorithm', Daimler Research Center, internal report, Ulm, Jan 2005

[15] K. Natroshvili, O. Loffeld, H. Nies, V. Peters, 'Determination of stationary scatterers in bistatic SAR images with spectral analysis and bandlimited extrapolation', *Proc. ASTRO06*, Montreal, Canada, Apr 2006

[16] K. Natroshvili, O. Loffeld, H. Nies, J. H. Ender, 2D inverse scaling bistatic processing and the focused image quality measurements, *Proc*. *IGARSS06, International Geoscience and Remote Sensing Symposium,* Denver, Colorado, US, Aug 2006

[17] A. M. Ortiz, O. Loffeld, S. Knedlik, H. Nies, K. Natroshvili, 'Comparison of Doppler Centroid Estimators in Bistatic Airborne SAR', *Proc*. *IGARSS05, International Geoscience and Remote Sensing Symposium,* Seoul, Korea, 2005

[18] A. Medrano Ortiz, O. Loffeld, S. Knedlik, H. Nies, K. Natroshvili, Comparison of geometry – based Doppler Centroid Estimators in Bistatic Airborne SAR, Proc. EUSAR06, *European Conference on Synthetic Aperture Radar*, Dresden, Germany, 2006

[19] H. Nies, O. Loffeld, K. Natroshvili, I. Walterscheid, A. R. Brenner, 'Parameter Estimation for Bistatic Constellations', *Proc*. *IGARSS05, International Geoscience and Remote Sensing Symposium,* Seoul, Korea, 2005

[20] H. Nies, O. Loffeld, K. Natroshvili, Analysis and Focusing of Bistatic Airborne SAR Data, *Proc. EUSAR06, European Conference on Synthetic Aperture Radar,* Dresden, Germany, 2006 (This publication got Best Poster Award)

[21] H. Nies O. Loffeld, K. Natroshvili, Analysis and Focusing of Bistatic Airborne SAR Data, *Transactions on Geoscience and Remote Sensing*, Vol. 45, Pages 3342-2249, Nov 2007

[22] U. Gebhardt, O. Loffeld, H. Nies, K. Natroshvili, J. Ender, ,Bistatic Airborne / Space borne Hybrid Experiment: Simulation and Analysis, Proc. EUSAR06, *Conference on Synthetic Aperture Radar,* Dresden, Germany, 2006

[23] U. Gebhardt, O. Loffeld, H. Nies, S. Knedlik, 'Bistatic airborne / spaceborne hybrid experiment: Basic considerations', presented at *SPIE international Symposium on Remote Sensing*, Brügge, Belgium, 2005

[24] A. Hein, ‚Verarbeitung von SAR – Daten unter besonderes Berücksichtigung interferometrischer Anwendungen', Doctoral work

[25] R. Wang, O. Loffeld, Q. Ul-Ann, H. Nies, A. Medrano Ortiz, A. Samarah, 'A Bistatic Point Target Reference Spectrum for General Bistatic SAS Processing', *Geoscience and Remote Sensing Letters*, Vol. 5, No. 3, July 2008

[26] R. Wang, O. Loffeld, Q. Ul-Ann, H. Nies, A. Medrano Ortiz, A. Samarah, 'Analysis and Processing of Spaceborne/Airborne Bistatic SAR Data', *Proc. IGARSS08, International Geoscience and Remote Sensing Symposium,* Boston, Massachusetts, US, July 2008

[27] D. D'Aria, A. Monti Guarnieri, F. Rocca, 'Focusing Bistatic Synthetic Aperture Radar using Dip Move Out', *IEEE Transactions Geoscience and Remote Sensing*, vol. 42, pp.1362-1376, July 2004

[28] A. Monti Guarnieri, F. Rocca, 'Reduction to Monostatic Focusing of Bistatic or Motion Uncompensated SAR Surveys', *Radar Sonar and Navigation, IEEE Proceedings*, Vol. 153, Issue 3, June 2006

[29] J. Ender, I. Walterscheid, A. Brennner, 'New Aspects of Bistatic SAR: Processing and Experiments', *Proc. IGARSS04, International Geoscience and Remote Sensing Symposium,* Anchorage, Sept 2004

[30] J. Ender, 'Bistatic SAR Processing', *Proc. EUSAR'04, European Conference on Synthetic Aperture Radar*, Ulm, Germany, May 2004

[31] I. Walterscheid, J. Ender, A. R. Brenner, O. Loffeld, 'Bistatic SAR Processing Using an Omega-k Type Algorithm', *Proc*. *IGARSS05, International Geoscience and Remote Sensing Symposium*, Seoul, Korea, 2005

[32] I. Walterscheid, A. Brenner, J. Ender, O. Loffeld, 'A bistatic Airborne SAR experiment and Processing Results', *presented at IRS, International Radar Symposium*, Berlin, Germany, 2005.

[33] I. Walterscheid, J. Klare, A. R. Brenner, J. Ender, O. Loffeld, 'Challenges of a Bistatic Spaceborne/Airborne SAR Experiment', *Proc. European Conference on Synthetic Aperture Radar,* Dresden, Germany, 2006

[34] A. Papoulis, 'Systems and Transforms with Applications in Optics', *McGraw-Hill*, pp. 203-204, New York, 1968

[35] R. Bamler, E. Boerner, 'On the Use of Numerically Computed Transfer Functions for Processing of Data from Bistatic SAR and High Squint Orbit SARs', *Proc. IGARSS05, International Geoscience and Remote Sensing Symposium*, Seoul, Korea, 2005

[36] R. Bamler, ‚Mehrdimensionale lineare Systeme-Fourier Transformation und δ Functionen'*, Springer Verlag, 1989,* ISBN 3-540-51069-9

[37] R. Bamler, 'A Comparison of Range-Doppler and Wavenumber Domain SAR Focussing Algorithms', *IEEE Transactions on Geoscience and Remote Sensing*, vol. 30, pp. 706-713, 1992

[38] H. Runge, R. Balmer, 'A Novel High Precision Focusing Algorithm Based on Chirp Scaling', *Proc. IGARSS92, International Geoscience and Remote Sensing Symposium,* pp.372-375, Houston, US, 1992

[39] A. Moreira, J. Mittermayer, R. Schreiber, 'Extended Chirp Scaling Algorithm for Air- and Spaceborne SAR Data Processing in Stripmap and ScanSAR Imaging Modes', *IEEE Transactions on Geoscience and Remote Sensing*, vol. 34, no 5, 1996

[40] A. Moreira, G. Krieger, I. Hainsek, D. Hounam, M. Werner, 'Tandem-X: A Terra SAR-X Add-On Satellite Single-Pass SAR Interferometry, *International Conference on Radar System,* Toulouse, France, 2004

[41] R. K. Raney, H. Runge, R. Bamler, I. Cumming, and F. H. Wong, 'Precision SAR Processing Using Chirp Scaling', *IEEE Transactions on Geoscience and Remote Sensing*, Vol. 32, pp. 786 - 799, 1994

[42] J. Mittermayer, A. Moriera, O. Loffeld, 'Spotlight SAR Data Processing Using the Frequency Scaling Algorithm', *IEEE Transactions on Geoscience and Remote Sensing,* Vol. 37, No. 5, Sept 1999

[43] G. Krieger, N. Gebert, A. Moreira, 'SAR Signal Reconstruction from Non-Uniform Displaced Phase Centre Sampling', *Proc. EUSAR'04, European Conference on Synthetic Aperture Radar,* Ulm, Germany, May 2004

[44] G. Krieger, 'Bi- and Multistatic SAR: Potentials and Challenges', *Proc. EUSAR04, European Conference on Synthetic Aperture Radar*, Ulm, Germany, May 2004

[45] G. Krieger, H. Fiedler, J Mittermayer, K. Papathanassiou, A. Morriera, 'Analysis of Multistatic Configurations for Spaceborne SAR Interferomerty', *IEEE Proc. Radar, Sonar, Navigation*, 150(3), 2003, pp. 87-96

[46] G. Krieger, H. Fielder, I. Hainsek, M. Einder, M. Werner, A. Moreira, 'TanDEM-X: Mission Concept and Performance Analysis', *Proc. IGARSS05, Geoscience and Remote Sensing Simposium,* Seul, Korea, 2005

[47] G. Krieger, A. Moreira, H. Fiedler, I. Hajnsek, M. Zink, M. Werner, 'TanDEM-X: Mission Concept, Product Definition and Performance Prediction', *European Conference on Synthetic Aperture Radar,* Dresden, Germany, 2006

[48] H. Cantalloube, M. Wendler, V. Giroux, P. Dubuoi-Fernandez, G. Krieger, 'Challenges in SAR Processing for Airborne Bistatic Acquisitions', *Proc. EUSAR04, European Conference on Synthetic Aperture Radar,* Ulm, Germany, May 2004

[49] D. Massonet, 'The Interferometric Cartwheel, a Constellation of Low Cost Receiving Satellites to Produce Radar Images that can be Coherently Combined'*, International Journal of Remote Sensing,* vol. 22, no. 12, pp. 2413-2430, 2001

[50] S. Maybeck, 'Stochastic Models, Estimation and Control', Vol I, Vol III, *Academic Press*, 1979

[51] A. Papoulis, 'Signal and Analysis', ISBN 0-07-048460-0, *McGraw-Hill Book Company*, 1977

[52] A. Papoulis, 'Probability, Random Variables and Stochastic Processes', *McGraw-Hill Series in Electrical Engineering*, 1984, ISBN 0-07-Y66465-X

[53] A. Papoulis, 'A New Algorithm in Spectral Analysis and Band-Limited Extrapolation', *Transactions on Circuits and Systems,* Vol cas-22, No 9, Sept 1975

[54] S. Mitra, M. P. Ekstrom 'Two Dimensional Digital Signal Processing'*, Dowden, Hutchinson & Ross, Inc.* 1978

[55] F. M. Wahl, ,Digitale Bilsignalverarbeitung', *Springer-Verlag* 1989, ISBN 0-387-13586-3

[56] W. K. Pratt, 'Digital Image Processing', *A Wiley-Interscience Publication*, 1978, ISBN-0-471-01888-0

[57] Snit K. Mitzra, M. P. Ekstrom, 'Two Dimensional Digital Signal Processing', *Dowen, Hutchinson & Ross, Inc.* 1978, ISBN 0-97933-320-0,

[58] C. Oliver, S. Quegan, 'Understanding Synthetic Aperture Radar Images', *Artech House, Inc*, 1998, ISBN 089006850X

[59] M. Soumekh, 'Synthetic Aperture Radar, Signal Processing with Matlab Algorithms', *John Wiley & Sons,* Inc1999, ISBN 0-471-29706-2

[60] H. Klausing, W. Holpp, 'Radar mit Realer und Synthetischer Aperture', *Oldenbourg Wissenschaftsverlag Gmbh, 2000, ISBN 3-486-23475-7*

[61] J. Radon, ‚Über die Bestimmung von Functionen durch ihre Integralwerte Läangs gewisser Mannigfaltigkeiten, Berichte über die Verhandlungen der Königlich Sächsischen Gesellschaft der Wissenschaften – Mathem. Physik. Klasse 69, 262-227, 1917

[62] C. Cafforio, C. Prati, and F. Rocca, "SAR Data Focusing using Seismic Migration Techniques," *IEEE Transactions on Aerospace and Electronic Systems*, vol. 27, pp. 194 - 207, 1991.

[63] R. Lanari, "A New Method for the Compensation of the SAR Range Cell Migration Based on the Chirp Z-Transform," *IEEE Transactions on Geoscience and Remote Sensing,* Pasadena, CA, USA, vol. 33, pp. 1296 - 1299, 1995.

[64] N. Willis, 'Bistatic Radar', *Artech House*, Boston 1991

[65] M. Martin, P. Klupar, S. Kilberg, J. Winter, 'Techsat 21 and Revolutionizing Space Missions using Microsatellites', *15th American Institute of Aeronautics and Astronautics Conference on Small Satellites*, Utah, 2001

[66] N. B. Evans, P. Lee, R, Gitrad, 'The RADARSAT 2/3 Topographic mission' EUSAR02, Cologne, Germany, 2002

[67] C. Prati, F. Rocca, D. Giancola, A. Monti Guarnieri, 'Passive Geosynchronous SAR System Reusing Backscattering Digital Audio Broadcasting Signals' *IEEE Trans. Geoscience and Remote Sensing,* Vol 36, No 6, pp. 1973-1976, 1978

[68] P. Doubois et al. Analysis of Bistatic Scattering Behavior of Natural Surfaces, EUSAR04, *European Conference on Synthetic Aperture Radar,* Ulm, Germany, 2004

[69] N. A. Goodman, S. C. Lin, D. Rajakrishna, J. M. Stiles, 'Processing of Multiple-Receiver Spaceborne Arrays for Wide Area SAR, *IEEE Transactions Geoscience and Remote Sensing* 40(4), pp 841-852, 2002

[70] G. Gerchberg, 'Super Resolution Through Error Energy Reduction', *Optica Acta,* 1974, Vol. 21, No 7009-720

[71] I. G. Cumming, F. H. Wong, 'Digital Processing of Synthetic Aperture Radar Data', Artech House, Inc., 2002, 1-58053-058-3

[72] F. M. Henderson, A. J. Lewis, 'Manual of Remote Sensing', Volume 2: Principles and applications of Image Radar. John Wiley & Sons, New York, 3rd edition, 1998

[73] R. H. Stolt, 'Migration by Fourier Transform', *Geophysics,* Vol43, No1, P23-48 Feb, 1978

[74] F. Wong, T. Yeo, 'New Applications of Nonlinear Chirp Scaling in SAR Data Processing', *IEEE Transactions of Geoscience and Remote Sensing*, Vol. 39, No. 5, May 2001

[75] Y. L. Neo, F. H. Wong, I. Cumming, 'Focusing Bistatic SAR Images using Non-Linear Chirp Scaling, Radar 2004*, International Conference on Radar Systems*

[76] Y. L. Neo, F. Wong, I. Cumming, 'A two-dimensional spectrum for bistatic SAR processing', *Geoscience and Remote Sensing Letters* (GRSL-00102-2006)

[77] R. Goldstein, P. Rosen, C. Werner, 'ERS-1 Bistatic Radar Images', *Proc. IGARSS94*, *International Geoscience and Remote Sensing Symposium*, Pasedena, 1994

[78] D. Ausherman, A. Kozma, J. Walker, H. Jones, E. Poggio, 'Developments in radar imaging, *IEEE Transactions on Aerospace and Electronic Systems*, Vol. 20, pp. 363, July 1984

[79] J. L. Auterman, 'Phase stability requirements for a bistatic SAR', *IEEE National Radar Conference*, Atlanta, US, March 1984